A STUDY OF LANTHANUM NICKELATE CATHODES FOR EMPLOYMENT IN SOLID OXIDE FUEL CELLS

by

CHRISTOPHER HARRISON

A thesis submitted to the University of Birmingham for the degree of

DOCTOR OF PHILOSOPHY

Centre for Doctoral Training in Fuel Cells and their Fuels

School of Chemical Engineering

College of Engineering and Physical Sciences

University of Birmingham

February 2023

UNIVERSITY OF
BIRMINGHAM

University of Birmingham Research Archive

e-theses repository

This unpublished thesis/dissertation is copyright of the author and/or third parties. The intellectual property rights of the author or third parties in respect of this work are as defined by The Copyright Designs and Patents Act 1988 or as modified by any successor legislation.

Any use made of information contained in this thesis/dissertation must be in accordance with that legislation and must be properly acknowledged. Further distribution or reproduction in any format is prohibited without the permission of the copyright holder.

Abstract

The current state-of-the-art cathode materials used in Solid Oxide Fuel Cells (SOFC) are doped lanthanum cobaltite perovskites (e.g. $La_{0.6}Sr_{0.4}Co_{0.2}Fe_{0.8}O_3$ (LSCF6428)). These ceramics, with the ability to transport both electrons and oxygen ions through their crystal lattice are employed in many commercial cells available today. However, there are several degradation-related concerns relating to these materials and there have been numerous attempts to explore alternatives. One family of materials that has been suggested to offer promise in overcoming these issues is the lanthanum nickelates (e.g. doped $LaNiO_3$, La_2NiO_4). In particular, it has been suggested by a number of researchers that these materials can alleviate the degradation associated with so-called chromium poisoning. However, despite some apparent associated advantages, a move away from the use of lanthanum cobaltite cathodes has failed to materialise. One possible reason for this is that, simply, these alternatives offer an inferior standard of performance in comparison with the conventional materials. However, given the sheer volume of research work in this area and the very many attempts to characterise and optimise electrode performance, it can be difficult to 'benchmark' materials and understand the performance range that is achievable. Further, many authors fail to offer direct comparisons with the state-of-the-art, often making results difficult to interpret due to a lack of a relative comparison. The work detailed in this thesis attempts to address this by offering a more direct understanding of how lanthanum nickelate electrodes perform in relation to the state-of-the art. Importantly, this can help to inform on future research directions in this area.

In this work, the lanthanum nickelates are shown to offer relatively inferior performance in comparison with the state-of-the-art LSCF. This is apparent both by considering data in the literature (Chapter 2) and by conducting direct comparisons under the same experimental conditions (Chapters 4 and 5). This would appear to contradict statements around the suitability of the lanthanum nickelates in replacing state-of-the-art electrodes. However, it is also apparent that the performance

of materials can be optimised via a number of routes. Notably, an increase in electrode sintering temperatures is shown to promote electrode performance. This improvement is thought likely to be associated with enhanced electrode morphology and particle connectivity. A further approach to boosting lanthanum nickelate electrode performance is to combine them with other phases to form composite electrodes. In particular, the combination of $LaNi_{0.6}Fe_{0.4}O_3$ (an excellent electronic conductor) with an oxide conducting phase (e.g. GDC) has been shown to offer real promise in this regard.

In addition to observations on the performance of the studied materials, the extent of the experimental work conducted in this thesis (and the breadth of the materials studied) allows for some comment on certain SOFC testing approaches. Firstly, it has been shown that the use of noble metal pastes (often applied to electrodes in experimental works to provide electrical contact) can disproportionately impact on the reported performance of electrode materials. For those electrode materials with relatively low electrical conductivity, for example, the addition of gold paste can significantly enhance electrode performance. This effect is lessened for materials with more favourable conductivity properties. This creates an interesting dilemma with respect to comparing results across different studies (where pastes may or may not be applied).

As is evident in the literature, the so-called symmetrical cell testing approach is a common means by which the performance of electrodes can be quantified. These tests have several advantages (including the ability to remove associated contributions from the anode side of the cell). However, as is shown in Chapter 5, the conclusions that may be drawn from such tests can be misleading; the results from the symmetrical cell testing methodology (performed at a 'zero current' condition) do not always correspond well with those recorded in more conventional 'single cell' testing approaches (i.e. performance under polarisation). This is a notable finding given the prevalence of this testing approach in the literature, with some authors using this as a sole means of identifying promising materials. The results from this thesis suggest that such a singular approach should be avoided.

Acknowledgements

I have been lucky enough to spend my PhD experience with some excellent friends in both the chemistry and chemical engineering departments at the University of Birmingham. This network of peers has offered both technical and emotional support throughout the last few years and this work would not have come to fruition without them. Special mentions must go to my SOFC pals Zeyu Jiang, Bhargav Pandya, Abigail Snowdon and Abu Siddiq who I have worked closely with over the last few years and to Matt James and Abbey Jarvis whose chemistry-based support in the early days of this PhD was invaluable. I would also like to take this opportunity to thank my supervisors, Professor Robert Steinberger-Wilckens, for granting me the opportunity to return to academia to study for this PhD and for his valued SOFC expertise during this work, and to Professor Peter Slater for helping me to navigate the intriguing world of solid-state chemistry. Additionally, I must also acknowledge the fantastic support I have received from, and thank, the many talented academics, technical staff and post-docs at the university and beyond (Dr Ahmad El-kharouf, Dr James Courtney, Dr Bernardo Sarruf, Dr Kun Zhang, Dr Satish Pandiyan, Dr Dino Klotz, Dr Alan Martin, Dr Ludwig Schneider, Dr Jackie Deans, Chyntol Kanhimbe and Manzo Brown). Thanks must also go to Dr Tom Harrison for his support with often quite random queries around the English language and academia, to Chloe Harrison for her unique perspectives on life and to my good friend Rich Walker, a constant inspiration. Finally, a special mention must go to Shirley Harrison, Eddie Harrison and Niamh Mobberley for their unwavering love and support; this thesis is dedicated to them.

Table of contents

Abstract I
Acknowledgements III
Table of contents IV
List of figures VIII
List of tables XV
Acronyms and abbreviations XVI
Nomenclature XVII
1 Introduction 1
1.1 Context 1
1.1.1 A crisis in climate and energy security 1
1.1.2 Renewables, electrification and its challenges 2
1.1.3 A 'hydrogen economy' and its challenges 4
1.2 Solid Oxide Fuel Cells 7
1.2.1 An introduction 7
1.2.2 Thermodynamics, efficiency and kinetics 9
1.2.3 Applications and industry advancement 12
1.3 SOFC materials 13
1.3.1 Material requirements 13
1.3.2 Electrolyte materials 16
1.3.3 Anode materials 17
1.3.4 Cathode materials 18
1.4 SOFC degradation processes 21
1.4.1 Fuel / oxidant impurities 21
1.4.2 Microstructural changes 22
1.4.3 Chemical incompatibility / secondary phase formation 23
1.5 Discussion 24
1.6 Overview of thesis goals 25
2 Literature review: replacing state-of-the-art cathode materials in SOFC 27
2.1 Overview of chapter 27
2.2 Drivers for change 27
2.2.1 Historical context: reducing operating temperature 27

2.2.2 Assessing degradation rates: are they too high? 28
2.2.3 Cathode degradation mechanisms 35
2.2.4 Cobalt: economic and ethical concerns 43
2.2.5 Discussion 44
2.3 Lanthanum nickelates – an alternative? 45
2.3.1 Background 45
2.3.2 Considerations on structure and stability 46
2.3.3 Properties 47
2.3.4 Fabrication challenges 55
2.3.5 Electrode performance 56
2.3.6 Degradation rates 65
2.4 Conclusion 71
3 Materials and methods 73
3.1 Overview of chapter 73
3.2 Synthesis methods 73
3.2.1 Solid-state 73
3.2.2 Pechini synthesis 74
3.3 Electrode preparation 76
3.3.1 Ball milling and sieving 76
3.3.2 Ink formulation 76
3.3.3 Deposition and sintering 76
3.4 Electrode testing 78
3.4.1 Symmetrical cell testing 79
3.4.2 Single cell testing 82
3.5 Physical characterisation techniques 88
3.5.1 X-Ray Diffraction 88
3.5.2 Scanning Electron Microscopy 91
4 Understanding the symmetrical cell performance of lanthanum nickelate electrodes: the effects of sintering temperature and Current Collector Layers 93
4.1 Overview of chapter 93
4.2 Synthesis 94
4.2.1 Solid State Route 95
4.2.2 Pechini Route 96
4.3 Symmetrical Cell Performance 100

4.3.1 Design of experiments 101
4.3.2 Comparison of Performance 103
4.3.3 Effect of precious metal contact layer 108
4.3.4 Effect of sintering temperatures 112
4.4 Phase behaviour analysis: the effect of sintering temperature 116
4.4.1 SEM imaging 116
4.4.2 Dilatometry 117
4.4.3 XRD reactivity study 118
4.4.4 Discussion on the effect of sintering temperature 125
4.5 Discussion on performance 125
4.5.1 Summarising the results from this study 125
4.5.2 Comparisons and comments on literature studies 127
4.6 Conclusions 128
5 On the performance of lanthanum nickelate electrodes under polarisation 131
5.1 Overview of chapter 131
5.2 Bench-Mark Testing with Commercial Single Cells 131
5.2.1 Procedural Development 132
5.2.2 Bench-mark metrics for LSCF-containing Commercial Cells 142
5.3 Assessing the performance of the La-Ni-O phases 144
5.3.1 Lanthanum nickelate cathodes 145
5.3.2 Analysis and Discussion 151
5.4 Conclusions from single cell tests 165
5.4.1 Main observations 165
5.4.2 Next Steps 168
6 Strategies for the optimisation of composite lanthanum electrode performance via appropriate material selection 170
6.1 Overview of chapter 170
6.2 Screening Electrodes (Symmetrical Cell Testing) 172
6.2.1 Overview of tests 172
6.2.2 LDC synthesis, reactivity and layer preparation 173
6.2.3 Symmetrical Cell Test Results 178
6.3 Single Cell Testing 185
6.4 Comparisons with literature data 193
6.5 Conclusions 195

7 Conclusions and outlook 198
7.1 Overview 198
7.2 The performance of lanthanum nickelate electrodes 198
7.3 Comments on SOFC testing approaches 202
7.4 Future Work 204
Appendix A - Fuel cell thermodynamics: the effect of operating temperature I
Appendix B - Conductivity and thermal expansion data v
Appendix C - Symmetrical cell performance ix
Appendix D - Single cell testing data from literature xix
Appendix E - XRD Data xxiv
Appendix F - Symmetrical cell data xxvii
Appendix G - Single cell data xxxv
Appendix H - LDCX Reactivity with LNO214 (1100˚C) xlii
Appendix I - Explainer of box and whisker plots xlvi
References xlvii

List of figures

Figure 1.1 - Extinction Rebellion protests in London, UK, attended by Greta Thunberg 1

Figure 1.2 - Energy usage in the UK; consumption of liquid fuels for transport, natural gas and electricity 4

Figure 1.3 - (a, left) Schematic of a Polymer Electrolyte Fuel Cell and (b, right) schematic of a Polymer Electrolyte Membrane Electrolyser. 6

Figure 1.4 - Schematics of (a, left) a Solid Oxide Fuel Cell and (b, right) a Solid Oxide Electrolyser. 8

Figure 1.5 - (a, top) The effect of different losses on the polarisation curve, (b, bottom) a comparison between the polarisation curves of a typical low and high temperature fuel cell.. 11

Figure 1.6 - Schematic of a planar fuel cell stack, illustrating the flow of gas, oxide ions and electrons. 13

Figure 1.7 - Different representations of the perovskite structure. 19

Figure 2.1 - Schematic showing the process of SrO segregation from LSCF. 36

Figure 2.2 - Voltage plot of galvanostatically-operated fuel cell stacks. The stacks contained an LSM-based cathode material and stainless-steel interconnects. 40

Figure 2.3 - Global cobalt production between 1970-2018. 43

Figure 2.4 - Cobalt production by country 44

Figure 2.5 - Conductivity of various La-Ni-O phases at 600, 700 and 800˚C, as reported in the literature. 49

Figure 2.6 - Effect of doping on the conductivity of ABO3-type lanthanum nickelates based on literature data 52

Figure 2.7 - Conductivity at 700˚C ($\sigma_{700^{\circ}C}$) vs thermal expansion coefficient (TEC) for various La-Ni-O perovskites.. 53

Figure 2.8 - Comparison of (a) tracer diffusion coefficients and (b) oxygen exchange coefficient for SOFC cathode various materials including La_2NiO_4, $LaNi_{0.6}Fe_{0.4}O_3$.. 54

Figure 2.9 - Nyquist diagram of an idealised RC circuit illustrating the relative position of the ohmic (R_o) and total (Z_{DC}) impedance values described in this chapter. 59

Figure 2.10 - Comparison of reported Rpol values across various studies for single phase electrodes. Chart shows the reported performance for La_2NiO_4 (n=1), $La_3Ni_2O_7$ (n=2), $La_4Ni_3O_{10}$ (n=3), $LaNi_{0.6}Fe_{0.4}O_3$ (LNF). 60

Figure 2.11 - Symmetrical Cell performance for different electrode configurations employing La_2NiO_4. Single phase ("S-P"), composite (Cmp) and infiltrated (Infil.) cathodes are shown. 62

Figure 2.12 - Symmetrical Cell performance for different electrode configurations employing $LaNi_{0.6}Fe_{0.4}O_3$. Single phase ("S-P"), composite (Cmp) and infiltrated (Infil.) cathodes are shown. 62
Figure 2.13 - Current density at 0.7V as reported in various articles; (a) Performance of single phase La-Ni-O electrodes, (b) performance of single phase, composite and infiltrated La_2NiO_4 electrodes, (c) performance of single phase, composite and infiltrated $LaNi_{0.6}Fe_{0.4}O_3$ electrodes. 64
Figure 3.1 - Schematic illustrations of the Pechini process. 75
Figure 3.2 - Schematic illustrating the (a) single cell and (b) symmetrical cell configurations 77
Figure 3.3 - Typical temperature ramp profile for electrode sintering in this study. 78
Figure 3.4 - Example of an electrode deposited via the described process. 78
Figure 3.5 - Schematic of symmetrical cell set-up. 81
Figure 3.6 - Disassembled cell holders with electrical, gas and thermocouple connections shown 84
Figure 3.7 - Schematic of cell holder with cell, current collector and mica gasket. 84
Figure 3.8 - Simplified schematic of cell test set-up. 85
Figure 3.9 - Temperature programme for heating and cooling employed for single cell testing. 86
Figure 3.10 - Schematic demonstrating the diffraction grating analogy of planes of atoms. 89
Figure 3.11 - (a) Schematic illustrating electron interactions, (b) schematic of electron interactions at atomic scale (c) schematic illustrating how SEI enables topographical information to be obtained and (d) a schematic illustrating the relative back- scattering abilities of two materials with different atomic numbers. 92
Figure 4.1 - Attempts at solid state synthesis of $La_2NiO_{4+\delta}$ under different annealing conditions; (a) 120h total anneal at 1000˚C, (b) 120 h total anneal at 1100˚C, (c) 24 h at 1200˚C. 97
Figure 4.2 - Unsuccessful solid state synthesis of $La_3Ni_2O_{7-\delta}$ under different annealing conditions; (a) 120 h total anneal at 1000˚C, (b) 120 h total anneal at 1100˚C, (c) 24 h at 1200˚C. 98
Figure 4.3 - XRD data taken from samples prepared by the Pechini route; (a) $La_2NiO_{4+\delta}$, (b) $La_3Ni_2O_{7-\delta}$, (c) $La_4Ni_3O_{10-\delta}$ and (d) $LaNi_{0.6}Fe_{0.4}O_{3-\delta}$. 99
Figure 4.4 - SEM images of (a) $La_2NiO_{4+\delta}$ powder synthesised via the Pechini route and (b) commercial LSCF6428 powder (Praxair). 100
Figure 4.5 - Nyquist plots from symmetrical cell tests; (a) LNO214, (b) LNO327, (c) LNO4310, (d) LNF64, (e) synthesised LSCF6428 (LSCF-Pech), (f) commercial (Praxair) LSCF6428 (LSCF6428-C) 105
Figure 4.6 - Kramers-Kronig residuals of the 'median' values of symmetrical cell tests). 106
Figure 4.7 - Comparison of results from initial symmetrical cell tests (TSint=1000˚C).. 107
Figure 4.8 - Effect of Au-paste on symmetrical cell performance of Ruddlesden-Popper phases $La_2NiO_{4+\delta}$, $La_3Ni_2O_{7-\delta}$ and $La_4Ni_3O_{10-\delta}$ 111

Figure 4.9 - Effect of Au-paste on symmetrical cell performance of perovskite phases LNF64 and commercial LSCF6428. 112
Figure 4.10 - Effect of sintering temperature on the performance of $La_2NiO_{4+\delta}$ electrodes in symmetrical cell configuration. 113
Figure 4.11 - Arrhenius plots (600-800˚C; 50˚C intervals) demonstrating the effect of sintering temperature on (a, b) $La_3Ni_2O_{7-\delta}$, (c, d) $La_4Ni_3O_{10-\delta}$, (e, f) $LaNi_{0.6}Fe_{0.4}O_{3-\delta}$ 115
Figure 4.12 - Arrhenius plots (600-800˚C; 50˚C intervals) demonstrating the effect of sintering temperature on LSCF6428 116
Figure 4.13 - SEM analysis of four symmetrical cell samples (LNO214) sintered at four temperatures (20,000x magnification). 117
Figure 4.14 - Dilatometry results; (a) LSM82, LSCF6428, LNO214 sintered at 1000˚C, (b) and LNO214 sintered at 1000 and 1150˚C. 118
Figure 4.15 - Powder reactivity test; LSCF6428-GDC10 (1:1 mass ratio). 120
Figure 4.16 - Powder reactivity test; LNO214-GDC10 (1:1 by mass).. 121
Figure 4.17 - Powder reactivity test; LNO327-GDC10 (1:1 mass ratio).. 122
Figure 4.18 - Powder reactivity test; LNO4310-GDC10 (1:1 mass ratio).. 123
Figure 4.19 - Powder reactivity test; LNF64-GDC10 (1:1 mass ratio). 124
Figure 4.20 - Summary of data taken from samples tested in this study; (a, b) R_o values measured at 600˚C and 800˚C, respectively, (c,d) R_{pol} values measured at 600˚C and 800˚C, respectively (e,f) Z_{DC} values measured at 600˚C and 800˚C, respectively 126
Figure 4.21 - Comparison of literature data and data from this study; (a) $La_2NiO_{4+\delta}$, (b) $La_3Ni_2O_{7-\delta}$, (c) $La_4Ni_3O_{10-\delta}$, (d) $LaNi_{0.6}Fe_{0.4}O_{3-\delta}$ 130
Figure 5.1 - Effect of contact configuration (i.e. use of Au contact paste) on cell performance; Effect of contact configuration on polarisation curves at (a) 800˚C, (b) 750˚C, (c) 700˚C and effect on the EIS spectra recorded at (d) 800˚C, (e) 750˚C and (f) 700˚C. 135
Figure 5.2 - Summary on the effects of contact paste on (a) ohmic resistance, R_o, and (b) polarisation resistance, R_{pol}, as measured from the EIS spectra taken at 'OCV-0.05V' condition. 136
Figure 5.3 - (a, b) Repeatability test at 800˚C using dry hydrogen (c, d) effect of fuel humidity on impedance and i-V curves of a cell [H_2=0.2 $Lmin^{-1}$, Air=0.5 $Lmin^{-1}$, T_{Op}=800˚C]. 137
Figure 5.4 - Comparison of three commercial SOFC cell tests using dry and humidified hydrogen (0.5 $Lmin^{-1}$); effect of humidification on (a) the polarisation curve at 800˚C and (b) the OCV impedance responses at 800˚C. 140
Figure 5.5 - Modelling the effect of humidifying hydrogen on the resulting current-voltage profile. Assumed conditions (T_{Op}=800˚C, $p(O_2)$=0.21 bar). 141

Figure 5.6 - Polarisation and EIS performance of three commercial cells (SOFCMan) containing LSCF cathodes; (a, c, d) polarisation curves, (b, d, e) EIS measurements conducted at OCV, (g, h) comparison of cells at an operating temperature of 800˚C. 143
Figure 5.7 - Performance of a commercial LSCF6428 sample deposited onto a commercial half-cell. 146
Figure 5.8 - Performance of $La_2NiO_{4+\delta}$ (LNO214) in single cell testing configuration. 147
Figure 5.9 - Performance of $La_3Ni_2O_{7-\delta}$ (LNO327) in single cell testing configuration. 148
Figure 5.10 - Performance of $La_4Ni_3O_{10-\delta}$ (LNO4310) in single cell testing configuration. 149
Figure 5.11 - Performance of $LaNi_{0.6}Fe_{0.4}O_{3-\delta}$ (LNF64) in single cell testing configuration.. 150
Figure 5.12 - Comparison of polarisation curves recorded for the different cathode materials as obtained at (a) 800˚C and (b) 700˚C.. 152
Figure 5.13 - Effect of sintering temperature on the current density at 0.7 V for different phases.. 153
Figure 5.14 - Images taken of SOFC cells on tear-down; (a) LNF64-1000˚C, (b) LNF64-1150˚C and (c) LSCF-1000˚C. 155
Figure 5.15 - Post-test SEM images of (a, top) in-tact LSCF cathode (T_{Sint}=1000˚C) and (b, bottom) the La-nickelate cathode (T_{Sint} = 1000˚C) was found to be completely delaminated, leaving the GDC layer. 156
Figure 5.16 - Summary of (a) R_{pol} values measured from single cell tests (various sintering temperatures) and (b) $i_{0.7V}$ values measured from single cell tests (various sintering temperatures). 158
Figure 5.17 - Comparison of polarisation resistances measured in symmetrical cell and single cell testing configurations (Note: comparisons are only drawn with those electrodes where Au-contact paste is applied). 159
Figure 5.18 - Comparison of measured current density at (a) 1 V and (b) 0.7 V vs the inverse of polarisation resistance measured at open circuit (single cell configuration) across various cells and operating temperatures..... 161
Figure 5.19 - EIS measurements taken at 700˚C with various operating voltages for (a) $La_2NiO_{4+\delta}$, (b) $La_3Ni_2O_{7-\delta}$, (c) $La_4Ni_3O_{10-\delta}$, (d) $LaNi_{0.6}Fe_{0.4}O_{3-\delta}$ and (e) a summary of R_{pol} values against operating voltage for these materials. 164
Figure 6.1 - XRD pattern of LDCX compositions against commercial CeO_2 material. 175
Figure 6.2 - Reactivity test of $La_2NiO_{4+\delta}$ and $La_{0.45}Ce_{0.55}O_2$; XRD results for (a) 50:50 mass% mix of materials prior to heating and (b) after heating to 1150˚C for 4 hours. 176
Figure 6.3 - Reactivity test of $LaNi_{0.6}Fe_{0.4}O_{3-\delta}$ and $La_{0.45}Ce_{0.55}O_2$; XRD results for (a) 50:50 mass% mix of materials prior to heating and (b) after heating to 1150˚C for 4 hours. 177

Figure 6.4 - LDC45 layer applied to a commercial half-cell by spin-coating. The leakage around the masking is highlighted.....178
Figure 6.5 - Nyquist plots of composites; LNO214-based composites (a) without CCL and (b) with CCL. LNF64-based composites (c) without CCL and (d) with CCL.. 180
Figure 6.6 - Symmetrical cell performance of $La_2NiO_{4+\delta}$ composite electrodes. 181
Figure 6.7 - Symmetrical cell performance of $La_3Ni_2O_{7-\delta}$ composite electrodes. 182
Figure 6.8 - Symmetrical cell performance of $La_4Ni_3O_{10-\delta}$ composite electrodes. 183
Figure 6.9 - Symmetrical cell performance of $LaNi_{0.6}Fe_{0.4}O_{3-\delta}$ composite electrodes. 184
Figure 6.10 - Polarisation curves of composite electrodes; (a) LNO214-GDC, (b) LNO214-LDC45, (c) LNF64-GDC, (d) LNF64-LDC45, (e) LNO214-LNF64 and (f) a comparison of $i_{0.7V}$ values compared against single phase electrodes (LNO214, LNF64 and LSCF) sintered at 1000˚C. 188
Figure 6.11 - EIS measurements recorded at OCV for composite electrodes; (a) LNO214-GDC, (b) LNO214-LDC45, (c) LNF64-GDC, (d) LNF64-LDC45, (e) LNO214-LNF64 and (f) a comparison of R_{pol} values compared against single phase electrodes (LNO214, LNF64 and LSCF) sintered at 1000˚C. 189
Figure 6.12 - Comparison of polarisation curves of single phase and composite phase electrodes (LNF, LNO214, LNF-LNO214) at an operating temperature of 800˚C with Au-CCL. 190
Figure 6.13 - XRD showing reactivity between LDC45 and 8YSZ. 191
Figure 6.14 - XRD showing the compatibility of GDC10 and 8YSZ. 192
Figure 6.15 - Comparison of $i_{0.7V}$ measured in this study and those measured in other studies; (a) LNO214 composites and (b) LN64 composites. 194
Figure A.1 - (a) effect of operating temperature on ΔgT, ΔhT, $T\Delta sT$ and (b) E_o and $\eta_{thermodymaic}$. IV
Figure E.1 - XRD data taken from scans of (a) commercial LSCF6428 and (b) Pechini-synthesised LSCF6428 compared with (c) data from the ISCSD database (ICSD#186173).....xxiv
Figure E.2 - Attempts to synthesise LNF64 via solid-state route at (a) 1000˚C, (b) 1100˚C and (c) 1200˚C xxv
Figure E.3 - Attempts to synthesise LNO4310 via solid-state route at (a) 1000˚C, (b) 1100˚C and (c) 1200˚C.....xxvi
Figure F.1 - Symmetrical cell testing data (Nyquist plots) for commercial LSCF6428 electrodes tested in this work (a-c) electrodes sintered at 1000˚C and (d-f) electrodes sintered at 1150˚C [tests without CCL] xxvii
Figure F.2 - Complete symmetrical cell testing data (Nyquist plots) for Pechini-synthesised LNO214 electrodes tested in this work (a-c) electrodes sintered at 1000˚C, (d) 1050˚C, (e) 1100˚C and (f-h) electrodes sintered at 1150˚C [tests without CCL] xxviii

Figure F.3 - Complete symmetrical cell testing data (Nyquist plots) for Pechini-synthesised LNO327 electrodes tested in this work (a-c) electrodes sintered at 1000˚C and (d-f) electrodes sintered at 1150˚C [tests without CCL] xxix
Figure F.4 - Complete symmetrical cell testing data (Nyquist plots) for Pechini-synthesised LNO4310 electrodes tested in this work (a-c) electrodes sintered at 1000˚C and (d-f) electrodes sintered at 1150˚C [tests without CCL] xxx
Figure F.5 - Complete symmetrical cell testing data (Nyquist plots) for Pechini-synthesised LNF64 electrodes tested in this work (a-c) electrodes sintered at 1000˚C and (d-f) electrodes sintered at 1150˚C [tests without CCL] xxxi
Figure F.6 - Complete symmetrical cell testing data (Nyquist plots) for Pechini-synthesised LSCF6428 electrodes tested in this work (a-c) electrodes sintered at 1000˚C and (d-f) electrodes sintered at 1150˚C [tests without CCL] xxxii
Figure F.7 - Effect of Au-CCL on electrodes sintered at 1150˚C; (a, b) LNO214, (c, d) LNO327, (e, f) LNO4310). Panels on the left show Nyquist results. Panels on the right show R_o and R_{pol} Arrenhius plots. xxxiii
Figure F.8 - Effect of Au-CCL on electrodes sintered at 1150˚C; (a, b) LNF64, (c, d) commercial LSCF6428. Panels on the left show Nyquist results. Panels on the right show R_o and R_{pol} Arrenhius plots. xxxiv
Figure G.1 - Voltage-current and impedance data for LNO214 electrodes sintered at (a, b) 1000˚C, (c, d) 1050˚C, (e, f) 1100˚C, (g, h) 1150˚C, ... xxxv
Figure G.2 - Voltage-current and impedance data for LNO327 electrodes sintered at (a, b) 1000˚C, (c, d) 1100˚C, (e, f) 1150˚C. xxxvi
Figure G.3 - Voltage-current and impedance data for LNO4310 electrodes sintered at (a, b) 1000˚C, (c, d) 1050˚C, (e, f) 1100˚C, (g, h) 1150˚C xxxvii
Figure G.4 - Voltage-current and impedance data for LNF64 electrodes sintered at (a, b) 1000˚C, (c, d) 1050˚C, (e, f) 1100˚C, (g, h) 1150˚C..... xxxviii
Figure G.5 - Kramers-Kronig residuals for lanthanum nickelate electrodes sintered at 1150˚C..... xxxix
Figure G.6 - Attempt to identify processes via DRT analysis of single cells with $La_2NiO_{4+\delta}$ electrode sintered at 1150˚C (part 1 – effect of temperature)..... xl
Figure G.7 - Attempt to identify processes via DRT analysis of single cells with $La_2NiO_{4+\delta}$ electrode sintered at 1150˚C (part 2 – effect of gas pressures) xli
Figure H.1 - Reactivity test of $La_2NiO_{4+\delta}$ and $La_{0.10}Ce_{0.90}O_2$; XRD results of (a) 50:50 mass% mix of materials prior to heating and (b) after heating to 1100˚C for 4 hours. xlii

Figure H.2 - Reactivity test of $La_2NiO_{4+\delta}$ and $La_{0.35}Ce_{0.65}O_2$; XRD results of (a) 50:50 mass% mix of materials prior to heating and (b) after heating to 1100˚C for 4 hours. xliii
Figure H.3 - Reactivity test of $La_2NiO_{4+\delta}$ and $La_{0.40}Ce_{0.60}O_2$; XRD results of (a) 50:50 mass% mix of materials prior to heating and (b) after heating to 1100˚C for 4 hours. xliv
Figure H.4 - Reactivity test of $La_2NiO_{4+\delta}$ and $La_{0.45}Ce_{0.55}O_2$; XRD results of (a) 50:50 mass% mix of materials prior to heating and (b) after heating to 1100˚C for 4 hours. xlv
Figure I.1 - Overview/explainer of box and whisker plot.. xlvi

List of tables

Table 1.1 – Table of requirements for fuel cell stack materials. 15
Table 2.1 – Average cell degradation rates for a 2-cell stack operated for 100,000 h..... 30
Table 2.2 - Long-term degradation studies on SOFC stacks. 31
Table 2.3 - Overview of Cr-phase formation in cathode materials and consideration of degradation rates relative to common cathode materials. 42
Table 2.4 - Consideration on degradation studies, ordered by operating time.. 67
Table 4.1 - Overview of electrodes prepared for the symmetrical cell testing detailed in this chapter 102
Table 5.1 – Overview of contact configurations tests. 132
Table 5.2 – Testing parameters employed to achieve repeatable results for bench-mark tests..... 142
Table 5.3 – EIS metrics for commercial cells tested at 800˚C OCV in accordance with conditions shown in Table 5.2 144
Table 5.4 – Metrics taken from polarisation curves conducted on commercial cells at T_{Op} = 800˚C . 144
Table 5.5 – Overview of single cell test samples prepared for testing. 145
Table 6.1 – Overview of symmetrical cell tests conducted in this chapter. Materials were mixed in 1:1 volume ratio. 173
Table 6.2 – Composition of LDC45 ink prepared for spin-coating process 178
Table A.1 – Standard values of the enthalpy and entropy of reaction at room temperature and standard pressure II
Table A.2 – Calculated values based on standard conditions and room temperature. II
Table B.1 – Electrical conductivity data taken from literature sources..... v
Table C.1 – Symmetrical cell performance of different lanthanum nickelate electrodes studied by various researchers. ix
Table D.1 – Single cell testing of lanthanum nickelate electrodes in various studies. Current density values measured at 0.7V ($i_{0.7V}$). xix

ASR - Area Specific Resistance

BEV - Battery Electric Vehicle

CCS - Carbon Capture and Storage

CE - Counter Electrode

CHP - Combined Heat and Power

COVID-19 - Corona Virus Disease (2019)

DRC - Democratic Republic of Congo

EBSD/BSE - Electron Backscattered Diffraction/Backscattered Electron

EDX - Electron Dispersive X-ray Spectroscopy

e-fuels - Electric fuels

EIS - Electrochemical Impedance Spectroscopy

EU - European Union

EV - Electric Vehicles

FRA - Frequency Response Analyser

GDC - Gadolinium Doped Ceria

GHG - Greenhouse Gas Emission

HHV - Higher Heating Value

HOR - Hydrogen Oxidation Reaction

H-SOFC - Proton (H+) conducting Solid Oxide Fuel Cells

HT - High Temperature

ICSD - International Centre for Diffraction Data

IPCC - Intergovernmental Panel on Climate Change

IRENA - International Renewable Energy Agency

LHV - Lower Heating Value

LNF64 - $LaNi_{0.6}Fe_{0.4}O_3$

LNO214 - La_2NiO_4

LNO327 - $La_3Ni_2O_7$

LNO4310 - $La_4Ni_3O_{10}$

LSC - $La_{1-x}Sr_xCoO_3$

LSCF - $La_{1-x}Sr_xCo_{1-y}Fe_yO_3$

LSCM - $La_{1-y}Sr_yMn_{1-x}Co_xO_3$

LSGM - $La_{1-x}Sr_xGa_{1-y}Mg_yO_3$

LSM - $La_{1-x}Sr_xMnO_3$

MFC - Mass Flow Controller

MIEC - Mixed Ionic Electronic Conductors

NEDO - New Energy and industrial technology Development Organisation

OCV - Open Circuit Voltage

ORR - Oxygen Reduction Reaction

PDF - Powder Diffraction File

PEFC - Polymer Electrolyte Fuel Cell

R&D - Research and Development

RE - Reference Electrode

SDC - Samarium Doped Ceria ($Sm_{1-x}Ce_xO_2$)

SECA - Solid State Energy Converson Alliance

SEI - Secondary Electron Image

SEM - Scanning Electron Microscope

SOC - Solid Oxide Cell

SOE - Solid Oxide Electrolyser

SOFC - Solid Oxide Fuel Cell

SASZ - Scandia alumina stabilized zirconia

SSZ - Scandia stabilized Zirconia

TEC - Thermal Expansion Coefficient

UK - United Kingdom

WE - Working Electrode

XRD - X-Ray Diffraction

YSZ - Yttria Stabilised Zirconia

Latin

c	*Speed of light*
D^*	*Oxygen tracer coefficient*
E	*Cell voltage*
E_o	*Thermodynamic voltage*
E_{wave}	*Energy of photon*
F	*Faraday's constant*
Δg_T	*Change in Gibbs free energy*
h	*Planck's constant*
$\Delta h^o_{f,LHV}$	*Enthalpy of formation (lower heating value)*
Δh_T	*Change in enthalpy at temperature T*
K_α	*Characteristic wavelength of X-ray*
k	*Surface exchange coefficient*
n	*Number of electrons transferred*
Δs_T	*Entropy at temperature T*
T	*Temperature*
R_{pol}	*Polarisation resistance (area specific)*
R_o	*Ohmic resistance (area specific)*
r_x	*Radius of ion 'x'*
S	*Electrode area*
t	*Goldschmitt tolerance factor*
tr	*Transference number*
w	*Work*
Z'	*Real impedance*
Z''	*Imaginary impedance*

Greek

λ	*Wavelength*
σ	*Electrical conductivity*
η	*Efficiency*
v	*Voltage loss*

1 Introduction

1.1 Context

1.1.1 A crisis in climate and energy security

A continued and unabated rise in the release of anthropogenic greenhouse gases (GHG) is driving a change in the composition of the Earth's atmosphere. Due to their ability to capture and trap solar radiation, surging quantities of these substances (including carbon dioxide and methane) are leading to an increase in average global temperatures. The subsequent effect of this phenomenon (i.e. '*Climate Change')* presents an existential crisis to the global community. Unless action is taken to reduce and offset GHG emissions, it is likely that the 21st century will play host to numerous catastrophic consequences. This includes rising sea-levels, an increase in the quantity and frequency of extreme weather events, and the extinction of many species [1]. Additionally, it is thought that such events will drive a mass migration of communities and rising human conflict as water and food-resources become more volatile [2]. Recent times have seen a raised profile for this key issue. In 2019, a series of international protests (e.g. Figure 1.1) served to galvanise public awareness on the matter, with particular emphasis placed on youth activism [3,4]. In a 2021 poll conducted by the United Nations, two-thirds of the participants supported the notion that climate change should be identified as a 'global emergency' [5].



Figure 1.1 - Extinction Rebellion protests in London, UK, attended by Greta Thunberg (right image). An example of growing public discourse on climate change and the need for action. Photo Credit: Graeme Hayes.

In addition to issues relating to climate change, humanity faces an uncertain future with respect to its access to secure supplies of primary energy sources. It is widely acknowledged that an unrelenting reliance on finite resources of fossil fuel (e.g. crude oil, natural gas) is unsustainable [6]. Urgent efforts are therefore required to overhaul the manner in which society interacts with its energy resources.

In accordance with the 2015 Paris Climate Agreement [7], the global community has committed to limiting average global temperature increases to 2˚C (measured against pre-industrial levels). To help meet this target, member states of the European Union (EU) have targeted '*Climate Neutrality*' by 2050 [8]. It is widely acknowledged that such goals represent a technological and economic challenge to countries around the world. Year-on-year global emissions have continued to rise in the last 5 decades (a few notable years aside) [9,10]. To reverse such trends, and drive-down GHG emissions, a wide-scale deployment of alternative, zero-carbon technologies will be required whilst also improving end-use efficiency [1]. Amongst other events, the recent COVID-19 pandemic is thought to have brought certain opportunities relating to industry, the economy and to the wider energy system [11,12]. As a result, many countries and blocs are looking to invest heavily in emerging industries and technologies that can help to reduce emissions [13–15].

1.1.2 Renewables, electrification and its challenges

Renewable energy technologies are playing an increasing role in the production of electrical power and heat around the world [16]. Over the last decade, an acceleration in wind turbine deployment has overseen a dramatic reduction in the carbon-intensity of the UK electricity grid [17]. Renewably produced electrical power is replacing the more traditional carbon-intensive options such as coal-fired thermal power stations, which are on the pathway to obsolescence. The political emphasis that has been placed on deploying these technologies has helped to reduce the costs of renewables. With the economics becoming increasingly favourable, the eventual market dominance of this technology seems inevitable. Nevertheless, there are a number of challenges which represent obstacles to a

completely ‘zero fossil-carbon’ energy system. How successfully these challenges are overcome will likely determine the success or failure of the decarbonisation effort.

One key issue with the deployment of renewable energy technologies is the inherent variability of the energy source (i.e. the fluctuating nature of solar radiation and wind currents) [17]. This, combined with the need to instantaneously balance electricity grid demand and generation, offers a major concern for the expansion of renewable generation. Conversely, an inherent advantage of solid, liquid or gaseous fuels is that they may be used to produce electricity (or heat) on demand. It is partly for this reason that fossil fuels have historically been so widely relied upon to help balance energy production and consumption. Inherently, fossil fuel resources represent a cheap form of energy storage [18]. Frustratingly, renewable generation is commonly paused (or *curtailed)* during periods of grid congestion [19,20]. Such procedures have an impact on the economic and environmental benefits of these technologies. To completely remove fossil fuels from the energy system, the deployment and development of energy storage technologies will be vital [21–23].

With an increasing availability of zero-carbon electricity, there is a drive to electrify many different sectors such as transport and domestic heat production [24,25]. Such transformations *could* rely heavily on the wide-spread adoption of emerging technologies such as Battery Electric Vehicles (BEVs) and heat pumps. The acceptance of these devices may require some habitual changes for many (e.g. BEV charging times). It remains to be seen how quickly (and to what extent) an uptake of such technologies can be achieved. Perhaps more concerning is the strain that increasing electrification will place on existing infrastructure (e.g. network distribution lines). In the UK, the cost projections to upgrade this infrastructure are not insignificant (an estimated £50bn by 2035 required for a rapid uptake of BEVs and heat pumps [26]). In isolation, the complete replacement of the natural gas grid with electric-based heating represents a sizeable challenge in itself. This can be appreciated by considering the current disparity between electricity generation and natural gas usage (see Figure 1.2) [27]. These observations would appear to suggest that the complete electrification of heat will be a

difficult task (in the UK at least) and there is some scepticism about the viability of this approach [27–29]. This implies that some low-carbon gas-network will need to be maintained to meet the energy demands of the UK whilst also meeting with climate targets. Whether this be in the form of bio-fuels or so-called 'e-fuels' is up for debate [28]. One possible solution that can help to overcome many of the issues discussed above is the widespread production and utilisation of hydrogen. Of course, whichever pathway is taken, this must also be combined with a reduction in overall energy demand. In part this can be achieved by improvements to end-use efficiency (e.g. building insulation), effectively helping to considerably reduce energy demand.

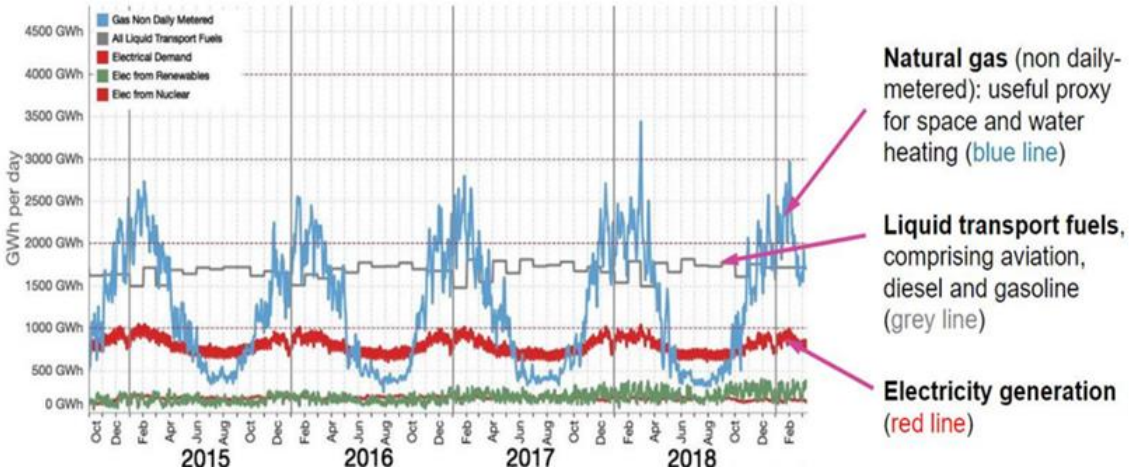


Figure 1.2 – Energy usage in the UK; consumption of liquid fuels for transport, natural gas and electricity [27].

1.1.3 A 'hydrogen economy' and its challenges

The use of hydrogen as an energy vector offers huge potential with respect to de-carbonising energy systems around the world. Reaction with oxygen is, from a thermodynamic perspective, a spontaneous process[1] which leads to a release of energy, without carbon emissions:

$$H_2(g) + \frac{1}{2}O_2(g) \rightarrow H_2O(g)\left(\Delta h^o_{f,LHV} = -241.83\ kJmol^{-1}\right) \text{ [Eq. 1.1]}$$

[1] For a spontaneous reaction, the Gibbs free energy of reaction is negative ($\Delta g_T < 0$) - the reaction shown in equation 1.1 follows this condition (except for temperatures well in excess of 1000 ˚C) – see Appendix A

Here, $\Delta h^{o}_{f,LHV}$ is the enthalpy of reaction for H_2O in the gaseous form (i.e. steam). This value excludes the latent heat energy[2] associated with a change of state (i.e. liquid to gas).

Although molecular hydrogen (H_2) does not exist in appreciable quantities in nature, it is the most abundant element in the universe. Hydrogen is most commonly found to be chemically bound within molecules such as water (H_2O), methane (CH_4) and ammonia (NH_3). In particular, the ability to extract molecular hydrogen from H_2O (and then employ it for the production of zero-carbon electricity and heat) is a tantalising prospect. Some commentators have theorised that an economy based on the production, transmission and utilisation of hydrogen can be engineered to meet the needs of society [30–32]. Importantly, such an economy could be achieved whilst ensuring a secure, zero-carbon energy system is realised. A society built on such a concept is commonly referred to as a 'hydrogen economy'.

Whilst hydrogen can be combusted like conventional fuels, it is its employment in fuel cells which offers the greatest opportunity. There are many different types[3] of fuel cell, each designed with different materials and offering different advantages and drawbacks. With such devices, hydrogen and oxygen can be electrochemically converted to produce electrical power and heat. The emission of water is the only resulting by-product of this process. This idea is illustrated for a Polymer Electrolyte Fuel Cell (PEFC) in Figure 1.3a. Aside from the avoidance of carbon emissions, fuel cell technology is not limited by the Carnot efficiency and, as such, can be significantly more efficient than combustion technologies. Fuel cells may also be operated in reverse in order to split water into hydrogen and oxygen (i.e. electrolysis), as seen in Figure 1.3b. Importantly, low-carbon electricity could be used to produce hydrogen during periods of over-production. Fuel cells can then be employed to reverse this process when there is a deficit between low-carbon electricity production and electrical demand.

[2] The 'higher heating value' (HHV) is -285.84 $kJmol^{-1}$

[3] This includes Alkaline Fuel Cells (AFC), Direct Methanol Fuel Cells (DMFC), Molten Carbonate Fuel Cells (MCFC), Phosphoric Acid Fuel Cells (PAFC), Polymer Electrolyte Fuel Cells (PEFC) and Solid Oxide Fuel Cells (SOFC) – the fundamental difference between these is the type of electrolyte employed. Each type of fuel cell has different characteristics with respect to their operation (e.g. tolerance to impurities, start-up times).

Given that hydrogen can be stored over long periods with relative ease, this approach is attractive for seasonal energy storage.

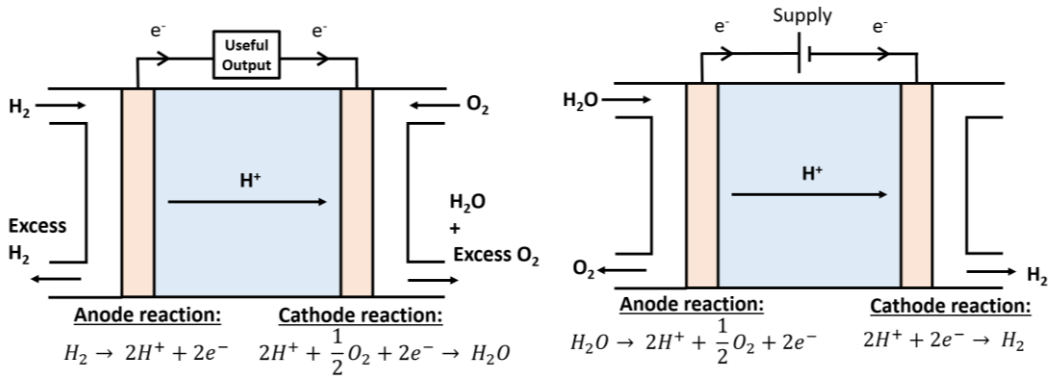


Figure 1.3 – (a, left) Schematic of a Polymer Electrolyte Fuel Cell and (b, right) schematic of a Polymer Electrolyte Membrane Electrolyser.

In truth, the concept of a hydrogen economy has been debated for a number of decades having been first proposed in the 1970s [33]. Indeed, this has no doubt contributed to the scrutiny and scepticism that hydrogen has faced in recent years. Opponents of hydrogen technology commonly argue that the current round-trip efficiency of producing so-called green hydrogen (i.e. that produced via electrolysis with zero-carbon electricity) and re-converting this to electricity (~35%) is far inferior to that achievable with battery systems (~90%). The high cost of green hydrogen has historically been viewed as a major barrier to its widespread production but prices are anticipated to fall in the coming decade [34,35]. Perhaps more pertinent today is the availability of sufficient zero-carbon electricity and the need for increased capacities of renewable generation [36][4]. Other hydrogen production routes are also possible. The synthesis of 'grey hydrogen' (i.e. that obtained from the reformation of natural gas) is a process that has been carried out on an industrial scale for decades. However, this approach is very carbon intensive [35,37] and negates the great benefit of H_2 (i.e. decarbonisation). This route can be combined with carbon capture and storage (CCS) technology to reduce the associated emissions and produce so-called 'blue hydrogen'. However, the addition of CCS leads to increased costs [38] and, given inefficiencies in this process and carbon emissions through the supply chain, there is some

[4] IRENA estimate 4-16TW of renewable electricity capacity will be needed to provide the required amount (19EJ) of hydrogen in 2050 [36] – IRENA note that this may be conservative based on other estimates

scepticism towards this route of H_2 production [39]. Whilst many other routes of production have been proposed, it is green hydrogen that is most commonly agreed to offer the greatest potential.

It is becoming increasingly accepted that hydrogen will need to play some role in future energy systems. This is particularly evident in those areas that will prove difficult (e.g. rural train routes) or even impossible (e.g. production of green ammonia) to electrify via other means. In 2020, the European Union have signalled their future intentions on this matter by issuing a '*hydrogen strategy*' [40]. The policy details plans to upscale and deploy electrolyser technology. Critically, the bloc intend to install 40 GW of electrolysis capacity by 2030, producing 10 million tonnes of zero-carbon, renewable hydrogen. Individual nations (e.g. Canada, Germany, the UK, France, Japan, South Korea) have also followed suit with their own individual strategies [35]. Each of these countries' proposals places hydrogen as an intrinsic part of the energy system. In the UK, a number of research projects (H_{21} [41], HyDeploy [42], Hy4Heat [43]) are underway to consider the feasibility of converting the natural gas grid to hydrogen. There are signs, therefore, that a hydrogen economy will come to the fore on some level in the coming years.

1.2 Solid Oxide Fuel Cells

1.2.1 An introduction

The Solid Oxide Fuel Cell (SOFC) is a technology that has been the matter of some scientific and engineering curiosity over many decades and is now beginning to find a place in energy networks around the world [44]. As will be discussed here, this technology can offer solutions to many of those issues discussed in Section 1.1. As can be appreciated from the schematic in Figure 1.4, the SOFC *generally*[5] employs an oxide-conducting electrolyte. The ceramic electrolytes require high temperatures (typically in excess of 600˚C) in order to achieve appreciable oxide ion conductivity. Depending on the operating temperatures (amongst other factors), a single SOFC cell can produce power density values above 1 Wcm^{-2} [45]. As is the case with other types of fuel cell, and to provide a

[5]SOFCs with a proton (H^+) conducting electrolyte have also been manufactured and demonstrated.

more sizeable power output, multiple cells of a determined area are arranged in series to produce the so-called SOFC '*stack*'. In the common series-connected system, the area of the cells dictates the total current output, whilst the number of cells determines the voltage. The modularity of this technology is one of its key, inherent advantages and means that SOFCs can be scaled according to power requirements. Like other types of fuel cell, the SOFC can be operated '*in reverse*' to produce hydrogen or carbon monoxide via electrolysis of water or carbon dioxide, respectively. In this case, the technology is referred to as a Solid Oxide Electrolyser (SOE) with the term Solid Oxide Cell (SOC) often used as a general description for the two technologies.

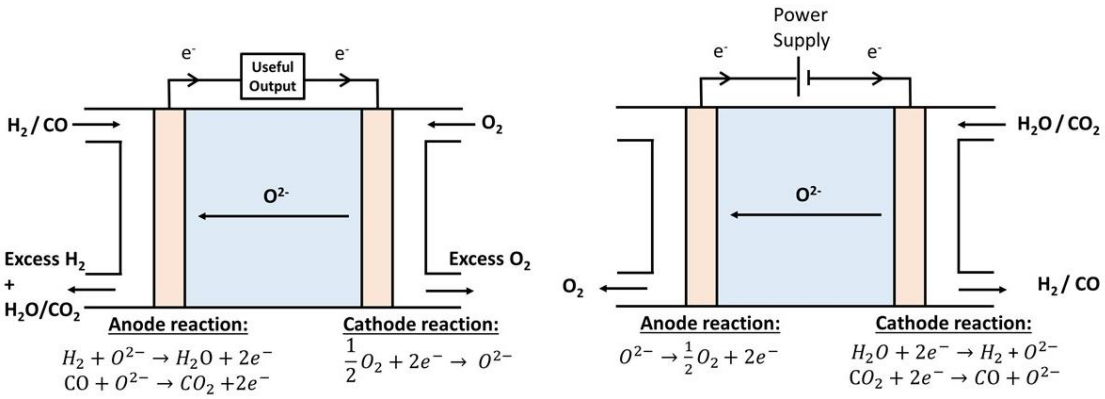


Figure 1.4 – Schematics of (a, left) a Solid Oxide Fuel Cell and (b, right) a Solid Oxide Electrolyser.

When comparing with other fuel cell types, a key advantage of the SOFC is the ability to utilise (or, more correctly, *oxidise*) a variety of fuels into electrical power and heat. This includes not only hydrogen but also carbon monoxide, and other carbon-containing fuels. The production of water (or, more correctly, steam) on the fuel-side of the SOFC enables 'internal reforming' to be conducted. Here, methane is fed directly to the anode compartment and split into H_2 and CO. These molecules are subsequently converted to H_2O and CO_2 via electrochemical reaction. Importantly, therefore, SOFCs are capable of avoiding poisoning from molecules (i.e. CO) that would otherwise degrade the cell performance of other types of fuel cell (e.g. PEFC). Perhaps more poignantly, the ability of SOFCs to use a wide-range of fuels grants them status as a bridging technology (linking the methane and hydrogen worlds) which would ease a transition between such systems. Further, the technology can

be viewed as a *low-regrets* option given its application does not rely on a wide-scale hydrogen infrastructure (as PEFC technology, for example, would undoubtedly require) and can be employed in many different future energy scenarios. In Section 1.1, the future energy landscape was discussed and, importantly, the likely future reliance on some low-carbon fuel network was described (be it biofuels or e-fuels). SOFC technology represents an opportunity to utilise such fuels with high efficiency and hence reduced environmental impact.

SOFCs have been operated at a range of different temperatures (500-1000˚C). The chosen operating temperature is, in part at least, determined by the cell materials which are reviewed in further detail shortly. On the one hand, higher temperatures are beneficial with respect to improving reaction kinetics but, on the other hand, they can offer some substantial engineering challenges.

1.2.2 Thermodynamics, efficiency and kinetics

To understand the cell output and efficiency of SOFCs, it is useful to first consider the fundamentals of fuel cell thermodynamics. The two key properties are the standard Gibbs Free Energy of reaction (Δg_T) and the enthalpy of reaction (Δh_T) at the temperature of reaction[6]. The former of these properties describes the maximum work ($w_{electrical}$) obtainable from the reaction, whereas the latter describes the total energy contained within the fuel (w_{total}). The crucial equations that relate these quantities with the thermodynamic cell voltage (E_O) and maximum theoretical thermodynamic efficiency ($\eta_{thermodynamic}$) are:

$$\eta_{thermodynamic} = \frac{w_{electrical}}{w_{total}} = \frac{\Delta g_T}{\Delta h_T} = \frac{\Delta h_T - T\Delta s_T}{\Delta h_T} = 1 - \frac{T\Delta s_T}{\Delta h_T} \; [Eq\ 1.2]$$

$$E_o = -\frac{\Delta g_T}{nF} == -\frac{\Delta h_T - T\Delta s_T}{nF} \; [Eq\ 1.3]$$

Where the remaining properties, n, F, T, Δs_r represent the number of electrons transferred in the reaction, Faraday's constant, the temperature of reaction and the corresponding entropy of reaction.

[6]The values of Gibbs free energy of formation, enthalpy of formation and entropy of formation are temperature-specific (see Appendix A)

A more comprehensive assessment of fuel cell thermodynamics is provided in Appendix A. It is apparent from Eq. 1.2 and 1.3, however, that the operating temperature (T) has a sizeable impact on the voltage and thermodynamic efficiency. At increased temperatures, these properties begin to decrease. Clearly, such a situation would indicate that high temperatures are undesirable. However, it is first important to remember that the thermodynamic efficiency is only a single factor determining the wider system performance:

$$\eta_{system} = \eta_{thermodynamic} \times \eta_{voltage} \times \eta_{thermal} \times \eta_{fuel\,utilisation} \times \eta_{BOP} \; [Eq\ 1.4]$$

Where $\eta_{voltage}$, $\eta_{thermal}$, $\eta_{fuel\ utilisation}$ and η_{BOP} represent the voltage efficiency, thermal efficiency, fuel utilisation efficiency and balance of plant efficiency, respectively. Further, and to the benefit of SOFC systems, the higher operating temperature ensures that the 'waste heat' ($T\Delta s_T$) becomes a more useful resource than that for lower operating temperatures. This heat can be recaptured and employed in heating or cooling processes (e.g. for Combined Heat and Power systems). Such an approach can enhance the system-level efficiency, with up to 90% efficiency said to be possible [46].

A key advantage of the SOFC when compared with other fuel cells is the improved reaction kinetics. The *practical* operating voltage (E) is associated with a number of voltage losses which can be described as (a) activation losses (v_{act}), (b) ohmic losses (v_{ohmic}) and (c) concentration losses (v_{conc}):

$$E = E_o - v_{act} - v_{ohmic} - v_{conc} \; [Eq\ 1.5]$$

The impact that these losses have on cell output can be appreciated when studying the '*polarisation curve'* (Figure 1.5a). The typical effects of operating temperature on these losses can be appreciated in Figure 1.5b. SOFCs, via their use of high temperatures, have much reduced activation losses and this is most apparent at low current densities (i.e. the left hand side of the graph).

As was briefly mentioned earlier in this chapter, a key advantage that Solid Oxide Cells[7] possess is the ability to operate 'in reverse' to perform electrolysis. It is important to note that this is a feature that

[7]Here the more general term 'Solid Oxide Cell' (SOC) is used to note that in, a reversible system, the cell operates in both 'Fuel Cell mode' and 'Electrolysis mode'

is not necessarily common across all types of fuel cell. Such an ability is advantageous for electrical energy storage in that it avoids the need for two separate devices to perform each function (i.e. reducing capital costs for electrical energy storage). Additionally, the thermodynamic[8] and kinetic performance of an SOC is superior to that of other types of low-temperature electrolysis system, meaning that very high conversion efficiencies can be achieved (and thus a reduced electrical input is required to achieved a given amount of hydrogen production, relative to lower temperature electrolysis). Although a thermal input is required for such processes, this can be achieved from waste heat (e.g. waste heat from nuclear power plants).

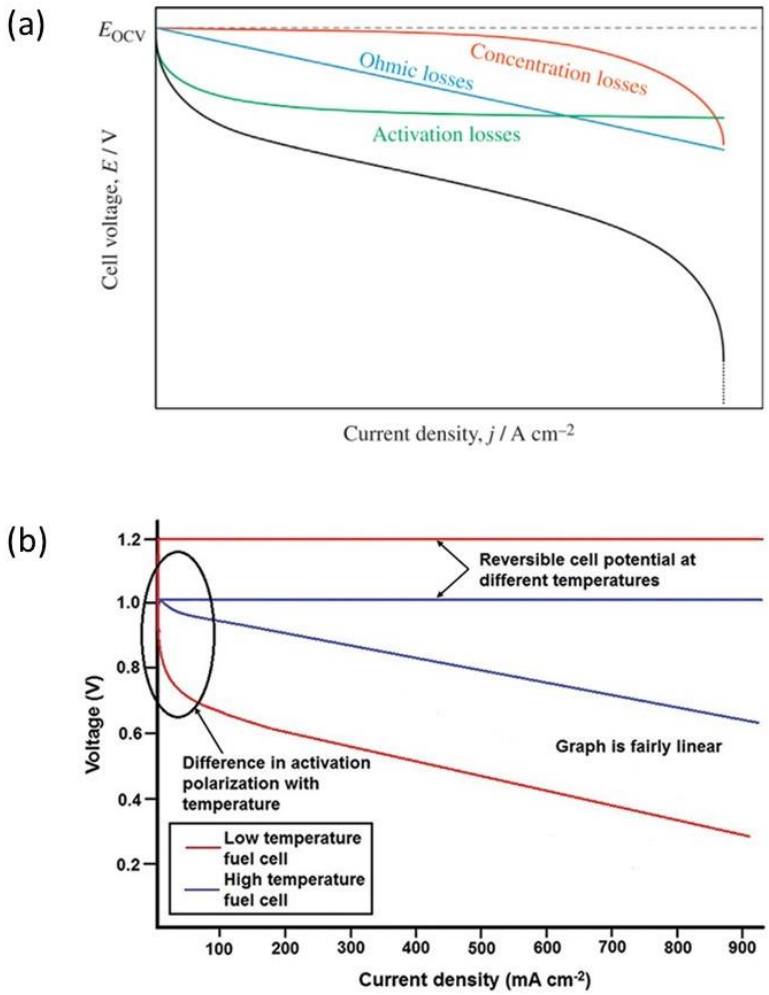


Figure 1.5 (a, top) The effect of different losses on the polarisation curve [47]*, (b, bottom) a comparison between the polarisation curves of a typical low and high temperature fuel cell* [48].

[8]In the case of electrolysis the thermodynamic efficiency is represented as: $\eta_{thermodynamic}=1-\frac{\Delta h_T}{T\Delta s_T}$

1.2.3 Applications and industry advancement

Although the uptake of SOFC technology since its inception has been slow, the last decade has seen some improving fortunes [44]. The key use-case for SOFC technology is often considered to be stationary power applications, with back-up power and uninterruptible power supply systems making up the majority of SOFC installations. In the transport sector, the start-up times of SOFCs (i.e. the time to heat-up to operating temperature) are considered a barrier to their application. Nevertheless, SOFC has garnered some interest for these applications. Mostly this is with respect to their use as Auxiliary Power Units (APUs) for heavy goods vehicles [49] and aircraft [50] where longer start-up times are less prohibitive. Automotive manufacturer Nissan, meanwhile, have developed a prototype vehicle with an SOFC power-train, suggesting that perceived issues with start-up *can* be overcome [51].

An increasing number of case studies around the world offer encouragement that SOFC technology will play a growing role in the provision of electrical power and heat. Bloom Energy in the United States have driven the commercialisation of their Uninterruptible Power Supply systems [52]. These 'energy servers' draw on SOFC technology and are designed to operate on natural gas. Here, 'big tech' companies (e.g. eBay, Amazon) have been identified as a key market. This is due to the value that these companies place on a reliable power supply. In Japan, led by years of hydrogen research, thousands of SOFC/PEFC micro-Combined Heat and Power (μ-CHP) systems have been installed across the country as part of the ENE-FARM scheme to accelerate the commercialisation of such technology [53]. These CHP systems are intended to improve the overall efficiency of the energy system by eliminating transmission losses and producing power and heat at the point of use. European manufacturers have joined the drive to produce domestic fuel cell products, with the EU-funded PACE project [54] providing incentives to improve awareness and uptake of μ-CHP systems, whilst driving reduced costs and an improved regional supply chain. In the UK, the development of the Steel Cell® at Ceres Power has brought about notable commercial interest due to the scalability and mechanical resilience of their SOFC stacks [55].

1.3 SOFC materials

SOFC materials have been intensely researched over the last 50 to 60 years to improve the performance and resilience of the technology [45]. Material selection is capable of delivering considerable improvements in cell performance in terms of power output. Importantly, there has been a drive to reduce the operating temperatures of SOFC and materials development has helped to achieve this. Here the requirements of each component are presented before a discussion of some of the mainstream materials. There are a number of comprehensive overviews on materials research for SOFC and further in-sight can be gained in those works [56–58].

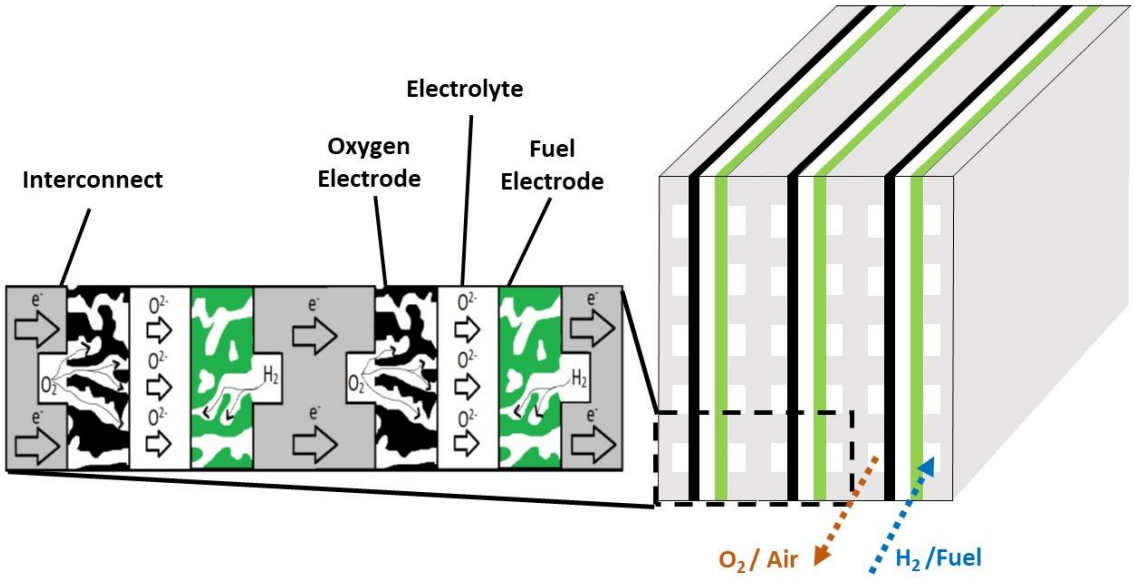


Figure 1.6 – Schematic of a planar fuel cell stack, illustrating the flow of gas, oxide ions and electrons.

1.3.1 Material requirements

The SOFC is comprised of several key components; anode, cathode, electrolyte and interconnects. Their assembly is illustrated in Figure 1.6. Each of these components is required to perform a different role within the cell and, as a result, the requirements placed on each is different. All of the components must perform their role over many 1000s of hours without significant degradation rates; lifetimes of around 10 years are seen as a fundamental requirement for many stationary systems [59]. Critically, degradation rates may be accelerated at high temperature, as ion migration and reaction between

materials is accelerated [60]. It is imperative that the materials are synchronised to avoid a mismatch with respect to thermal expansion or to avoid chemical reaction between neighbouring components.

As with all fuel cells, the electrolyte represents the central component of the SOFC and is engineered to operate within both the reducing and oxidising environments observed at the anode and cathode side of the cell, respectively. In effect, the electrolyte serves to extend the reaction between H_2 and O_2 (i.e. the exchange of electrons) over the macroscopic scale rather than at the atomic scale[9]. This is a fundamental principle in the operation of all types of fuel cell. The key for an electrolyte material is to permit the transport of ions whilst preventing the flow of electrons. A critical parameter for an electrolyte material is the transference number (tr) which represents the ratio of ionic conductivity to total conductivity. A transference number close to unity is preferable for the electrolyte.

In the case of the anode and the cathode, the key requirement is to promote the Hydrogen Oxidation Reaction (HOR) and the Oxygen Reduction Reaction (ORR), respectively:

$$H_2(g) + O^{2-} + 2e^- \rightarrow H_2O(g)\ (HOR)\ [Eq\ 1.6]$$

$$\frac{1}{2}O^2(g) + 2e^- \rightarrow O^{2-}\ (ORR) [Eq\ 1.7]$$

A key attribute of fuel cell electrodes is to provide the necessary electronic and ionic transport properties to promote these reactions (i.e. transport of electrons, ions, oxygen and fuel). In order to ensure sufficient fuel/oxygen is transported through the electrode, the anode and cathode are generally porous. In an SOFC, composite electrodes (of two or more phases) are often employed in order to reap the relative benefits of two different materials. Often this translates to an electron-conducting phase and an oxide-ion-conducting phase. An alternative to these composite electrodes would be the employment of single-phase materials that are capable of conducting both electrons

[9] The electron transfer process occurs at two spatially separate sites (anode and cathode) rather than directly between the molecules themselves. In other word, instead of electrons being transferred directly between H_2 and O_2 molecules (e.g. in a combustion reaction), the electrolyte creates a physical barrier between the reactant molecules and causes the electron transfer process to be diverted via an external circuit (i.e. 'useful power').

and oxide ions. These materials are referred to as Mixed Ionic Electronic Conductors (MIEC) and are deemed to be a preferred option.

The interconnects that separate cells have several functions and are primarily used to supply electrons, fuel and oxidant to the electrodes. In contrast to the electrolyte, the interconnects should have high electrical conductivity and low oxide ion conductivity (i.e. $tr \approx 0$). A key requirement for interconnect materials is that they should offer good stability and should be reasonably easy to machine/manufacture into shape (given the need to have pathways/grooves for the gas to be provided to the cells). An overview of the various requirements placed on the described components may be observed in Table 1.1. As may be appreciated, a demanding set of requirements places serious limitations on the materials which may be employed in the SOFC application. Given these constraints, it can be considered a testament to SOFC researchers that this technology has been brought to the early stages of commercialisation. Although there are a great number of materials proposed in the academic literature, we shall first consider the state-of-the-art to offer an overview of those materials that have already been developed and are part of the current commercialisation efforts.

Table 1.1 – Table of requirements for fuel cell stack materials; ✓✓ denotes a critical requirement ✓ denotes a preferred characteristic - denotes a requirement that is not applicable or not required ✗ denotes a property that should be avoided.

	Electrolyte	**Cathode**	**Anode**	**Interconnect**
Oxide Ion Conductivity	✓✓	✓	✓	✗
Electronic Conductivity	✗	✓✓	✓✓	✓✓
Stability in HT Reducing Conditions	✓✓	-	✓✓	✓✓
Stability in HT Oxidising Conditions	✓✓	✓✓	-	✓✓
Thermal Expansion match	✓✓	✓✓	✓✓	✓✓
Catalytically active for HOR	-	-	✓✓	-
Catalytically active for ORR	-	✓✓	-	-
HT Chemical stability with electrolyte	-	✓✓	✓✓	-
HT Chemical stability with interconnect	-	✓✓	✓✓	-
Low Cost	✓✓	✓✓	✓✓	✓✓
Machinability	-	-	-	✓✓

1.3.2 Electrolyte materials

1.3.2.1 Zirconia-based

Electrolytes based on zirconia (ZrO_2) are probably the most widely considered subset of materials which have found application in SOFCs. Zirconia itself does not offer appreciable oxide conductivity but doping with trivalent cation species (e.g. Y^{3+} in Y_2O_3), leads to the formation of oxygen vacancies. This can be represented by Kroger-Vink notation:

$$Y_2O_3 \ + \ 2Zr_{Zr}^{x} + \ O_O^x \ \rightarrow 2Y_{Zr}' + \ V_O^{\cdot\cdot} + 2ZrO_2 \ [Eq\ 1.8]$$

The formation of these oxide vacancies enables the oxide ions to migrate through the ionic lattice. This is achieved via a hopping mechanism whereby the O^{2-} moves to the vacant site and occupies it, leaving a vacant side behind it. Given this relationship, it may be assumed that oxide conductivity increases proportionally with an increasing dopant concentration. However, it is found that there is a limitation to this relationship and, for the YSZ system at least, this is found to be around 8mol% of Y_2O_3 concentration (corresponding to $Y_{0.15}Zr_{0.85}O_{1.925}$, 15% yttrium on the zirconium site) [61]. Above this concentration, the oxide vacancies begin to form associations with the dopant species. The result is a 'clustering' of the defect species, leading to a reduction in vacancy mobility and, hence, conductivity [62,63].

A host of dopant materials have been utilised for the development of ZrO_2-type electrolyte materials, including Y_2O_3 (yttria-stabilized zirconia, denoted YSZ), Sc_2O_3 (scandia-stabilized zirconia, denoted SSZ) and double-doped Sc_2O_3 and Al_2O_3 compositions (scandia-alumina-stabilized zirconia, denoted SASZ). The use of scandia offers particularly high conductivity due to the dopant ionic radius being similar to that of the host cation [58]. However, for cost reasons, YSZ is commonly preferred and found to offer good electrolyte properties.

1.3.2.2 Ceria-based

CeO_2-type oxide conductors are another class of materials used as SOFC electrolytes. Sm-doped ceria (SDC) and Gd-doped Ceria (GDC) have become the more employed CeO_2-based systems for use as

electrolyte materials. Generally speaking, ceria-type electrolytes offer higher ionic conductivity than the ZrO_2 compositions already described. The materials are particularly attractive at lower operating temperatures (below 600˚C). At higher temperatures, however, electronic conductivity begins to increase. This is a result of the favourable reduction of Ce^{4+} to Ce^{3+} at such temperatures [64]. As such, the issue of electronic conductivity restricts the employment of CeO_2 electrolytes above 600˚C. As will be described later, however, CeO_2 materials *are* employed at intermediate-to-high operating temperatures for purposes that will become apparent later.

1.3.2.3 Other

Although both ceria and zirconia-based electrolytes are generally seen as the state-of-the-art, there are a number of alternative electrolyte materials which have been studied. Whilst more widely used as cathode materials, perovskite phases (general formula ABO_3) have garnered some interest [65]. $La_{1-x}Sr_xGa_{1-y}Mg_yO_3$ (LSGM) is perhaps the most widely acknowledged of these in the literature. In this system, the preferred formation of oxide vacancies on doping (rather than electron holes as seen in many other perovskites) leads to high oxide conductivity and negligible electronic conductivity.

In recent times, proton conducting SOFCs (sometimes denoted H-SOFC) have become an area of interest [66,67]. The core of this technology is a ceramic electrolyte that can allow H^+ ion transport. A key benefit of this is the greater ease with which protons are able to move compared to the oxide ion. As a result, lower temperatures may be employed with these materials. Again, perovskite materials have found application here. Electrolytes of type $BaCeO_3$ and $BaZrO_3$ (doped with a trivalent cation) have both been employed for the use in proton conducting SOFCs.

1.3.3 Anode materials

1.3.3.1 Ni-based electrodes (e.g. Ni-YSZ)

The state-of-the-art SOFC anode is a porous, *cermet* (a ceramic-metal composite) comprised of a Ni-catalyst and an oxide-conducting phase, commonly YSZ [60,68,69]. This draws on the electronic conduction and catalytic properties of Ni and the oxide-conducting properties of the YSZ. Importantly,

the percolating network that results extends the so-called 'Triple Phase Boundaries' (TPB) away from the electrolyte-cathode interface. These TPBs are defined as points at which the reactions can occur. Referring back to the HOR (and hence the case of the anode), this occurs where the gaseous hydrogen, oxide ions (transported via the oxide-conducting phase) and the electrons (transported via the electron-conducting phase), meet. As an alternative to Ni-YSZ, some SOFC cell designs employ a Ni-GDC cermet. In this instance, the GDC performs the ion-conducting function. The perceived advantages of this combination of materials (in comparison with Ni-YSZ) relate to the conducting properties of the CeO_2 phase (see Section 1.3.2.2) and also an improved tolerance to poisoning processes [70].

1.3.3.2 Other

Although Ni-based anodes are the overwhelming favourite anode material, some alternatives have been proposed. One familiar issue with Ni-based anodes is their tendency to form carbon deposits when employed with methane (i.e. coking). The use of Cu as a catalyst has been shown to go some way in reducing this phenomenon but, conversely, Cu is an inferior catalyst to Ni so such anodes can lead to reduced cell output [58]. Another popular class of anode materials amongst the research community are doped-$SrTiO_3$ perovskite systems [65,71]. These materials are stable within the reducing environment of the SOFC anode, with growing interest in Ni doped analogues of these, which lead to exsolution of Ni nanoparticles on reduction. The development of all-perovskite SOFCs is thought to have certain benefits with respect to the structural cohesion that results.

1.3.4 Cathode materials

1.3.4.1 Perovskites

Today, cathode materials are perhaps the most widely researched component of the fuel cell stack. A rich quantity of materials have been proposed, synthesised and characterised. Previously, we mentioned the possible employment of perovskites as electrolytes and anode materials, but their role in the SOFC is most notable for their use as cathode materials. The interest surrounding perovskites

reflects the broad range of systems and properties that are observed within this series [65]. As an example, conductivity properties are found to range from pure electronic to pure ionic, with examples of mixed conductivity in between.

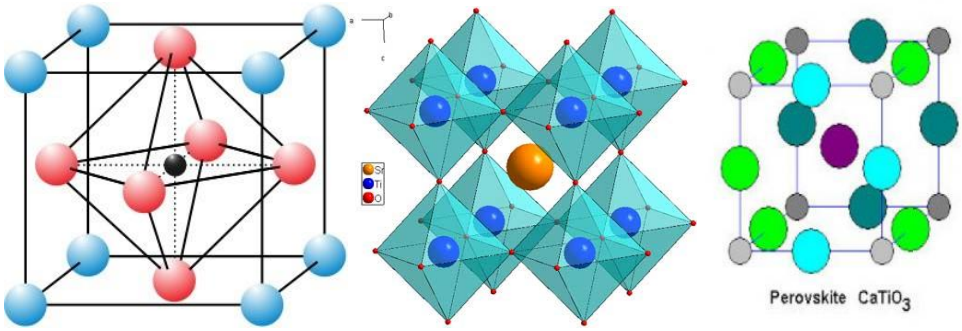


Figure 1.7 - Different representations of the perovskite structure [72–74].

The perovskite structure has a general formula of ABO_3 (e.g. $SrTiO_3$), where cation species are found at the A and B-sites of the crystal structure. This structure is shown in Figure 1.7. In SOFC cathodes, at the A-site sits a lanthanide (e.g. La, Pr) or alkaline earth element (e.g. most commonly Sr or Ba).The B-site, meanwhile, is taken up by a first-row transition metal (e.g. Ni, Co, Fe, Mn). In the ideal state, the structure possesses a cubic lattice, with the Goldschmitt tolerance factor (t) used to describe the tendency to deviate from this condition:

$$t = \frac{(r_A + r_B)}{\sqrt{2}(r_B + r_O)} \quad [Eq\ 1.9]$$

Where r_A and r_B are the radii of the ions at the A and B-site and r_O is the radius of the oxygen ion. For perovskites, the tolerance factor varies between 0.8 and 1.1, with a cubic system favoured for values close to 1. Ishihara [65] has provided an excellent text on the use of perovskite oxides for SOFCs. The authors describe the stability, as well as the crystal structure, of the perovskite to be "*determined by the ratio of the ionic radii of the A and B crystals*" as well as on the co-ordination preference of the A and B cations.

1.3.4.1.1 $LaMnO_3$-based perovskites

Similar to the manner in which ZrO_2 does not possess appreciable oxide conductivity, $LaMnO_3$ is itself not a greatly attractive proposition as an SOFC electrode material. The material possesses intrinsically low conductivity [75]. However, the use of dopants is capable of changing this significantly. The A-site doped $La_{1-x}Sr_xMnO_3$ represents one of the most used cathode compositions and, until around the 2000s [45], was deemed the state-the-of-art. This material ($La_{0.8}Sr_{0.2}MnO_3$ or $La_{0.6}Sr_{0.4}MnO_3$ are commercially available compositions) has appreciable electrical conductivity at operating temperatures as well as favourable thermal expansion and chemical stability properties (in relation to the neighbouring electrolyte materials discussed previously).

As was described for the Ni-YSZ anodes, the employment of composite cathode materials has been found to offer beneficial performance. Again, the combination of a predominantly ionic-conducting phase with an electronically conducting one offers a promotion of cathode performance (i.e. LSM-YSZ). In this case, LSM (stable in high temperature, oxidising conditions) replaces the Ni which would otherwise oxidise to NiO under cathode conditions.

1.3.4.1.2 $LaCoO_3$-based perovskites

Reducing the temperatures of SOFC operation is deemed to have a number of beneficial effects. In order to achieve this, however, materials with appreciable performance (i.e. ionic and electrical conductivity at reduced temperatures) are required. So-called *Mixed Ionic Electronic Conductors* (MIEC) are today seen as the preferred materials for SOFC cathodes, replacing the metal-ceramic cermet (LSM-YSZ) described previously. $La_{1-x}Sr_xCoO_3$ (LSC) and $La_{1-x}Sr_xCo_{1-y}Fe_yO_3$ (LSCF) have been shown to offer particularly good performance in-situ and have enabled a reduction in operating temperatures to be achieved [45]. These materials have appreciable electronic *and* oxide conductivity, extending the amount of reaction sites through the thickness of the cathode. A great body of research work has been afforded to these materials in terms of understanding their performance and degradation modes.

1.3.4.2 Alternative structures

Although perovskites are no doubt the most researched family of materials with respect to SOFC cathode materials, alternatives are also considered in the literature. Mostly, these alternatives relate to the perovskite structure including the Brownmillerite, double perovskite and Ruddlesden-Popper phases [76]. The Ruddlesden-Popper phases, in particular, have gained some substantial research attention due to their favourable oxide-conducting properties. We shall review some of the work in this area in greater detail in Chapter 2 since these are integral to the subject matter of this thesis.

1.4 SOFC degradation processes

SOFC degradation rates are a key issue for the development of the technology [60]. High operating temperatures are capable of accelerating degradation processes, driving thermal instabilities and chemical reaction between neighbouring components as well as leading to structural changes (i.e. grain coarsening/loss of catalyst surface area). These phenomena can lead to a lowering of the cell output (i.e. power density output). Broadly speaking, degradation can be categorised into three types:

- Passivation of catalysts via impurities from fuel or oxidant
- Microstructural changes
- Thermal/chemical instabilities of materials or reaction between cell and stack components

We will briefly discuss these to identify the main issues which limit SOFC cell life-times. From this, it is possible to appreciate where the greatest improvements may be required for the next generation of SOFCs. A more focussed discussion on certain phenomena is provided in Chapter 2.

1.4.1 Fuel / oxidant impurities

Given the wide breadth of fuels that can be employed within SOFC systems (e.g. hydrogen, natural gas, biofuels), it is of little surprise that significant research has been placed into understanding the effect of various common impurities (e.g. H_2S, NH_3, siloxanes) on SOFC anodes [77,78]. Sulphur species, in particular, are known to have a strong poisoning effect on the common Ni-catalyst of the cells [79,80]. Exposure to molecules such as H_2S can lead to a rapid loss in power output. Sulphur has

been shown to have the ability[10] to negatively influence SOFC performance when its fuel-stream content is as low as 0.05 ppm [80]. On the cathode side of the SOFC, the use of '*real-world*' atmospheric air means that a host of minor species may be present [81]. This may include NO_X and SO_X species.

The deposition of solid carbon (i.e. coking) as a result of employing carbonaceous fuels can also impact the anode performance [82]. Again, the deposited carbon is capable of passivating the catalytic behaviour of Ni or even blocking pores and hindering gas diffusion. To avoid such issues, the oxygen-to-carbon ratio needs to be carefully chosen in the fuel stream (a ratio of around 1.5-to-1 is suggested to be necessary in reference [83]).

1.4.2 Microstructural changes

The microstructure of the SOFC cells is known to have an important impact on cell performance. Fabrication conditions are tuned carefully in order to ensure good adhesion between cell layers and to ensure suitable porosity and catalyst surface area is provided for the ORR and HOR. Under the conditions of SOFC operation, these features can be degraded [84].

The cracking of electrolytes can ultimately be fatal for an SOFC [85]. Such features enable fuel and oxidant to cross through the electrolyte and for direct combustion to occur. This can lead to the formation of hot-spots and, ultimately, the fracture or failure of the cell. Given that thin electrolytes are preferred to improve cell performance, care needs to be taken to prevent cracks forming during assembly. With respect to Ni-based anodes, meanwhile, so-called 'redox' cycling where the Ni is cyclically oxidised (to NiO) and reduced (back to Ni) can cause structural damage to the cell [84,86]. The cyclic expansion and contraction of the cell can lead to cracking of the cell or delamination of the electrode.

[10] The effect of sulphur species is influenced by other factors including operating temperature

Electrode de-lamination is an often-cited issue that can lead to a loss in performance (e.g. [87]). This can be exacerbated by a thermal expansion mismatch between materials; this is an issue which is known for $LaCoO_3$ type cathode materials which have much higher thermal expansion coefficients (~20 x 10^{-6}°C^{-1} [88]) than those of conventional electrolyte materials like YSZ and GDC (~12 x 10^{-6}°C^{-1} [89]). Such a mismatch in thermal expansion properties can offer issues during both fabrication and during operation (any exposure to thermal cycling).

Nickel agglomeration or coarsening is another issue which commonly features in academic literature (e.g. [90]). The coarsening of grains and resulting loss of catalytic area can have a deleterious effect on the performance of the anode (and cell). These effects can be further heightened by the presence of steam which has been found to accelerate coarsening processes. Coarsening is also a known issue at the oxygen electrode side of the SOFC. This is particularly problematic for nano-structured or 'infiltrated' cathodes which have become popular amongst the research community in recent times.

1.4.3 Chemical incompatibility / secondary phase formation

1.4.3.1 Instability and chemical reactivity

A key issue with operating at high temperatures is the effects that this can have on the cell materials in isolation of one another. As an example of this, Sr-containing cathode materials can suffer from the segregation of Sr in the form of SrO [91]. In itself this has a damaging effect, leading to a lowering of surface exchange properties. Additionally, the resulting SrO can react with species such as CO_2 to form $SrCO_3$. In such a case, the SrO acts as a 'getter' for such species and the formation of these phases can further affect the finely-tuned performance of the cell.

Under SOFC operating conditions, there has been shown to be a tendency for cation diffusion into neighbouring components and a formation of secondary phases. Perhaps most commonly, a reaction between YSZ and common cathode materials such as LSCF or LSC is known to occur. The formation of $La_2Zr_2O_7$ or $SrZrO_3$ between these layers can have a negative effect on cell output [92]. This effect is usually observed during sintering processes (>1000 ˚C). To overcome this, an 'interlayer' between the

electrolyte and the cathode material is often used. Commonly GDC layers of just a few microns are employed, protecting the materials from reaction with one another. Alternatively, YSZ can be removed altogether with a GDC electrolyte employed instead. However, as discussed earlier, such an approach would likely limit operating temperatures to below 600˚C given the mixed conductivity of CeO_2 phases above this temperature.

1.4.3.2 Chromium Poisoning

The phenomenon of '*chromium poisoning*' is known to significantly hamper the lifetime of SOFC cells and is described in detail in our recent review paper on this matter [93]. Chromium from the stainless steel interconnects is vaporised in the form of CrO_3 and $CrO_2(OH)_2$ and migrates to the cathode where it deposits in solid form. The solid chromium species that is subsequently deposited is heavily dependent on the cathode material itself. The resulting effect, therefore, is not identical for all materials. In the case of LSCF and LSC, chromium vapours are found to react with segregated SrO to form $SrCrO_4$. This phase is highly insulating and can rapidly deteriorate cell performance. Today, interconnects are commonly coated with ceramics (e.g. $(Mn,Co)_3O_4$) to prevent significant migration of chromium but these are not completely effective and can have their own degradation effects [94]. We will further consider the role of chromium poisoning on cell lifetime in Chapter 2.

1.5 Discussion

So far in this chapter, we have discussed an overview of some of the common SOFC materials and some of the general degradation effects which can inhibit their performance. Today, the overall trend for SOFC research is to lower the operating temperature (below 800˚C and towards 600˚C). This has a number of beneficial effects:

- Ability to use lower cost stainless steel interconnects rather than ceramics which are used at higher operating temperatures (900-1000˚C)
- Reduction in thermal effects (i.e. thermomechanical effects and high temperature instabilities)

- Reduced time for system start-ups

However, this also places extra demand on finding materials which can offer suitable performance at such temperatures. The challenge is perhaps most demanding on the oxygen electrode side of the cell where the kinetics of the ORR are slower than the HOR. Producing materials with suitable performance at reduced temperature whilst simultaneously avoiding degradation processes has proven to be a delicate balancing act.

In our aforementioned review on chromium poisoning, we identified that Cr-poisoning was a major degradation process in SOFCs and that La-nickelate materials have been shown to offer some promise in avoiding or reducing these effects. This includes perovskite-type materials like $LaNi_{0.6}Fe_{0.4}O_{3-\delta}$ as well as the Ruddlesden-Popper type materials such as $La_2NiO_{4+\delta}$. Whilst such materials do not appear to be immune to the effects of chromium poisoning, the literature would indicate they may be able to offer a noted improvement in comparison with conventional materials like LSM, LSC and LSCF. However, such considerations on degradation rates do not necessarily factor in the performance of the nickelates in comparison with such materials. Clearly, a material which has far inferior performance but greater stability is unlikely to offer a serious alternative to conventional choices. To provide clarity, this work will look to offer a comprehensive analysis on the in-situ performance of La-nickelates as oxygen electrode materials in SOFC technology.

1.6 Overview of thesis goals

In this thesis, we look to offer insight into whether or not La-Ni-O cathode materials offer a serious alternative to conventional cathode materials like LSCF. The aims of the thesis are as follows:

- Identify and assess the relative performance of the popular lanthanum nickelate electrode materials in relation to the state-of-the-art materials.
- Understand the advantages and challenges associated with the use of these materials.
- Consider the most promising routes for electrode optimisation with these materials with a focus on the use of composite electrodes.

- Additionally, consider whether there are any short-falls and/or inconsistencies associated with the electrode-level testing that is detailed in the existing literature.

There already exists a large body of work with respect to these materials and, in Chapter 2, we will consider the current literature available. Importantly, we aim to assess the present understanding of these materials and compare it with that of conventional materials. This includes considerations on both the fundamental properties of these materials as well as their short and long-term performance in-situ. This work is conducted with an emphasis on comparison with the state-of-the-art. The remaining chapters of the thesis will detail our experimental work on the materials, with the methodology outlined in Chapter 3. Chapter 4 considers the performance of various lanthanum nickelates when employed as oxygen electrode materials in a symmetrical cell testing set-up. Then, in Chapter 5, an analysis of the same materials is conducted in a 'single cell' testing configuration (i.e. testing under polarisation). In both of these chapters, an emphasis is placed on drawing reference to the state-of-the-art material (LSCF) and with further reference to literature data. Further, the breadth of materials studied in these chapters makes it possible to consider the appropriateness of some SOFC testing principles and to determine which approaches are most suitable. Finally in Chapter 6, some efforts to identify optimisation routes are explored.

2 Literature review: replacing state-of-the-art cathode materials in SOFC

2.1 Overview of chapter

One intense area of research in the field of SOFC technology is the exploration of cathode materials, with the aim of offering improved performance and reduced degradation rates. In this chapter, the literature in this area is discussed. This begins with an assessment on some of the drivers for change and is followed by an exploration of work conducted on a group of alternative cathode materials; the lanthanum nickelates. The work in this chapter draws, modifies and extends on our two review papers in these areas [93,95].

2.2 Drivers for change

2.2.1 Historical context: reducing operating temperature

The development of SOFC cathode materials spans many decades and, in the most part, has revolved around the employment of electrochemically active ceramics, capable of promoting the Oxygen Reduction Reaction (ORR). The requirements placed on SOFC cathodes were described in the introductory chapter of this thesis, as was an overview of some of the state-of-the-art solutions to address these challenges. This chapter will look at identifying where improvements have been sought and where challenges remain.

The high temperature (~1000˚C) operating regime of the early SOFC offered some engineering and materials-science based challenges. As was described earlier, this broadly revolved around the development of components with suitable resilience and performance. Most notably, the temperature range required the use of ceramic interconnect materials (typically $LaCrO_3$-based). The SOFC interconnects, which transport both electrons and gases to the cells, require complex geometries which offers fabrication difficulties and hence high expense. A move towards an 'intermediate temperature' regime (500 to 750˚C as defined in [96]) was thought to be beneficial in helping to alleviate this issue [47,96,97]. Importantly, such an approach enabled the introduction of

stainless steel alloys which can be fabricated at lower cost. Furthermore, such a reduction in operating temperature can lead to a decrease of many thermally-driven degradation issues.

Although a decrease in operating temperature offers many attractive benefits, a number of challenges are brought to the fore as a direct result [96]. The transport and reaction kinetics are inevitably reduced and, as a consequence, cell performance is diminished. Such behaviour is clearly disadvantageous but materials-based research has proven this can be offset somewhat by a suitable selection of materials and a fine-tuning of microstructure. Perhaps most significantly, $LaMnO_3$-type perovskites are replaced by doped $LaCoO_3$-perovskites such as $La_{1-x}Sr_xCo_{1-y}Fe_yO_{3-\delta}$ (LSCF) and $La_{1-x}Sr_xCoO_{3-\delta}$ (LSC) [98,99]. These materials, due to their superior ionic and electronic conductivity, increase the amount of potential sites for the ORR to occur; from 'single points' at triple phase boundaries (e.g. where the LSM, YSZ and gas phases meet) to a two-dimensional coverage of the MIEC electrode surface. This leads to a resulting improvement on performance when compared with $La_{1-x}Sr_xMnO_{3-\delta}$ (LSM) and, as a result of such factors, doped lanthanum cobaltites are generally seen as the preferred SOFC cathode material in commercial cells.

2.2.2 Assessing degradation rates: are they too high?

In achieving successful commercial SOFC systems, long-term degradation rates are of key importance. Given the environment under which SOFCs are fabricated (>1000˚C) and operated (600 to 800˚C), it is perhaps unsurprising that a sizeable challenge is presented. The commonly discussed requirement for stationary power applications (currently the area for SOFC market expansion) is to offer around 10 years (~90,000 h) of continuous operation [59]. The Solid State Energy Conversion Alliance (SECA) in the US aim to achieve average degradation rates of no greater than 0.2% per 1000 h by 2030 [100]. Elsewhere, Japan's '*New Energy and Industrial Technology Development Organisation*' (NEDO) have targeted a more stringent degradation rate of ≤0.1%/1000 h over a 90,000 h lifetime [101]. Understandably, there is relatively little data available for the case where state-of-the-art cells have been operated for such periods. In fact, to the best of our knowledge, only one SOFC stack has

completed testing for such a period [102]. Analysis of this test therefore becomes of keen interest. The average degradation rates for the cells in the stack are observed in Table 2.1 and defined for several time periods. It is observed that the loss in performance measured over the time period exceed the aforementioned requirement, although the degradation rate itself is not linear and evolves over the life of the SOFC cell. It is notable in the aforementioned study that the authors indicate an improvement can be anticipated due to an already-developed advancement in the technology. More specifically, this relates to an improved interconnect coating (i.e. $(Mn,Co,Fe)_2O_4$ rather than MnO_X) which alleviates the effects of chromium poisoning to a greater extent. 'Chromium poisoning' is identified as a key degradation driver in the study (particularly during the first 40,000 hours of operation) and will be discussed in more detail in Section 2.2.3.3.

Although there is a scarcity of data studying cell or stack degradation over the full, desired 10-year lifetime, there are a number of studies considering different cell configurations for shorter time periods. This includes a notable body of work by key research players Jülich in Europe [98] and by NEDO in Japan [99]. A selection of long-term SOFC stack tests are shown in Table 2.2. These studies indicate that degradation rates can vary significantly (no doubt a result of the range of cell materials and testing parameters) but have been demonstrated to be as low as targeted degradation rates in at least one instance. Perhaps notably, the stack to have achieved this was operated at 900˚C and employed an LSCM cathode material and a Sm-doped-Ceria interlayer (i.e. not the often preferred intermediate temperatures range utilising an LSCF cathode and GDC interlayer). Aside from that result, it is notable from the evidence presented that reported long-term degradation rates have mostly been found to remain above the SECA and NEDO targets and as high as 2.6%/1000 h in some instances. Skafte et al.[101] have provided further analysis of stack degradation rates and the reader is referred to that work for a more detailed discussion.

Table 2.1 – Average cell degradation rates for a 2-cell stack operated for 100,000 h as presented in [102]*. Cells of type LSCF6428 | GDC | YSZ | Ni-YSZ in contact with MnO_X-coated stainless steel interconnects were employed for this work.*

	Period I	**Period II**	**Period III**	**Period IV**	**Period V**	**Total**
Time	~3000 h	3000 to 16,000 h	16,000 to 39,000 h	39,000 to 69,000 h	69,000 to 93,000 h	~93,000 h
Voltage Deg. Rate (%/kh)	1.4	0.7	1.1	0.3	<0.1	0.5 (Average)
ASR Deg. Rate (%/kh)	6.6	3.6	5.1	1.4	0.2	2.5 (Average)

A key issue in interpreting the data from literature is in understanding how degradation rates can be broken down into different contributions. Many authors have employed physical characterisation techniques (e.g. SEM/EDX) to explore the causes of degradation. In a number of these studies, several noteworthy degradation mechanisms associated with the cathode are described (migration of cations and formation of new phases) [103–105]. These phenomena will be explored in further detail in subsequent sections. In work by Yokokawa [106] and later by Ido et al.[107] the contributions of the cathode are shown to offer a sizeable portion of the overall degradation rate. Interestingly, in the former study, the largest contributions to degradation are associated with ohmic losses. However, as is noted by the authors, "*it is not easy to find out proper places for resistivity increase along the electrical paths*". In other words, degradation of the ohmic contribution could result from numerous effects relating to different components within the cell. As is discussed by Yokokawa et al.[99], this may include (a) phase changes in the electrolyte or (b) the formation of insulating phases within the cell. In the latter case, this may relate to phenomena related to the cathode (e.g. $SrZrO_3$ or $SrCrO_4$ formation). The evidence available in the literature supports the common perception that cell degradation is heavily influenced by cathode material selection. In turn, this suggests that material selection can further help to reduce degradation rates. To develop additional understanding on how this could be achieved, the attention will now be switched to understanding some of the key degradation routes.

Table 2.2 - Long-term degradation studies on SOFC stacks. LMCC=$La_{0.97}Mn_{0.4}Co_{0.3}Cu_{0.3}O_3$ (Contact Layer).

Institute [Stack Ref.]	**Cell Config.**	**Interconnect (Coating)**	**Time period**	**Temp.**	**Fuel / Oxidant [utilisation]**	**Current density (Acm^{-2})**	**Degradation Rates**	**Ref**
Jülich [F1002-97]	Ni-YSZ | YSZ | GDC | LSCF	ITM Interconnector (MnO_X)	~100,000 h	700˚C	H_2 / Air [40% utilisation]	0.5	0.5%/1000 h (V) 2.5%/1000 h (ASR) [See Table 2.1 for further details]	[102]
Westinghouse	Ni-YSZ | YSZ | Doped $LaMnO_3$	Doped $LaCrO_3$	50,000 h	~1000˚C	Not specified	Not specified	<0.5%/1000 h (V)	[108]
Jülich [F1004-21]	Ni-YSZ | YSZ | GDC | LSCF | LMCC [Planar]	Crofer 22 APU ($Mn_{1.0}Co_{1.9}Fe_{0.1}O_4$)	34,000 h	700˚C	H_2 (21%H_2O) / Air [40% utilisation]	0.5	0.3%/1000 h (V) 2%/1000 h (ASR)	[109]
Jülich [F1004-67]	Ni-based | YSZ | GDC | LSCF	Crofer 22 APU (MCF)	>23,500 h	700˚C	H_2 / Air [40%]	0.5	0.3%/1000 h	[110]
Jülich [F1004-08]	Ni-based | YSZ | LSM-YSZ | LCC10	Crofer 22 APU (MCF)	19,036 h	800˚C	H_2 / Air [40%]	0.5	0.4%/1000 h	[110]

Morimua	MORIMURA Materials not specified [Planar]	Not specified	≤18,800 h	700˚C	$H_2/CO_2/H_2O$ (64/16/20%) / Air	0.518	0.31%/1000 h [80% FU] – 18,800 h 0.34%/1000 h [85% FU] – 11,300 h	[107]
EPFL [#18000]	Ni-YSZ | YSZ | GDC | LSCF-GDC	K41 / AISII Steel ($MnCo_2O_4$)	~18,000 h	720 to 780˚C	N_2/H_2 / Air	0.25 (0 to 12,000 h) 0.05 (12 to 18,000 h)	Not specified.	[111]
Jülich [F1002-95]	Ni-based | YSZ | GDC | LSCF | LCC12	Crofer 22 APU (MnO_X)	17,660 h	700˚C	H_2 / Air [40%]	0.5	1 to 1.4%/1000 h	[110]
MHPS	Ni-YSZ | YSZ | SmDC | LSCM ["Segment-in-series"]	LST	16,000 h	900˚C	Not specified	0.15	0.1%/1000 h	[99]
Jülich [F1002-132]	Ni-based | YSZ | GDC | LSCF | LCC12	Crofer 22 APU (MnO_X)	15,144 h	800 ˚C	H_2 / Air [40%]	0.5	1.5%/1000 h	[110]
Kyocera	Ni-YSZ | YSZ | doped-CeO_2 | LSF [Flattened Tubular]	Not specified	~15,000 h	750˚C	$H_2/CO_2/H_2O$ (64/16/20%) / Air	0.36	0.34%/1000 h [80% Fuel Utilisation] 0.5%/1000 h [85% Fuel Utilisation]	[107]

NTK	<Anode> | YSZ | <Barrier Layer> | LSCF	Not specified	10,000 h	700˚C	Not specified	0.2	0.6%/1000 h	[99]
TOTO	Ni-CeO_2 | LSGM | LSCF [Micro-tubular]	Metal-based	10,000 h	700˚C	Not specified	0.21	0.5%/1000 h	[99]
Kyocera	Ni-YSZ | YSZ | Doped-CeO_2 | LSF-based	Metal Based with $LaCrO_3$ separator	10,000 h	750˚C	Not specified	0.2	0.2%/1000 h	[99]
NGK	*NGK Stack:* Ni-YSZ | YSZ | GDC | LSCF	Not specified	8,000 h	750˚C	Not specified	0.23	0.5%/1000 h	[99]
Jülich [F'''2018-07]	Ni-based | YSZ | GDC LSCF | LCC10	Crofer 22 APU (MCF)	5450 h	700˚C	CH_4-H2 / Air [70-80%]	0.5	0.3%/1000 h	[110]
Versa Power Systems	Not specified. [Planar]	Ferritic Stainless Steel	~5000 h	705˚C	Nat. Gas / Air [61.6% / 14.8% util.]	0.364	2.6%/1000 h	[112]

Huazhong University of Science and Technology	Ni-YSZ | YSZ | YSZ-based composite | LNC64	SUS 4310 [No coating]	~4400 h	750˚C	H_2 / Air	0.355	1.5%/1000 h	[113]
Jülich [F1002-56]	Ni-YSZ | YSZ | LSM-YSZ | LSM | LCC10 [Planar]	JS3 Steel Interconnect	3000 h	800˚C	Hydrogen / Air [40% FU]	0.5	86 mΩcm^2 kh^{-1} (Cell1) [+23%/1000 h][A] 50 mΩ cm^2 kh^{-1} (Cell2) [+13.9%/1000 h][A] 68 mΩ cm^2 kh^{-1} (**Avg.**) [+18.9%/1000 h][A]	[114] [98]
Jülich [F1002-68]	Ni-YSZ | YSZ | LSM-YSZ | LSM | LCC10 [Planar]	IT11 Steel Interconnect	3000 h	800˚C	Hydrogen / Air [40% FU]	0.5	57 mΩ cm^2 kh^{-1} (Cell1) 29 mΩ cm^2 kh^{-1} (Cell2) 43 mΩ cm^2 kh^{-1} (**Avg.**) [6 to 8%/1000 h][B]	[114] [98]
Murata	Ni-ScSZ | ScSZ | GDC | LSCF	Not specified	3,000 h	750˚C	Not specified	0.35	2.6%/1000 h	[99]

[A] Calculated based on a starting ASR value of 0.36 Ωcm^2 detailed in [114]

[B]Degradation rates specified in [98]

[C]Calculated based on a starting ASR value of 0.26 Ωcm^2 detailed in [114]

2.2.3 Cathode degradation mechanisms

2.2.3.1 Surface segregation

The stability of cathode materials is a known issue contributing to the long-term performance of SOFCs. As was briefly touched upon in Chapter 1, one of the most noteworthy observations for doped oxides like LSCF is the segregation of Sr^{2+} in the form of SrO. There are a number of good reviews studying this area in great detail (e.g. [91,115,116]) and, for a more comprehensive overview, the reader is referred to those papers. Here, we shall summarise some key ideas laid out in those articles. As described in Figure 2.1, Sr-segregation begins with a rearrangement of the atoms from the bulk material to the surface, before a precipitation of secondary phases as the amount of segregated ions exceeds the solubility limit. The effect of *A-site* segregation is worsened at high temperature and in oxidising environments (i.e. the conditions of an SOFC cathode material). The effects of this phenomenon can be appreciable. The precipitation of SrO on the surface of the LSCF grains can lead to a deactivation of the electrochemically active sites. This effect has been evidenced via consideration of the electrode performance before and after chemical etching of the segregated SrO [117,118]. In part, the precipitation of SrO can have a deactivating effect on the grounds of the insulating properties of the phase as well as due to the inferior oxygen exchange properties. Perhaps most significantly, however, the migration of Sr^{2+} can lead to the formation of more damaging insulating phases. This includes a reaction with ZrO_2-based electrolytes to form $SrZrO_3$ [119,120], as well as offering a 'getter' for impurities like CO_2, SO_2 and Cr-species [121]. It is important to note that other species (other than Sr) are also known to segregate out of the bulk material (e.g. Ba^{2+} in the case of BSCF, Mn^{2+} in the case of LSM and Co^{2+} in the case of LSC/LSCF).

The driver for cation segregation is deemed to be related to a lattice strain relaxation as well as due to electrostatic interactions between the surface and bulk. Importantly, larger dopants (relative to the host ion) are known to segregate out of the bulk more easily due to the greater strain created within the matrix [122]. This has led to some efforts to study dopants which offer a better match with the host cation (e.g. Ca^{2+}) [122]. Other attempts to alleviate this issue via a reduction in the strain energy

include the use of A-site sub-stoichiometry [123] and the use of alternative, smaller B-site cations [124]. Particularly relevant for our later discussion on La-Ni-O systems, it has been observed that the use of Co or Ni can help to suppress the segregation of Sr in comparison with Mn and Fe [124].

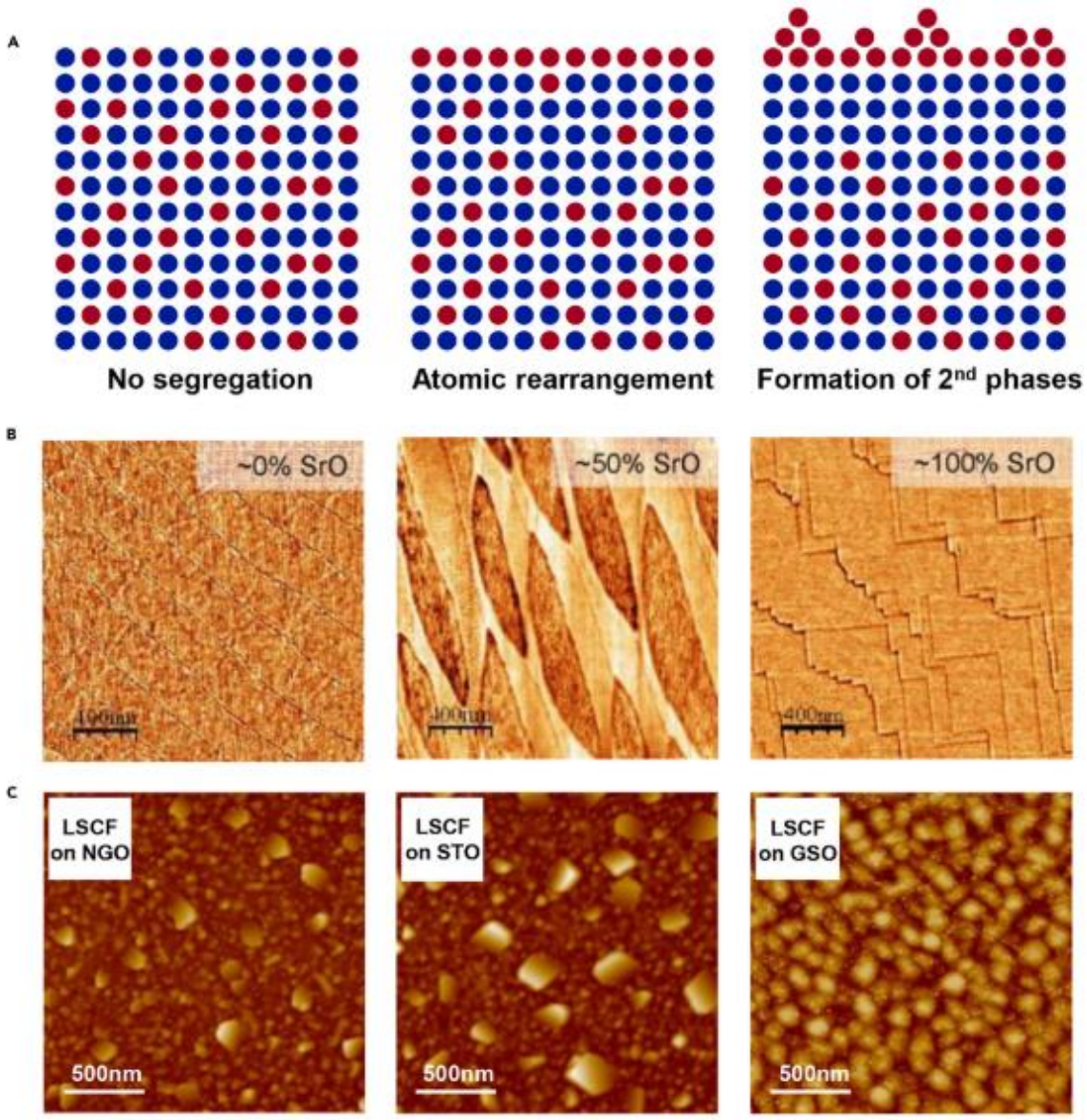


Figure 2.1 - The process of SrO segregation from LSCF [91]. *(A) Schematic images depicting the atomic re-ordering of Sr atoms (red circles) from the bulk phase and their subsequent surface-deposition. (B) Atomic Force Microscopy (AFM) analysis of $SrTiO_3$ substrate surface annealed at 1300˚C for 2 hr, 12 hr and 72 hr (left to right) showing the formation of SrO. (C) AFM images of LSCF6428 surface on three different substrate materials ($NdGaO_3$ (NGO), $SrTiO_3$ (STO) and $GdScO_3$ (GSO)) - each sample was subject to a 10-hour 800˚C heat treatment and found to precipitate secondary phases (to varying extents).*

2.2.3.2 Electrolyte incompatibility

As was previously discussed, a key requirement for SOFC materials is their compatibility (both chemically and thermomechanically) with neighbouring stack materials. With respect to chemical interactions, it is well regarded that reaction between LSCF and YSZ leads to the formation of insulating phases such as $La_2Zr_2O_7$ and/or $SrZrO_3$ [125]. It is for this reason, therefore, that a CeO_2-type 'barrier layer' (typically $Ce_{1-x}Gd_xO_2$ (GDC) interlayer) is commonly employed in the state-of-the-art SOFC cell [99]. This barrier layer separates the ZrO_2-electrolyte and the LSCF cathode. Ideally this could be removed (i.e. by finding a more compatible combination of materials) to reduce the complexity and number of steps involved in the cell manufacture. Furthermore, it has been found that cation diffusion can occur across the CeO_2 layer and $SrZrO_3$ formation can occur even in the presence of the barrier layer [106], although the effect is no-doubt reduced due to the barrier layer. Today, the use of an interlayer is generally accepted as a satisfactory solution, with excellent performance having been found to be achievable via this route. However, it is apparent that finding a material with improved stability could have several benefits. Perhaps of greater concern for $LaCoO_3$-type cathodes, however, is the coefficient of thermal expansion (17 to 20 x 10^{-6} $^{\circ}C^{-1}$ [126]), which is significantly larger than those of standard electrolyte materials [126]. The common perception is that a sizeable thermal differential expansion can compromise the structural integrity of the cells on heating and cooling of the stack. Indeed, evidence in the literature indicates that this can lead to delamination of the electrode layer and means that temperature ramp rates need to be carefully selected [87]. It is often stated within the literature that a move to a more favourable TEC would offer advantages.

2.2.3.3 Chromium poisoning[11]

2.2.3.3.1 Background

As described previously, the use of stainless steel alloys offers a number of key advantages. However, as a side effect of utilising metallic interconnects, conventional cathode materials have been shown

[11] This section draws on the author's published review paper in this area [93]

to suffer from a chromium-related poisoning phenomenon that deteriorates the performance of the SOFC. Highlighting the importance of studies in this area, Arregui et al. [127] analysed a number of operational and manufacturing parameters for a small sub-section of SOFC cathode materials and concluded that the most influential factor, with respect to performance degradation, was the introduction of a chromium source. The US Department of Energy have also commented on the need to mitigate the effects of chromium poisoning**,** labelling the phenomenon a "*major contributor to performance degradation and reduced system reliability*" [100]. NEDO have highlighted this issue as one of the main factors in the degradation of SOFC stacks [53]**.**

The use of chromium in ferritic stainless steels enables the formation of a protective chromia (Cr_2O_3) surface-layer; this layer provides the alloy's resistance to the degradative effects of corrosion. Since other metals are capable of forming a similar protective layer (e.g. the formation of Al_2O_3 on alumina-forming steel alloys), there may remain a question as to why chromium-containing alloys specifically are the preferred material. The answer to this is related to the all-important electrical conductivity of the oxide species, the adherence of the oxide scale to the bulk material, and the slow growth of the oxide scale [128,129]. It is with these considerations that chromium-containing metallic alloys have been identified as the most suitable for application under SOFC conditions. The issue of chromium poisoning, therefore, persists.

The chromium poisoning literature is broadly divided into two topics; (a) Cr-species evaporation from interconnects and (b) the formation of Cr-phases within the cathode. Under SOFC operating conditions there is a tendency for the chromia species to react with oxygen and moisture and migrate towards the cathode in gaseous form. The vaporisation of this chromia layer has been studied thermodynamically [119,130,131] and experimentally [128,132]. It is generally agreed [128,130,131,133] that CrO_3 and $CrO_2(OH)_2$ are the most common and abundant species that are formed. This occurs via the following reactions [131]:

$$Cr_2O_3(s) + 1.5O_2(g) \rightarrow 2CrO_3(g) \text{ [Eq. 2.1]}$$

$$Cr_2O_3(s) + 1.5O_2(g) + 2\,H_2O(g) \rightarrow 2CrO_2(OH)_2(g)$$ [Eq. 2.2]

It has been shown that the relative quantities of such species vary as a strong function of oxygen partial pressure and humidity [119,130,134]. Lower valency Cr-gases are capable of becoming dominant at lower oxygen partial pressures [134]. In addition, a thermodynamic study conducted by Yin et al.[119] has shown that chromium evaporation rates increase at higher temperatures. In particular, the formation of the CrO_3 species increases significantly as the temperature is increased from 600 to 1000˚C.

An appreciable body of research has sought to reduce the rate at which chromium is evaporated from steel interconnect materials. Indeed, there are a range of interconnect alloys that have been considered within the SOFC literature and there are several reviews [135–137] which summarise the developments in this area. The use of alloys that are capable of forming Cr-Mn spinel layers has been shown to reduce degradation effects [138–140]. These spinel phases form on top of the Cr_2O_3 layer and reduce the rate at which chromium is vaporised from the interconnect. Researchers have successfully engineered spinel phases (e.g, Cu-Mn spinel, Co-Mn spinels etc) as coating materials in attempts to deliberately reduce volatilisation rates [141–143]; perovskite coatings [128,142,144] have also been shown to offer great promise in achieving this. The use of suitable interconnect materials can help to alleviate the issue of chromium poisoning but the studies of such materials have also shown that although reduced, the chromium release rate still remains too high to safeguard sufficient SOFC lifetime for stationary applications (i.e. ~10 years). It is worth noting that the selection of suitable interconnect alloys represents a key step with respect to mitigating the effects of chromium poisoning. The additional application of protective coatings will no-doubt also be necessary.

2.2.3.3.2 Effect on cathode materials

The impacts of migrating chromium on SOFC cathodes are many and varied dependent on the materials in question. Generally speaking, chromium is able to migrate (either via solid-state diffusion or in the gaseous-phase) into the electrode structure where it is deposited as a solid phase. The

formation of such phases, like other degradation mechanisms, have the effect of deteriorating the cell output over the cell lifetime, as seen in Figure 2.2. It seems apparent from the literature that the resulting phase and its location are characteristic of the cathode itself. In the case of LSM, for instance, chromium has been reported to exist at the electrode-electrolyte interface, in the form of Cr_2O_3 and/or $(Cr,Mn)_2O_4$ [132,145–147]. On the other hand, LSCF and LSC cathodes are seen to form a $SrCrO_4$ layer on the contacting surface between the interconnect and electrode [138,148–150]. As described earlier, SrO is capable of segregating out of the bulk perovskite phase and this subsequently acts as a 'getter' for the chromium species [148]. The behaviours of other SOFC cathode materials in the presence of chromium have been explored and are discussed in our recent review on this matter [93]. Some observations on different materials are summarised in Table 2.3.

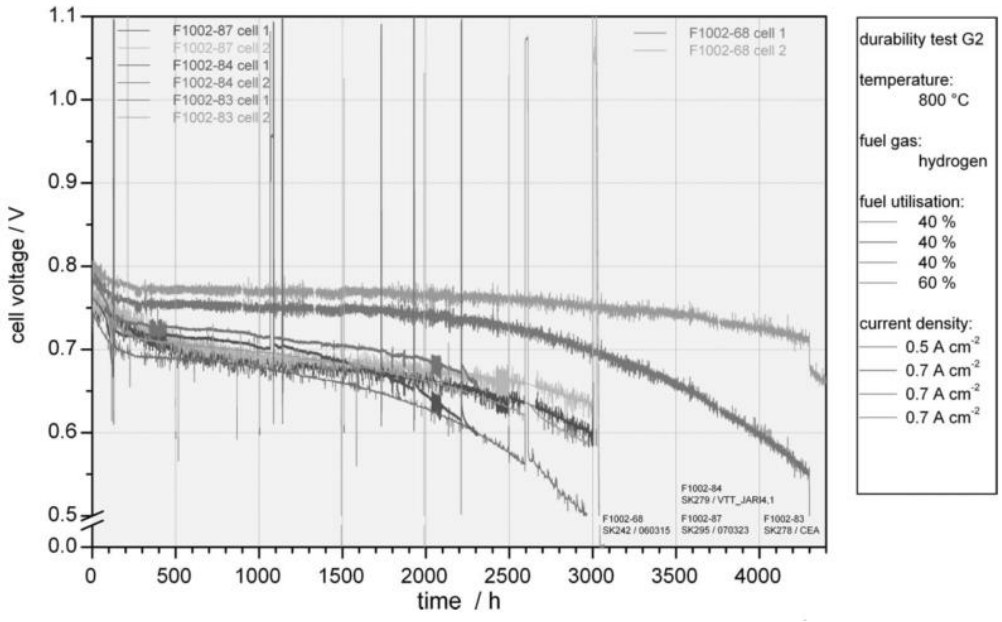


Figure 2.2 – Voltage plot of galvanostatically-operated fuel cell stacks [114]*. The stacks contained an LSM-based cathode material and stainless-steel interconnects.*

Researchers have studied numerous effects of different variables on the poisoning phenomenon, including temperature [132,151] and humidity [138,152–154] as well as considering the role of electrode polarisation [146,147,152,155]. The latter two of these variables are known to have a harmful impact on cell performance. Humidification of the air-line notably leads to the production of greater quantities of Cr-VI gas and therefore a stronger poisoning impact is largely unsurprising [152–

154]. However, the accelerated poisoning effect at higher current densities is possibly of greater interest and alludes to the mechanism by which cathodes are poisoned.

The exact generalised causes of chromium poisoning are debated within the literature. Initially, many authors pointed to an electrochemical reduction of the Cr-VI gases which migrate into the electrode [130,134]. This would appear to be supported by the observation that increased polarisation (i.e. higher current densities) leads to increased chromium deposition and hence degradation rates. Contrary to this, however, Jiang et al. [147,149,151,156,157] have proposed a chemical reaction route whereby so-called 'nucleation agents' like Sr^{2+}, Ba^{2+} and Mn^{2+} lead to the formation of the solid Cr-species. The case for this seems compelling, with a significant amount of evidence offered in the aforementioned studies. Importantly, it is further suggested that 'chromium-tolerant' cathodes can be engineered via an avoidance of these aforementioned nucleation agents [158]. The use of lanthanum nickelate materials (a key subject of the second part of this chapter) have been demonstrated to offer improved resilience to chromium poisoning (i.e. lower degradation rates) [158–162], although it is apparent that these materials are not immune from such effects. Nevertheless, a number of authors have suggested these materials offer some promise and are worthy of further consideration [163–165]. It is notable, however, that such statements are generally given with respect to degradation rates and comparisons or comments on the general cell performance are not commonly discussed. In Section 2.3 of this literature review a consideration of these materials in more detail is offered with emphasis placed on understanding in-situ performance.

*Table 2.3 - Overview of Cr-phase formation in cathode materials and consideration of degradation rates relative to common cathode materials ; *Tests run for less than 100h [A]Test taken at 750˚C; Y/N– 'Yes'/'No' (i.e. Y=evidence of lower deg. rate) ; For comparisons with LSM, A-site stoichiometry is denoted (e.g. $^{0.9}$=$(La_{0.8}Sr_{0.2})_{0.9}MnO_3$). Original version published in* [93].

Material Group	Composition	Degradative Chromium Phase Observed Reported in Literature						Evidence for Lower Deg. Rate than $(La_{0.8}Sr_{0.2})_xMnO_3$ in presence of Chromium			Evidence for Lower Deg. Rate than $La_{0.6}Sr_{0.4}Co_{0.2}Fe_{0.8}O_3$ in presence of Cr		
		Cr_2O_3	$(Cr,Mn)_3O_4$	$SrCrO_4$	$BaCrO_4$	$La(Cr,M)O_3$ (e.g. M=Fe)	Other Cr Phases / Secondary Phases / Comments	700˚C	800˚C	900˚C	700˚C	800˚C	900˚C
LSM	$(La_{0.8}Sr_{0.2})_xMnO_3$ (x=0.9-1)							-	-	-	-	N[167][1]	N [166]*[/0.9]
LSM-YSZ	$(La_{0.8}Sr_{0.2})_{0.9}MnO_3$ /8YSZ (90%-10%)	✓	✓			✓	Increasing YSZ content shows reduced degradation rates [166]. Use of LSM-YSZ Functional Layers also seen to reduce the degradation rate [155].	-	-	Y [166]*[/0.9]	-	-	N [166]*[/0.9]
	$(La_{0.8}Sr_{0.2})_{0.9}MnO_3$ /8YSZ (70%-30%)							-	-	Y [166]*[/0.9]	-	-	N [166]*[/0.9]
	$(La_{0.8}Sr_{0.2})_{0.9}MnO_3$ /8YSZ (50%-50%)							-	-	Y [166]*[/0.9]	-	-	N [166]*[/0.9]
LSM-GDC	$(La_{0.8}Sr_{0.2})_{0.9}MnO_3$ /GDC							-	-	Y [166]*[/0.9]	-	-	Y [166]*[/0.9]
LSC	$La_{0.8}Sr_{0.2}CoO_3$			✓			Formation/Precipitation of Co_3O_4, Co-Cr spinel also reported [168]	-	-	Y [169]*[/0.95]	-	-	-
	$La_{0.6}Sr_{0.4}CoO_3$			✓		✓		-	-	-	-	-	-
LSCF	$La_{0.6}Sr_{0.4}Co_{0.2}Fe_{0.8}O_3$			✓			Formation of $(La,Sr,Cr)(CoFe)O_3$ [170] & Co-Cr spinel [161] has also been reported	-	Y [167][1.0]	Y [162]*[/0.9]	-	-	-
LSF	$La_{0.8}Sr_{0.2}FeO_3$	✓		✓		✓	Precipitation of $SrFe_{12}O_{19}$ reported [139]. Unclear if different Cr-phases related to Sr-content	Y [171][0.95]	Y [139][A 0.99]	-	-	N [25][A]	-
	$La_{0.6}Sr_{0.4}FeO_3$			✓				-	-	-	-	-	-
Pt	Pt						No Cr-deposits observed.	-	-	N [149]*[/0.9]	-	-	N [149]*
LNF	$LaNi_{0.6}Fe_{0.4}O_3$					✓	$(Ni,Fe)(Fe,Cr)_2O_4$ [165]. $(Ni,Cr)_2O_4$, NiO [161]	Y [160][1.0]	-	Y [162]*[/0.9]	Y [161]	-	Y [162]*
LBCF	$La_{0.6}Ba_{0.4}Co_{0.2}Fe_{0.8}O_3$				✓			-	-	Y [162]*[/0.9]	-	-	Y [172]*
LSCM	$(La_{0.8}Sr_{0.2})_{0.95}Mn_{0.8}Co_{0.2}O_3$		✓	✓			More Mn leads to more Cr-Mn spinel at electrolyte surface, more Co leads to more $SrCrO_4$ at surface. Degradation is largest when Co=0.4 and smallest when Co=0.8 or 1. [169]*	-	-	N [169]*[/0.95]	-	-	-
	$(La_{0.8}Sr_{0.2})_{0.95}Mn_{0.6}Co_{0.4}O_3$							-	-	N [169]*[/0.95]	-	-	-
	$(La_{0.8}Sr_{0.2})_{0.95}Mn_{0.4}Co_{0.6}O_3$							-	-	N [169]*[/0.95]	-	-	-
	$(La_{0.8}Sr_{0.2})_{0.95}Mn_{0.2}Co_{0.8}O_3$							-	-	Y [169]*[/0.95]	-	-	-
LSBCF	$La_{0.6}Sr_{0.3}Ba_{0.1}Co_{0.2}Fe_{0.8}O_3$			✓	✓		Chromium deposition is reduced with increasing Ba-content. In general, increasing Ba-content reduces degradation [173]	-	-	-	-	-	N [173]*
	$La_{0.6}Sr_{0.2}Ba_{0.2}Co_{0.2}Fe_{0.8}O_3$							-	-	-	-	-	Y [173]*
	$La_{0.6}Sr_{0.1}Ba_{0.3}Co_{0.2}Fe_{0.8}O_3$							-	-	-	-	-	Y [173]*
LSBCFN	$La_{0.24}Sr_{0.16}Ba_{0.6}Co_{0.5}Fe_{0.44}Nb_{0.06}O_3$				✓		$BaCr_2O_4$ is a possible reaction product [174]*	-	-	-	-	-	**Y** [174]*
BSCF	$Ba_{0.5}Sr_{0.5}Co_{0.2}Fe_{0.8}O_3$				✓		No $SrCrO_4$ formation reported [175]	-	-	-	N [175]	N [175]	N [174]*
	$Ba_{0.3}Sr_{0.7}Co_{0.8}Fe_{0.2}O_3$			✓	✓		Increasing Sr-content leads to increasing $SrCrO_4$ formation and increased performance loss [176]. $(Co,Fe)CrO_4$ reported for BSCF-5582 [177]	-	-	-	-	-	-
	$Ba_{0.5}Sr_{0.5}Co_{0.8}Fe_{0.2}O_3$							Y [178][0.98]	-	-	-	-	-
	$Ba_{0.7}Sr_{0.3}Co_{0.8}Fe_{0.2}O_3$							-	-	-	-	-	-
BCFN	$Ba_xCo_{0.7}Fe_{0.2}Nb_{0.1}O_3$ (x=0.9, 1)				✓		Conflicting conclusions on Cr-stability [179,180]	-	-	-	-	-	Y [174]*
SmSCF	$Sm_{0.5}Sr_{0.5}Co_{0.2}Fe_{0.8}O_3$			✓			Very similar degradation behaviour to LSCF [175]	-	-	-	N [175]	N [175]	-
SmSM	$Sm_{0.5}Sr_{0.5}MnO_3$			✓				-	Y [181][A]	-	-	-	-
SmSBCFN	$Sm_{0.25}Sr_{0.25}Ba_{0.5}Co_{0.85}Fe_{0.1}Nb_{0.05}O_3$						Cr deposited in cathode (phase unknown) [179]	-	-	-	-	-	Y [179]*
PrSM	$Pr_{0.8}Sr_{0.2}MnO_3$						Cr-poisoning is apparent for PrSM and NdSM. Cr-Mn spinel and Cr_2O_3 probable [178]	N [178][0.98]	-	-	N [182]*	-	-
NdSM	$Nd_{0.8}Sr_{0.2}MnO_3$							N [178][0.98]	-	-	-	-	-
LNO	La_2NiO_4					✓	NiO precipitation [183]	-	Y [184][0.95]	-	-	-	-
NNO	Nd_2NiO_4						$NdCrO_4$, NiO [185]	-	-	-	-	-	-
NNCuO	$Nd_2Ni_{0.95}Cu_{0.5}O_4$							-	-	-	-	-	Y [186]*
PBCO	$PrBaCo_2O_5$				✓		Co_3O_4, $Pr_4Co_3O_{10}$ precipitated [187]	-	-	-	-	-	-
SBCO	$SmBaCo_2O_5$	✓			✓		$SmCoO_3$, Co_3O_4 precipitated [188]	-	-	-	-	-	-
NBCO	$NdBaCo_2O_5$				✓		$CrNdO_3$, $CoCr_2O_4$ reported [189]	-	-	-	-	-	-

2.2.4 Cobalt: economic and ethical concerns

Aside from the aforementioned SOFC performance-related factors, the employment of electrodes containing cobalt offers some economical and ethical concerns [190]. The expansion in deployment of Li-ion batteries has led to a major up-scaling in global cobalt production (as shown in Figure 2.3). This trend is anticipated to continue, with an acceleration of vehicle electrification. In recent years the costs of cobalt have been shown to be extremely volatile with the commodity hitting a peak in March 2018 ($95,000/tonne) [191,192]. Compared with the prices of other transition metals which have been explored for use in perovskites (e.g. Ni, Mn, Fe), this may offer a crucial drawback, particularly for those Co-rich systems such as $La_{1-x}Sr_xCoO_3$. However, we are unaware of any major assessment of cathode material cost in this regard and this offers difficulties with regards to assessing the extent of any price advantages or disadvantages that may be gained from the removal or reduction of Co from SOFC technology.

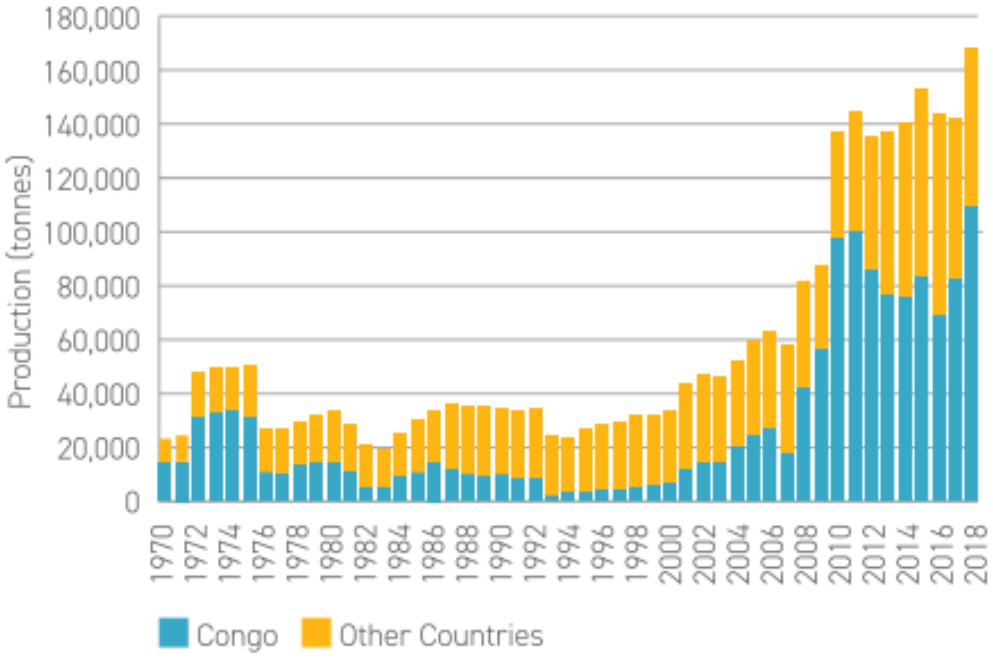


Figure 2.3 - Global cobalt production between 1970-2018 [190].

As shown in Figure 2.4, the great majority of cobalt produced today is derived from the Democratic Republic of Congo (DRC) where the resource is heavily concentrated. The human rights record of the DRC has been the subject of much discussion, more specifically relating to the troubling issues of child

labour and modern slavery [190]. In the field of batteries, this issue has been the matter of some scrutiny but is mostly overlooked in the SOFC literature (with commentators preferring to concentrate on the materials effects and performance). Relatively speaking, the quantity of cobalt employed within SOFC is likely to be a fraction of that used in the Li-ion field. Nevertheless, future supply will be derived from the same source and, therefore, the concerns raised here should not be overlooked.

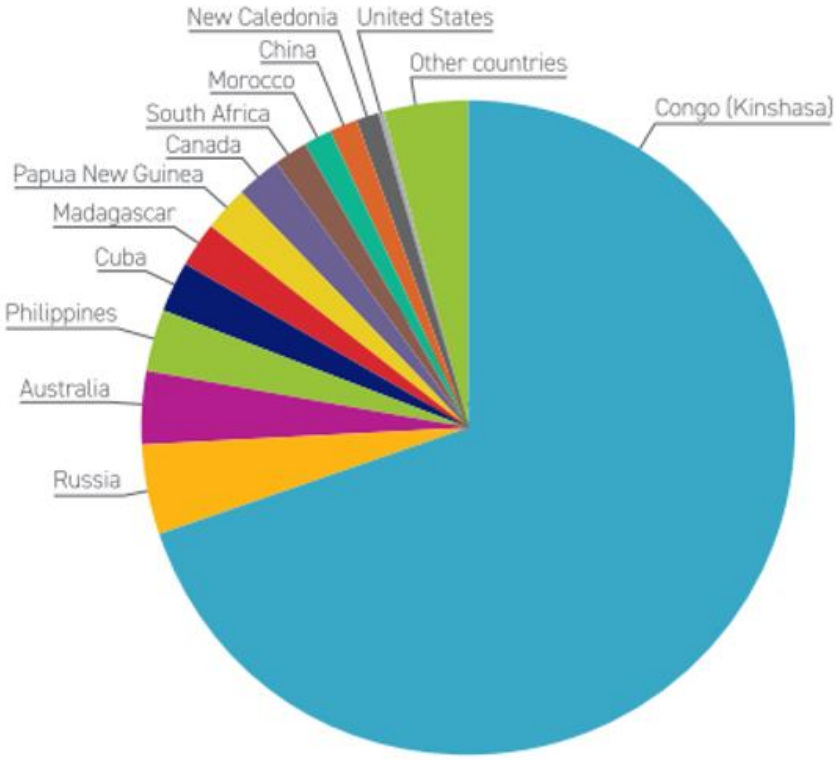


Figure 2.4 - Cobalt production by country [190].

2.2.5 Discussion

In this first part of this literature review, some draw-backs of Sr-doped lanthanum cobaltites have been explored; (a) Sr-segregation, (b) electrolyte incompatibility issues, (c) Cr-poisoning and (d) the ethical and economic concerns surrounding Co-use. Whilst the data across the various papers are not always comparable, some general trends and understanding can be extracted. What is apparent from the previous discussion points is that the removal of Sr- (or other alkaline earth elements such as Ba or even Ca) and Co- from the cathode materials, would offer some advantages. Indeed, the first part

of this literature review would appear to offer a relatively strong argument for replacing state-of-the-art cathode materials. However, such a statement neglects the many positive aspects of these materials. Indeed, it would no doubt represent a relatively 'radical' approach to explore the replacement of cathode materials given the historical context of materials development in SOFC. The wide body of work and understanding on LSCF presents an issue with respect to its replacement (i.e. "better the devil you know"). However, to obtain further improvements in terms of degradation rates (and to meet with SECA/NEDO degradation targets) the exploration of alternative materials may offer the best (or even, only) option.

2.3 Lanthanum nickelates – an alternative?

2.3.1 Background

As previously described, there are a number of drivers for the replacement of $LaCoO_3$-type cathode materials. Perhaps most poignantly, there is a sense within the literature that a material with improved long-term stability/reduced degradation rates would be desirable and, in turn, would help to improve the lifetime (and, therefore, lifetime cost) of the stack. Many authors have suggested that the lanthanum nickelates offer such promise. This includes variants of the doped $LaNiO_3$ perovskite (e.g. $LaNi_{0.6}Fe_{0.4}O_3$) as well as the Ruddlesden-Popper materials of general formula $La_{n+1}Ni_nO_{3n+1}$. However, such statements on the promise of low degradation rates commonly overlook the wider need to offer materials with competitive *overall* performance.

It is notable that, despite considerable research on these materials, there is yet to be any kind of move towards nickelate-type materials in the commercial market. These materials have largely remained a lab-scale endeavour. It is debatable as to whether or not this is a result of limited evidence to drive such a change or whether or not this is simply because these materials do not offer a truly desirable alternative. It seems unlikely that materials with excellent long-term stability but offering inferior performance when compared with the state-of-the-art (i.e. higher impedance values, lower power output) can make an impact on the commercial market. However, in many articles the lanthanum

nickelates are described as '*alternative*' or '*promising*' materials. But to what extent is this true? Do these materials represent a realistic alternative? In this section we will assess some of the various considerations that relate to these materials in order to assess the evidence that is available. This is in order to offer a '*warts and all'* analysis of these materials in the context of the state-of-the-art and to identify gaps in the literature.

2.3.2 Considerations on structure and stability

There are several structurally-related lanthanum nickelate-type phases which have been explored for use in SOFC stacks. The linking factor amongst these materials is that they are perceived to offer reasonable tolerance to chromium poisoning. Similar to those state-of-the-art materials discussed earlier, and in the simplest case, this includes a perovskite variant ($LaNiO_3$). Although the electrical conductivity properties of $LaNiO_3$ are rather attractive when compared with (for instance) the un-doped $LaMnO_3$, it is notable that the material is highly unstable at temperatures above 900˚C in air [193–195]. Indeed $LaNiO_3$ is described by Konysheva et al. [196] as the "*most unstable among $LaBO_3$ perovskites (B=Cr, Mn, Fe, Co, Ni)"*. Importantly, SOFC fabrication usually requires cathode sintering at temperatures in excess of 1000˚C to achieve good adhesion and particle connectivity. The precipitation of NiO and La_2NiO_4 when $LaNiO_3$ is heated in such conditions offers a point of concern here (although the extent to which this is likely to deteriorate cell performance is rarely considered in the literature, if at all):

$$2LaNiO_3 \rightarrow La_2NiO_4 + NiO + \frac{1}{2}O_2 \text{ (T > 980˚C [197])} \quad \text{[Eq 2.3]}$$

It is for the reasons of stability, therefore, that $LaNiO_3$ itself is not deemed to be an attractive electrode material. However, it has been demonstrated that the addition of dopants such as Fe and Co have the ability to stabilise the perovskite structure and prevents the precipitation of secondary phases under fabrication conditions [198,199]. In particular, $LaNi_{0.6}Fe_{0.4}O_3$ and $LaNi_{0.6}Co_{0.4}O_3$ have become well-studied compositions. As might be expected, these materials represent something of a hybrid

between the $LaNiO_3$ and $LaCoO_3$/$LaFeO_3$ systems and their properties are reflective of this (as will be described later).

The Ruddlesden-Popper phases have a crystal structure closely related to that of the perovskite phase, comprised of $LaNiO_3$ perovskite layers separated by NaCl-type La_2O_2 layers. There has been significant interest in the $La_2NiO_{4+\delta}$, $La_3Ni_2O_{7-\delta}$ and $La_4Ni_3O_{10-\delta}$ systems (n=1, 2 and 3, respectively), in particular the former of these materials [200]. The number of perovskite-to-NaCl layers increases with the increasing n-value. $LaNiO_3$ is commonly said to represent the n=∞ instance. Perhaps the most interesting physical feature of these materials is their tendency to incorporate oxygen interstitials into the NaCl-layers and this leads to strong oxygen transport properties as demonstrated by Boehm et al. [201] and by Skinner and Kilner [202]. A key advantage of LNO214 is its excellent phase stability at high temperatures (and a wide oxygen pressure window) which offers obvious advantages for fabrication and long-term operation (i.e. avoidance of secondary phase precipitation) [194,197,203,204]. The importance of good long-term stability (and the avoidance of phase changes) can be appreciated in [197]. There, a sizeable drop in conductivity is shown to correlate with stability limits (i.e. the formation of secondary phases). For the higher order Ruddlesden-Popper phases, the literature shows that stability is reduced, with a tendency to precipitate lower order phases and NiO in air at temperature above 1150˚C [197]. Interestingly, however, it has been commented on by Amow et al.[205] that the higher order Ruddlesden-Popper phases possess better stability at temperatures below 900˚C due to the relative stability of Ni^{2+}/Ni^{3+}. This would appear to indicate that these phases could offer a better option for long-term operation in the IT-SOFC temperature regime (i.e. 600-800˚C).

2.3.3 Properties

The fundamental properties of the lanthanum nickelates have been well studied and are reported in numerous articles. Typically such articles consider the electrical conductivity, oxygen transport and thermal expansion properties. We have summarised some properties for these various phases in

Appendix B. There is noteworthy variation in the reported values from study-to-study, possibly a result of differences in testing approaches or sample preparation (i.e. pellet sintering temperature). Nevertheless, a consideration of some of these properties can offer some insight into the role of doping and the relative attributes of these materials in relation to the state-of-the-art. To the best of our knowledge, an attempt to analyse the rich data available in the literature has not been considered. This is likely a result of the sheer volume of data available as well as the difficulties relating to its extraction from the papers in which it is buried. An attempt to develop some insight is therefore provided in the following.

2.3.3.1 Electrical conductivity

The total electrical conductivity (i.e. the ease with which charge can be transferred through a system) is commonly identified as a key consideration in the screening of materials for use in SOFC application. This is understandable given the key requirement of promoting charge transfer through the electrode. There is a sizeable quantity of data available in this area within the literature (as shown in Appendix B). With respect to the aforementioned lanthanum nickelate phases, it is generally observed that an increase in conductivity is found with an increasing n-value [197,206–208]. Higher conductivity values are typically reported with the perovskite phase (i.e. $LaNiO_3$, and its doped variants), in comparison with the Ruddlesden-Popper phases (n=1 to 3). Indeed, this is broadly the relationship observed in Figure 2.5. Here, data from a number of studies are shown; it can be appreciated that a wide spread of data is observed amongst the studies analysed. This is likely a reflection of the very many variables (e.g. pellet quality) which can impact electrical conductivity measurements. Analysis of the conductivity of $LaNiO_3$ (n=∞), in particular, is likely to be affected by the instability of the phase under typical pellet sintering temperatures (i.e. >1000˚C). Regardless of these shortcomings, the general trend of increasing conductivity with higher order phases does seem to be apparent. This behaviour is commented on by Amow and Skinner [209] to be a result of the mechanism by which electrons are conducted (i.e. mainly through the perovskite layer); therefore, an increase in the number of perovskite layers to rock-salt layers leads to the effect of increasing conductivity.

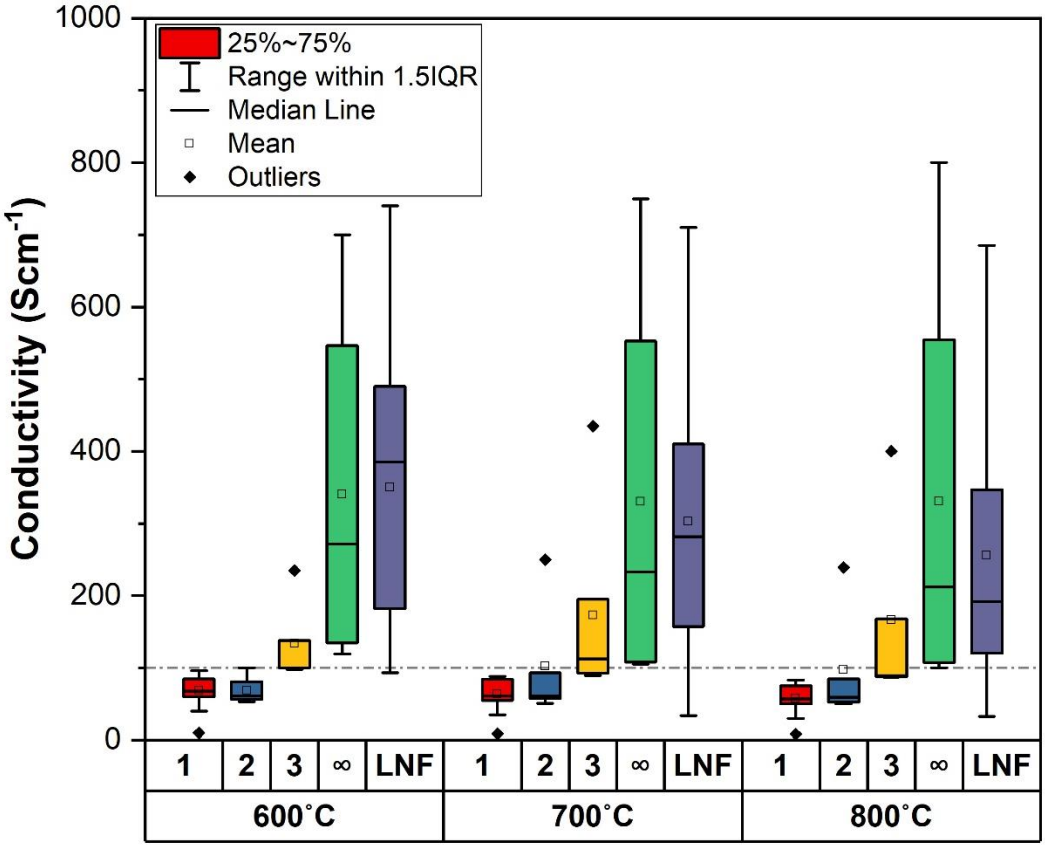


Figure 2.5 - Conductivity of various La-Ni-O phases at 600, 700 and 800˚C, as reported in the literature. $LaNi_{0.6}Fe_{0.4}O_3$, $LaNiO_3$, La_2NiO_4, $La_3Ni_2O_7$ and $La_4Ni_3O_{10}$ are denoted by 'LNF', '∞', '1', '2', '3', respectively. 'Range within 1.5IQR' describes the means of identifying outliers. Dotted line is indicative of the electrical conductivity 'requirement' (100 Scm^{-1}). Underlying data and references can be observed in Appendix B. For reference, and to aid with interpretation, an explainer of box and whisker plots is shown in Appendix I.

It is notable that a commonly cited requirement for cathode materials is to achieve an electrical conductivity of at least 100 Scm^{-1} [210,211]. In itself, such a requirement is perhaps questionable given that the current crop of favoured cathode materials have electrical conductivities well in excess of this value. Indeed, the lanthanum nickelates (particularly LNO214) are typically shown to have inferior conductivity when compared with the state-of-the-art LSCF and LSC (>2000 Scm^{-1} in some instances - see Appendix B). Of course, electrical conductivity is not the only factor to consider in achieving a good quality SOFC cathode material but it is no doubt a crucial parameter.

Dopants can be employed in order to improve the conductivity of perovskite materials. This is achieved via the modification of the defect structure by introducing ions with lower valence than the host site (i.e. via the introduction of electron or oxide holes). The effect of various dopants (and their

concentration) on the $LaNiO_3$-perovskite can be seen in Figure 2.6. The underlying data for this figure can be seen in the Appendix B (where multiple values are reported in the literature, a median value has been taken). Several key observations are apparent. Firstly, it is clear that the replacement of Ni with Co has a strong positive influence on the conductivity (as does the replacement of La^{3+} with Sr^{2+}). It is notable that those state-of-the-art cobaltite materials (LSC, LSCF) have much greater conductivity than many doped nickelates, with only those Co-rich/Ni-poor materials (i.e. Ni=0-0.4) offering comparable values of conductivity. However, such materials are likely to present similar problems to those reported for other Sr- and Co-containing materials as was discussed in the earlier part of this chapter. Indeed, when comparing the thermal expansion properties of the $LaNiO_3$ this becomes apparent (as seen in Figure 2.7). It is apparent that the addition of Co as a dopant has the effect of increasing the thermal expansion coefficient well beyond that of typical electrolyte materials (i.e. typically 10 to 12 x 10^{-6} °C^{-1}).

2.3.3.2 Oxygen transport properties

Another key material property, is the oxygen transport behaviour of perovskites and other phases. It is widely regarded that so-called 'mixed conductivity' (i.e. ability to transport oxide ions and electrons) is preferential for cathode materials and contributes towards improved cell performance. This is achieved by an extension of the potential reaction zone (i.e. beyond the triple phase boundaries that are achieved using composite electrodes). The characterisation of oxide conductivity is more complex than other properties such as electrical conductivity and thermal expansion. One approach to assess oxygen transport is the use of Ion Exchange Depth Profiling (IEDP) with Secondary Ion Mass Spectroscopy (SIMS) and these experiments are reported in the literature for various materials.

Significantly, La_2NiO_4 is known to have excellent oxygen transport properties and displays a tracer diffusion coefficient larger than even LSCF or LSC compositions (see Figure 2.8a) which are well regarded for their mixed conductivity properties [202,212]. The ability of La_2NiO_4 to transport oxygen to such an extent is commonly assigned to the ability of the material to incorporate oxygen interstitials

into the rock salt-type layers which are then able to migrate (or, more colloquially, 'hop') through these layers [213]. Unfortunately, the relatively low stability of the higher order Ruddlesden-Popper phases at very high temperature (and indeed the undoped $LaNiO_3$-perovkite) makes it difficult to conduct reliable tracer diffusion experiments (i.e. due to the need to provide a dense pellet, temperatures in excess of 1100˚C are required). Nevertheless, evidence in the literature would appear to indicate that the higher order Ruddlesden-Popper materials ($La_3Ni_2O_7$ and $La_4Ni_3O_{10}$) possess favourable oxygen conductivity although inferior to that of LNO214 [208]. This latter observation would appear to support the notion that oxide ions are mostly conducted in the rock-salt layers (i.e. more rock salt layers leads to higher oxide conductivity). As described earlier, of course, there would appear to be a trade-off between the electrical conductivity and ionic conductivity, with the higher order phases showing high overall electrical conductivity but reduced oxide transport properties.

.

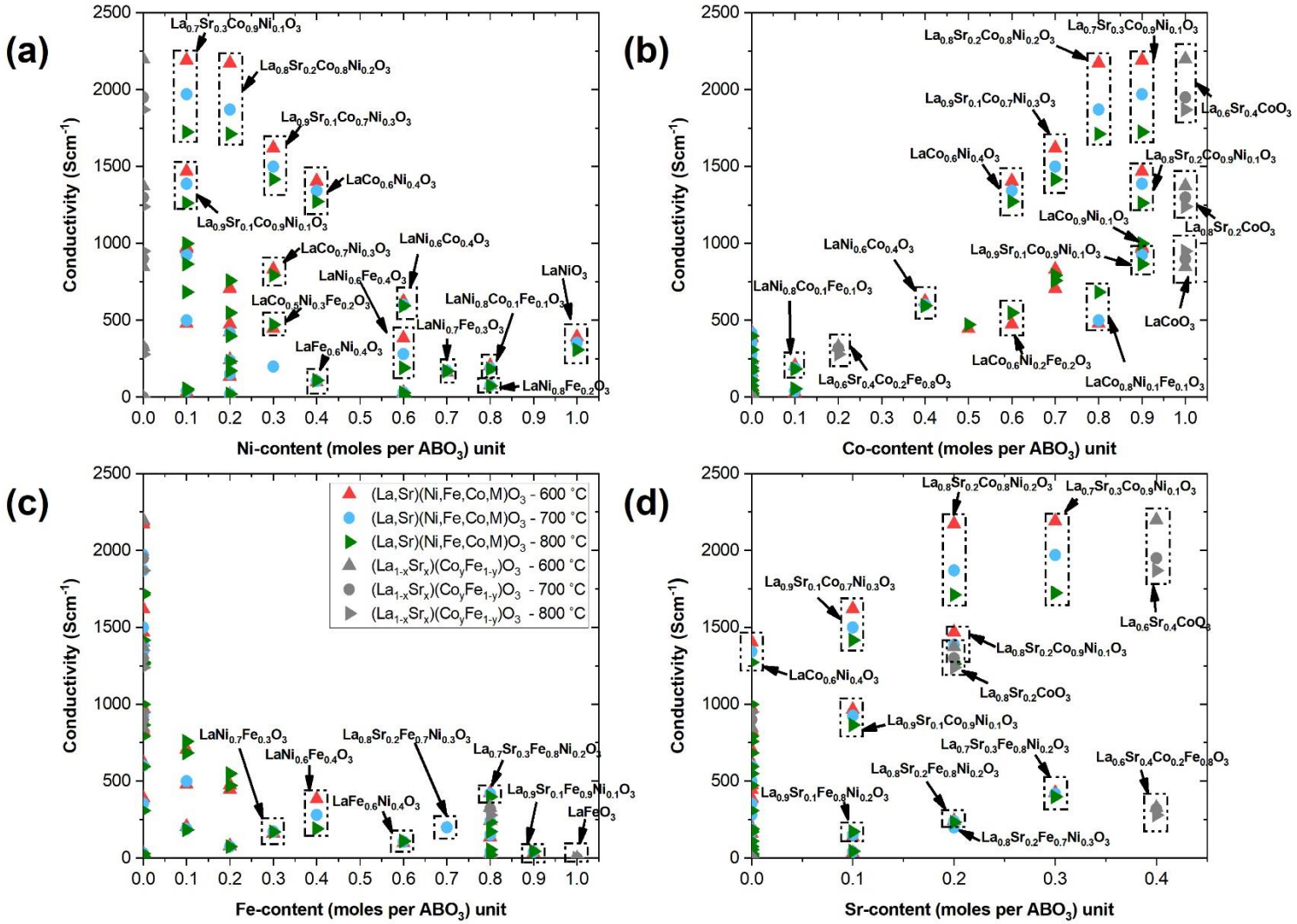


*Figure 2.6 – Effect of doping on the conductivity of **ABO_3-type** lanthanum nickelates based on literature data. Median values are presented where multiple values have been obtained from the literature. Original version published in* [95]. *Data and references are shown in Appendix B.*

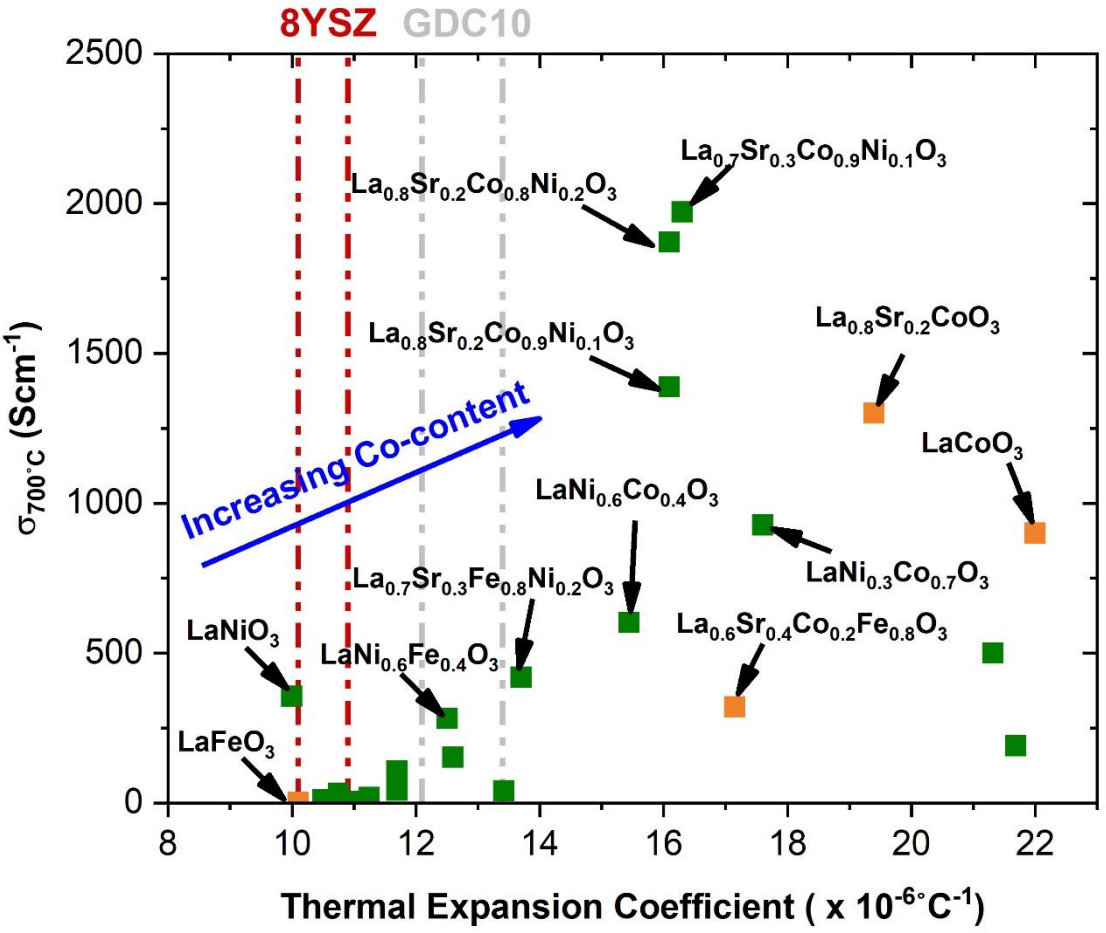


Figure 2.7 - Conductivity at 700˚C ($\sigma_{700°C}$) vs thermal expansion coefficient (TEC) for various La-Ni-O perovskites. Values for $LaCoO_3$-type materials are shown. For reference, TEC values for 8YSZ [89] *and GDC10* [214,215] *are shown. Original version published in* [95]. *Remaining data and references are shown in Appendix B.*

The described observations on the relative electronic and oxide ion conductivity values of the Ruddleden-Popper phases raises a question as to the relative importance of these properties in selecting appropriate electrode materials (i.e. which property is more important?). It is unlikely that materials with 'pure' electronic or oxide conductivity would offer serious options as electrodes for SOFC. It could be theorised that the transport of electrons through the electrode material is the more important of the two properties. Evidence for this could be found in observations that pure electronic conductors (e.g. noble metals) are likely to make for better electrodes compared with pure oxide conductors such as YSZ. Given the excellent catalytic behaviours of these materials, however, this is perhaps an unfair comparison. Evidence from the literature suggests that electrode materials must typically demonstrate both behaviours in order to replace state-of-the-art materials which offer this

attribute and have been shown to display excellent performance. A further discussion on the relative impact of these properties is considered later in this thesis.

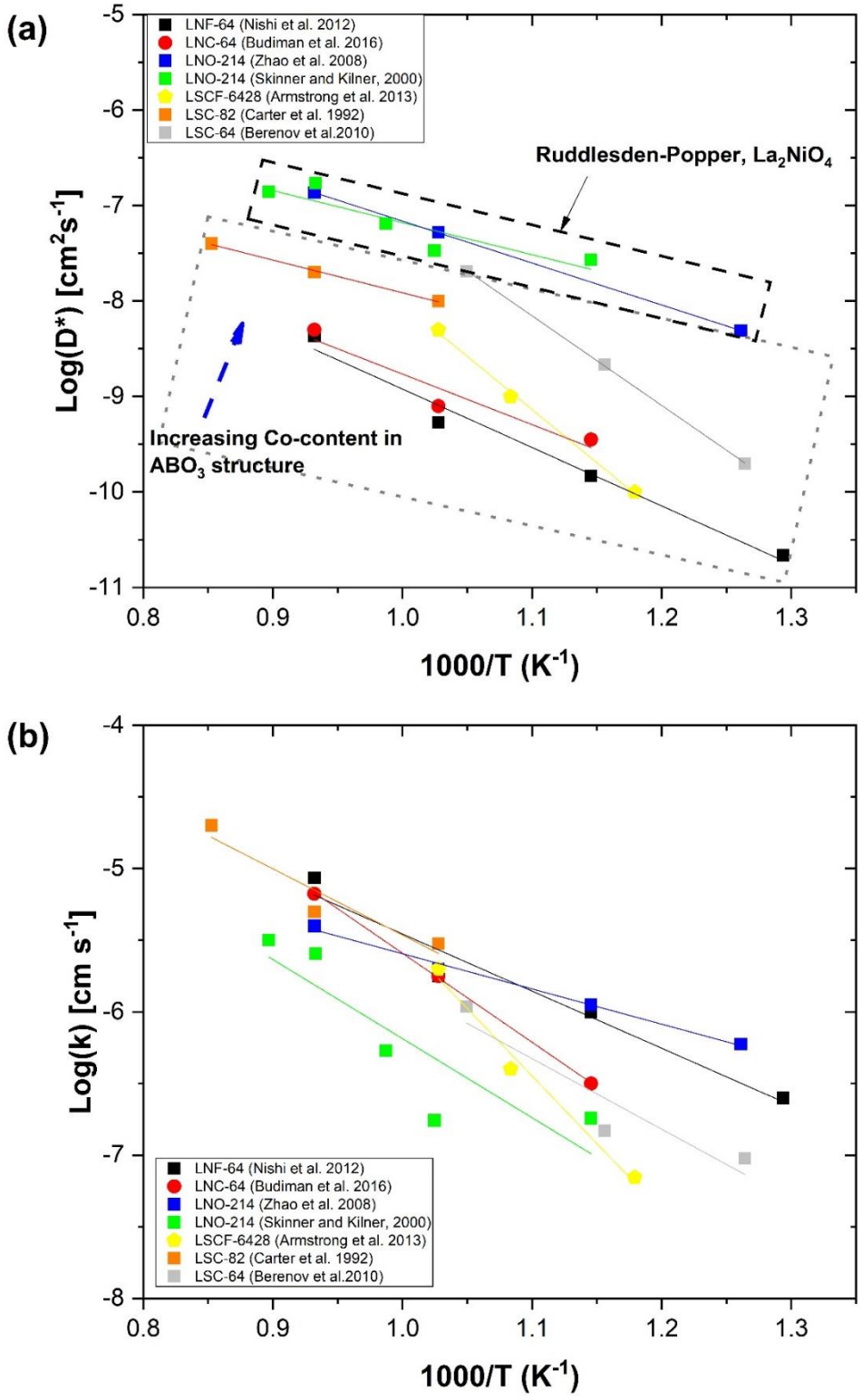


Figure 2.8 - Comparison of (a) tracer diffusion coefficients and (b) oxygen exchange coefficient for SOFC cathode various materials including La_2NiO_4, $LaNi_{0.6}Fe_{0.4}O_3$ [202,212,216–220]*. Originally published in* [95].

2.3.4 Fabrication challenges

As described earlier, electrolyte-electrode compatibility can offer a key issue with respect to fabrication and the subsequent cell performance achievable with SOFCs. The aforementioned reaction between LSCF and YSZ is a known degradation effect with the use of doped-CeO_2 barrier layers (e.g. GDC, SDC) now common in commercial cells. Reactions between lanthanum nickelates and YSZ are also widely reported, with the formation of $La_2Zr_2O_7$ evident for LNF64 [221], as well as for La_2NiO_4 [212]. There is additionally some evidence of reactivity between LNO214 and GDC or SDC at temperatures as low as 700˚C [222–227]. A migration of the lanthanum into the GDC structure and subsequent re-structuring of the RP phase to higher order phase has been reported. This is not, however, reported to the same extent for the LNF64 perovskite which has been found to be stable with GDC up to 1150˚C [107]. It is interesting to note that there also appears to be some level of inconsistency in the literature [228–230] with respect to the reactivity between ZrO_2- and CeO_2-type electrolytes and the higher order lanthanum nickelates (i.e. $La_3Ni_2O_7$ and $La_4Ni_3O_{10}$). Some authors have suggested that these phases do not form new phases in the presence of electrolyte materials and, this would indicate, an advantage over the more commonly utilised LNO214. However, there is no systematic study on the reactivity of these materials and this will be addressed later.

In addition to problems relating to the reactivity of the cathode materials with electrolyte materials, there is evidence [231] within the literature to indicate that the lanthanum nickelates suffer from inferior sintering characterstics when compared with the typical state-of-the-art materials. This indicates that elevated temperatures are required for these phases in order to achieve well-adhered, well-connected electrodes. This is particulary interesting given that many researchers employ a sintering temperature of 1000˚C when using these phases and report the subsequent electrode behaviour. This is in order to avoid reaction with the electrolytes but this is likely at the expense of inferior connectivity. The effect of sintering temperature on performance will be further considered later in this thesis.

2.3.5 Electrode performance

2.3.5.1 Optimisation

To further understand the applicability of the lanthanum nickelate phases to the SOFC application, an understanding on their in-situ performance is important. There is a strong body of work in this area but, crucially, the available data is largely overlooked (i.e. an attempted summary is missing within the literature). It is, therefore, difficult to understand how the performances of these materials relate to one another and how they compare with the state-of-the-art. An attempt to offer such an overview is offered in Section 2.3.5.2 and 2.3.5.3. For now, some general observations from the literature will be discussed.

A number of authors have attempted to explore how electrode performance can be optimised with the lanthanum nickelate materials (in the most part La_2NiO_4 and $LaNi_{0.6}Fe_{0.4}O_3$). This commonly includes the use of specifically tailored microstructures (e.g. [232]), the employment of composite electrodes (e.g. [233]) or via the use of infiltration techniques (e.g. [234]). Each of these techniques offers its own benefits and drawbacks. Infiltration, which can offer significant improvements in terms of the increase in electrode performance (in part due to the enhancement in the surface area) is no-doubt a promising route but issues relating to degradation rates (due to particle growth) are noted by Ding et al. [234] to be a point of concern here. Furthermore, it is questionable as to the scalability of such techniques for the commercial market, and how such methods would be integrated with well-developed and understood techniques like cathode screen-printing already common-place today.

The use of composite electrodes (i.e. the combination of two or more oxides) is another common route for promoting performance. In this case, the objective is to combine the favourable properties of one material (e.g. good electronic conduction properties) with the favourable properties of a second phase (e.g. good ionic conduction properties). Most typically this involves the mixing of two or more oxide materials to form a layer of interconnected phases. Often the benefits of this approach are discussed in terms of increasing the size of the potential sites for reaction. Indeed, this was a

common route with the early LSM-YSZ electrodes which have been previously mentioned. In that case, the use of a good ionic conductor (YSZ) helps to extend the oxygen transport in the solid phase and extends the amount of reaction sites that are available. Similar approaches have been explored in the literature with the lanthanum nickelates, often combining these phases with GDC [230,235] or other electrolyte phases [236,237]. The general effect of combining phases is no-doubt favourable. There is, however, no agreed preferred combination of materials (or, moreover, properties) that are likely to offer the optimum outcome. It is notable that a number of authors have attempted to combine the Ruddlesden-Popper phases (in particular La_2NiO_4) with electrolyte phases to enhance performance. However, as described earlier, these phases suffer from relatively poor electronic conductivity whilst displaying reasonably high ionic conductivity (indeed this is seen as a key favourable property). This would suggest that such materials could be more favourably mixed with phases that have much higher electronic conductivity. One interesting route which has been explored by several authors is to combine the various lanthanum nickelates phases with one another in an attempt to take advantage of the different properties which are displayed by these materials [238–241].

The use of layered electrode structures is discussed in the literature, either by employing layers of the same material but different microstructures [242,243] or by using layers of different phases [244]. The use of dense, intermediate LNF64 interlayers in between an electrolyte phase and a thicker LNF64 layer is explored by Chrzan et al. [245] and by Molin and Jasinski [243]. In both of these works a sizeable performance improvement is observed. In the latter case, the maximum power density is increased from 0.4 W/cm^2 to 1 W/cm^2 as a result of introducing the interlayer. This is possibly a result of better adhesion, connectivity and hence charge transfer. Similar observations are also reported for dense La_2NiO_4 interlayers [246,247]**.** Elsewhere, Chiba et al.[248] employed the use of different doped CeO_2 'active layers' with an LNF64 current collecting layer; again a performance enhancement was noted. Huang et al.[249] demonstrated that the use of 'graded' structures (i.e. gradually changing the composition of the electrode in layers) helped to improve adhesion and hence cell performance. In work by Wooley and Skinner [250] a similar approach was taken, employing LNO214 at the electrolyte

interface and LNO4310 as a current collecting layer, with an intermediate layer (mixture of LNO4310 and LNO214) in between.

2.3.5.2 Symmetrical cell performance: data analysis

As previously described it is rather easy to draw various qualitative relationships from numerous papers within the literature. It is somewhat more difficult, however, to get an appreciation of how this 'fits in' with the overall picture or, more specifically, how the behaviours of the lanthanum nickelates compare with the LSCF. As was shown to also be true for the case of fundamental properties (e.g. electrical conductivity) in Section 2.3.3, there are a great number of examples within the literature that detail the in-situ electrode performance of lanthanum nickelates. There are a wide range of behaviours that are described. To date we are unware of any attempt to analyse the rich body of electrode performance data that is available within the literature. As such, it is difficult to understand how the performance of certain materials (i.e. the lanthanum nickelates) relates to the state-of-the-art materials. However, such an analysis is made somewhat difficult by the manner in which the data is presented within articles (i.e. often 'buried away' in graphical form). For the analysis detailed herein, we have assessed selected articles in order to offer some insight into the success of these materials and the extent to which optimisation has been performed. Several different routes have been utilised within the literature in order to define electrode performance. This includes the employment of 'symmetrical', 'single cell' or 'three-electrode' testing.

In relation to symmetrical cell studies, there is some inconsistency in the literature with respect to the definition of the key metric defining performance. Generally, this is defined to be the polarisation resistance (R_{pol}) which is represented by many [226,241,251–253] as:

$$R_{pol} = (Z_{DC} - R_o).\frac{1}{2} \text{ [Eq. 2.4]}$$

Where Z_{DC} and R_o are the area-specific impedance values (normalised by the electrode area, S) at the high and low frequency intercepts (as shown in the Figure 2.9). The equation includes a multiplication of ½ to account for the two electrodes involved in a symmetrical cell. Given that R_{pol} is in fact an area-

specific term (with units of Ωcm^2), some authors prefer the term Area Specific Resistance (ASR) to directly replace the definition of R_{pol} [254–256] . To offer a source of further difficulty, this ASR term is elsewhere used to define the total impedance value of the cell and thus includes the ohmic contribution R_o (i.e. that defined as Z_{DC} in Figure 2.9). However, to follow the most common convention, R_{pol} will be used herein. As described, the variety in definitions across the literature are not always consistent and this makes analysis across studies more challenging.

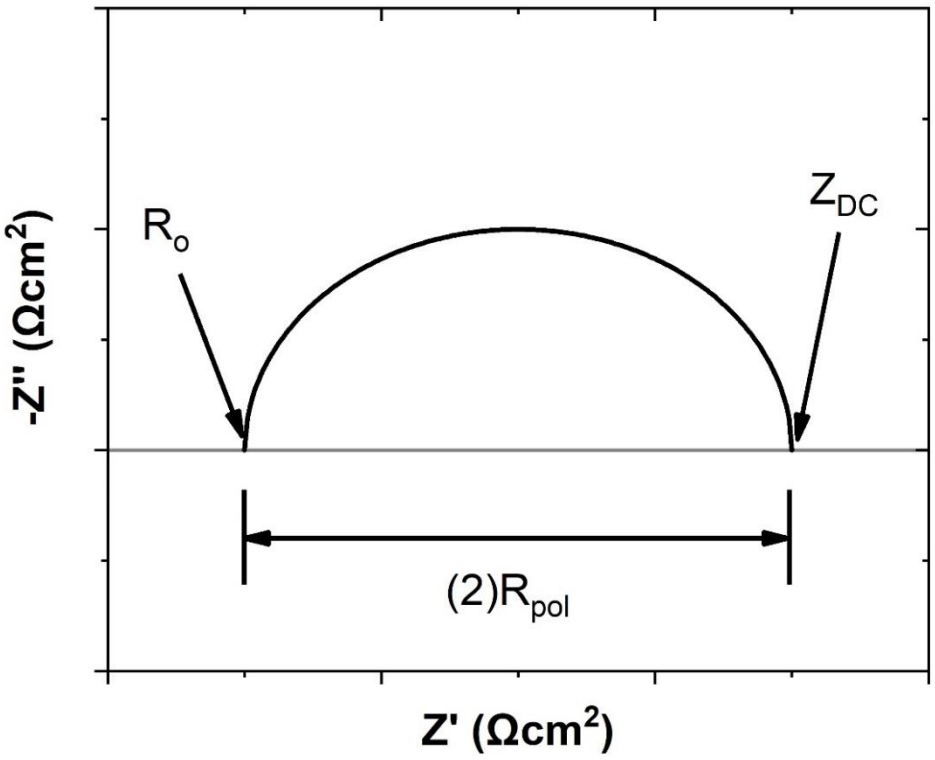


Figure 2.9 - Nyquist diagram of an idealised RC circuit illustrating the relative position of the ohmic (R_o) and total (Z_{DC}) impedance values described in this chapter. The polarisation resistance (R_{pol}) is defined as the width of the arc. In the case of symmetrical cells this is divided by two in order to accounting for the two identical electrodes in the symmetrical cell.

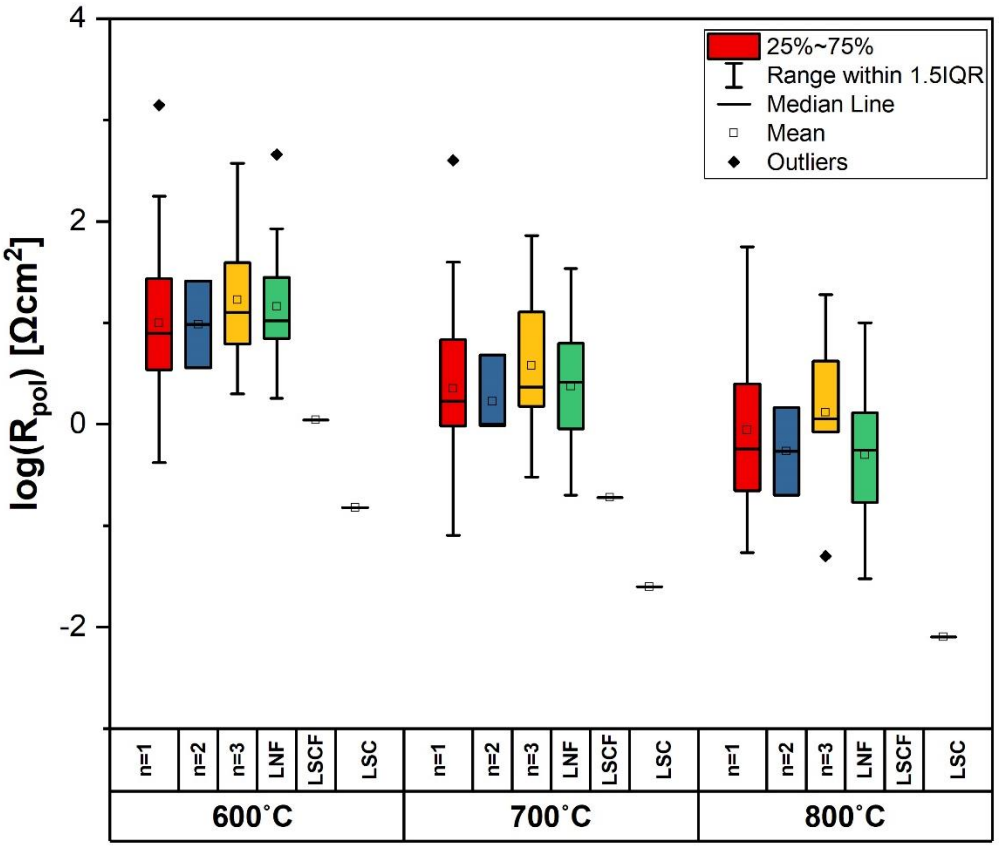


Figure 2.10 – Comparison of reported R_{pol} values across various studies for single phase electrodes. Chart shows the reported performance for La_2NiO_4 (n=1 ; red), $La_3Ni_2O_7$ (n=2 ; blue), $La_4Ni_3O_{10}$ (n=3; yellow), $LaNi_{0.6}Fe_{0.4}O_3$ (LNF; green). Additionally values reported for "state-of-the-art cathodes" are also shown. Underlying data can be found in Appendix C. For reference, and to aid with interpretation, an explainer of box and whisker plots is shown in Appendix I.

As there are numerous different approaches to the fabrication of high-performing electrodes, a very wide body of R_{pol} values are reported within the literature. Indeed, a range of values are often reported for any one material. This is no doubt a reflection on the quality of the starting materials themselves (e.g. particle size and purity), different cell fabrication conditions (e.g. sintering temperatures), electrode microstructures (e.g. use of 'Functional Layers') and different testing set-ups (e.g. the contact configuration). In Figure 2.10, the R_{pol} values reported in a number of studies are summarised. In this case, this analysis includes the available data for *single-phase* electrodes only. For reference, the performance of state-of-the-art cathodes LSC and LSCF (as reported by Hjalmarsson and Mogensen [257] and Lou et al. [258], respectively) are also shown. Several conclusions can be drawn. As mentioned above, there are dramatic variations in reported electrode performance (in some cases, several orders of magnitude). Further, despite the promising properties of the lanthanum nickelates,

the data would appear to indicate that their performance is inferior to those cobaltite cathodes (e.g. LSCF and LSC) which are widely regarded as the state-of-the-art. Based on the dataset shown, it is difficult to discern which of the lanthanum nickelate materials offers the greatest promise. Considerations of the median and range values may indicate that La_2NiO_4 demonstrates the most attractive performance. However, it is worth noting that there are many more studies considering this phase and, therefore, a more mature optimisation has no doubt been achieved. There *are* several articles considering the relative performance of the Ruddlesden-Popper materials but the results of these studies are not entirely consistent with one another [205,207,225,233,240]. Further comparisons between these phases and $LaNi_{0.6}Fe_{0.4}O_3$ (or other perovskite variants) are even less frequent.

In Figure 2.11 and Figure 2.12, the effect of different approaches to developing electrode structures is considered for La_2NiO_4 and $LaNi_{0.6}Fe_{0.4}O_3$, respectively). In both cases, the introduction of secondary phases and infiltrated species is shown to have a marked effect on the performance. This demonstrates the potential of using such routes but this does not consider what the effect on long-term degradation rates is likely to be.

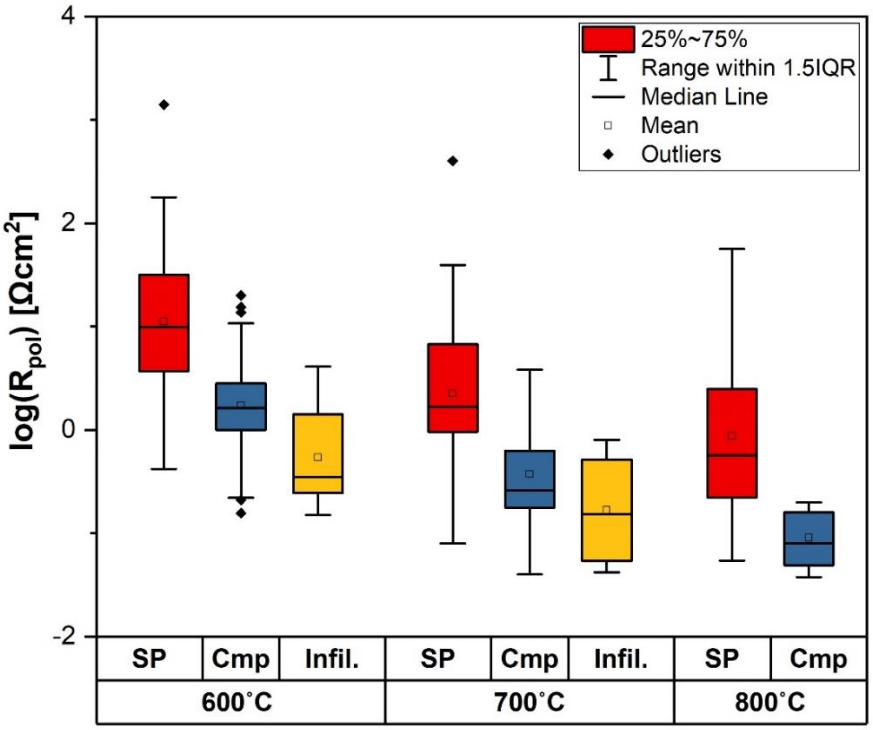


Figure 2.11 - Symmetrical Cell performance for different electrode configurations employing ***La_2NiO_4****. Single phase ("S-P"; Red), composite (Cmp) and infiltrated (Infil.) cathodes are shown. Underlying data can be found in Appendix C. For reference, and to aid with interpretation, an explainer of box and whisker plots is shown in Appendix I.*

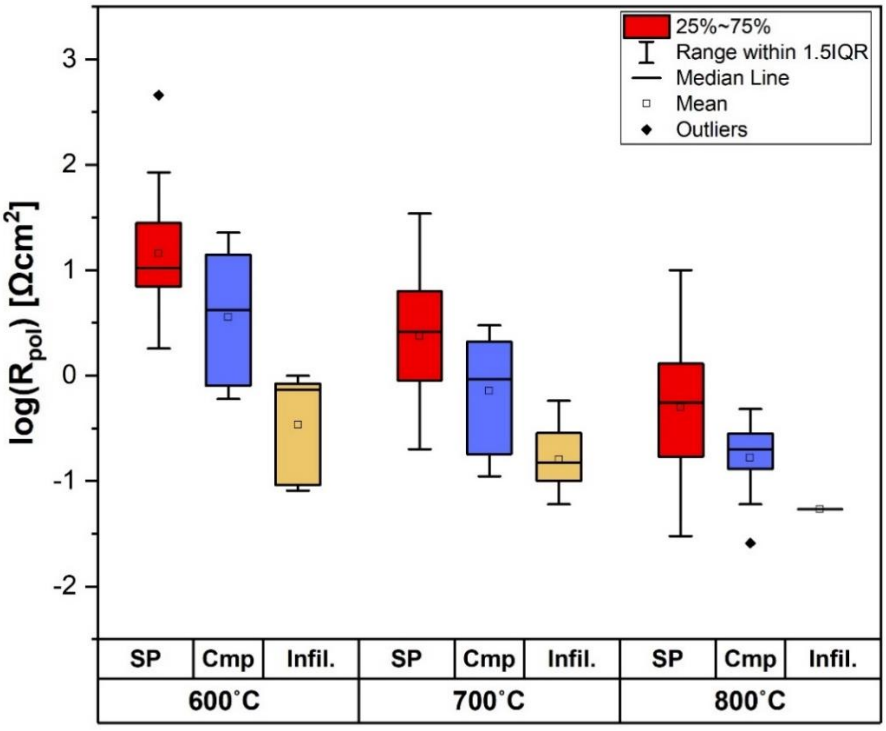


Figure 2.12 - Symmetrical Cell performance for different electrode configurations employing ***$LaNi_{0.6}Fe_{0.4}O_3$****. Single phase ("S-P"; Red), composite (Cmp) and infiltrated (Infil.) cathodes are shown. Original version published in* [95]*. Underlying data can be found in Appendix C. For reference, and to aid with interpretation, an explainer of box and whisker plots is shown in Appendix I.*

2.3.5.3 Single cell testing: data analysis

In addition to the aforementioned symmetrical cell testing, there is a further body of data available across the literature that describes the polarisation performance of single cells containing La-Ni-O cathodes. A key issue with such studies is that they are clearly influenced by factors other than the cathode itself (e.g. electrolyte thickness, anode materials etc). Nevertheless, it is of interest to consider this detail to obtain an understanding of the achievements to date and how they compare with the 'state-of-the-art' materials. In Figure 2.13, such a comparison is offered. Comparisons between studies on lanthanum nickelates and the 'state-of-the-art' performance reported by researchers at Jülich is shown (for LSM, LSM-YSZ, LSCF and LSC cathode materials). The current density at a voltage of 0.7 V is selected as the parameter for comparison. It is notable that many authors commonly report the maximum power density although it is noted by others [259] that such a condition is of little practical significance and that measurements at some voltage away from the point are preferred. As was shown in the case of the symmetrical cell tests, there is again a very wide spread of data. It is observable that, again, the composite and infiltrated electrodes are capable of offering superior performance compared with single phase electrodes. However, the materials of interest are yet to demonstrate the ability to offer similar performance to that which has been shown to be achievable with the optimised LSC and LSCF-containing single cells. It is, however, important to point out that this data is taken from numerous studies. Direct comparisons (such as in Figure 2.13) do not properly accommodate for differences in cell fabrication and testing conditions. It is arguable that reduced degradation rates could mean that the 'initial performance' of a given electrode material does not need to match that of the current state-of-the-art. There must, however, be proof that a life-time benefit is achievable or that a cost benefit can be attained.

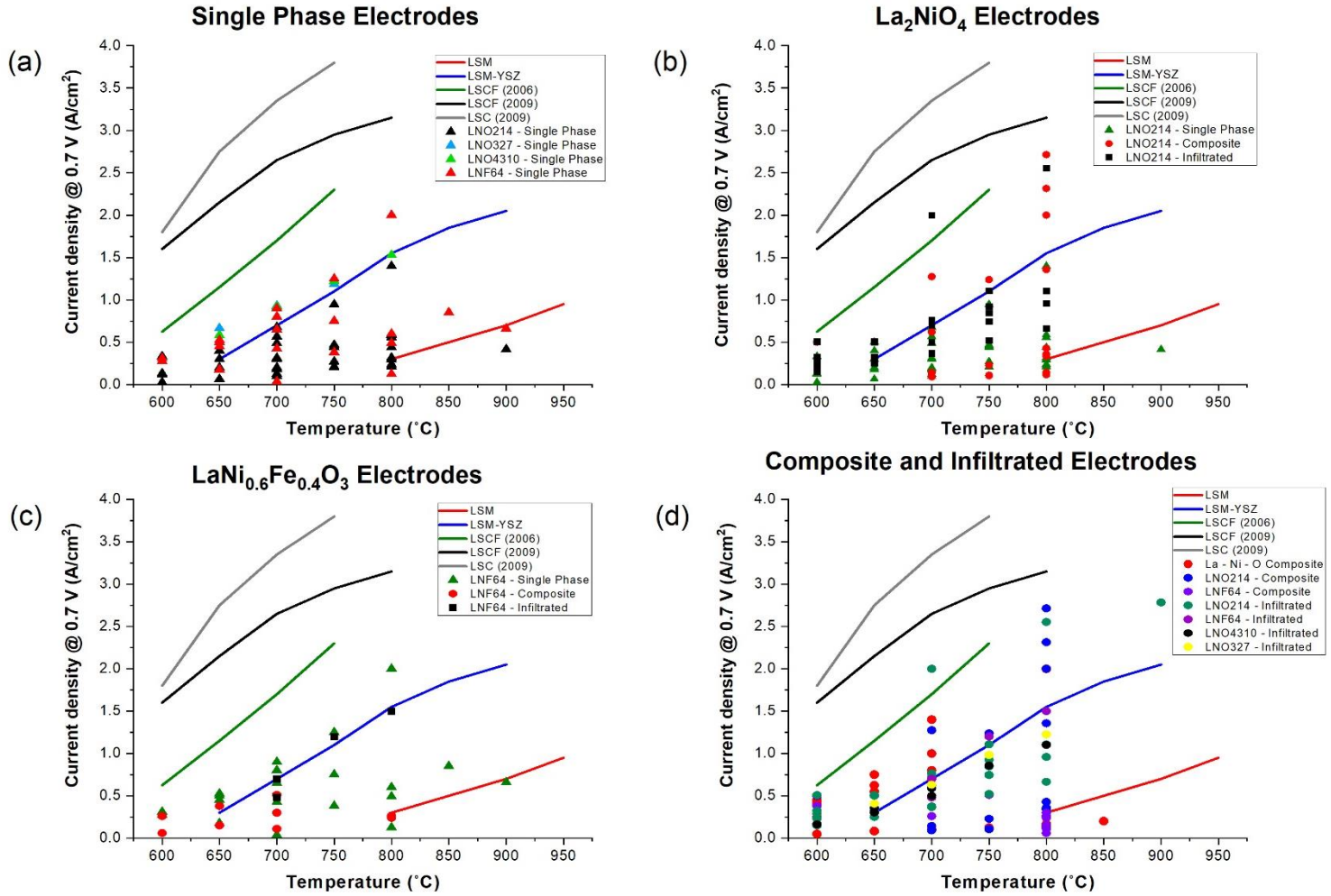


Figure 2.13 – Current density at 0.7 V as reported in various articles; (a) Performance of single phase La-Ni-O electrodes, (b) performance of single phase, composite and infiltrated La_2NiO_4 electrodes, (c) performance of single phase, composite and infiltrated $LaNi_{0.6}Fe_{0.4}O_3$ electrodes (original version published in [95]*) and (d) performance of composite and infiltrated electrode. Underlying data can be found in Appendix D. Lines on the plot show results reported at Jülich and are taken from reference [45] (Note: a key difference between "LSCF (2009)" and "LSC (2009)" is the use of a thin-film electrolyte (1-2 µm) whereas "LSM", "LSM-YSZ" and "LSCF (2006)" employ a thicker 7-10 µm electrolyte).*

2.3.6 Degradation rates

As described earlier in this chapter, degradation rates are of key interest in the development of SOFC technology. It has already been noted that typical stack degradation rates are often above the targeted 0.1%/1000 h objective although there is a large range of degradation rates reported within the literature and some stacks have come close to this target. There has historically been a perception that lanthanum nickelates can contribute towards a reduction in degradation rates (relative to LSCF). This perception no doubt stems from a number of studies associating these phases with a resilience to chromium poisoning [158–162]. It is apparent from the literature, however, that the perception of lanthanum nickelates as 'chromium resistant' must be tempered at least a little. A number of studies [164,260,261] have shown that sizeable degradation rates can result under certain conditions (e.g. higher current density as seen in [260]). The evidence available, however, would appear to suggest that these materials can offer an improvement (although it is rather difficult to quantify how great this improvement would be). Work by Zhen et al [257] indicates that a sizeable loss in performance can be expected for LSCF and LSM-type cathodes in a relatively short time which may be avoided with composite LNC64-GDC electrodes. However, any such improvement that can be reaped in this respect is also somewhat lessened by the advances in chromium-blocking layers which are now applied to the state-of-the-art SOFC interconnects. Although such barrier layers are prone to their own degradation mechanisms and are not 100% effective over the lifetime of the stack, the need to offer a chromium tolerant cathode is reduced.

Unfortunately, the number of *long-term* (i.e. >1000 h) degradation studies that consider the relative degradation rates of the lanthanum nickelates with the state-of-the-art is limited. An overview of degradation studies for electrodes based on various La-Ni-O cathodes can be seen in Table 2.4. The majority of these studies are focussed on LNF64 and LNO214-based electrodes. Given the varied testing approaches and parameters (e.g. temperature, polarisation conditions, electrode set-ups) comparing degradation rates from study to study is likely to be fraught with misjudgement. Nevertheless, such degradation studies can offer some insight. Those works where comparisons are

made against the state-of-the-art materials are no doubt of most value. Unfortunately, there remain only a relatively small number of such studies and these typically consider relatively short operating times (i.e. <100h). This is certainly an area for future work although not considered further in this thesis. Considering the articles offering direct comparison, it would appear that La-Ni-O type materials can offer some reduction in degradation rates [162,253,262]. However, such a conclusion is hardly straightforward with some authors reporting very large degradation rates even in the absence of chromium [261,263].

It seems evident that the major perceived benefit that the La-Ni-O phases are assumed to offer is a reduced degradation rate. However, the data available to support this is far from complete. In some instances research has been shown to support this hypothesis and, in others, the benefit is less evident. The extent to which degradation rates can be reduced is very difficult to offer insight into without direct comparison between the various materials in question. Clearly, the conditions of operation are likely to have an impact on which material offers the greatest long-term performance.

*Table 2.4 - Consideration on degradation studies, ordered by operating time. (WE, RE and CE denote "*Working Electrode*", "*Reference Electrode*" and "*Counter Electrode*", respectively).*

Cell Type	Operating Time	Polarisation Condition	Operating Temperature	Cr-source?	Degradation Metric	Degradation Rate / Observation	Direct Comparison with state-of-the-art?	Ref
LNF64 | SASZ | Ni-SASZ	6000 h	0.4 A/cm^2	800˚C	Yes	Voltage	0.4%/1000 h ***Includes 1 thermal cycle**	No	[264]
LNF64 | LNF64-SDC | SASZ | Ni-SASZ	5200 h	0.4 A/cm^2	800˚C	Yes	Voltage	0-2300 h; 0%/1000 h 0-5670 h; 1.4%/1000 h***** ***Includes 2 thermal cycles**	No	[265]
LNF64 | Not specified.	3000 h	0.16 A/cm^2 0.24 A/cm^2	800˚C	Yes	Voltage	0.3%/1000 h	No	[98]
LNF64 | LNF-GDC | SASZ | Ni-SASZ	1200 h	1.0 A/cm^2	800˚C	Yes	Voltage	63 mV/1200 h	No	[260]
		1.5 A/cm^2				138 mV/1200 h		
LNF64(WE), Pt(RE) | GDC | YSZ | Pt (CE)	1050 h	0.4 A/cm^2	800˚C	Yes	Change in overpotential	$\eta_{Initial}$ = 100 mV η_{after} = 430 mV	No	[164]
	1042 h	0.05 A/cm^2	750˚C	Yes	ΔR_{ohmic} ΔR_{pol}	ΔR_{ohmic} = 0.48 Ωcm^2 (100%) $\Delta R_{pol.}$ = 2.99 Ωcm^2 (2300%)	No	[261]

GDC-infil.-into-LNF64 | ScSZ (Symmetrical)				No	ΔR_{ohmic} ΔR_{pol}	ΔR_{ohmic} = 0.18 Ωcm^2 (38%) $\Delta R_{pol.}$ = 0.25 Ωcm^2 (192%)		
LNF64 | LNF64-GDC | SASZ | Ni-SASZ	950 h	2.3 A/cm^2	800˚C	Yes	Voltage	-0.2 V/950 h	No	[260]
	750 h	0.3 A/cm^2				Negligible		
LNO214 | GDC | YSZ | GDC | LNO214	750 h	0 A/cm^2	700˚C	No	ΔR_{pol}	ΔR_{pol} = 0.05 Ωcm^2 (27%)	No	[263]
	1800 h	0.3 A/cm^2	700˚C		ΔR_{pol}	ΔR_{pol} = ~1.92 Ωcm^2 (1110%)		
LNF64 | SASZ | Ni-SASZ [1Kw stack test]	~700 h	0.28 A/cm^2	800˚C	Yes	Change in electrical efficiency	~0.1 %/700 h	No	[266]
LNO214-Infil.-LSCF | GDC | YSZ | Ni-YSZ	500 h	0.25 A/cm^2	750˚C		ΔV	0.36 %/500 h	Yes (LSCF; 0.39%/500 h)	[253]
LNF64(WE) | Pt(RE) | GDC | YSZ | Pt (CE)	500h	0.4 A/cm^2	800˚C	No	Change in overpotential	$\eta_{Initial}$ = 63 mV η_{after} = 90 mV	No	[164]

LNF64 | ScSZ | LNF64 (Symmetrical)	370 h	0.05 A/cm^2	750˚C	Yes	ΔR_{ohmic} ΔR_{pol}	ΔR_{ohmic} = 1.85 Ωcm^2 (342%) $\Delta R_{pol.}$ = 42.16 Ωcm^2 (6000%)	No	[261]
				No	ΔR_{ohmic} ΔR_{pol}	ΔR_{ohmic} = 0.2 Ωcm^2 (37%) $\Delta R_{pol.}$ = 1.61 Ωcm^2 (230%)		
Nano-LNF64-GDC | ScCeSZ | Ni-ScCeSZ	300 h	0.64 A/cm^2	750˚C	Yes	ΔV	"Stable electrochemical performance"	Yes (LSCF-GDC ; ΔV=-6%/100 h)	[262]
LNF64-GDC | ScCeSZ | Ni-ScCeSZ	100 h	0.64 A/cm^2	750˚C	Yes				
LNO214-SDC | SDC | LNO214-SDC	210 h	0.15 A/cm^2	650˚C	No	ΔV	"*Kept stable*"	No	[267]
LNO214 | LSGM | SDC | NI-SDC	144 h	0.448 A/cm^2	800˚C	No	ΔV	"*stable across the period*" "*The values of voltage, power density and total resistance had hardly changed*"	No	[268]
LNF64 (WE), Pt (RE) | Pr_6O_{11} | GDC | SASZ | Pt (CE)	140 h	0.25 A/cm^2	800˚C	-	Cathode potential vs reference	"*Cathode potential retained its value*"	No	[269]

LNO214 nano-rods-Infil.-into-YSZ | YSZ | Ni-YSZ	130 h	0.7 A/cm^2	700˚C	No	ΔV	"*A stable performance was maintained*"	No	[256]
LNO214-SDC | SDC | Ni-SDC	40 h	0.558 A/cm^2	850˚C	No	ΔV	"*Did not observe a decrease in the cell performance*"	No	[270]
Ni-YSZ | YSZ | LNO327	30 h	0.6 A/cm^2	750˚C	No	Δp	"*Showed stable performance*"	No	[228]
LNF64 (WE), Pt (RE) | YSZ | Pt (CE)	20 h	0.2 A/cm^2	900˚C	Yes	Change in overpotential	"*Very stable*"	Yes: LSM (Δη=482%) LSCF (Δη=1500%)	[162]

2.4 Conclusion

In this chapter we have assessed the drivers for the replacement of the state-of-the-art SOFC cathodes and considered the possibility of La-Ni-O type electrode materials. There is a sizeable body of work in this area already. Many review articles have concluded that these materials are '*promising*' materials for the next generation of SOFCs. However, such statements largely ignore the rich data which is available in the literature. The assessment provided here suggests that the lanthanum nickelates offer inferior performance when compared with LSC or LSCF. A clear caveat with the analysis provided in this literature review is that it provides comparisons across many studies in which different testing protocols were employed. A 'clean' comparison (i.e. material synthesis conditions, same electrode deposition technique and the same test bench) of each of these materials may offer a more rounded and comprehensive view. An attempt to offer such an analysis is a key component of the work in this thesis. This will cover analysis of both symmetrical cell testing (Chapter 4) and single cell testing (Chapter 5) approaches that have been shown to be common in the literature. This will cover several popular lanthanum nickelate materials (LNF64, LNO214, LNO327, LNO4310) in addition to the state-of-the-art material LSCF6428. Further, a consideration of different parameters (e.g. sintering temperature) will be considered to offer a more in-depth view on the effect of these contributions.

It is interesting to note that the perovskite and Ruddlesden-Popper variants of the lanthanum nickelates are often discussed in isolation of one another. This is despite the fact that a number of authors have noted that the $LaNiO_3$-phase can be considered to be the 'end member' ($n=\infty$) of the Ruddlesden-Popper series. Although $LaNiO_3$ offers poor stability, it has already been discussed how this can be improved via suitable doping strategies. As such, a series of phases with a range of properties are observed. Not only could a combination of these materials offer a good solution to promoting cell performance (with comparable TEC values and apparent resistance to chromium poisoning), but these materials also offer an interesting case study on the relative role of these materials in achieving favourable performance. For instance, do those materials with better electronic conductivity or ionic conductivity make for a better electrode material? To consider this in more detail

and draw direct comparison with the ‘single-phase’ electrodes also studied, a further study of the effects of different ‘secondary phases’ is offered in Chapter 6 of this thesis.

Another notable observation from the literature review provided in this chapter is the apparent prevalence of symmetrical cell testing across many of the articles studied. We are unaware of any major works exploring the role of symmetrical cell testing in SOFC testing (even though it is often recommended in EIS articles) and, importantly, little consideration of how effective this approach is in identifying ‘high-performing’ cathode materials. Considering these factors, an exploration of how well this technique corresponds to more conventional ‘single cell testing’ is also identified to be a matter of further interest. This will be explored in the coming chapters.

3 Materials and methods

3.1 Overview of chapter

In order to offer further insight into the employment of lanthanum nickelates as SOFC cathode materials, a variety of techniques and methods are drawn on in the coming chapters of this work. An overview of these methods is provided here. Firstly, and on the most fundamental level, this includes an introduction to the synthesis and physical characterisation of the materials under consideration. In order to conduct suitable in-situ testing, several methods to produce and test SOFC electrodes are discussed. Attempts have been made to maintain consistency across each of the detailed tests (e.g. particle morphology and size, electrode area and thickness, cell testing parameters). This is with a view to promoting representative and repeatable results (e.g. minimising the potentially significant effects of variables such as particle size). In addition to this, testing is conducted with reference to the commercial, state-of-the-art alternatives. This is with a view to offering a relative understanding of the performance of the lanthanum nickelates. This provides value given that many literature sources overlook such direct comparisons in their analysis of cathode materials.

3.2 Synthesis methods

Although the advancement of SOFC technology has led to the commercial availability of many cell materials, the majority of those studied in this work are yet to be brought to the marketplace. As a result of this, the work detailed in this thesis begins with a discussion of the synthesis of the lanthanum nickelate phases (i.e. La_2NiO_4, $La_3Ni_2O_7$, $La_4Ni_3O_{10}$, $LaNi_{0.6}Fe_{0.4}O_3$), for which two approaches were considered. The characterisation techniques employed to analyse the resulting materials are detailed later in this chapter.

3.2.1 Solid-state

Solid-state synthesis is no doubt the simplest approach for preparing mixed metal oxide phases. In essence, this approach involves the direct reaction between calculated quantities of metal salt

reagents (e.g. metal oxides) to produce a specific, targeted phase. Taking the example of La_2NiO_4, for instance, the following reaction is anticipated:

$$La_2O_3(s) + NiO(s) \rightarrow La_2NiO_4(s) \quad \text{[Eq. 3.1]}$$

Naturally, the extent to which high quality single-phase materials can be synthesised is a function of thermodynamics (i.e. temperature and oxygen pressure) as well as diffusion-related limitations (i.e. particle size). Many side reactions may occur during this process and this can place a difficulty on achieving pure phases.

In an attempt to prepare lanthanum nickelate phases via the solid-state-route, La_2O_3 (*Aldrich, 99.99% purity)*, NiO (*Aldrich, 99.99% purity)* and Fe_2O_3 (*Aldrich, 97% purity*) were employed as starting materials. Given its hygroscopic nature, La_2O_3 was first heated to release any residual H_2O content. The oxide powders were then measured out in stoichiometric quantities and ground together using an agate pestle and mortar. The resulting mixtures were then transferred to an alumina crucible and heated to high temperature (≥1000˚C) in a Carbolite furnace. Several re-grinding and annealing steps were employed to improve the quality of the sample and to ensure the completion of the solid-state reaction.

3.2.2 Pechini synthesis

The Pechini process [271] is a type of '*sol-gel'* synthesis route which enables the lowering of calcination temperatures and can help to significantly shorten preparation times. This is realised by overcoming the diffusion-related limitations which are associated with the solid state route [272–274]. Importantly, by initially placing the starting materials into solution, it is possible to ensure an "*atomic level mixing*" of the cations. In the Pechini process, metal nitrates are dissolved in deionised water with ethylene glycol and citric acid. This approach forms a precursor solution that contains metal-citrate chelate complexes [272]. The interaction between the ethylene glycol and citric acid forms a polymer network with a homogenous distribution of the metal cations. This precursor is then combusted in an initial heat treatment step in order to remove the organic matrix, leaving a well-

dispersed mixture of reactant oxides. A second heat treatment step at higher temperature is then employed to obtain a high quality single-phase material.

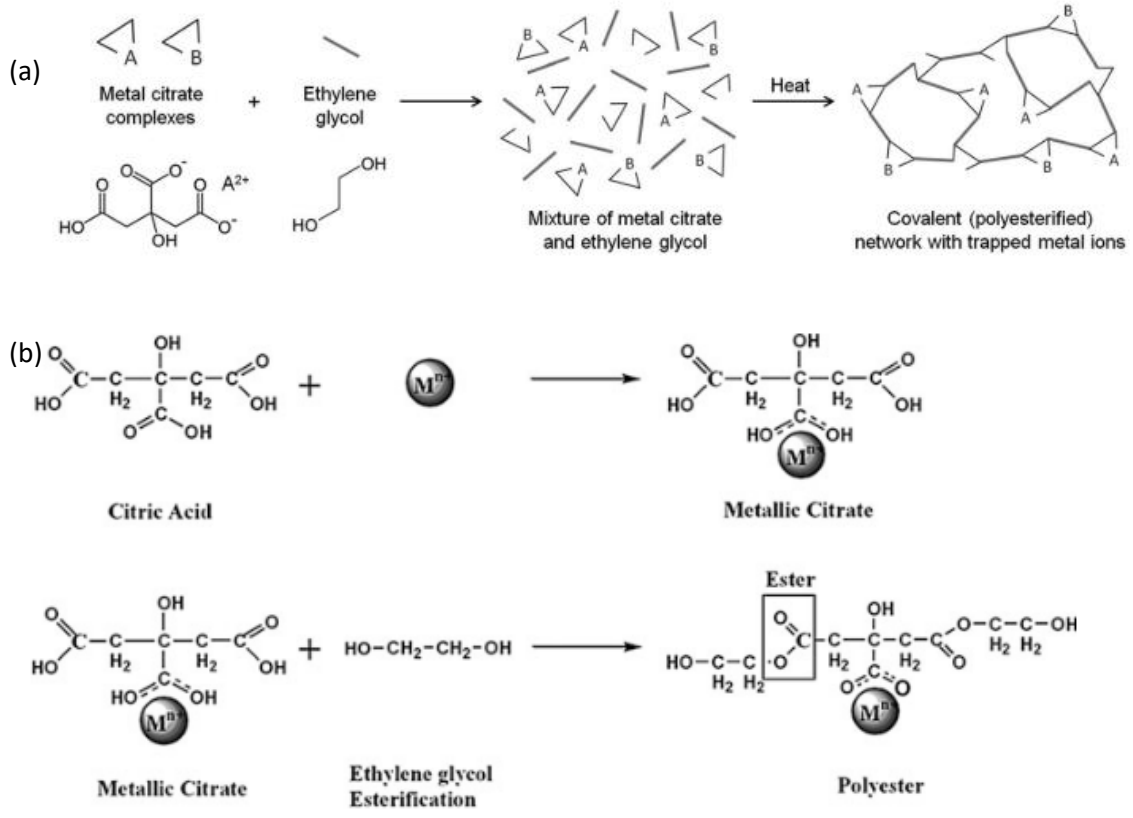


Figure 3.1 – Schematic illustrations of the Pechini process as shown (a) in [272] *and (b) in* [274].

For the preparation of the La-nickelate Ruddlesden-Popper compounds, nickel (II) nitrate hexahydrate ($Ni(NO_3)_2.6H_2O$) and lanthanum (III) nitrate hexahydrate ($La(NO_3)_3.6H_2O$) were employed as the starting materials. Iron (III) nitrate nonahydrate ($Fe(NO)_3.9H_2O$) was additionally used for the preparation of $LaNi_{0.6}Fe_{0.4}O_3$. After dispensing the correct stoichiometric quantities of these reagents, the metal nitrate powders were dissolved in deionized water to form a homogenous solution. Ethylene glycol (*VWR*) and citric acid (*Sigma Aldrich, 99%*) were then added to the resulting solution. These materials were then stirred on a hot plate at 80˚C for approximately 1 to 2 hours to obtain a polymeric gel. The gel was then heated in an oven to 350˚C and held at temperature for 8 hours (for the work discussed here, a ramp rate of 5˚C/min was employed). During this heat-treatment process, the gel was observed to expand, combust and form an ash-type honeycomb structure. This was then ground

in an agate pestle and mortar to obtain a fine dispersion of metal oxide powders. To obtain the final phase, the material was then placed in an alumina crucible and heated at a higher temperature (i.e. ≥ 1000˚C) in a Carbolite furnace (again a ramp rate and cooling rate of 5˚C/min was utilised). In some instances, particularly for larger samples, several calcination steps were conducted, with intermediate grinding steps between each heat-treatment. The phase quality was confirmed via the use of X-Ray Diffraction (XRD) techniques as described later in this chapter.

3.3 Electrode preparation

3.3.1 Ball milling and sieving

In order to achieve sufficient material for ink preparation and deposition, samples were prepared and combined from small batches (5 to 7g), to achieve a larger (~40g) sample of each material. In order to reduce particle size and break up any remaining agglomerates, these larger samples were ball-milled for 72 hours utilising a roller mill. Any remaining agglomerates were then removed using a 25 µm sieve in combination with a sieve shaker (*Fritsch analysette Pro*). The control of particle size by this approach was deemed to improve the repeatability of the analysis.

3.3.2 Ink formulation

For the production of cathode inks, a commercial α-Terpineol-based ink vehicle (*Fuel Cell materials*) was mixed with the ceramic powders. The powders were first combined with the ink vehicle in a defined mass ratio (66 wt% powder to match similar commercial cathode inks) to achieve a given '*solid loading*'. The mixture was then loosely mixed prior to a homogenisation of the resulting slurry via the use of a triple-roll mill. This is an approach conducted by many researchers in the SOFC field and is discussed in some detail by Somalu et al. [275].

3.3.3 Deposition and sintering

The simplest approach to depositing SOFC electrode layers is to hand-paint inks on to the ceramic substrate (i.e. electrolyte layer) in question. Although this approach offers relatively poor control over electrode thickness and microstructure compared with other techniques, it is commonly employed

within many of the articles reviewed in Chapter 2. For the sake of simplicity, and to minimise the wastage[12] of synthesised materials and inks, this is the approach employed in this thesis. As will be described in more detail in Section 3.4, two types of SOFC test are conducted in this work; (1) 'single-cell' testing and (2) 'symmetrical cell' testing. For single-cell testing (the configuration shown in Figure 3.2a), the electrode inks were deposited on commercial half-cells (*SOFCMan)* of the following type:

Ni-YSZ (400 µm) | YSZ (10-15 µm) | GDC (2-3 µm)

For symmetrical cell tests (Figure 3.2b), the electrodes were deposited on both sides of commercial electrolyte sheets (*SOFCMan*) of the following type:

GDC (5 µm) | YSZ (200 µm) | GDC (5 µm) |

In each instance, the edges of the substrates were covered with a 5mm masking tape to leave a 40 mm x 40 mm exposed area. The ink was then brush coated on this area. These 'coupons' were weighed both before and after the application of the ink in order to deposit a similar quantity of material in all instances (0.1g). After painting, the electrodes were subsequently dried in an oven at 100˚C. Finally, the electrodes were sintered in a Carbolite furnace (≥1000 ˚C) employing the temperature ramp profile shown in Figure 3.3. An example of a resulting electrode is shown in Figure 3.4

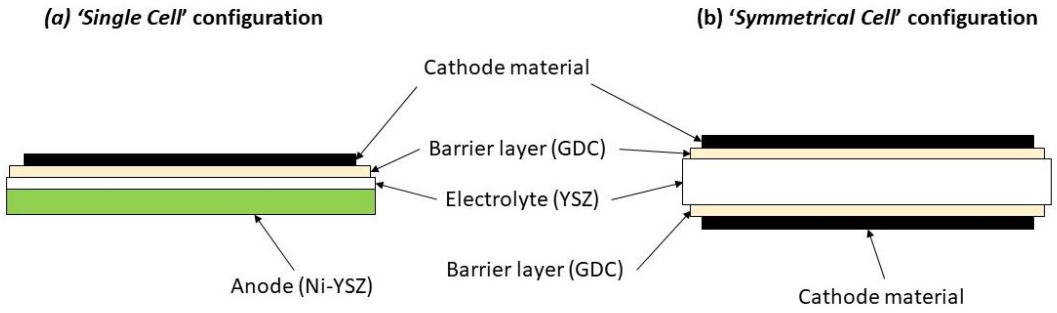


Figure 3.2 – Schematic illustrating the (a) single cell and (b) symmetrical cell configurations. For the work in this thesis, cathode materials (black) were deposited on commercial substrates ('Ni-YSZ | YSZ | GDC' and 'GDC | YSZ | GDC'). Schematic not to scale.

[12] More complex routes such as spin-coating can lead to a wastage of materials which can be lost during the deposition process

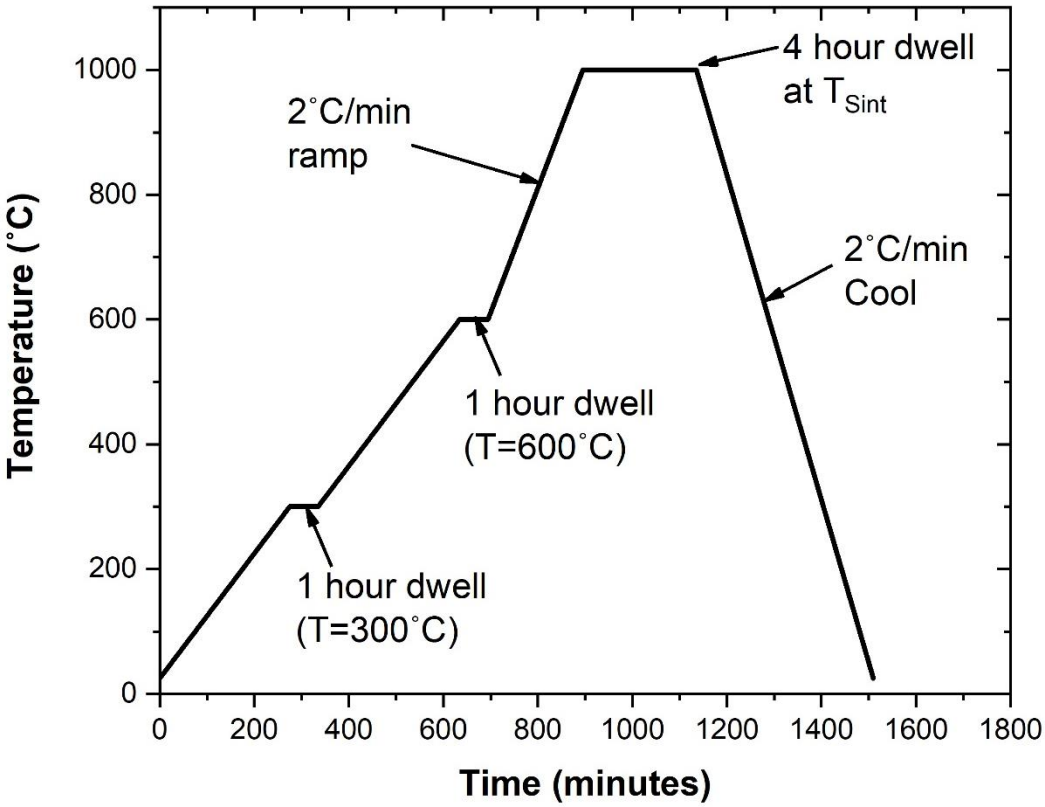


Figure 3.3 – Typical temperature ramp profile for electrode sintering in this study.

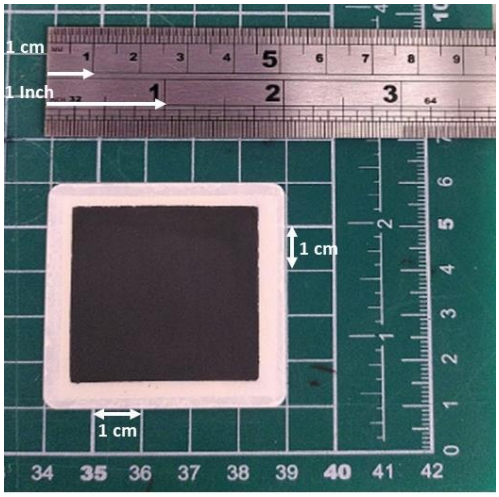


Figure 3.4 – Example of an electrode deposited via the described process.

3.4 Electrode testing

In order to assess the performance of the electrode materials in question, it is necessary to assess their behaviour via in-situ testing methodologies. Following the application and sintering of electrodes as described in Section 3.3, the electrochemical performance of the cells (both symmetrical and single

cell) were tested under SOFC conditions. Where possible, the development of testing procedures has drawn on the available literature in this area to ensure reliable data is obtained [259,276]. In addition, and in the case of the full cell testing approach, a discussion of suitable testing parameters (e.g. gas flow rates, humidification and contact configurations) will be offered in Chapters 4 and 5. A key difficulty in the testing of fuel cells is the de-convolution of the contribution of individual components (e.g. electrodes) within the cell. This essentially results from the fact that it is impossible to measure the voltage of a single electrode; such measurements must always be conducted with reference to a second electrode. In the context of this thesis, several testing approaches are employed to help assess the performance of each electrode material. This included different cell configurations as well as conducting tests under different conditions and combining with state-of-the-art analysis techniques.

For the work described in this thesis, testing of the electrode performance was divided into two different cell configurations; (1) symmetrical cell testing and (2) single cell testing. These two approaches are both widely used within the literature and are employed to offer complimentary information on the quality of electrode materials. An alternative (and *theoretically* superior) approach to understanding the performance of a specific electrode would be to employ a three-electrode set-up. Such a configuration utilises a working, counter and reference electrode (WE, CE and RE, respectively). In such a case, the voltage/performance of the electrode of interest can be understood via measurement with respect to a third electrode. However, such an approach is often reported to be difficult in practise given stringent geometrical requirements for the placement of reference electrodes [259,276–280]. To achieve *true* 3-electrode systems, complex electrolyte structures are required which are not considered further in this thesis but can be seen in reference [281].

3.4.1 Symmetrical cell testing

3.4.1.1 Background

As was described in Chapter 2, symmetrical cell testing is a variant of SOFC testing of particular interest for those researchers studying a specific electrode (or, moreover, electrode material). As indicated in

Section 3.3.3 and shown in Figure 3.2, a symmetrical cell involves the deposition of an identical electrode on both sides of an electrolyte substrate. Each electrode is then exposed to an identical environment (air can be employed in the case of a cathode material). *Electrochemical Impedance Spectroscopy* (EIS) measurements are then performed on these samples. EIS is a method of analysing cell performance widely employed in the study of SOFCs. Impedance analyses within the literature vary from very basic performance data (i.e. reporting of R_{pol} values) to very detailed analyses of fundamental processes. For a detailed background understanding of the EIS technique, the reader is referred to [282]. Briefly, however, EIS involves the application of an A/C input signal (of a known frequency) and the measurement of the resulting current response. Analysis of this response provides an impedance value which is comprised of both a real (Z') and imaginary (Z'') contribution. Importantly, the impedance measured is characteristic of the frequency of the original input signal. Furthermore, various phenomena are found to dominate the impedance response at differing frequencies. Measurements are taken at a range of frequencies (typically from the MHz to the mHz range) to construct an impedance spectrum. Importantly, the resulting spectrum (often represented as a Nyquist diagram) is commonly modelled to offer further physical insight into the processes taking place within the cell. As a result of this approach, therefore, the electrochemical engineer can begin to quantify and build-up an understanding of the various physical processes taking place in an electrochemical system. In recent times, several add-on techniques to studying impedance spectra have become increasingly popular. This includes the Kramers-Kronig test (for validation purposes) and the Distribution of Relaxation Times (DRT) methodology (for the identification and quantification of contributing phenomena). These techniques are further described in [282]. Employment of these approaches will be detailed later in the thesis work.

During EIS measurements of symmetrical cells, each electrode switches from anodic to cathodic polarisation. At any one time, one electrode acts in 'electrolysis mode' whereas the other works in 'fuel cell mode'. A drawback of symmetrical cell testing is that tests must be conducted in an open-circuit like condition (i.e. $i \sim 0 Acm^{-2}$) [225,283] and, as a result, an understanding of the electrode

behaviour under polarisation conditions is not possible. Nevertheless, and as described previously, this type of test is commonly used for assessing the performance of electrode materials; the 'suitability' of symmetrical cell testing in developing an understanding of electrode performance is explored in Chapter 5.

3.4.1.2 Experimental set-up

For EIS measurements to be conducted on symmetrical cells, a cell and contact assembly was prepared and placed in a horizontal furnace as is shown in Figure 3.5. This offered a similar set-up to that described by Jorgensen and Mogensen [284]. To achieve suitable electrical contact between the electrode and the current collecting materials, a 175g alumina weight was placed on top of the Au meshes. EIS measurements were conducted using a Solatron 1470E Potentiostat in conjunction with a Solatron 1455 Frequency Response Analyser. The effect of applying Au paste as a contact material between the mesh and the electrode was also studied and is described Chapter 4.

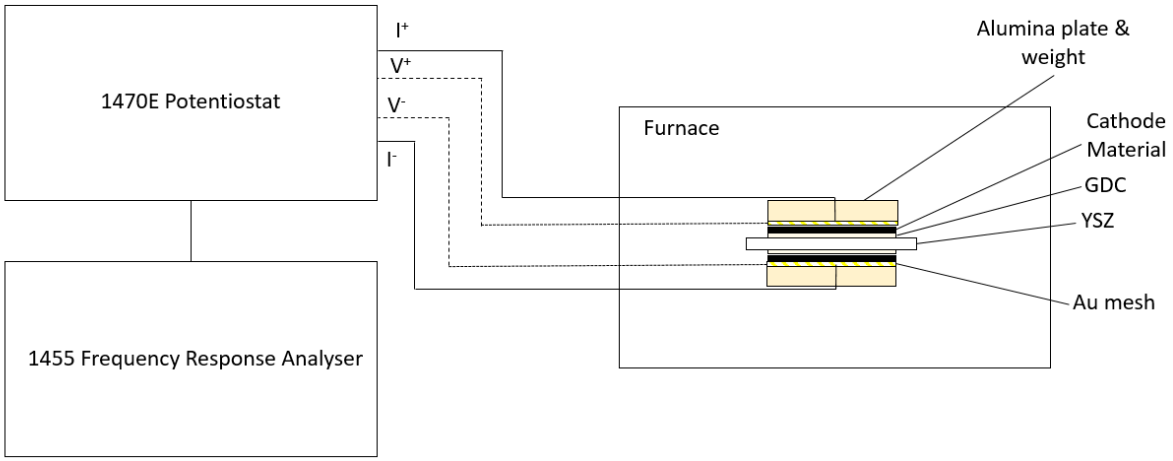


Figure 3.5 - Schematic of symmetrical cell set-up.

3.4.1.3 Experimental procedure

EIS measurements were carried out on the symmetrical cells in static air at temperatures between 600 and 800˚C (intervals of 50˚C). A perturbation amplitude of 10 mV was employed with 2 cycles

integration and 1 delay cycle[13]. For each measurement, the cell was held at temperature for 12 h prior to EIS measurements being recorded. This testing configuration was observed to offer good quality impedance spectra with minimal noise observed. Polarisation (R_{pol}) and ohmic (R_o) resistance values were calculated for each test, using the conventions and equation described in Chapter 2 (see Section 2.3.5.2). For the calculation of these values, the area of the electrode is taken to be 16cm^2.

3.4.2 Single cell testing

3.4.2.1 Background

The most commonly used cell configuration employed across the SOFC literature is that which we will herein describe as a "single cell". In this instance, the conventional and well-known cell structure is employed, comprising the following key components for fuel cell operation:

Anode (fuel) | Electrolyte | Cathode (oxidant)

To study such SOFC cells, there are several key techniques and principles which are of major significance in performance bench-marking. *Polarisation curves,* which were discussed in the introductory chapter of this thesis, represent the most common and well-known of these methods. Such an approach effectively charts the current (or power) output of the cell over a defined voltage range (typically the open circuit voltage to around 0.6 V). Both current (I) and power (P) are commonly normalised per unit area and represented as *current density (i)* and *power density (p),* with units of Acm^{-2} and Wcm^{-2}, respectively . Within the literature, it is commonplace to report or bench-mark such properties at a given voltage rating (often at 0.7 V). In some papers, the maximum values of power and/or current density are also reported. However, Klotz et al. [259] label this parameter as "*irrelevant to SOFCs*" given the inefficiencies and instabilities associated with such conditions. Although polarisation curves are of importance in understanding the performance of a single cell, such a test is

[13]Integration cycles define the number of complete sinusoidal waves that are conducted by the potentiostat software to calculate the impedance value at each frequency. 'Delay' cycles determine the number of complete cycles that are conducted before the impedance measurement is commenced (allowing for a 'settling period').

capable of offering only limited understanding on the various phenomena that contribute towards cell output. Additional tests are typically required/employed to probe the relative contributions of cell components or transport processes (i.e. charge transfer and diffusion).

3.4.2.2 Experimental set-up

To conduct single cell SOFC testing, several key requirements are fundamental. Importantly, this includes the stable provision of (1) a suitable operating temperature, and (2) a supply of fuel and oxidant to the cell. Further, the necessary electrical connections to conduct *highly sensitive* electrical measurements at high temperatures must be ensured. Without suitable accuracy, sizeable error can be introduced into the cell measurements as detailed in [259]. As an example of this, instabilities in gas flow can cause fluctuations in the operating voltage of the cell which can prevent the acquisition of good quality impedance measurements.

Within the literature, numerous test set-ups are detailed but these are fundamentally comprised of the same key components. For the work described here, an electronically controlled Carbolite furnace in conjunction with an alumina cell-housing (Chino Corporation, Japan) was adopted. The housing was comprised of two sections (Figure 3.6) and fitted with gas, electrical and thermocouple connections. The set-up employed a typical two electrode four wire set-up which has also been employed in numerous other reports (e.g. [284,285]). The SOFC cell was assembled into the holders along with sealing materials and current collecting meshes. A schematic of the cell-holder assembly is shown in Figure 3.7. Importantly, the current collecting meshes were in direct contact with lead-out wires which enabled electrical connections to the cell to be made with the external control units. On the anode side of the cell, a 0.5 mm Ni-mesh (Chino) was employed in direct contact with the Ni-YSZ anode. On the cathode of the cell, a 0.5 mm Ag-mesh (Chino) was used[14] and, additionally, a thin layer of contact paste was also employed on the cathode side. The reasons for this are detailed in Chapter 5. To achieve

[14] The employment of Ag mesh is thought to be unfavourable given the promotional catalytic effect that Ag can have on cell-performance as documented by Egger and Sitte [402]. Attempts to employ Au were carried out but for spatial and re-use/cost purposes, good quality results were difficult to achieve (in terms of impedance response and power outputs).

suitable sealing, two mica gaskets (Chino) were fixed to the cell housing, with the cell placed in-between. The achievement of a good quality seal was particularly important on the anode-side of the cell, given leakages could lead to thermal gradients across the cell (e.g. due to hydrogen flames) and offer difficulties with respect to obtaining good quality data.

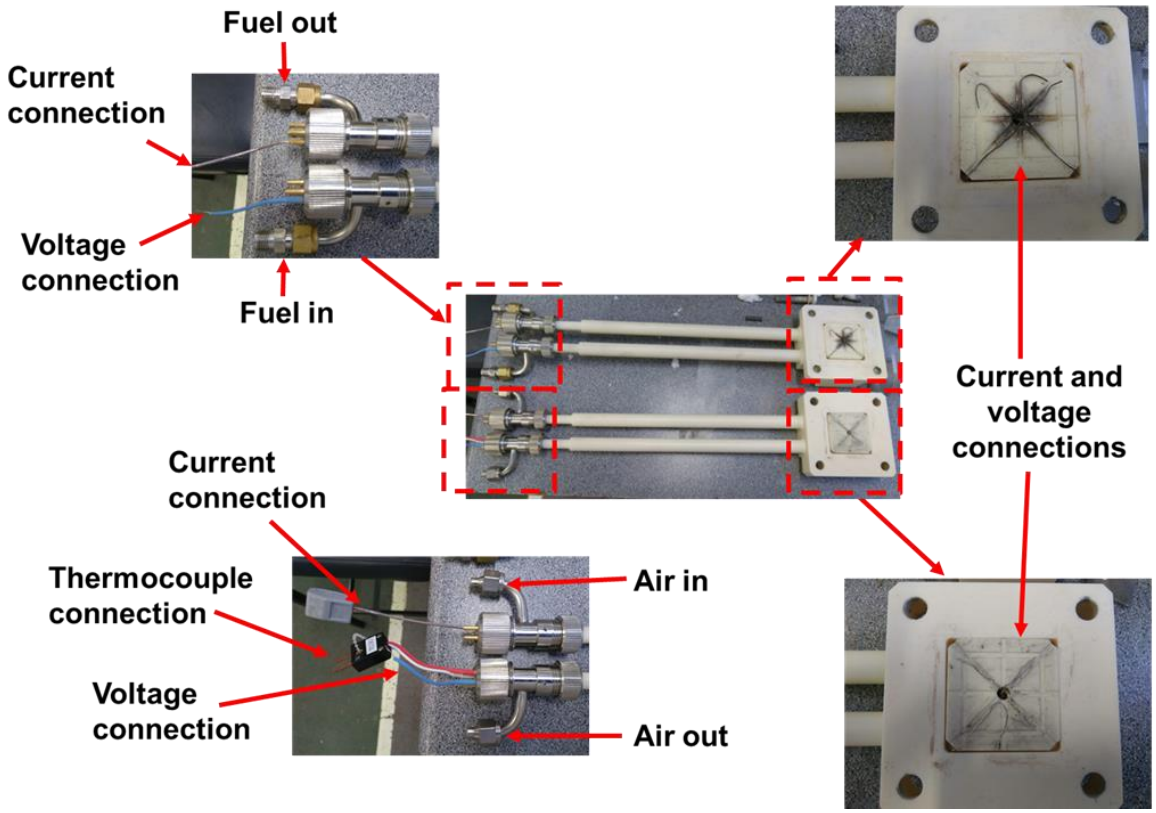


Figure 3.6 – Disassembled cell holders with electrical, gas and thermocouple connections shown.

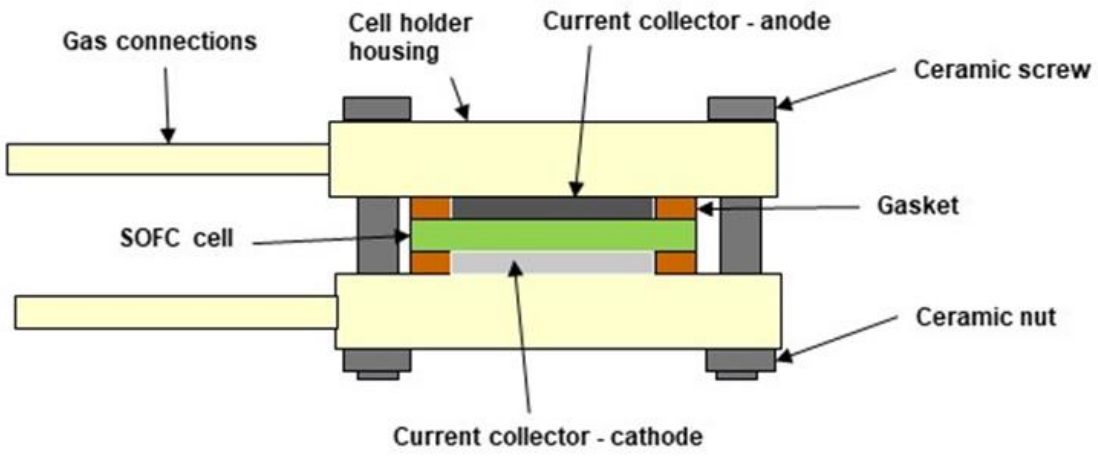


Figure 3.7 – Schematic of cell holder with cell, current collector and mica gasket.

A schematic of the experimental set-up is shown in Figure 3.8, illustrating the gas and electrical connections. Bronkhorst Mass Flow Controllers (MFCs) were used to control hydrogen, nitrogen, and air flow-rates to the cells. For later tests, the rig was adjusted to test the cathode under oxygen-nitrogen blends to study the effect on the cell. For the purposes of electrical measurement and control, the cell holders were connected to a Solatron 1470E potentiostat via a 25A/125W booster unit. To enable EIS measurements to be performed, a Solatron 1455 Frequency Response Analyser (FRA) was also connected to this set-up. The potentiostat and FRA were controlled by Multistat software (*Ametek*).

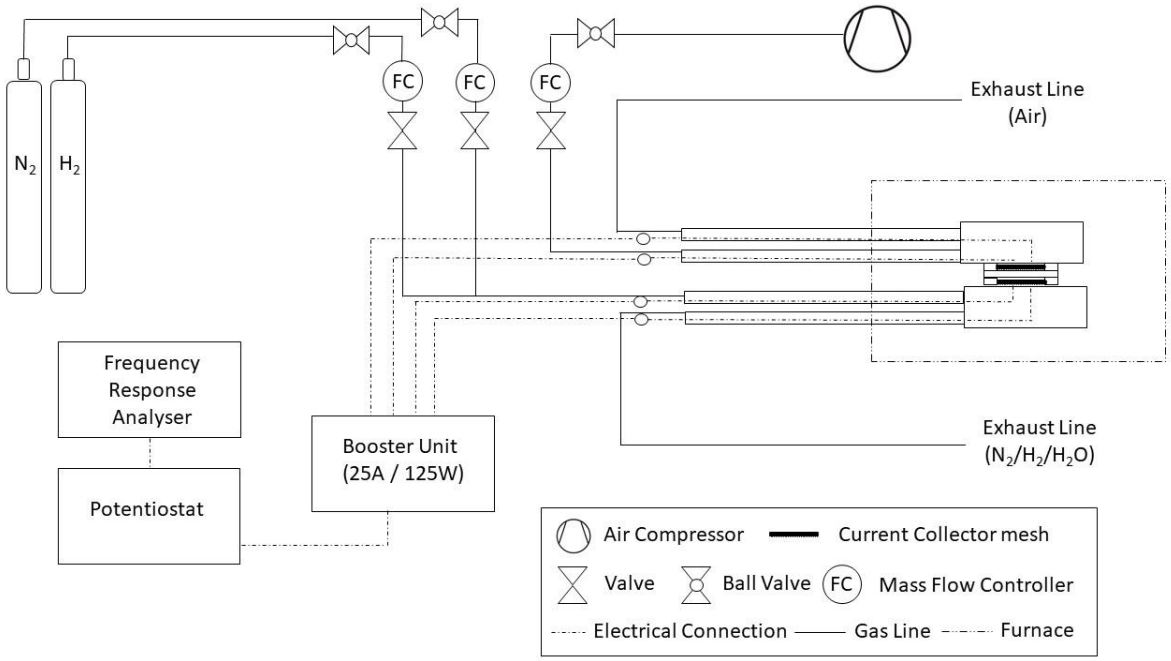


Figure 3.8 - Simplified schematic of cell test set-up.

3.4.2.3 Experimental procedure

After the preparation of the cell holder as described above, the assembly was placed into the furnace with gas and electrical connections fitted. In accordance with guidelines from the rig supplier, the heating profile and gas flow conditions were set as described by Figure 3.9. A slow ramp rate of 1˚C/min was employed to avoid any structural issues (i.e. cell cracking or delamination) associated with the differing thermal expansion of the various materials in the assembly. The reduction of the

NiO-based anode was commenced at 800˚C, employing a H_2-N_2 mixture[15] containing an initial 16vol% H_2. This condition was maintained for 24 h to ensure the full reduction of the anode prior to increasing the H_2-content to a 100vol% H_2 (0.2 to 0.5 l/min) condition. The voltage was then left for a further 1 to 2 hours prior to collecting measurements, in order to allow the stabilisation of the cell at the given operating condition. The use of humidified hydrogen and its effect on SOFC testing with the described set-up will also be detailed in Chapter 5.

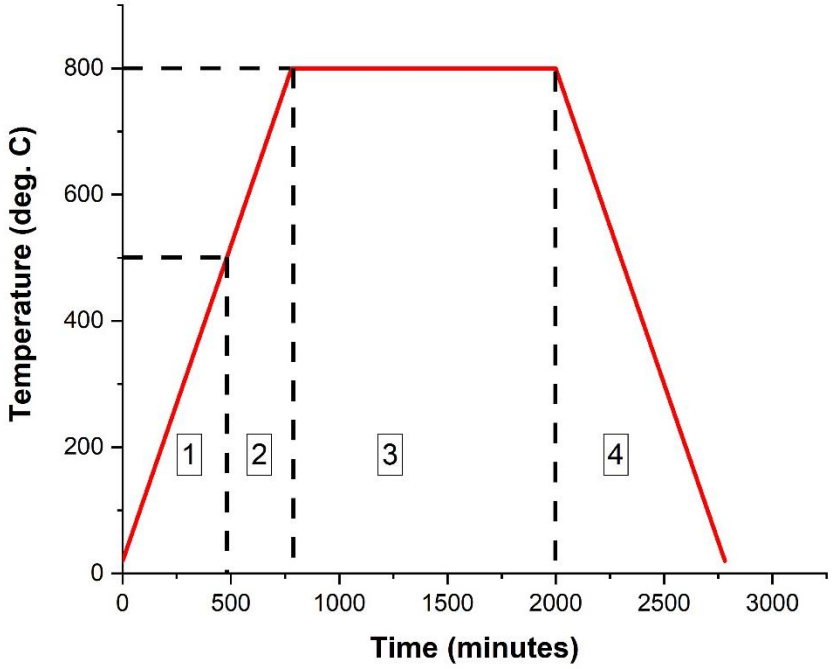


Figure 3.9 - Temperature programme for heating and cooling employed for single cell testing. Gas flows were set as follows: region (1) no anode gas flow, 0.2 l/min air on cathode side, region (2) 0.2 l/min N_2 anode side, 0.2 l/min air on cathode side, region (3) 24 hour supply of 16vol% H_2-84vol% N_2 before a gradual increase to 100% H_2 (0.2-0.5 l/min) and 0.5 l/min flow of air. For cooling (region (4)) 16vol% H_2-84vol% N_2 employed to prevent oxidation of the anode.

For the procurement of polarisation curves during cell testing, a “voltage step” test was conducted. In such an instance, the voltage is periodically reduced in (10 mV) steps and held for a 30 second period, with the current recorded during this time. Such an approach is deemed to be preferable to a continuous scan speed [259]. For each cell studied, polarisation curves were recorded at temperatures between 800 and 650˚C in 50˚C intervals.

[15] A Hydrogen-nitrogen mixture was employed to prevent a rapid contraction of the anode during reduction. Reduction in a 100% hydrogen atmosphere was observed to lead to cell cracking in one instance.

In the case of recording EIS measurements, measurements were recorded at open circuit voltage. A voltage perturbation amplitude of 50 mV was employed and a frequency range of 1 MHz to 0.05 Hz. It is noted that a small perturbation amplitude is commonly preferred (10 to 30mV is more commonly employed within the literature) but with the set-up described a larger amplitude was found to be necessary to minimise noise. Commonly, integration times (the amount of time or the number of cycles the FRA runs at each frequency) can be customised to improve the quality of impedance data. A trade-off between experimental time and noise reduction should be considered. For the testing work conducted here, 2 integration cycles were employed in each case with an additional 1 cycle of delay. This procedure was in agreement with that which has been recommended by Klotz et al.[259].

In order to conduct a DRT analysis of each cell (and in an attempt to identify the relevant anode or cathode contributions), EIS measurements were conducted under a variety of conditions. In the most basic case, this included an EIS measurement at each operating temperature (600 to 800˚C). Further to this, measurements were also conducted under different anode and cathode gas compositions in an attempt to isolate the cathode contributions from the anode contributions. This use of different gas compositions is a technique also applied in other studies [286] in order to aid the deconvolution of contributions via DRT analysis. This was achieved by mixing nitrogen into the fuel or oxidant gas-streams to offer a diluting effect. An EIS measurement was then conducted at each condition, with the cell allowed to equilibrate (with respect to voltage and temperature) prior to this, by maintaining the cell at OCV for approximately 1 hour.

In order to assess the quality of the impedance data via a study of residuals, Kramers-Kronig analysis was performed in *Lin-KK* software [287]. DRT analysis was performed on the EIS spectra using an in-house developed script, with a view to identifying the number and magnitude of constituent electrochemical processes. Following this, modelling of the EIS spectra was conducted using ZView. Here, each electrochemical process was modelled using an ‘RQ element’ (see [282]).

3.5 Physical characterisation techniques

In addition to electrochemical analysis via the aforementioned cell testing methods, analysis of the materials and cells was conducted using several physical characterisation techniques. This included X-Ray Diffraction (XRD) to perform phase analysis and the use of Scanning Electron Microscope (SEM) techniques to study microstructures. Here, these approaches are described.

3.5.1 X-Ray Diffraction

3.5.1.1 Background

In order to assess the success of the synthesis approaches detailed in Section 3.2, XRD techniques were routinely utilised for the purposes of phase analysis. This approach is common for characterising the atomic structure of crystalline materials [273] and is widely employed in SOFC R&D. For the purposes of this technique, X-rays are first generated from a defined metal-source (e.g. Cu, Co). As a result of this bombardment, electrons are liberated from the source material. In turn, outer-shell electrons within the source material fall to lower (now unoccupied) energy states. The result of this interaction is the release of electromagnetic radiation with a characteristic wavelength, described by the Planck-Einstein relation:

$$E_{wave} = h\nu = \frac{hc}{\lambda} \ (Eq. 3.1)$$

where E_{wave}, h, ν, c and λ denote the energy of the wave, Planck's constant, wave frequency, the speed of light and the wavelength, respectively. The wavelength of these resulting photons corresponds to the range referred to as X-ray radiation (λ ~1A). This wavelength is comparable to that which is seen for interatomic spacing of crystalline materials. This is of great importance for reasons to be described.

A key defining feature of crystalline materials is their long-range atomic order. When X-Rays are directed at such materials, they are seen to be scattered in a characteristic and repeatable manner. The common analogy which is offered in textbooks on this subject is that the planes of atoms act in a

similar manner to how an optical grating scatters (or diffracts) visible light. In that case, visible light is diffracted when the grating separation is of similar size (or slightly larger) to the wavelength of the light which is incident upon it (380 to 700 nm). Beyond the grating, constructive and destructive interference then leads to a series of peaks (light fringes) and troughs (dark fringes). X-rays are often described to act in a similar manner when they are incident upon a plane of atoms; the small wavelength of the X-Rays (below that of the interatomic spacing) enables this to occur. The constructive and destructive interference of the X-rays can be utilised to obtain information on lattice parameters and crystal symmetry.

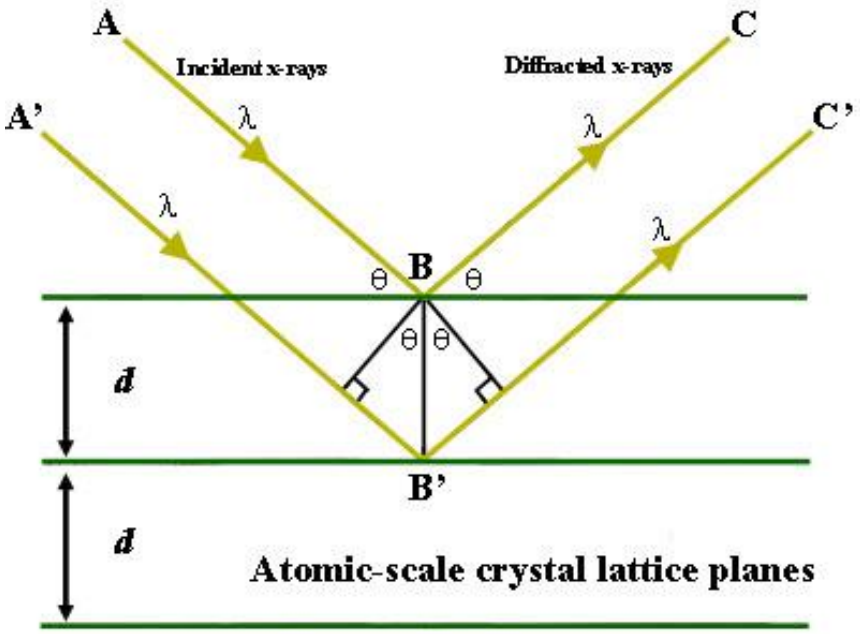


Figure 3.10 - Schematic demonstrating the diffraction grating analogy of planes of atoms [288].

The concepts discussed so far are perhaps best understood when studying Figure 3.10. Constructive interference occurs between two diffracted X-rays when the path difference ($2dsin\theta$) is equal to a whole number (n) of wavelengths (λ). This relationship is represented by the Bragg equation:

$$n\lambda = 2dsin\theta \text{ (Eq. 3.2)}$$

As such, given information on the X-ray wavelength and the angle of incidence, atomic spacing may be calculated. Or perhaps, more importantly, the angles at which a peak is observed offers information on the atomic distance of a given plan. To ensure all dimensions of a phase can be determined,

measurements in numerous orientations are required. As such, XRD is conducted on a powdered sample where the random and numerous orientations enable such a consideration. Whilst the angle of the peaks relates to the atomic separation, the amplitude/intensity of the peaks is associated with the type and position of the atoms in the lattice. These two factors mean that each crystalline phase has a characteristic '*fingerprint*'. XRD can, therefore, be employed in order to detect specific phases within solid samples. Importantly, the technique can be used to detect the presence of impurity phases and hence becomes a tool of great importance in the synthesis and analysis of crystalline materials.

Whilst the idea of Bragg's law involves relatively simple mathematics (and is, therefore, rather convenient) it is notable that this remains only a representative model of the real-life scattering effect. The reality is more complex. The true cause of X-ray scattering is a result of the interactions with the periodic electron clouds found in crystals. The correlation between measured XRD data and a crystal structure is related by a Fourier transform of the so-called "reciprocal space". Despite this, Bragg's law and the associated theory is widely regarded as a good approximation of XRD effects.

3.5.1.2 Data collection and phase identification

For the XRD measurements described in this thesis a Bruker D2 Phaser Diffractometer (Co-source; $\lambda_{K\alpha}$=1.79 Å) was employed. The diffractometer, equipped with an auto sampler, enabled a quick and convenient approach to conduct measurements on multiple samples. Further, the use of Co-radiation helped to reduce the possibility of fluorescence effects on Co-, Fe- (and to a lesser extent) Ni-containing systems. Importantly, this helped to minimise background noise and, as a result, aided with the identification of phases. For phase identification, data was compared with the Powder Diffraction File (International Centre for Diffraction Data) database [289] using the DIFFRAC.EVA (*Bruker*) software [290].

3.5.2 Scanning Electron Microscopy

3.5.2.1 Background

Where necessary, Scanning Electron Microscopy (SEM) has been employed in order to analyse materials and substrates at high magnification (up to ~10,000x). Notably, SEM is universally employed in SOFC literature to explore the microstructure of cell components and materials and, as such, is an important tool in the SOFC researcher's arsenal. For the works described in this thesis, a Phillips XL30 ESEM FEG (Environmental Scanning Electron Microscope - Field Emission Gun) has been employed. Both powder-based samples as well as solid substrates have been analysed via SEM in this thesis.

Although SEM is a widely used technique amongst the scientific community, we will here briefly re-cap some key principles.

Whilst an optical microscope makes use of light and a series of focussing lenses to increase image magnification, SEM employs electrons and magnetic fields to achieve even greater magnification and resolving power. Electrons are first directed at the surface of samples with an electron gun. A detector, placed above the sample, is then used to develop an image of the surface based upon how the electrons are scattered. There are several ways in which electrons can interact with a sample surface and these may be appreciated in Figure 3.11a. So-called 'Secondary Electrons' and 'Backscattered electrons' are used to produce Secondary Electron Images (SEI) and Electron Backscattered Diffraction (EBSD/BSE) images. Secondary electrons are produced via surface and near-surface inelastic electron interactions and SEI is most typically utilised to obtain topographical images (see Figure 3.11b and c). EBSD imaging is typically preferred for showing comparisons between phases given that the scattering ability of a material is related to atomic number. For reasons that are apparent in Figure 3.11b and d, heavier atoms which back-scatter a greater number of electrons are shown up with brighter contrast in EBSD images.

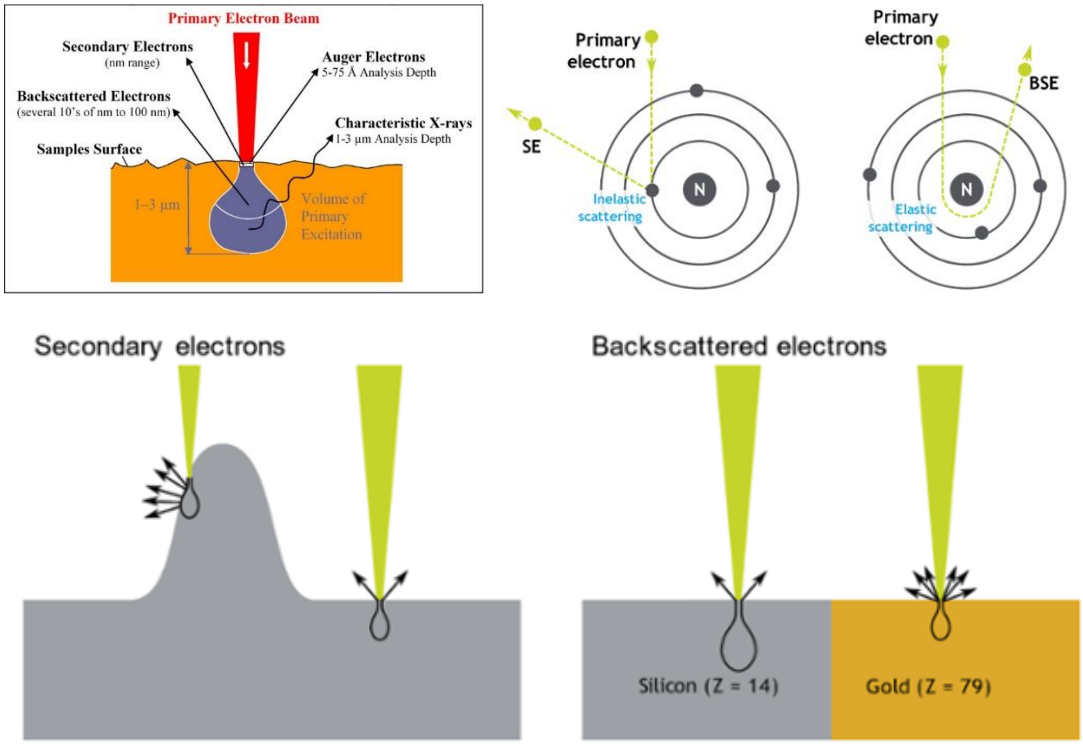


Figure 3.11 – (a, top left) Schematic illustrating electron interactions [291]*, (b, top right) schematic of electron interactions at atomic scale* [292] *(c, bottom left) schematic illustrating how SEI enables topographical information to be obtained* [292] *and (d, bottom right) a schematic illustrating the relative back- scattering abilities of two materials with different atomic numbers* [292]*.*

3.5.2.2 Data collection

For the SEM analysis of powdered samples, a small quantity of material was mounted onto double-sided-adhesive-carbon-stubs. This was to ensure the material was not liberated during the creation of the vacuum in the SEM and also to ensure a conductive pathway was available for the impinging electrons. This was deemed important to prevent charging effects and to prevent the destruction of the sample itself.

In the case of solid substrates, samples were mounted in epoxy and polished with 0.2 to 0.05 µm alumina suspension (*Buehler*) and polishing cloths. This was in order to provide an optimum image for analysis. After polishing, the samples were sputter-coated with carbon to prevent charging effects. Sputter-coating was found to be particularly important for these epoxy-mounted samples given the notable charging effects observed during analysis. This is a largely unsurprising observation given the poor conductivity of the polymer matrix. The use of carbon sputtering was selected due to the avoidance of K_α values of key elements.

4 Understanding the symmetrical cell performance of lanthanum nickelate electrodes: the effects of sintering temperature and Current Collector Layers

4.1 Overview of chapter

As described earlier in this thesis, a selection of lanthanum nickelate materials have been proposed for application in Solid Oxide Fuel Cells. More specifically, their use as oxygen electrodes has been the subject of some significant interest from a number of research groups [205,224,226,239,242,243,246,251,252,254,255,293–301]. However, despite many efforts to characterise these materials via a variety of different experimental approaches, their relative performance to one another and, moreover, to the state-of-the-art SOFC cathode material ($La_{1-y}Sr_yCo_{1-x}Fe_xO_3$) remains rather difficult to interpret based on the data within the literature. An attempt at conducting an analysis of this rich body of data was provided in Chapter 2 but it was noted that such an analysis is subject to many caveats. Significantly, and for each of the studied phases, a broad range of polarisation resistance values have been reported in the literature. This presents something of a problem for the SOFC community in defining the quality of these materials as oxygen electrodes.

The drawing of comparisons between experiments undertaken by different research groups is complicated by the many different approaches that are detailed in the various reports. To offer a more specific example, some researchers have described the use of Pt, Ag or Au-contact paste in testing methodologies [245,246,255,256,294,301]. These pastes, often used in conjunction with noble-metal meshes, are applied to the electrode surface in order to reduce the contact resistance between the electrodes and electrical connections to the potentiostat. In other publications (e.g., [233,247,293,297]), the use of such pastes is avoided and, in those instances, the contact is limited to a solid-to-solid interaction. Given that these two different approaches are capable of influencing electrode performance [302], this presents a problem in interpretation of results. Comparison of electrode performance across studies becomes difficult and the conclusions obscured (i.e. how much does the contacting technique 'skew' the result in the favour of a given material? Is the effect the

same in each instance? Or, more likely, is it also a function of the underlying material properties of the electrode?). The variation in testing set-ups (e.g. magnitude of compressive force placed on cell) and fabrication routes (e.g. sintering temperatures, deposition routes) makes it difficult to offer any robust assessment of the materials in question based on the literature data. In this chapter, therefore, we begin to offer a more comprehensive and a more balanced comparison between the materials in question. Further, we look to assess the effect of several variables in order to offer comment on how certain fabrication or testing approaches may influence results and, hence, the resulting conclusions that are drawn.

In addition to developing an understanding on the performance of the materials themselves, the breadth of phases considered in this study (from those with good electronic conductivity to those with good ionic conductivity) is of interest in understanding different approaches to SOFC testing and how conclusions may be influenced by the chosen methodology and materials. After a short discussion on the synthesis of the lanthanum nickelates, this chapter looks to explore the following key points:

- What is the performance of the lanthanum nickelates in relation to state-of-the-art oxygen electrode materials?
- Which of the studied La-Ni-O phases offer the most promise for further optimisation?
- What impact does the sintering temperature have on symmetrical cell performance and is this effect common across all the studied materials?
- How does the application of noble metal contact paste alter the performance of the underlying electrode? Do such effects offer any insight into how La-Ni-O electrodes may be best optimised? Does this reveal any key issues relating to SOFC testing?

4.2 Synthesis

Within the literature it is apparent that the effect of particle size and shape (i.e. of the starting materials) can influence the resultant performance of electrodes [262,303]. In turn, different synthesis routes are known to impact upon particle morphology [304]. In an acknowledgement of these

observations, an initial objective of this work was to identify a single process by which all the studied phases could be derived. This was in an attempt to synthesise materials with similar properties (i.e. particle size and morphology) and therefore offer a balanced comparison between the materials in question. Within the literature, there are several key methodologies employed in the synthesis of a number of different lanthanum nickelate phases. Authors have reported success in this regard via solid state [194,305,306], spray pyrolysis [307], microwave [308], and sol-gel approaches [309–311]. Here, two of these methodologies are considered for the synthesis of materials to be utilised in the remainder of the thesis.

4.2.1 Solid State Route

In order to assess the suitability of the solid-state route for the production of $La_2NiO_{4+\delta}$, $La_3Ni_2O_{7-\delta}$, $La_4Ni_3O_{10-\delta}$ and $LaNi_{0.6}Fe_{0.4}O_{3-\delta,}$ a series of synthesis experiments was performed employing several synthesis temperature (T=1000, 1100, 1200˚C). In each instance, and as described in Chapter 3, constituent metal oxides (La_2O_3, NiO, Fe_2O_3) were weighed, intimately mixed and then heated for up to 120 h to produce each phase. To aid the formation of the desired phases, several intermediate grinding steps (at t=12, 24 and 72 h) were performed. The importance of selecting the correct synthesis conditions can be appreciated in Figure 4.1 in which three separate attempts to synthesise $La_2NiO_{4+\delta}$ are shown. After heating at lower temperatures (T=1000, 1100˚C), the materials were found to remain as a mixture of reactants (e.g. La_2O_3 and NiO) and intermediate phases, even after 120 h of total annealing time. This likely pertains to the need to overcome diffusion related limitations via thermal effects. In the case of the highest temperature synthesis condition (T=1200˚C), a single-phase material was found to be achievable after just 24 h of heating. However, whilst the first order Ruddlesden-Popper phase could be readily synthesised via this route, the remaining phases of interest were found to be far more difficult to produce. This is typified in Figure 4.2 for the $La_3Ni_2O_{7-\delta}$ phase (the remaining data are shown in Appendix E). The difficulty in synthesising the higher-order Ruddlesden-Popper phases is an observation also reported by Voronin et al. [312]. Takahasi et al. [207], on the other hand, described better success in producing $La_3Ni_2O_{7-\delta}$ and $La_4Ni_3O_{10-\delta}$ via the solid

state route. In that instance, the authors employed heating periods of up to 6 days, using relatively low annealing temperatures (<1100˚C). However, even under such conditions, evidence of minor impurities was noted. The difficulties found in obtaining these materials (in this study and the literature) likely relates to (a) the aforementioned need to overcome diffusion-related limitations via high temperatures, and (b) the favourable thermodynamic stability of Ni^{2+} relative to Ni^{3+} (and hence the relative favourability of $La_2NiO_{4+\delta}$ formation) at temperatures in excess of 900 to 1000˚C [205,309]. Given the desire to find a single route by which all materials could be prepared, an alternative approach was pursued that could enable lower temperature synthesis.

4.2.2 Pechini Route

4.2.2.1 Phase analysis

By overcoming diffusion-related issues observed in the reaction of solid-state materials, the employment of sol-gel synthesis routes is capable of reducing the energy intensity that relates to the production of complex metal oxides. More specifically, this can reduce the synthesis temperature and the number of heating steps required. The Pechini process (described in Chapter 3), in addition to other variants of the sol-gel technique, has been employed elsewhere in the literature (e.g. [206,313]) to synthesise lanthanum nickelate materials, most commonly $La_2NiO_{4+\delta}$ and $LaNi_{0.6}Fe_{0.4}O_{3-\delta}$. In this work, and for each phase, a polymeric gel was formed via a dissolution of metal nitrate powders in deionised water and the further addition of citric acid and ethylene glycol (see Chapter 3). After heating at 350˚C the resulting ash-like precursor was annealed at higher temperature to achieve the desired phase. For $La_2NiO_{4+\delta}$ and $LaNi_{0.6}Fe_{0.4}O_{3-\delta}$ the pre-cursor was heated to 1000˚C and, for the $La_3Ni_2O_{7-\delta}$ and $La_4Ni_3O_{10-\delta}$ phases, to 1150˚C. A number of batches of each material were synthesised, with XRD analysis performed on each batch to confirm the correct phase was produced. Smaller batches were then combined into a larger sample (~40g), ball-milled and sieved using a 25 micron mesh. The final samples were then analysed via XRD. In Figure 4.3 the raw data are compared with exemplary data from the ICSD database [314]. The success of this route in preparing the required phases is evident from this comparison.

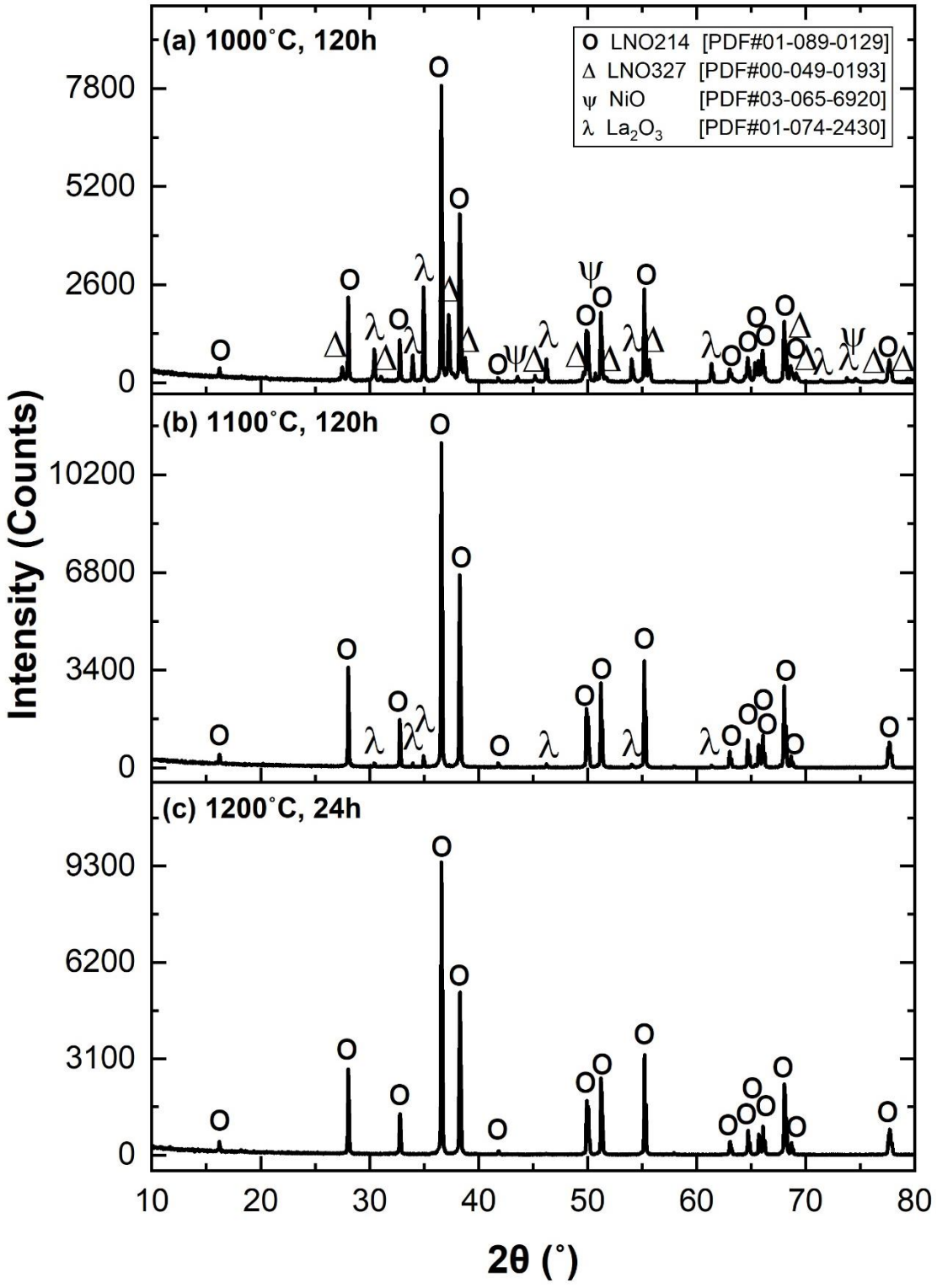


Figure 4.1 – Attempts at solid state synthesis of $La_2NiO_{4+\delta}$ under different annealing conditions; (a) 120h total anneal at 1000˚C, (b) 120 h total anneal at 1100˚C, (c) 24 h at 1200˚C.

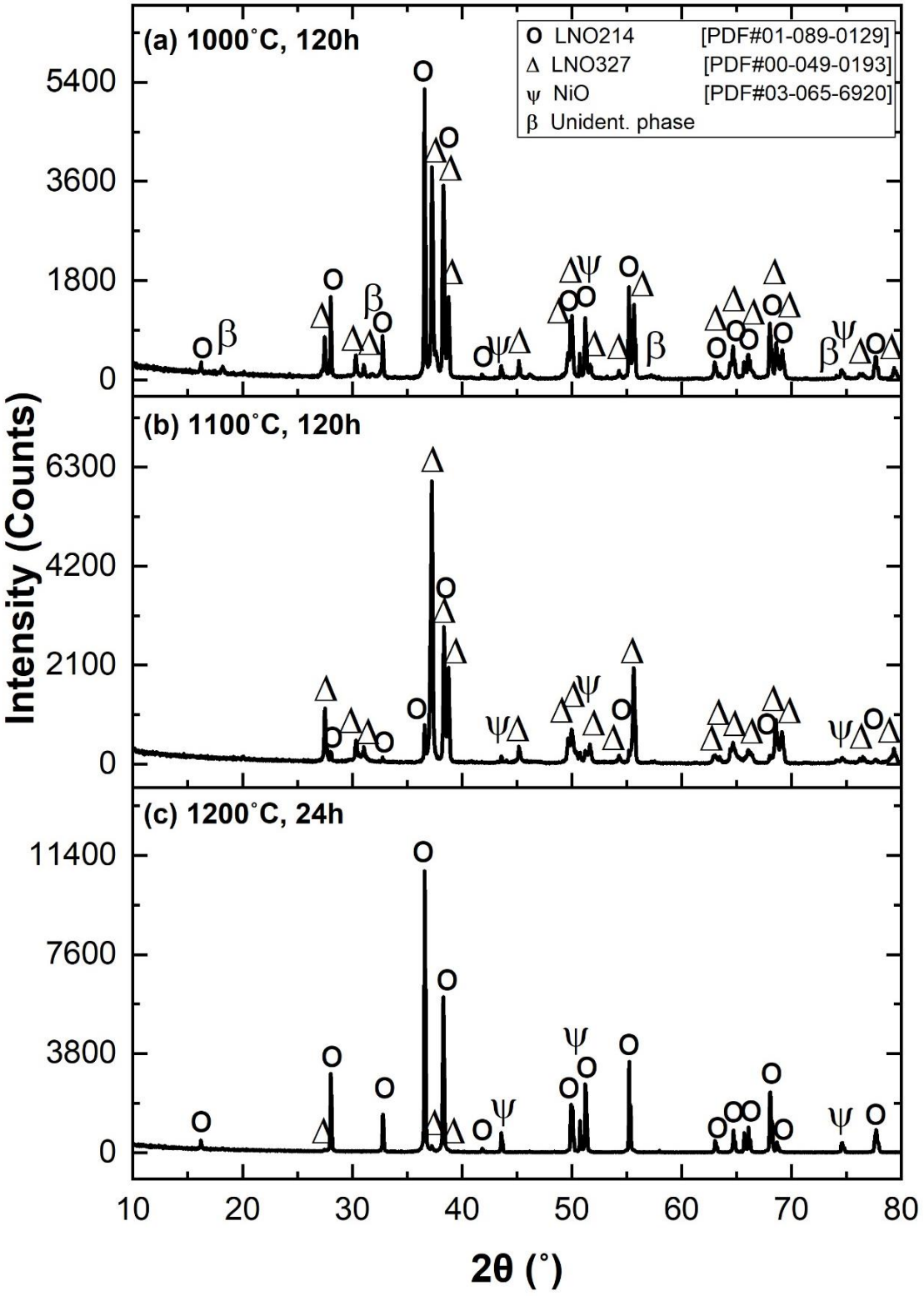


Figure 4.2 – Unsuccessful solid state synthesis of $La_3Ni_2O_{7-\delta}$ under different annealing conditions; (a) 120 h total anneal at 1000˚C, (b) 120 h total anneal at 1100˚C, (c) 24 h at 1200˚C.

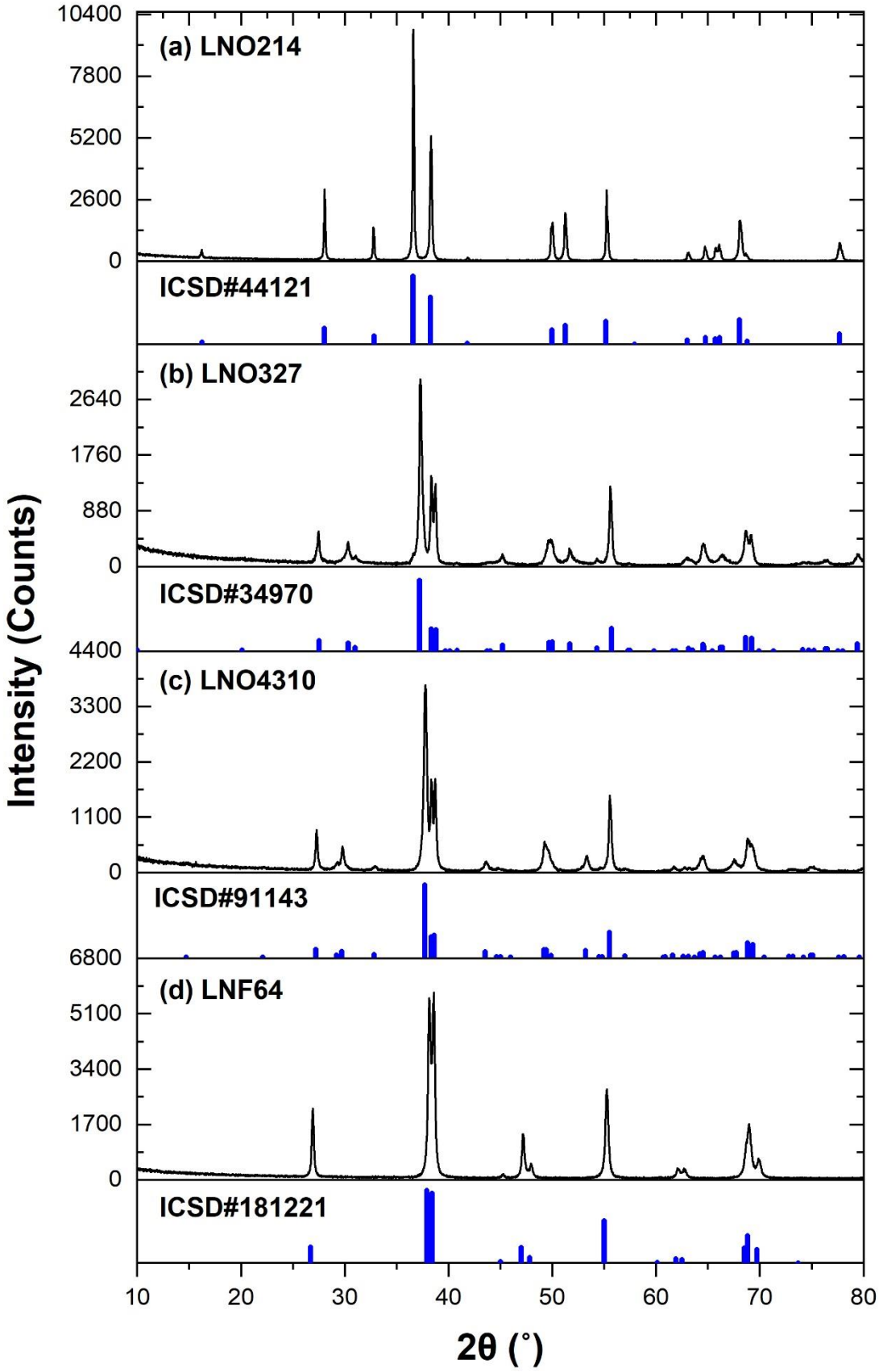


Figure 4.3 – XRD data taken from samples prepared by the Pechini route; (a) $La_2NiO_{4+\delta}$, (b) $La_3Ni_2O_{7-\delta}$, (c) $La_4Ni_3O_{10-\delta}$ and (d) $LaNi_{0.6}Fe_{0.4}O_{3-\delta}$. Comparisons with data from the ICSD database are shown beneath each spectrum. A version of this figure is intended for publication [315].

4.2.2.2 Particle Morphology

To analyse particle morphology, powdered samples were mounted onto adhesive carbon tabs and analysed via Scanning Electron Microscopy (SEM). Images of the $La_2NiO_{4+\delta}$ and commercial $La_{0.6}Sr_{0.4}Co_{0.2}Fe_{0.8}O_{3-\delta}$ samples are shown in Figure 4.4a and Figure 4.4b, respectively. This analysis was complicated by clumping of the materials, which meant a more quantitative study was difficult[16]. Nevertheless, it was apparent that particles that were prepared by the Pechini route (and subsequently milled and sieved) were mostly of irregular shape (<2 µm). The commercial material (LSCF6428) was characterised by more regular, spherical particles. Given that this has the potential to impact both the fabrication and performance of electrodes, an LSCF6428 sample was also synthesised via the Pechini route (XRD results of this synthesis route are shown in Appendix E) with a view to assessing the performance of this material in parallel to that of the commercial one.

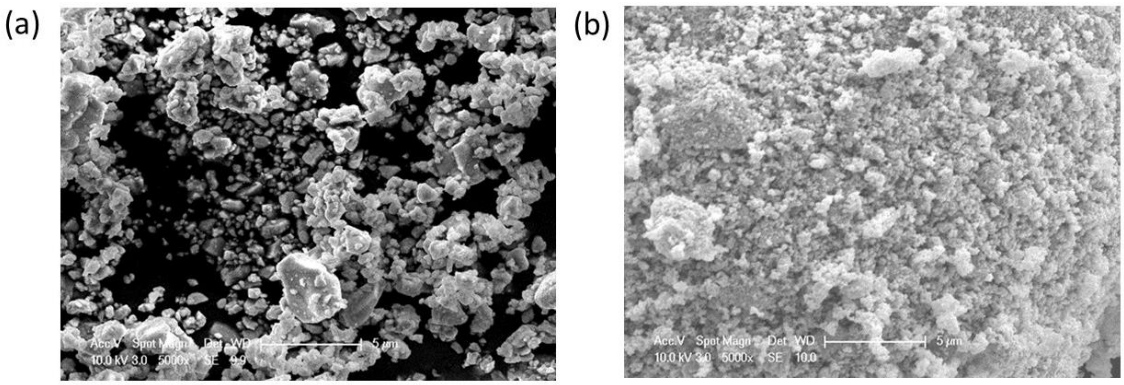


Figure 4.4 – SEM images of (a) $La_2NiO_{4+\delta}$ powder synthesised via the Pechini route and (b) commercial LSCF6428 powder (Praxair).

4.3 Symmetrical Cell Performance

A common approach to assessing and optimising oxygen electrode materials is to perform so-called "*symmetrical cell*" tests. This involves the deposition of the same electrode materials both sides of an electrolyte substrate and then the subsequent acquisition of EIS measurements under what is in-effect an OCV-like condition (i.e. i≈0 Acm^{-2}). In this instance, the aim is to obtain information about the

[16] Attempts to conduct quantitative analysis using both laser particle size analyser and SEM image processing techniques were found to be difficult – this was believed to be due to the clumping of particles. Attempts to overcome this were trialled (e.g. use of dispersants, drop-casting) but did not alleviate the issue.

oxygen reduction process for the electrode in question. The key benefit of such experiments is the ability to remove the contribution of the anode and to, in-effect, isolate the performance of the oxygen electrode. The main disadvantage, meanwhile, is that such tests are incapable of offering any significant information on the behaviour of electrodes under polarisation (i.e. i>0 Acm^{-2}). The expectation, therefore, is that the insight offered is limited to that seen under equilibrium conditions (i.e. in the initial 'activation' region of the polarisation curve). Nevertheless, symmetrical cell tests are an important aspect of electrode performance testing and, as described earlier, are widely employed in the literature. The SOFC community [259,316] have identified these tests as a recommended component of electrode testing. This technique is employed here to offer insight into the performance of the different electrode materials and to understand how sintering temperature and contact layers impact on such performance. Key terms that are referred to in the following discussion are the so-called ohmic resistance (R_o) and polarisation resistance (R_{pol}). As described in Chapter 2 (see Figure 2.9), the polarisation resistance is defined as the difference between the total impedance (Z_{DC}) and ohmic contribution (and, in the case of a symmetrical cell, commonly divided by two to account for the two electrodes). Each of these metrics is normalised to the area of the electrode as is convention.

4.3.1 Design of experiments

After the aforementioned synthesis processes, an ink of each sample was obtained via mixture with a commercial, terpineol-based ink vehicle. Symmetrical cells were then prepared by brush-painting each of these inks on to commercial electrolyte coupons (GDC | YSZ | GDC). For initial testing, all samples were sintered at 1000˚C for 4 hours. EIS measurements were then performed on the symmetrical cells in static air, at operating temperatures (T_{Op}) between 600 and 800˚C (results described in section 4.3.2). For this initial work, electrical contact was provided via an Au-mesh which was placed in contact with the underlying electrode material. An alumina weight (175 g) was placed on top of the electrode-mesh-assembly to ensure good contact between these components. At this stage, no additional contact paste (e.g. Pt, Au, Ag-paste) was employed so as to avoid any 'artificial enhancement' of the electrode. This does, however, result in electron transfer being limited to a number of contact points

where the mesh and electrode material touch. The exact effect of this is, at this stage, an unknown. One point to consider is that different contact configurations may impact different phases to different extents (e.g. a greater effect may be seen for those materials with poorer electronic conductivity and/or larger particle sizes). This is considered further in Section 4.3.3.

A further parameter of interest in exploring the performance of electrodes, is the effect of sintering temperatures. This is explored in Section 4.3.4. In the case of $La_2NiO_{4+\delta}$, and in addition to the earlier described condition (T_{Sint}=1000˚C), electrodes were sintered at 1050, 1100 and 1150˚C. Repeat tests were conducted at the temperature extremes (i.e. 1000˚C and 1150˚C) in order to confirm observations. Subsequent materials ($La_3Ni_2O_{7-\delta}$, $La_4Ni_3O_{10-\delta}$, $LaNi_{0.6}Fe_{0.4}O_{3-\delta}$, $La_{0.6}Sr_{0.4}Co_{0.2}Fe_{0.8}O_{3-\delta}$) were then tested at these temperature extremes, with repeats conducted for each sintering condition. An overview of the samples tested in this work is shown in Table 4.1.

Table 4.1 - Overview of electrodes prepared for the symmetrical cell testing detailed in this chapter

✓ - One symmetrical cell test conducted (No Au contact paste)

$✓^{+Au}$ - One test conducted without Au contact paste and then tested again with Au-paste

	Electrode Sintering Temperature			
Phases	**1000˚C**	**1050˚C**	**1100˚C**	**1150˚C**
$La_2NiO_{4+\delta}$	$✓✓✓^{+Au}$	✓	✓	$✓✓✓^{+Au}$
$La_3Ni_2O_{7-\delta}$	$✓✓✓^{+Au}$	-	-	$✓✓✓^{+Au}$
$La_4Ni_3O_{10-\delta}$	$✓✓✓^{+Au}$	-	-	$✓✓✓^{+Au}$
$LaNi_{0.6}Fe_{0.4}O_{3-\delta}$	$✓✓✓^{+Au}$	-	-	$✓✓✓^{+Au}$
$La_{0.6}Sr_{0.4}Co_{0.2}Fe_{0.8}O_{3-\delta}$ (commercial)	$✓✓✓^{+Au}$	-	-	$✓✓✓^{+Au}$
$La_{0.6}Sr_{0.4}Co_{0.2}Fe_{0.8}O_{3-\delta}$ (synthesised)	✓✓✓	-	-	✓✓✓

4.3.2 Comparison of Performance

Nyquist plots taken from the initial symmetrical cell testing at sintering temperature T_{Sint}=1000˚C can be observed in Figure 4.5. Here, the median[17] data are shown for each phase. A complete set of data (covering all repeat tests) can be found in Appendix F. In each instance, and in order to aid in the identification of different contributions, the data are presented on an equally-scaled axis as suggested in reference [259]. For the sake of comparison, the ohmic contribution has been removed from these plots (i.e. setting R_o=0 Ωcm^2) as is convention. The EIS data were generally observed to be of good quality, although some noise was evident in the lower frequency range. This appeared to be particularly apparent for those materials with poorer electronic conductivity (LNO214, LNO327), but interestingly also for the commercial LSCF6428 phase. The quality of the data was also validated from the Kramers-Kronig (K-K) analysis (see Figure 4.6); residual values were found to be low in each case indicating the data complied with the K-K laws. A summary and comparison of these results is shown in Figure 4.7. As is exposed, each material shows different behaviour which is now considered.

Polarisation resistance: As has been alluded to earlier in this thesis, a key focus of many oxygen electrode studies is on the polarisation resistance values of symmetrical cells. Figure 4.7b shows the R_{pol} values of samples sintered at 1000˚C, represented as Arrhenius plots. The error bars represent the upper and lower results from the repeat testing. It is notable from these results that the commercial LSCF6428 material offers the most favourable performance of all the studied materials in this particular comparison of R_{pol} values. Whilst the synthesised LSCF6428 material ("LSCF6428-P") is inferior to the commercial material (likely due to particle morphology factors) it outperforms the lanthanum nickelates synthesised via the same route. This appears to indicate that the lanthanum nickelate phases are incapable of matching the performance of the state-of-the-art LSCF6428. This is consistent with conclusions drawn in Chapter 2 and appears particularly apparent at the lower operating temperatures. However, it is also notable that the nickelate phases display a very broad set

[17] In this case we define the 'median data' to be that associated with the median R_{pol} value of the three repeat tests. The #number in each plot describes the test/cell number (1 to 3) with which the median was observed.

of behaviours, with LNO327 displaying the lowest polarisation of the nickelates. At higher temperatures (800˚C), LNF64 is also competitive.

An interesting observation from Figure 4.7b is the apparent divergence from Arrhenius-type behaviours for the commercial LSCF6428 material. There appears to be two specific behaviours (or gradients) on the Arrhenius plot for this material, suggesting a change in the rate-limiting step of the measurement. This can be understood by consideration of the Nyquist plot for this material (Figure 4.5f). As is shown in the inset, the EIS spectra is comprised of two separate arcs or contributions. These can be thought of as two separate processes with different time constants ($\tau=RC$). For discussion purposes these processes will be described as HF (high frequency) and LF (low frequency) contributions. The LF contribution can be observed at all temperatures for the commercial LSCF6428 material and remains of a similar size under all measured conditions. This suggests that this contribution is not heavily influenced by temperature, potentially alluding to a diffusion-related process. In contrast, the HF contribution is significantly reduced with increasing temperature, likely suggesting an electrochemical process. The relative size of these contributions to one another is dramatically changed between the operating temperatures of 600 and 800˚C. This causes the noted behaviour in the Arrhenius plot. Further, this LF process can also be seen for the other electrode materials. However, due to the much larger impedances, this only becomes apparent at higher temperatures (see the inset plots in Figure 4.5). Given these observations, this process is likely to be unrelated to electrochemical behaviour of the materials and more due to some diffusion-related effect. Indeed, consideration of the literature reveals similar observations which are also placed down to gas conversion [317]. Ideally, this contribution could be removed for an assessment of the electrodes (given this is not an effect influenced by the materials themselves) but this became difficult in many instances.

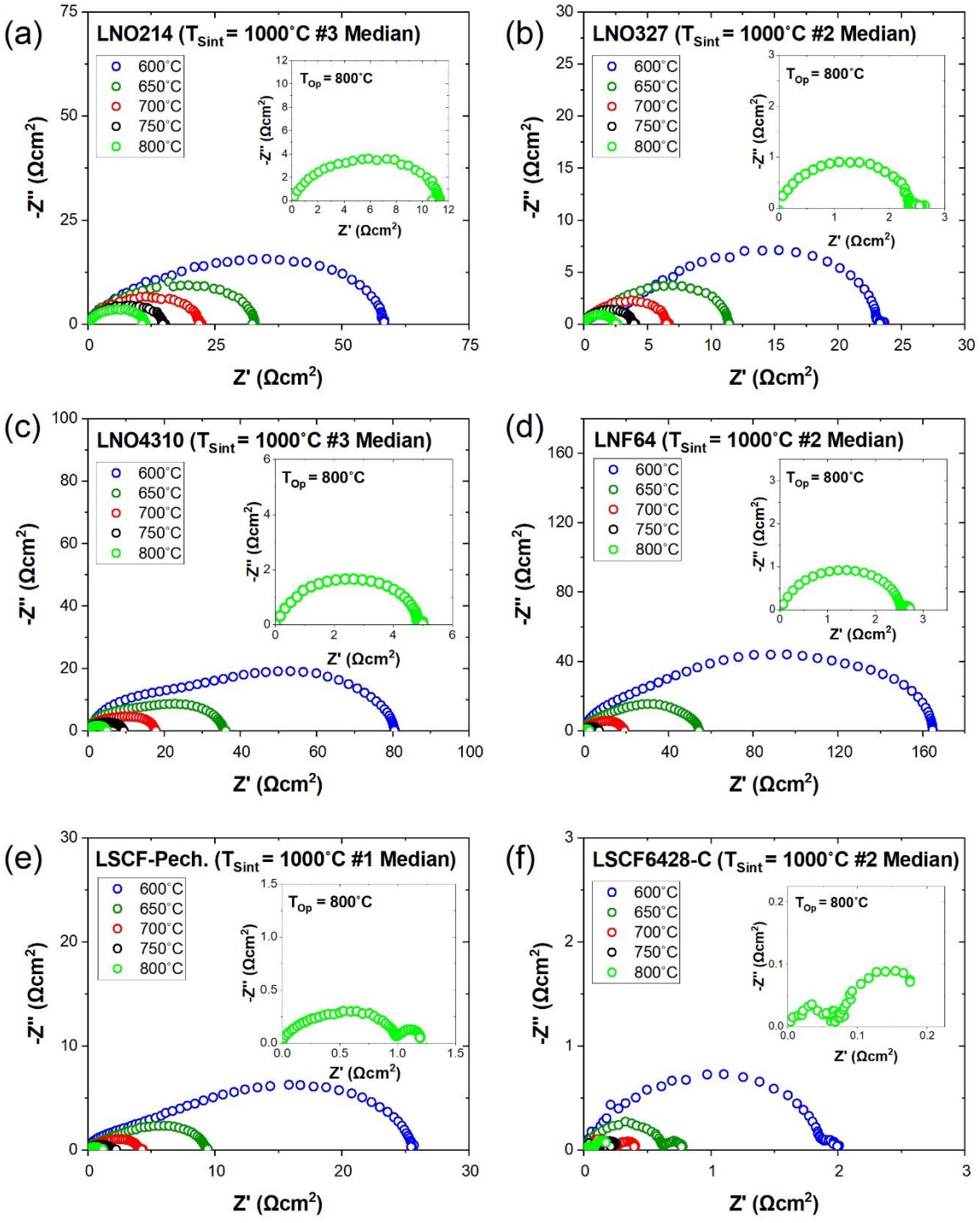


Figure 4.5 – Nyquist plots from symmetrical cell tests; (a) LNO214, (b) LNO327, (c) LNO4310, (d) LNF64, (e) synthesised LSCF6428 (LSCF-Pech), (f) commercial (Praxair) LSCF6428 (LSCF6428-C). Number next to '#' denotes the test/cell number from which the result is shown (i.e. #2=Cell Number 2 of the 3 repeat tests). The displaced result corresponds to the median R_{pol} result in each instance. See Appendix F for full set of data.

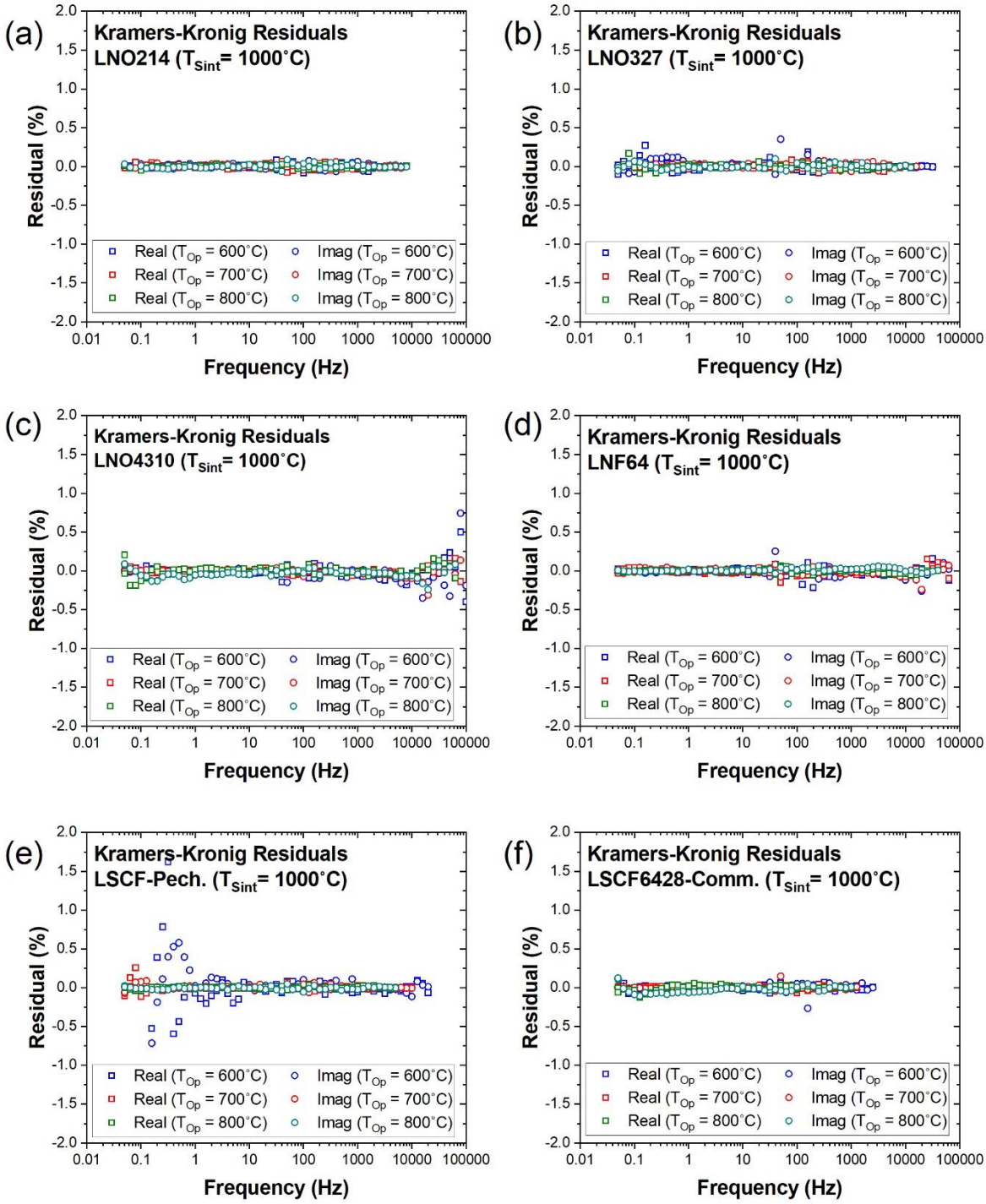


Figure 4.6 – Kramers-Kronig residuals of the 'median' values of symmetrical cell tests; (a) LNO214, (b) LNO327, (c) LNO4310, (d) LNF64, (e) synthesised LSCF6428 (LSCF-Pech), (f) commercial (Praxair) LSCF6428 (LSCF6428-C).

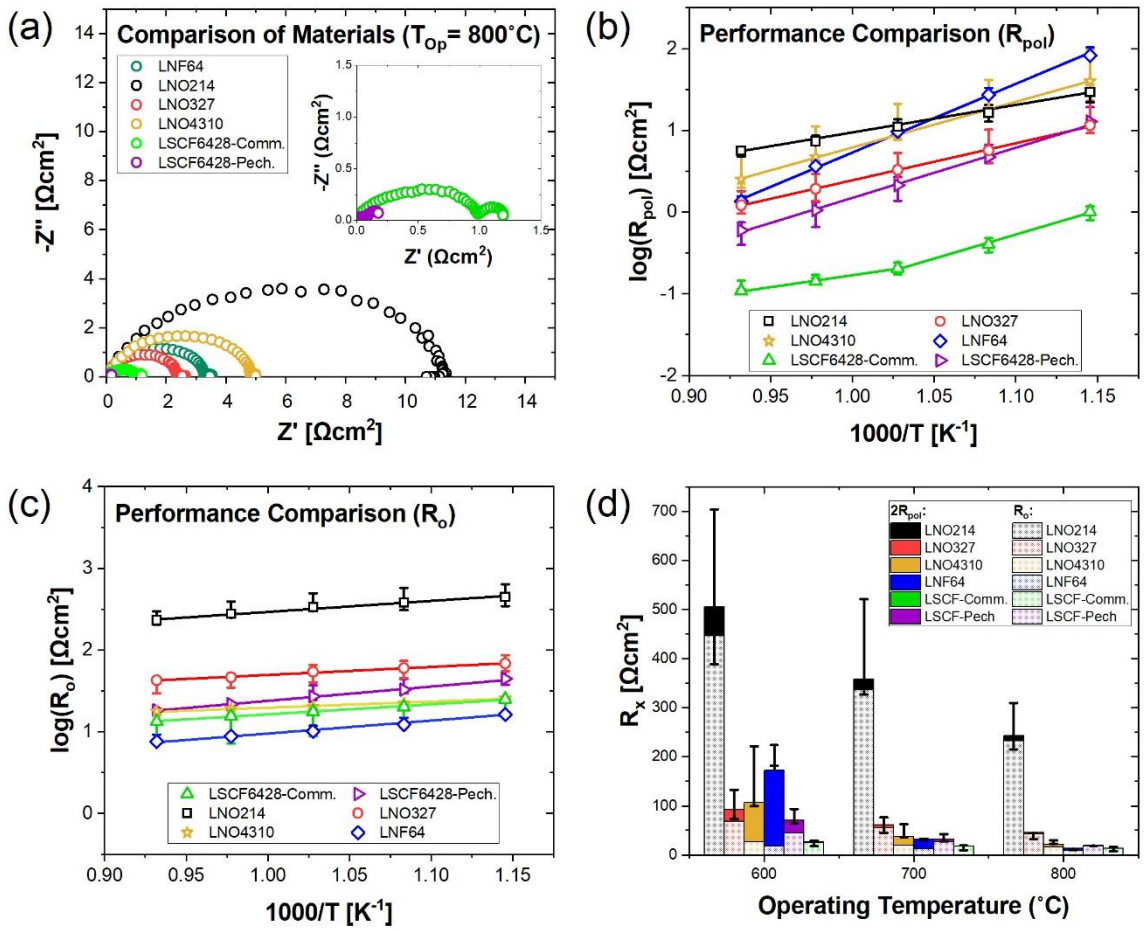


Figure 4.7 - Comparison of results from initial symmetrical cell tests (T_{Sint}=1000˚C); (a) Nyquist plot for data recorded at 800˚C, (b) Arrhenius plot of polarisation resistance (R_{pol}), (c) Arrhenius plot (600-800˚C; 50˚C intervals) of ohmic resistance (R_o) and (d) bar chart showing the total impedance and the relative contributions of R_o and R_{pol} [error bars represent the upper and lower values from repeat testing].

Ohmic resistance: Within the literature, there is often very little consideration of the ohmic resistance values of symmetrical cells. This metric, it is often assumed, is predominantly associated with electrolyte losses and also the wiring configurations employed in testing set-ups. As a result of this, a number of authors overlook this value in favour of R_{pol}. However, an interesting observation in the data studied here is the dramatic difference in R_o values between samples (Figure 4.7c). In some cases there is more than an order of magnitude difference between samples. Given that identical commercial electrolyte substrates are employed in each case, it is evident that this difference is related to the electrode material. Indeed, a close study of Figure 4.7c describes behaviours that may be expected based on the conductivity of these phases (see Chapter 2). $La_2NiO_{4+\delta}$, with the lowest electronic conductivity of all of the studied materials, demonstrates the highest R_o values. R_o values

decrease for the higher order Ruddlesden-Popper phases and are shown to be lowest for the perovskite phase LNF64 (i.e. R_o decreases in the order LNO214 > LNO327 > LNO4310 > LNF64). In fact, by this metric, LNF64 out-performs both the commercial and synthesised LSCF6428 phases thus supporting its potential as a contact material.

The significance of the observations on ohmic resistance can be appreciated in Figure 4.7d in which the **total area specific resistance** (Z_{DC}) of the symmetrical cell samples is shown. In many cases, R_o dominates the total resistance of the samples. Importantly, this affects the conclusions drawn from the testing. For instance, $La_2NiO_{4+\delta}$ might be considered to be one of the better performing lanthanum nickelate materials at 600˚C when considering only R_{pol} values. However, it is clearly seen that the very large ohmic losses lead to the highest overall resistances. LNF64, meanwhile, offers comparable Z_{DC} values to LSCF6428 between 700 and 800˚C. Given that cell performance is ultimately determined by all resistive losses, an argument could be made that the most appropriate term for authors to use is the Z_{DC} value rather than R_{pol} that is commonly referenced in studies. Further analysis on the relative performance of the materials is offered in Section 4.5.

4.3.3 Effect of precious metal contact layer

As was noted in the previous section, the ohmic contribution of a sample can be significant and was observed to be heavily dependent on the electrode material. In some instances, R_o was found to dominate the overall EIS measurement. To further explore this, and to also consider the influence of different testing approaches employed in the literature, an analysis of the effects of an additional Au-current contacting layer (Au-CCL) is now provided. To conduct this assessment, a commercial Au-contact ink (*Fuel Cell Materials*) was applied to samples tested as part of the work described in 4.3.2. These cells were then tested once more, this time with the newly applied Au-CCL. This approach helped to directly identify the effect of conductive layers on the performance of an underlying electrode material. The results of these tests and comparison with cells without the Au-CCL layer are

summarised in Figure 4.8 and Figure 4.9. Additional results for symmetrical cell tests sintered at 1150˚C can be seen in Appendix F.

A number of key points should be noted when discussing the effects of the Au-CCL on the performance of the symmetrical cells. Firstly, the quality of the data was improved; the noise that was evident for samples without the Au-CCL was almost entirely eradicated. The change in the electrode performance, meanwhile, offered some rather interesting conclusions. In all cases, the ohmic resistance values were reduced (shown in the Arrhenius plots in Figure 4.8 and Figure 4.9). Given the excellent electronic conductivity of Au, this is mostly an unsurprising finding. It is notable that the improvement was, understandably, most prominent for the electrode materials with inferior conductivity properties (i.e. LNO214). However, what is perhaps a little more surprising, is the effect that the Au-CCL has on the polarisation performance of each of the materials, given that R_{pol} is not commonly associated with contact resistance. In the case of LNO214, the change in R_{pol} is remarkable (a reduction in an order of magnitude at 800˚C). In the case of the perovskite materials LSCF6428 and LNF64 (Figure 4.9), on the other hand, the change in R_{pol} is minimal. Observation of the Ruddlesden-Popper phases (Figure 4.8) shows that the effect on R_{pol} increases with increasing 'n' (or, more pertinently, increasing electronic conductivity). This observation can be explained by consideration of the oxygen reduction reaction:

$$\frac{1}{2}O_2 + 2e^- \rightarrow O^{2-}$$

In the case of poorer electronic conductors, the rate-limiting reaction is likely to be determined by electron transport, whereas in other materials it is more likely determined by oxygen transport phenomena. These findings are significant for several reasons:

1. The impact of precious metal current contacting layers can have a significant effect on performance but this is also very dependent on the underlying electrode material; this has implications with respect to comparing electrodes between studies where different contact configurations were employed.

2. The evidence from the two testing approaches (with and without Au-CCL) suggests that different conclusions may be drawn when conducting tests between dissimilar materials (e.g., consider that LNO327 outperformed LNO214 when no Au-CCL was applied whereas the reverse case was seen when an Au-CCL was employed). This creates a problem for identifying superior materials (i.e. which is the "correct" benchmark when assessing materials?).
3. The dramatic improvement in performance shown from the LNO214 suggests that this particular material can be improved using 'layered' electrode structures, e.g. a layer optimised for O_2 exchange in contact with the electrolyte and a layer optimised for electron exchange adjacent to the current collector. This need not necessarily be a noble-metal material and could, instead, be a layer of LNF64 which has been shown earlier to offer similar performance to that of LSCF.

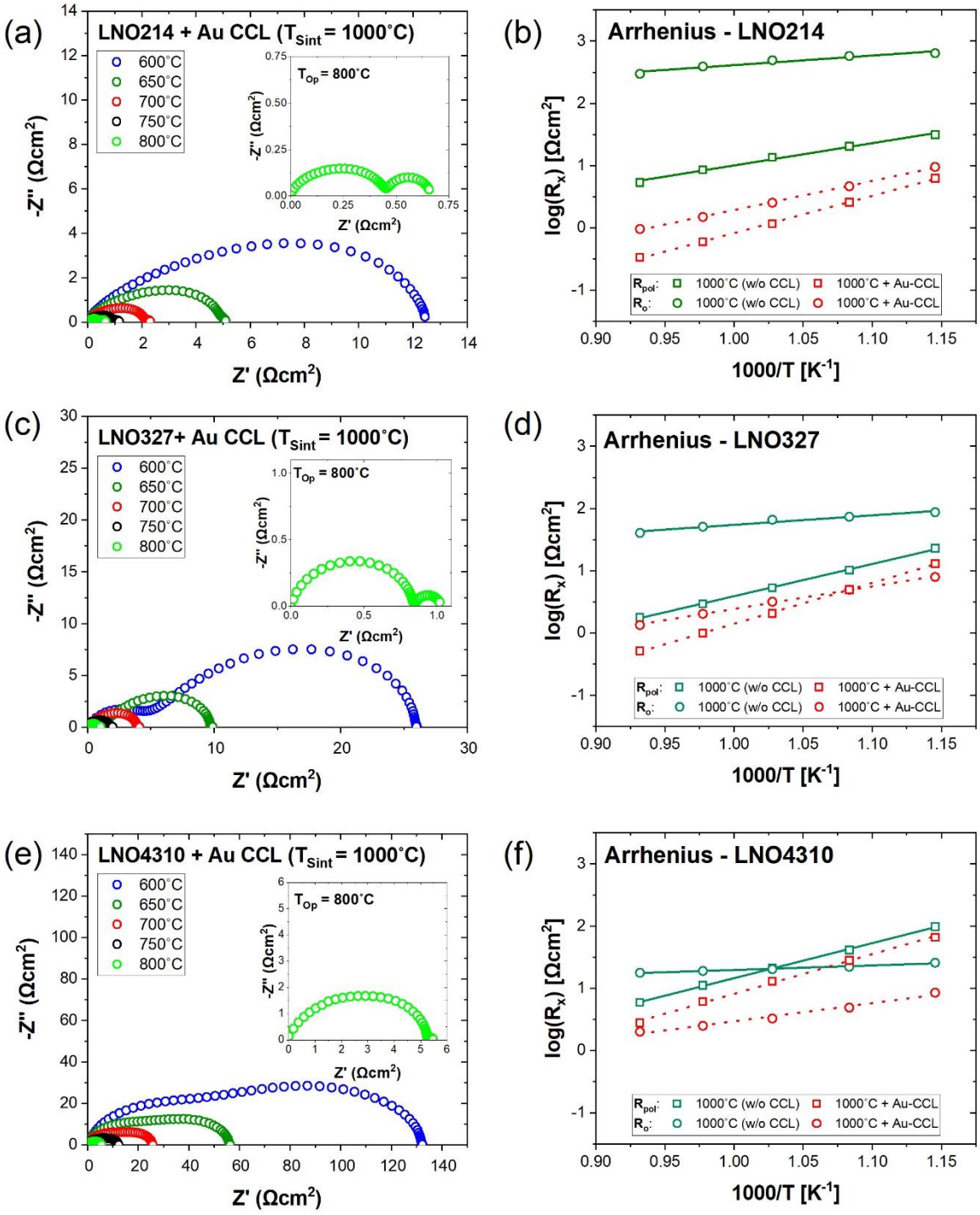


Figure 4.8 – Effect of Au-paste on symmetrical cell performance of Ruddlesden-Popper phases $La_2NiO_{4+\delta}$, $La_3Ni_2O_{7-\delta}$ and $La_4Ni_3O_{10-\delta}$; (a, c, e) Nyquist plots, (b, d, f) Arrhenius plots (600-800˚C; 50˚C intervals) showing comparison between the symmetrical cell with and without the Au-Current Contact Layer (Au CCL). A version of this figure is intended for publication [315].

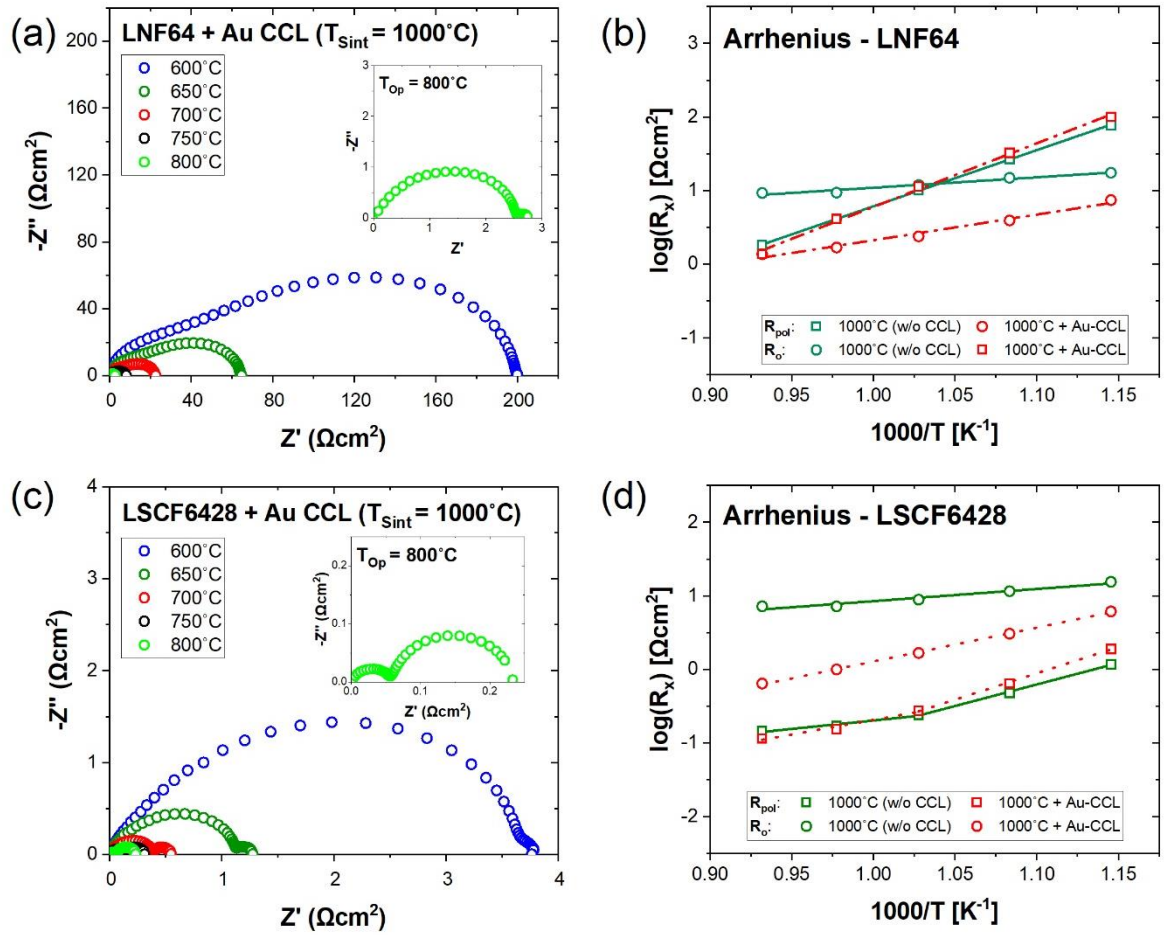


Figure 4.9 - Effect of Au-paste on symmetrical cell performance of perovskite phases LNF64 and commercial LSCF6428; (a, c) Nyquist plots, (b, d) Arrhenius plots (600-800˚C; 50˚C intervals) showing comparison between the symmetrical cell with and without the Au-Current Contact Layer (Au-CCL).

4.3.4 Effect of sintering temperatures

A notable feature of studies from the literature was that a range of electrode sintering temperatures has been employed for the fabrication of samples. Typically these temperatures range from 1000-1150˚C. However, there is only relatively limited work studying the role that different sintering temperatures have on the performance of the various lanthanum nickelate phases. Specifically, we are unaware of any work comparing these effects across different electrode materials. Here, an analysis was conducted in order to identify the role of sintering temperature in developing high-performing electrodes and to understand how these behaviours compare with state-of-the-art materials. In the case of $La_2NiO_{4+\delta}$, an increase in sintering temperature was shown to significantly improve the electrode performance (Figure 4.10). The most evident improvement observed was with

respect to the ohmic resistance (from a median value of 231.98 Ωcm^2 to 49.09 Ωcm^2 at an operating temperature of 800˚C). Here, and as was also evident in Section 4.3.3, an improvement in the ohmic contribution was found to correlate with a reduction in polarisation resistance. At an operating temperature of 800˚C, R_{pol} was reduced from a median value of 5.35 Ωcm^2 to 0.61 Ωcm^2 by an increase in T_{Sint}.

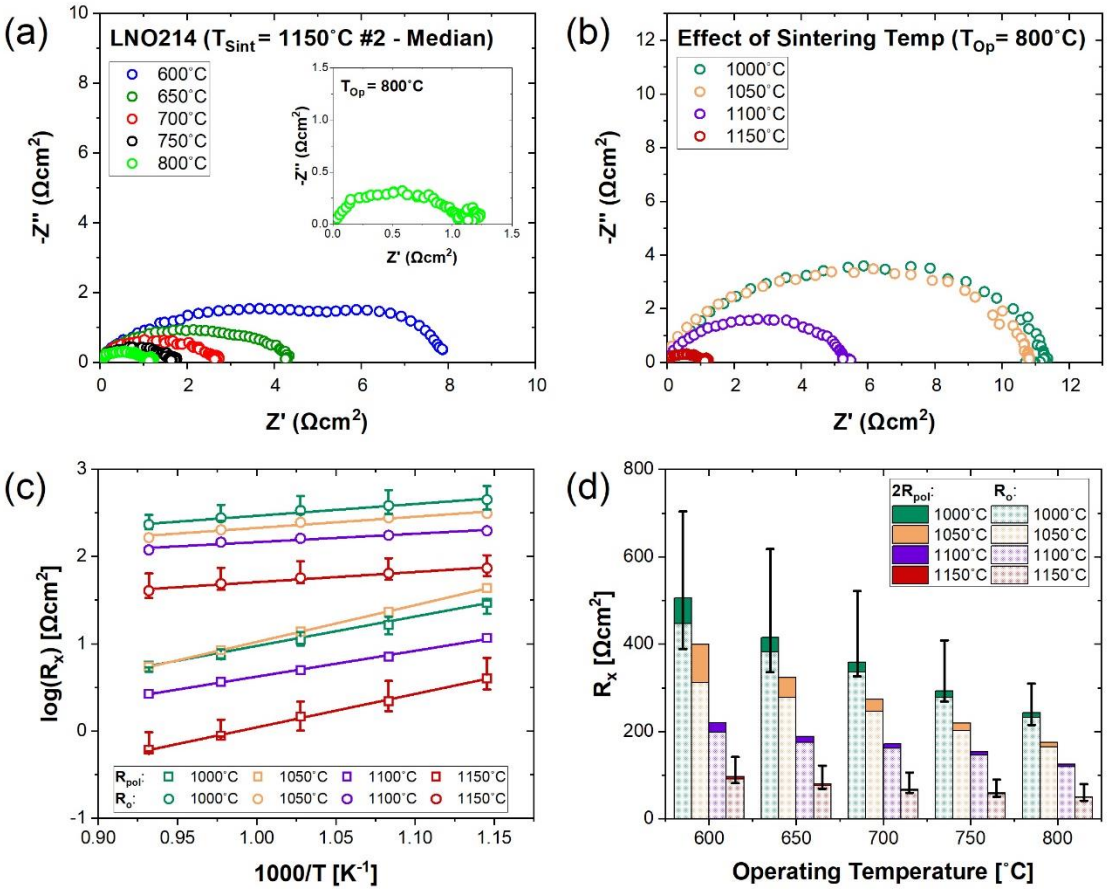


Figure 4.10 - Effect of sintering temperature on the performance of $La_2NiO_{4+\delta}$ electrodes in symmetrical cell configuration. (a) Nyquist plots of electrode sintered at 1150˚C, (b) comparison of Nyquist plots recorded at an operating temperature of 800˚C, (c) Arrhenius plot (600-800˚C; 50˚C intervals) showing R_{pol} (squares) and R_o (circles) and (d) bar chart showing Total impedance value and relative contribution of R_o and R_{pol}. [Note: error bars represent the upper and lower values from repeat testing]. A version of this figure is intended for publication [315].

Based on observations from the literature review, two *plausible* causes/theories for the improvements observed can be proposed:

1. An improved electrode morphology (e.g. improved particle connectivity or electrode-electrolyte adhesion) leading to a reduction in ion and electron transport-related bottlenecks at grain boundaries.
2. Formation of secondary phases with favourable electrode properties (e.g. improved conductivity or catalytic activity).

In order to investigate which of these effects (if any) drive the improved electrode performance, further analysis is provided in Section 4.4 of this chapter. For the remaining lanthanum nickelate materials, meanwhile, the effects of sintering temperature are summarised in Figure 4.11. It can be noted that the performance of these phases could be improved throughout by elevated sintering temperatures. However, with respect to the effect on R_{pol}, this becomes marginal compared to $La_2NiO_{4+\delta}$. Nevertheless, in all cases considered thus far, the better electrode performance is generally achieved at a sintering temperature of 1150˚C. In the case of the commercial LSCF6428 material (Figure 4.12a and b), it is interesting to see a quite different behaviour, though. In that instance, a decline in the electrode performance is noted (i.e. Z_{DC} increases) with increasing sintering temperature. This is possibly driven by a densification of the cathode and a subsequent loss of porosity or catalytic area. In any case, comparison of this effect and that seen for the lanthanum nickelates indicates some phase-specific characteristics (i.e. different optimum sintering temperatures). However, it is seen that the same approach for the Pechini-synthesised LSCF6428 is much less supportive of this theory, suggesting that the behaviour observed is not simply phase-specific but also related to the morphology of the particles. In any case, however, it seems apparent that there is *some* phase-specific effect (i.e. the improvement in performance that is achievable from higher sintering temperatures is partially phase-specific). This is evidenced by the strong impact seen on the LNO214 phase and the much less pronounced impact on the Pechini-synthesised LSCF6428.

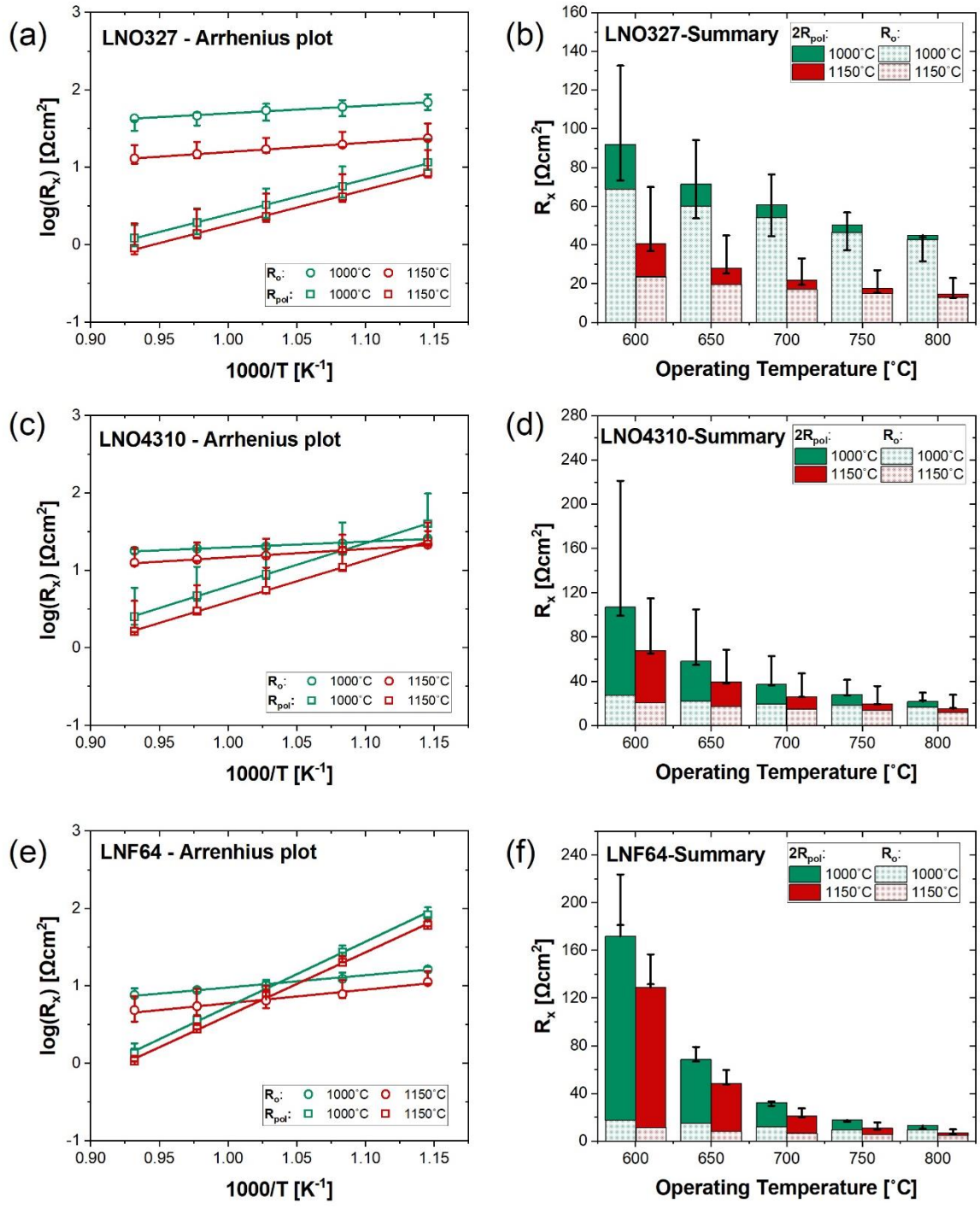


Figure 4.11 – Arrhenius plots(600-800˚C; 50˚C intervals) demonstrating the effect of sintering temperature on (a, b) $La_3Ni_2O_{7-\delta}$, (c, d) $La_4Ni_3O_{10-\delta}$, (e, f) $LaNi_{0.6}Fe_{0.4}O_{3-\delta}$. Left hand panels display Arrhenius plots for R_o and R_{pol}. Right-hand panels display the total impedance values (comprised of R_o and $2R_{pol}$). [Note: error bars represent the upper and lower values from repeat testing].

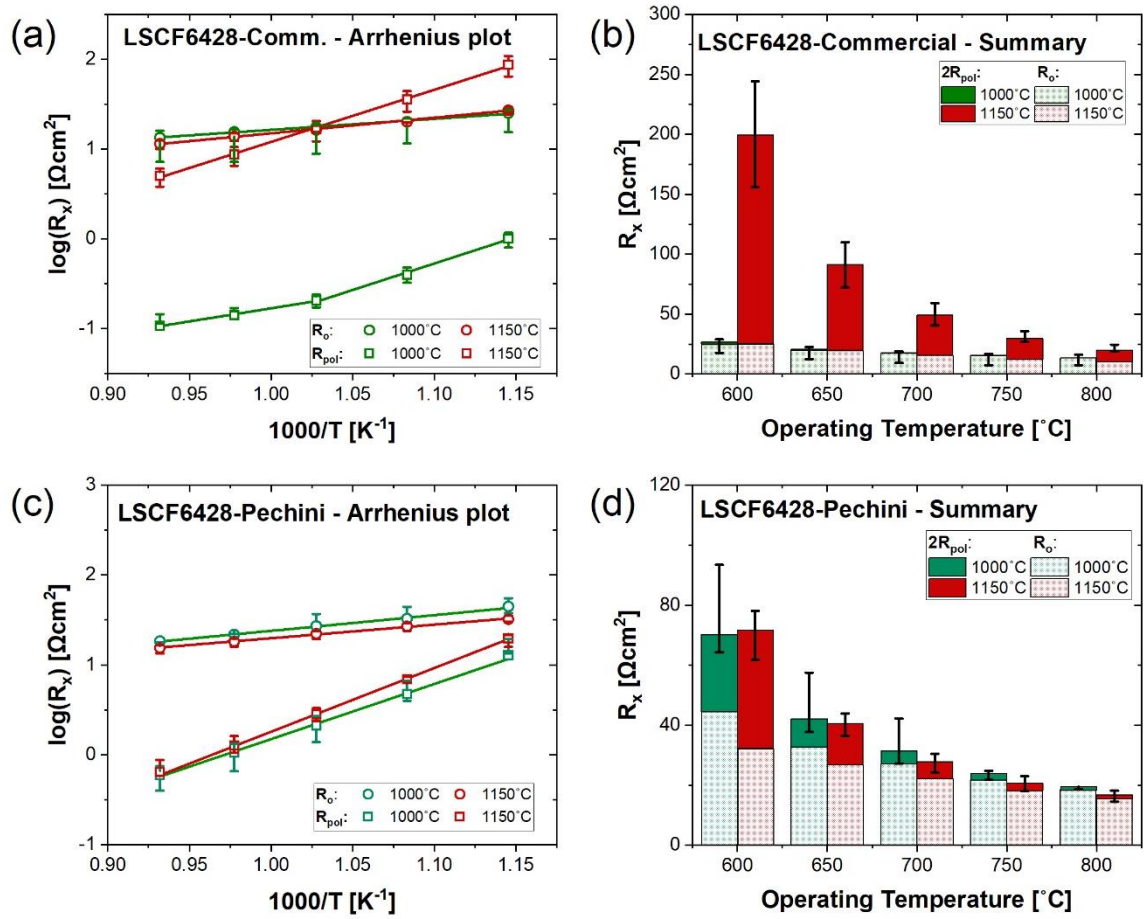


Figure 4.12 – Arrhenius plots (600-800˚C; 50˚C intervals) demonstrating the effect of sintering temperature on LSCF6428. Both commercial (a, b) and synthesised (c, d) materials were analysed. Left hand panels display Arrhenius plots for R_o and R_{pol}. Right-hand panels display the total impedance values (comprised of R_o and $2R_{pol}$). [Note: error bars represent the upper and lower values from repeat testing].

4.4 Phase behaviour analysis: the effect of sintering temperature

The results from Section 4.3.4 suggest that lanthanum nickelate phases, in particular, undergo some significant physical and/or chemical transformations at sintering temperatures in excess of 1000˚C. To further study the causes of improved performance at higher sintering temperature, a set of ex-situ tests are now described. A focus is applied to LNO214 given that this material was found to offer the most extreme change in performance with the increase in sintering temperature.

4.4.1 SEM imaging

The LNO214-symmetrical cells that were previously tested were studied via Scanning Electron Microscopy (SEM). Samples were prepared in accordance with the methodology described in Chapter 3. At high magnification, the cross-section of these samples indicates improved particle connectivity

at higher sintering temperatures (Figure 4.13). In the case of the LNO214 sample sintered at 1000˚C, the electrode is defined by isolated particles with relatively poor connectivity whereas, at 1100˚C and 1150˚C, the particles appear to coalesce more effectively

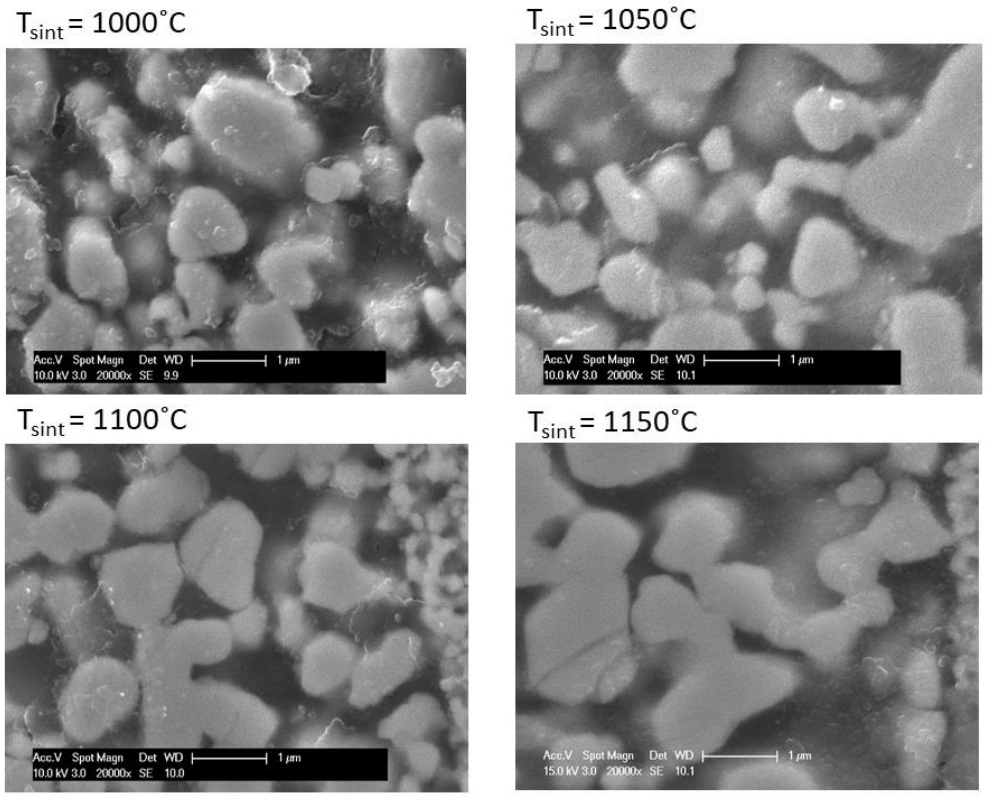


Figure 4.13 - SEM analysis of four symmetrical cell samples (LNO214) sintered at four temperatures (20,000x magnification). A version of this figure is intended for publication [315].

4.4.2 Dilatometry

To further consider the sintering behaviour of $La_2NiO_{4+\delta}$, dilatometry experiments were conducted on pelletised samples and compared against commercial LSCF6428 and also $La_{0.8}Sr_{0.2}MnO_{3-\delta}$ (LSM82). Comparisons were made at a sintering temperature of 1000˚C as shown in Figure 4.14a with the samples held at this temperature for 4 hours. As is shown, the onset of sintering for LNO214 is observed to occur at a higher temperature than that of the state-of-the-art materials. Further, the extent to which the nickelate pellet shrinks is far below that of the commercial materials. A further experiment was conducted at a higher sintering temperature of 1150˚C which facilitated a much greater shrinkage in comparison (see Figure 4.14b).

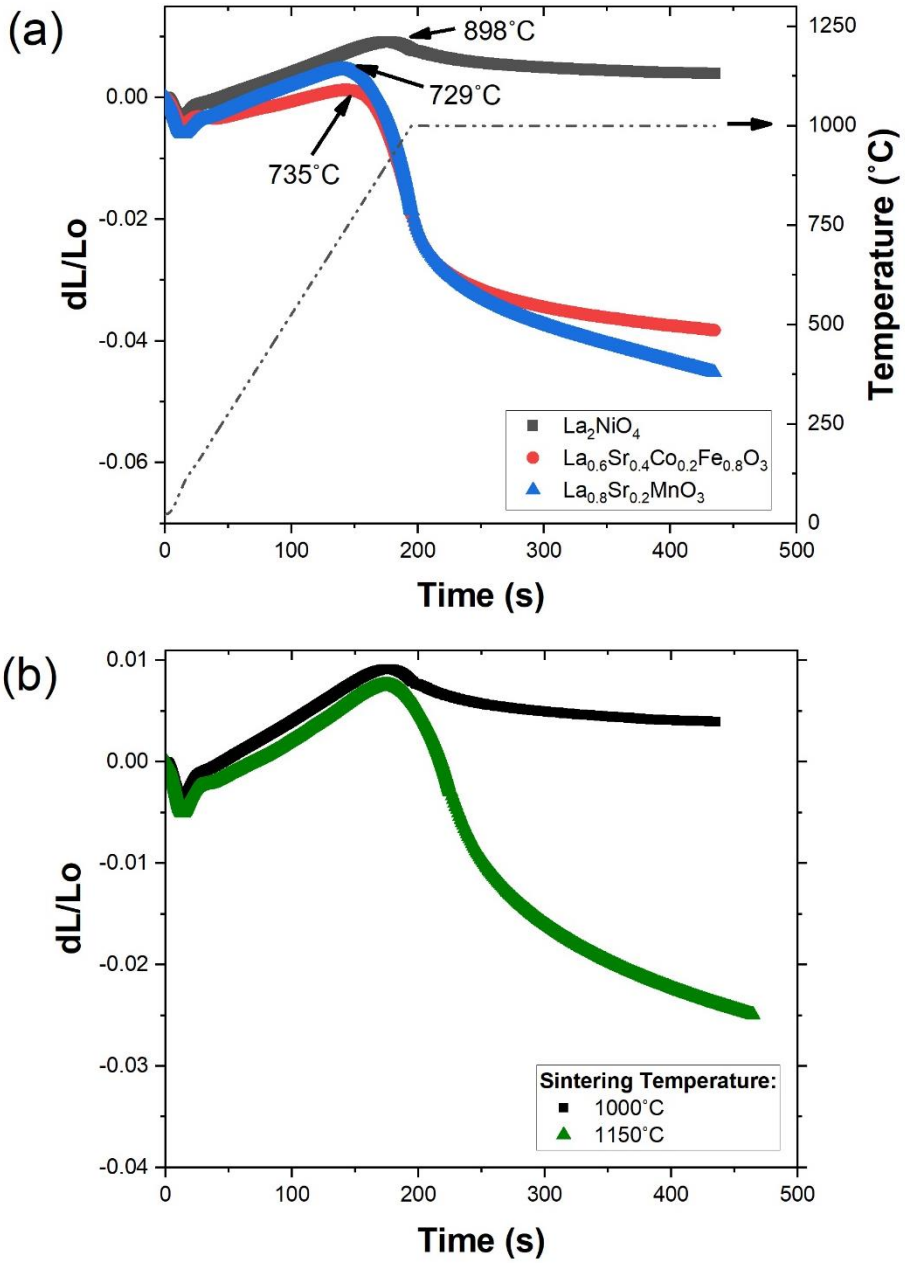


Figure 4.14 – Dilatometry results; (a) LSM82, LSCF6428, LNO214 sintered at 1000˚C, (b) and LNO214 sintered at 1000 and 1150˚C. A version of this figure is intended for publication [315].

4.4.3 XRD reactivity study

Considerations in the literature indicate that some interactions between $La_2NiO_{4+\delta}$ and CeO_2-based electrolyte phases are expected at high temperature sintering conditions [222,224,227,318,319]. Similar behaviour has been reported for $LaNi_{0.6}Fe_{0.4}O_{3-\delta}$ [320]. However, effects on higher RP phases are less well studied. Interestingly, Choi et al. [230] reported no reaction between GDC and $La_4Ni_3O_{10-\delta}$ after experiments at 1000˚C. To offer a more comprehensive assessment, a number of experiments

were conducted to identify any key reaction product between GDC10 and the electrode materials under consideration. An approach of grinding symmetrical cell samples after testing and performing XRD analysis did not offer any major insight into any such phases formed during fabrication and/or testing. This was largely an expected finding given that any such secondary phases were likely to be limited to electrolyte-electrode interfaces and, as such, likely to comprise only of trace quantities. In order, therefore, to overcome this and to effectively 'simulate' the reaction at the electrode-electrolyte interface, a series of powder-based experiments were conducted. Materials were mixed in a 1:1 mass ratio and then heated under the sintering conditions considered in Section 4.3.4. XRD analysis was conducted on the samples before and after the heating process, phase analysis being conducted via the PDF database [289] in EVA [290]. The results are summarised in Figure 4.15 to Figure 4.19.

In the case of the commercial LSCF6428 sample, no significant reactivity between the electrode phase and the GDC10 phase could be identified at either sintering temperature (1000˚C or 1150˚C). This is consistent with the literature; indeed, the GDC10 layer is introduced to *prevent* interactions with YSZ electrolytes so this is unsurprising. However, this was not found to be the case for the remaining nickelate phases, particularly at the higher sintering temperatures. Indeed, in the case of LNO214, there was seen to be the formation of additional phases even at 1000˚C. In that case, the presence of LNO327 is observed in addition to a (La,Ce)O_2 phase. For the remaining nickelates, there was no major secondary phase formation at 1000˚C. However, at the higher sintering temperature condition (1150˚C), the reaction between the nickelates and the GDC phase became more apparent. The main phenomenon was the migration of lanthanum into the ceria phase, the formation of a La-Ce-O phase, and a re-structuring of the nickelate phase through formation of a higher order Ruddlesden-Popper phase and/or precipitation of NiO.

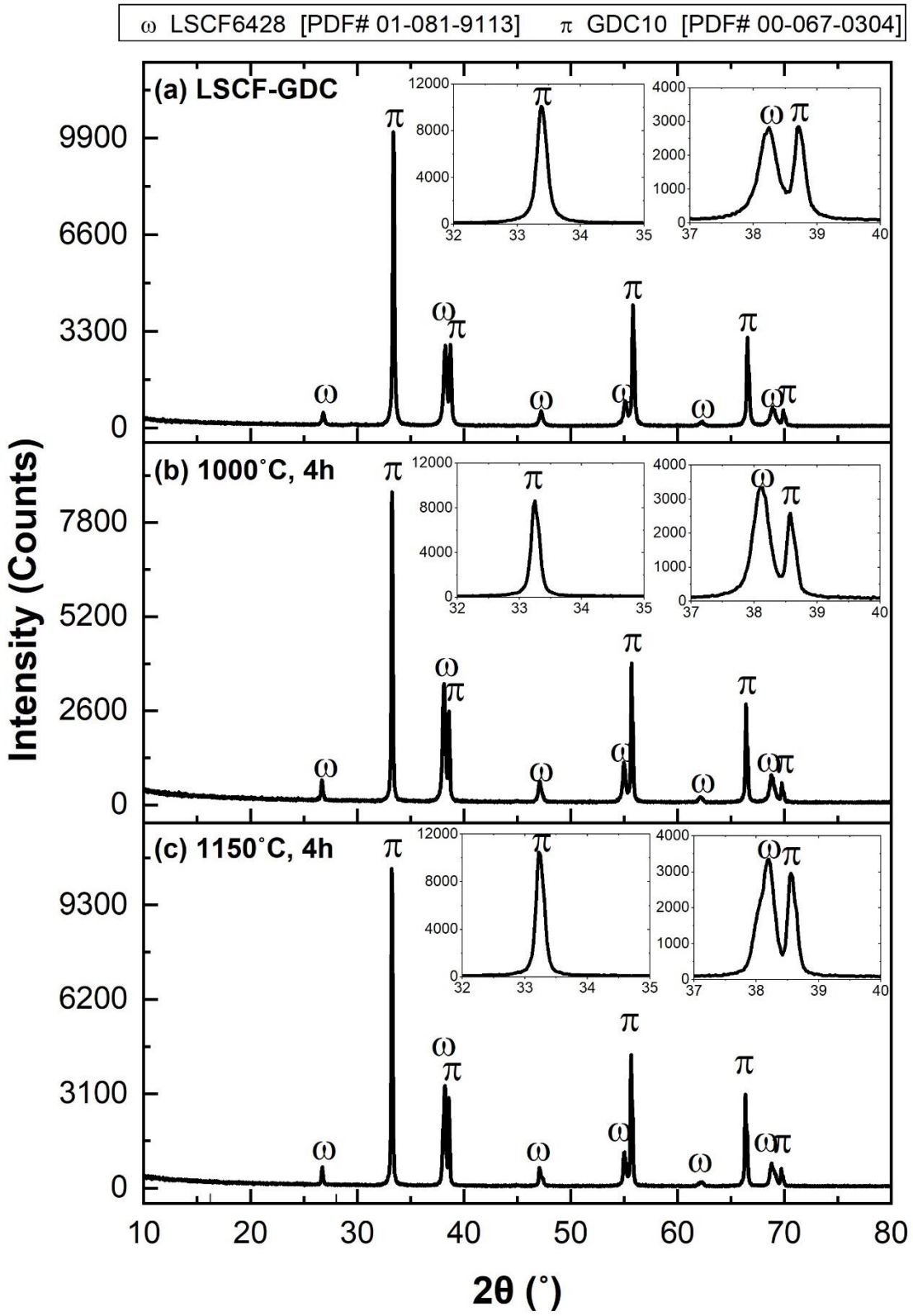


Figure 4.15 – Powder reactivity test; LSCF6428-GDC10 (1:1 mass ratio). (a) XRD scan of powder mixture prior to heat treatment, (b) XRD scan of powder mixture #1 after heat treatment at 1000˚C for 4 hours and (c) XRD scan of powder mixture #2 after heat treatment at 1150˚C for 4 hours.

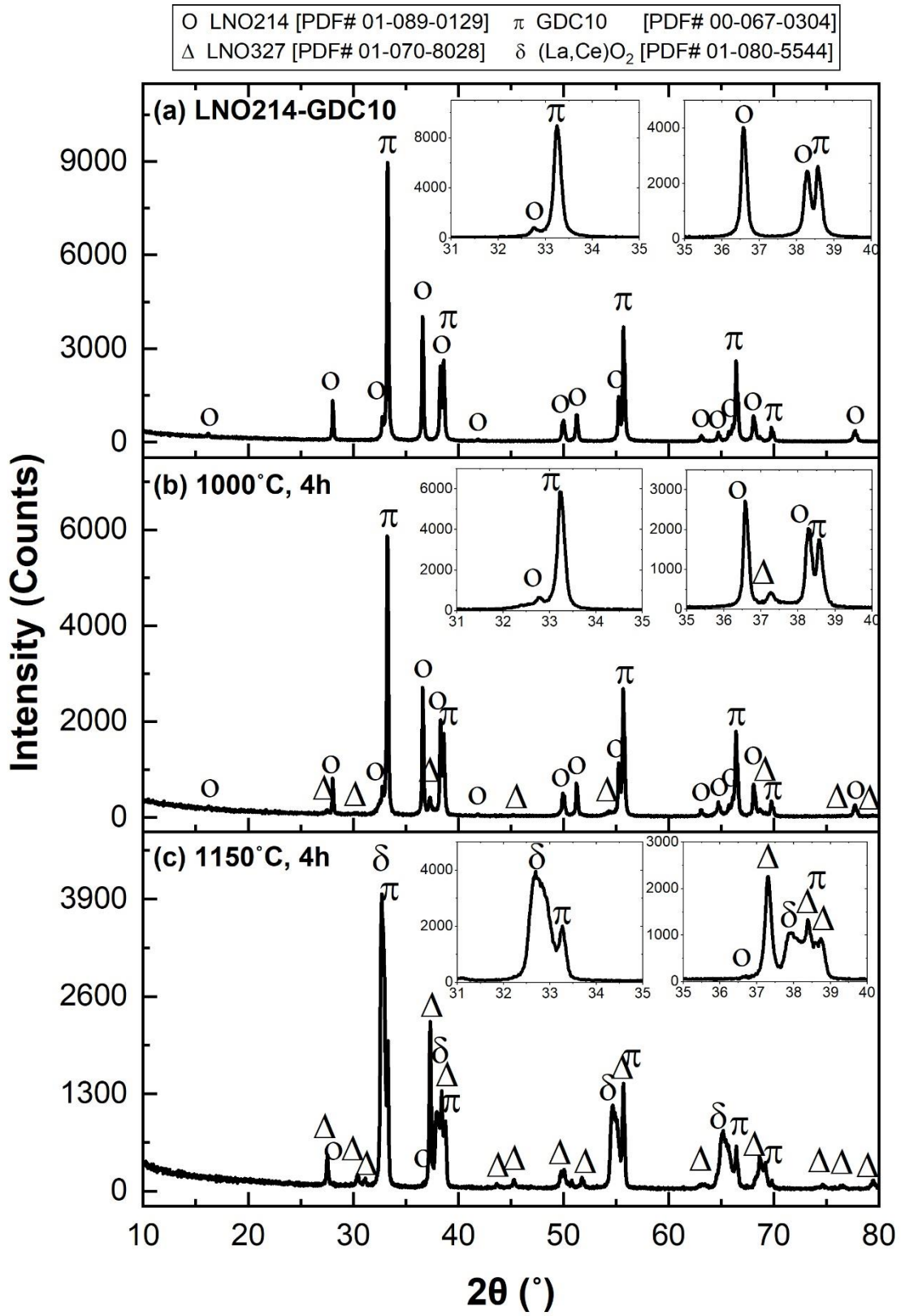


Figure 4.16 – Powder reactivity test; LNO214-GDC10 (1:1 by mass). (a) XRD scan of powder mixture prior to heat treatment, (b) XRD scan of powder mixture #1 after heat treatment at 1000˚C for 4 hours and (c) XRD scan of powder mixture #2 after heat treatment at 1150˚C for 4 hours. A version of this figure is intended for publication [315].

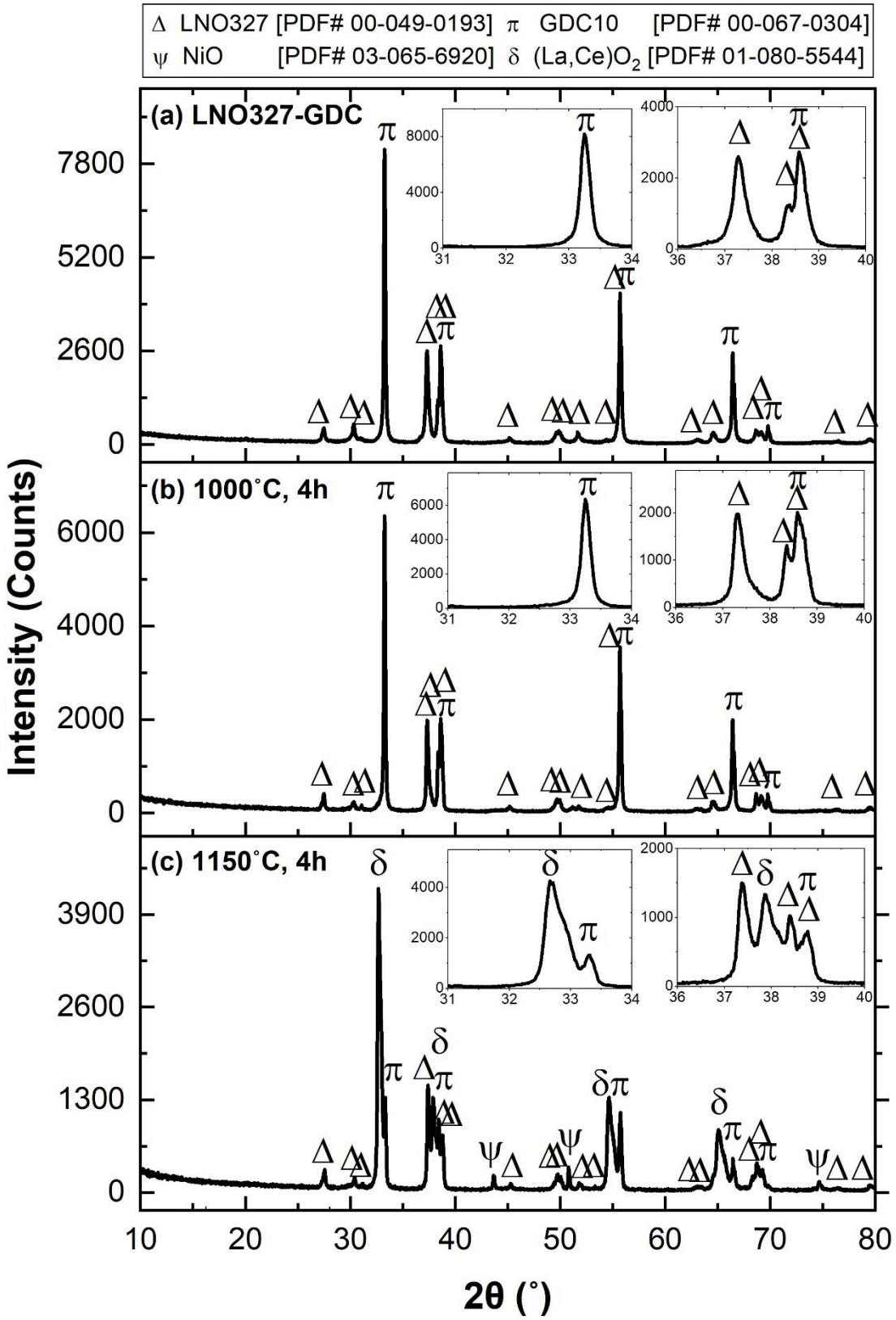


Figure 4.17 – Powder reactivity test; LNO327-GDC10 (1:1 mass ratio). (a) XRD scan of powder mixture prior to heat treatment, (b) XRD scan of powder mixture #1 after heat treatment at 1000˚C for 4 hours and (c) XRD scan of powder mixture #2 after heat treatment at 1150˚C for 4 hours.

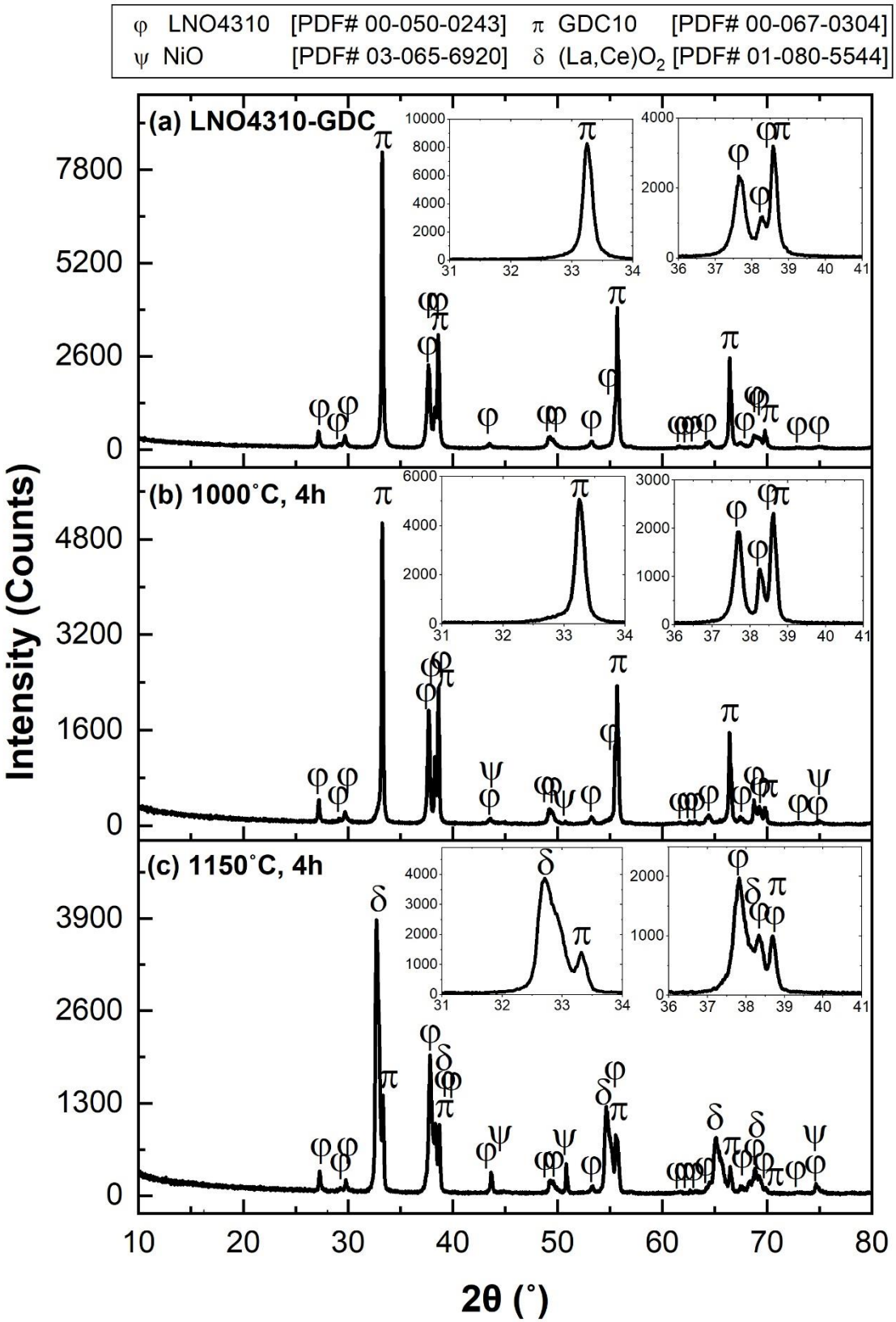


Figure 4.18 - Powder reactivity test; LNO4310-GDC10 (1:1 mass ratio). (a) XRD scan of powder mixture prior to heat treatment, (b) XRD scan of powder mixture #1 after heat treatment at 1000˚C for 4 hours and (c) XRD scan of powder mixture #2 after heat treatment at 1150˚C for 4 hours.

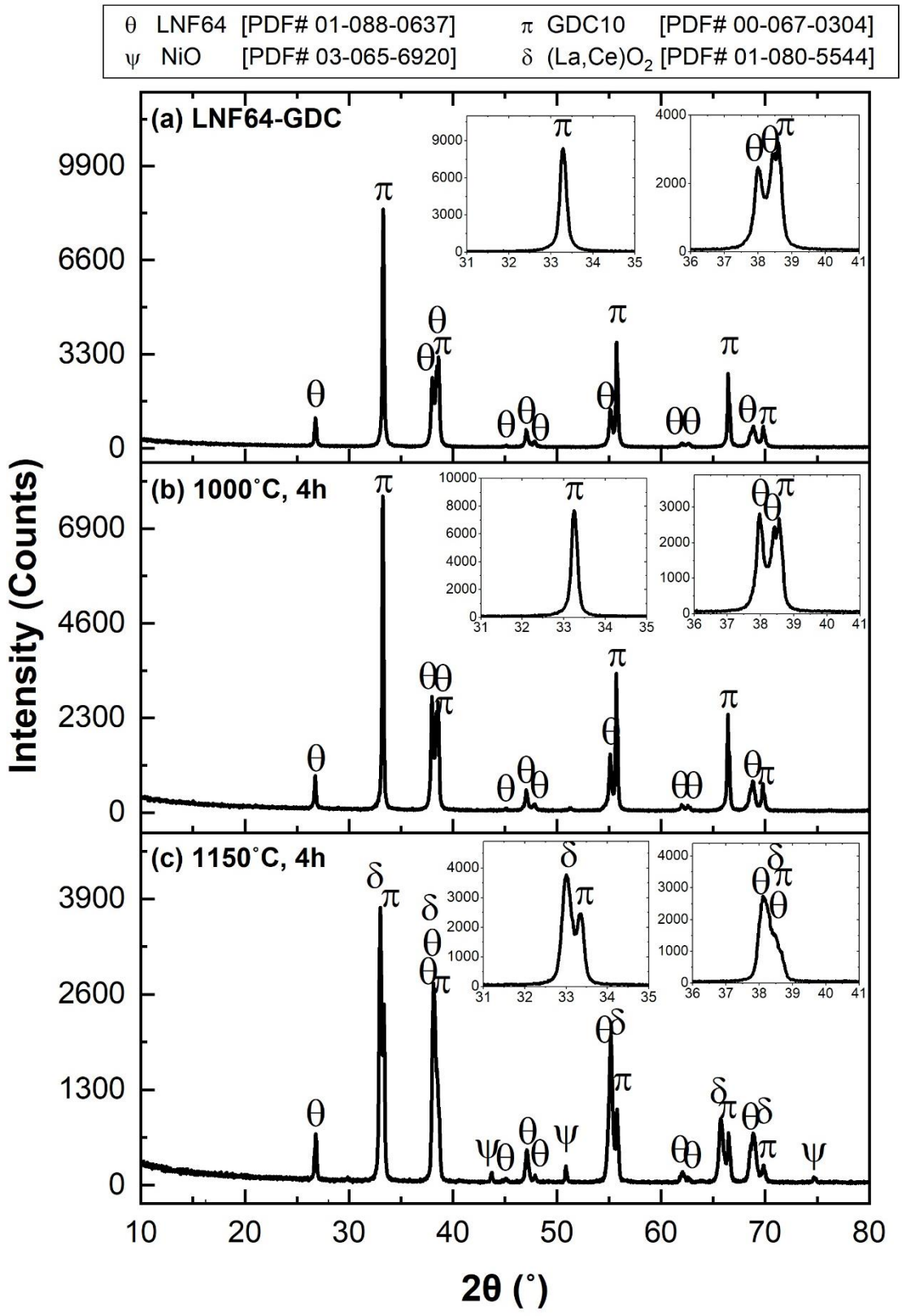


Figure 4.19 - Powder reactivity test; LNF64-GDC10 (1:1 mass ratio). (a) XRD scan of powder mixture prior to heat treatment, (b) XRD scan of powder mixture #1 after heat treatment at 1000˚C for 4 hours and (c) XRD scan of powder mixture #2 after heat treatment at 1150˚C for 4 hours.

4.4.4 Discussion on the effect of sintering temperature

Earlier in this chapter it was noted that the sintering temperature had a significant impact on the performance of lanthanum nickelates cathodes. The possible reasons for this have been explored, via several experimental approaches. Two general observations are apparent; (a) lanthanum nickelate materials suffer from inferior sintering behaviour compared with state-of-the art materials, and (b) there is some level of reaction between GDC[18] and the nickelate phases during high-temperature fabrication processes. The improved particle connectivity which was shown to be brought about by higher sintering temperatures is likely to improve charge transport behaviour (i.e. by an improvement in grain contact). It seems plausible that this is the cause of the improved performance that has been observed when higher sintering temperatures are employed. However, at the same time, it is difficult to categorically rule out the possibility that the formation of secondary phases could have had a positive effect on performance. In the case of $La_2NiO_{4+\delta}$ for instance, the formation of $La_3Ni_2O_{7-\delta}$ could be theorised to promote electronic transport due to the improved[19] electronic conductivity of the latter phase. The relative extent to which each of these phenomena may improve or hamper the performance is difficult to confirm. This issue is identified as a matter for future work and is not explored further in this thesis.

4.5 Discussion on performance

4.5.1 Summarising the results from this study

In this chapter a number of different experiments were reported considering the performance of lanthanum nickelate electrodes and additionally analysing the role of different factors in symmetrical cell studies. For comparison, the data recorded at an operating temperature of 600˚C and 800˚C are shown in Figure 4.20. As has already been commented on, the metric by which the electrodes are

[18] As described in Chapter 2, the lanthanum nickelates are also reactive with YSZ [212,221]
[19] See Appendix B for further data; LNO214 (~10-80 Scm^{-1} at 800˚C), LNO327 (50-239 Scm^{-1})

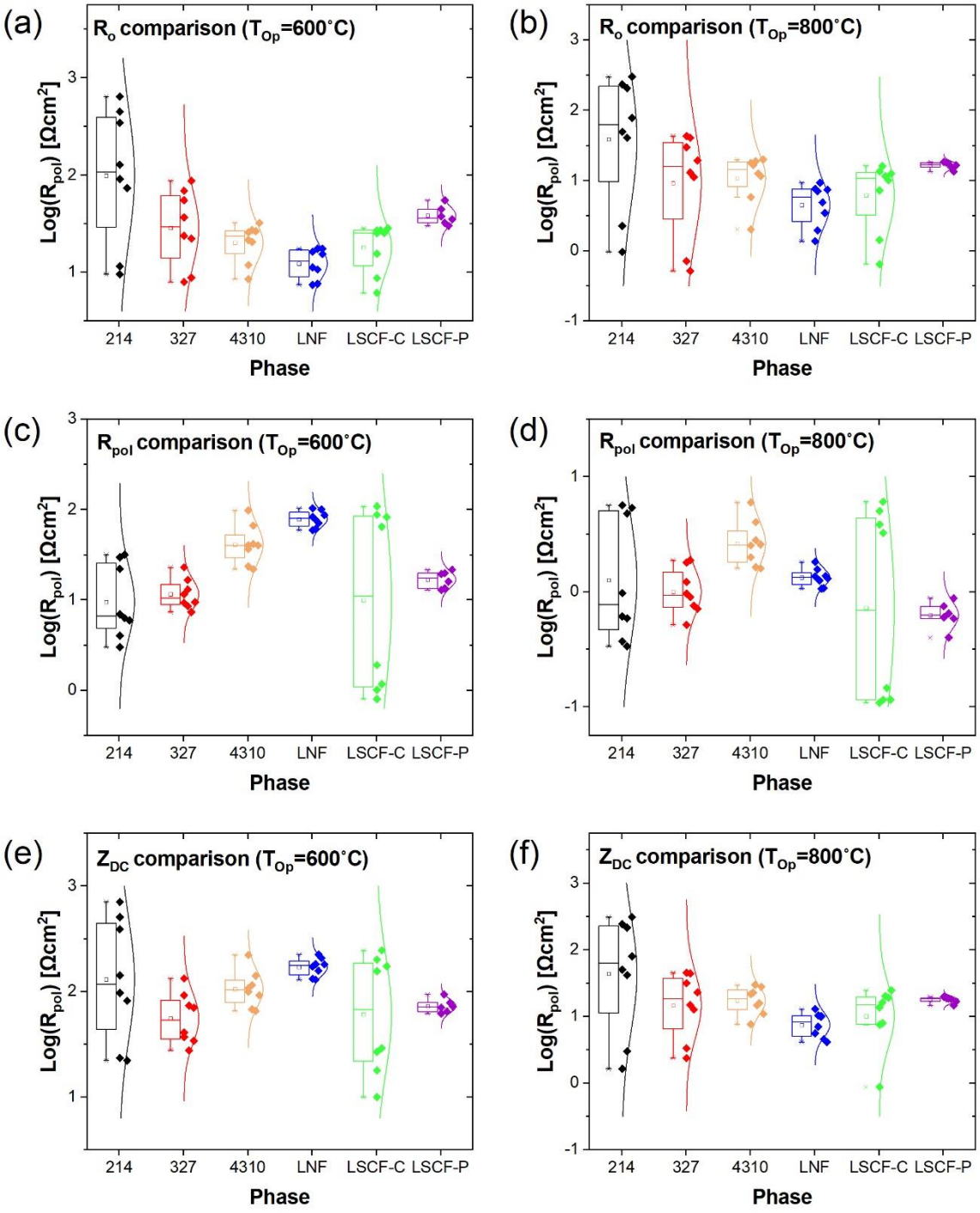


Figure 4.20 – Summary of data taken from samples tested in this study; (a, b) R_o values measured at 600˚C and 800˚C, respectively, (c,d) R_{pol} values measured at 600˚C and 800˚C, respectively (e,f) Z_{DC} values measured at 600˚C and 800˚C, respectively. Data shown includes tests conducted under different sintering temperatures and with/without Au contact paste. For reference, and to aid with interpretation, an explainer of box and whisker plots is shown in Appendix I.

bench-marked has an impact on the conclusions that are drawn from the test results. The intention of Figure 4.20 is to show the variation in performance that is possible with different materials; in some cases this is very significant (e.g. LNO214) and in others (e.g. LNF64) the effect is less prominent. These are a result of changes to fabrication conditions and testing procedures. As has already been discussed, the range of variation is most notable for materials with lower electronic conductivity. These materials clearly benefitted from the addition of the Au-CCL and increased sintering temperatures.

The data shown so far highlight that defining a single performance value for electrode materials is very difficult (rather a 'range' of performances for each material would be more appropriate). To this end, we suggest that researchers in this field should be more comprehensive in providing comparisons with the state-of-the-art and consider similar 'sensitivity analyses' to understand how individual materials can be best optimised to compete with LSCF6428. To further supplement the analysis of the data recorded in this study attention is now switched to comparisons with literature data.

4.5.2 Comparisons and comments on literature studies

Given that many researchers have studied the symmetrical cell performance of lanthanum nickelate phases, it is of interest to compare the data obtained from this study with the literature. Figure 4.21 shows the data from literature (diamond symbols and box plot) against the data recorded in this study at 600˚C, 700˚C and 800˚C. As was shown earlier in this chapter, ohmic resistance measurements are a function of the electrode phase and, in some instances, this can vary significantly. However, many authors argue that this is dominated by electrolyte resistance and simply ignore this contribution; R_{pol} values are typically reported in the literature. As such, comparisons below are restricted to these values although it is acknowledged that a more valid assessment may be to compare total resistance values (as was done earlier in this chapter). It has already been recognised that large variations in performance are achievable via a change in certain fabrication and testing conditions. In particular this is shown for LNO214 (both from our study and from the literature data) although it is also notable

that this phase has received the most attention from other authors. Importantly, given the very wide range of behaviour reported, it is difficult to categorically assign a 'winning' material out of the selected phases, i.e. the one that offers greatest promise as an alternative to the state-of-the-art LSCF. It is notable, however, that many of the studies in the literature employ Pt- based current collection materials (e.g. Pt paste). Given the favourable catalytic activity of Pt, it is plausible that this contributes to the much better symmetrical cell performance shown in some other work (it was shown earlier that the application of Au-paste could have such an effect). As a result of these observations, we highlight the need for more comprehensive studies and consideration of multiple factors as performed in the experiments reported in this chapter.

4.6 Conclusions

In this chapter, a broad study was conducted on symmetrical cell samples comprised of a variety of lanthanum nickelate phases, in addition to the state-of-the-art LSCF6428 phase. A number of key observations and conclusions were drawn from this work:

- Generally, the LSCF6428 material was found to offer the more favourable R_{pol} values and in particular offered better performance at lower operating temperatures (T_{Op}=600˚C) than the lanthanum nickelate materials. At higher temperatures, and also when considering other test parameters (R_o and Z_{DC}) the lanthanum nickelates offered a more competitive impedance response.
- Considering the ohmic resistance of the symmetrical cells, the lanthanum nickelates improved in the order LNO214 > LNO327 > LNO4310 > LNF64, consistent with the underlying electronic conductivity of these materials.
- There is a rather significant performance range which can be dictated by fabrication conditions (sintering temperatures were observed to influence performance considerably) and this can make the materials more viable as alternatives to LSCF6428. The variation in performance observed was different across the materials studied, indicating phase-specific

effects. For instance, the performance of LNO214 (in terms of R_{pol}, R_o and Z_{DC}) was greatly improved via an increase in sintering temperature whereas, for materials with better electronic conductivity (e.g LNF64, LSCF6428), this effect was not as pronounced.

- Despite the potential for reaction between lanthanum nickelate materials and CeO_2-based electrolyte phases, higher sintering temperatures (1150˚C) led to better performance with the synthesised phases – this is thought to be due to improved electrode morphology, but the possibility that the resulting reaction phases offer a beneficial effect on electrical conductivity or catalytic performance is not ruled out.
- The impact of contact paste is shown to greatly influence electrode performance whilst the impact on different materials differed to some extent. For instance, the performance of LNO214, which is known to have very poor electronic conductivity compared to other electrode phases, can be significantly improved by the addition of an Au-CCL. This suggests this material could be optimised by combination with an electronic conducting phase such as LNF64.
- Many authors concentrate on the use of R_{pol} values in defining electrode 'performance' but in this work it has been shown the R_o behaviour is also influenced by the electrode material and a key conclusion is that researchers should also consider these values in the analysis of materials.

From this initial testing work, a number of further research queries are put forward:

- Are the relationships observed in this chapter (e.g. effect of sintering temperature) also observed in single cell testing conditions?
- As an approach to assessing electrode performance, how well does the symmetrical cell testing configuration capture the polarisation performance of electrode materials?
- Alternatively, do different electrode materials perform differently according to different testing approaches?

- How can the performance of the lanthanum nickelate phases be further enhanced to rival that of state-of-the-art materials?

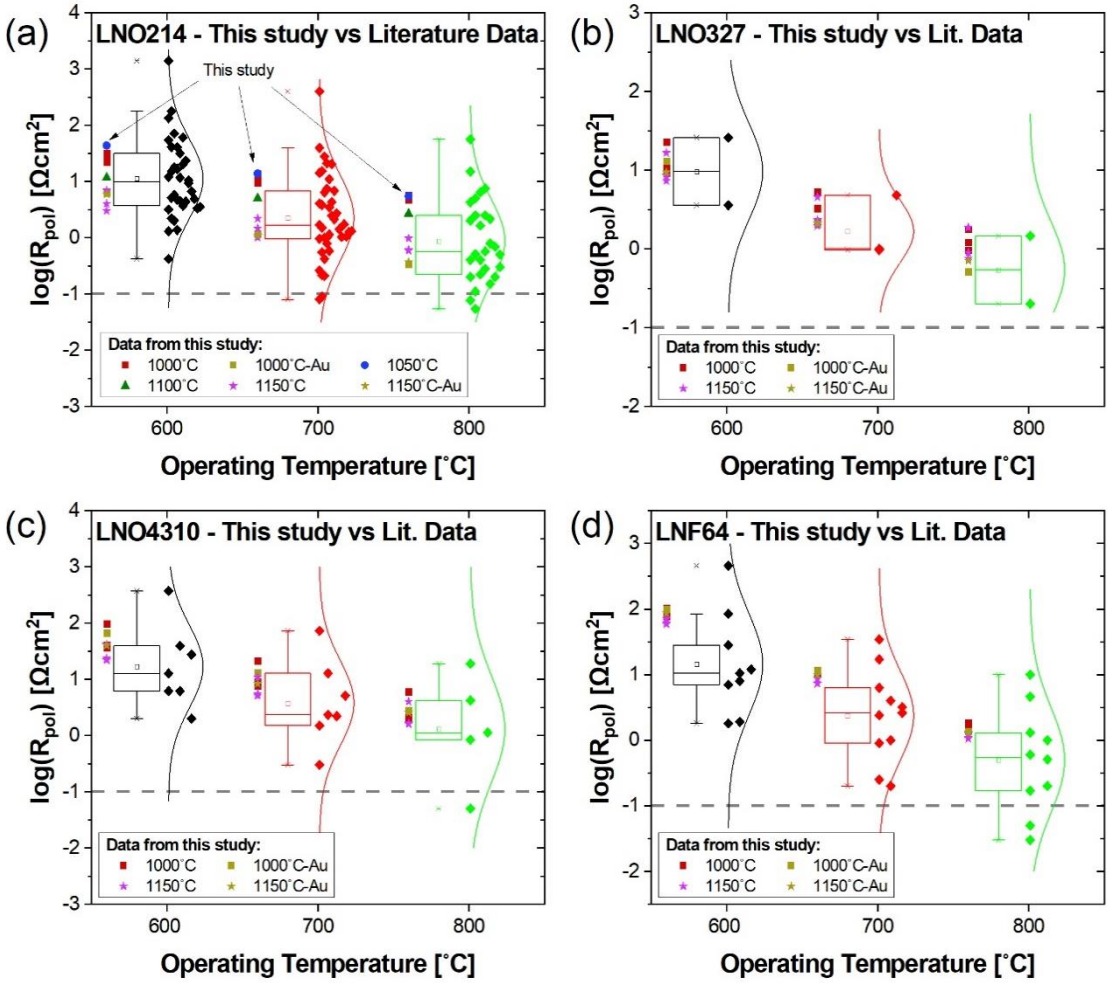


Figure 4.21 - Comparison of literature data and data from this study; (a) $La_2NiO_{4+\delta}$, (b) $La_3Ni_2O_{7-\delta}$, (c) $La_4Ni_3O_{10-\delta}$, (d) $LaNi_{0.6}Fe_{0.4}O_{3-\delta}$. For reference, and to aid with interpretation, an explainer of box and whisker plots is shown in Appendix I. A version of this figure is intended for publication [315].

5 On the performance of lanthanum nickelate electrodes under polarisation

5.1 Overview of chapter

Following on from the study of symmetrical cell testing described in the previous chapter, the following chapter explores the performance of the lanthanum nickelate electrodes under polarisation. Prior to this, an analysis of tests conducted on commercial SOFC cells is first described. These cells employ a state-of-the-art LSCF cathode. This preliminary work will outline several important observations. Firstly, these tests help to identify a bench-mark 'standard' which will later be compared directly with tests conducted on the La-Ni-O phases. This avoids the complications of comparison with other studies (e.g. results reported at Jülich [45]) where differences in performance could be influenced by test set-ups and improvements to other cell components (e.g. thinner electrolytes or better-performing anode materials and structures). Further, the work here will also describe some initial efforts to determine suitable testing parameters for subsequent tests. Notably, this includes both a consideration of contact configurations (which was already discussed in Chapter 4) and additionally on gas flow conditions. In the latter case, this is shown to be of significance due to the repeatability of the results. The optimised testing parameters are subsequently employed for testing of the lanthanum nickelates. Thus, a direct comparison between these materials and the commercially fabricated electrodes can be made. In the latter part of this chapter an analysis on the relative performance metrics is offered and compared with test results from symmetrical cell testing.

5.2 Bench-Mark Testing with Commercial Single Cells

SOFC testing is influenced by a number of variables (e.g. gas pressures, fuel leakages, contact configuration) [259,281]. These variables offer complications in understanding the performance of the various cell components and, more specifically for the case here, of the cathode. As has been previously described, there are numerous approaches to cell and electrode testing which are detailed

in the literature. Despite several efforts[20] to address this, there remains no standardised methodology that is universally employed across the many research institutes around the world. Comparisons of electrode performance across studies therefore become difficult. Here, an initial consideration on the effect of different testing parameters with respect to achieving *representative* and *repeatable* results is offered. This work relates to the commercial Chino Corporation test bench set-up described in Chapter 3.

5.2.1 Procedural Development

5.2.1.1 Considerations on contact configuration

Commonly, so-called *'contact materials'* (i.e. materials with excellent electronic conductivity) are applied between electrodes and their neighbouring current collectors [302]. This is with a view to reducing the contact resistance of the cell and achieving optimum cell performance. Whilst the use of precious metals is an undesirable solution at a commercial level (where tailor-designed perovskites are more preferable [302]), at lab-scale it is common for such materials to be employed. Following on from the work in Chapter 4 to understand the effects of gold contact paste on symmetrical cells, a similar assessment is outlined here with respect to single cell testing. To this end, three different contact configurations were studied in order to understand which enabled the procurement of good quality data and consequently reliable assessment of the electrode materials in question. These configurations are summarised in Table 5.1.

Table 5.1 – Overview of contact configurations tests (NOTE: current collector meshes supplied by Chino Corporation).

Test Point	Anode Side of Cell	Cathode Side of Cell
1	Ni mesh only	Ag mesh only
2	Au-paste + Ni mesh	Au-paste + Ag mesh
3	Ni mesh only	Au-paste + Ag mesh

[20] This includes the EU-projects FCTESTNET, FCTESQA and SOCTESQA

As described by Table 5.1, Au-paste (*Fuel Cell Materials*) was selected as a supplementary[21] contacting medium, rather than other materials such as Ag or Pt. This was due to the relative inactivity of Au in catalysing the Oxygen Reduction Reaction, when compared with these other materials [321]. As was described in Chapter 4, it is relevant to minimise any 'artificial' performance-enhancement that may be brought about by the presence of other phases (also see reference [322]). Indeed, it was observed in Chapter 4 that improvements in contact resistance can disproportionately impact electrodes dependent on the underlying material properties. An avoidance of such materials (i.e. *Test point 1* in Table 5.1) is, therefore, preferable. However, this must also be balanced with the ability to collect good quality data. It is worth re-highlighting that real SOFC stacks are likely to deploy electronically-conductive ceramic contact pastes between the electrodes and current collecting plates (in effect replicating the role of the Au-contact paste here). The application of contacting materials, therefore, need not necessarily be considered an 'unrealistic' approach.

For all tests described in this chapter, polarisation and EIS tests are reported. For the initial tests shown in Table 5.1, cells were tested in dry hydrogen (0.20 $Lmin^{-1}$) and dry air (0.50 $Lmin^{-1}$) on the anode and cathode sides, respectively. The results of the contact configuration tests are shown in Figure 5.1. As a first point of call, the polarisation curves shall be discussed. The iV behaviour of the three contact configurations are seen in Figure 5.1a, Figure 5.1c and Figure 5.1e (800, 750 and 700˚C, respectively). In each case, the open circuit voltage was observed to be around 1.1 V at an operating temperature of 800˚C, indicating the avoidance of any major leakage or electrolyte cracking. In relation to the testing set-up and parameter selection employed in this study, it is apparent that the Au-contact paste is critical in achieving appreciable current output. It is noted, however, that the application of Au to the anode side of the cell appears to offer no significant improvement in this regard. On the contrary, the addition of a Au-layer on the fuel electrode was observed to offer a detrimental effect on performance (i.e. reduced current density at lower voltages). This is clearly appreciated in Figure 5.1

[21] Ag- and Ni-mesh are additionally employed on the cathode and anode sides of the cell, respectively (as per the rig supplier instructions).

via a comparison of test points 2 and 3. This behaviour has been found to be a repeatable observation in follow-up tests. It is probable that this loss of performance was a result of a diffusion-based limitation, i.e. the Au paste on the anode side blocking the gas flow. Indeed, via comparison of the polarisation curves at 800˚C (see Figure 5.1a) the performance of the cell with Au paste on both electrodes increasingly diverges from that of test point 2 as current is drawn from the cell. Further, it appears that this cell begins to enter into a 'mass-flow limiting' regime between 0.5-0.6 Acm^{-2}, suggesting the onset of a diffusion-related limitation. In any case, it is apparent from the test results that the contact issue is largely associated with a high contact resistance between the Ag contact mesh and the underlying cathode and not in relation to the Ni-on-Ni contact on the fuel side of the cell.

With respect to the impedance results from these initial tests (Figure 5.1b, Figure 5.1d, Figure 5.1f), several key observations are apparent. Generally speaking, the shape and magnitude of the impedance responses taken for the three cells is very similar. However, the EIS spectra taken from the configuration without contact paste (test point 1) is seen to be translated along the x-axis (Z') relative to the other cell tests. This confirms the anticipated increase in the ohmic resistance of that assembly in relation to the others. The effect is further summarised in Figure 5.2a. It becomes evident that the addition of the contact paste on the anode side of the cell offers a marginal improvement with regards to the measured R_o values. Equally, the polarisation performance (R_{pol}) measured around the OCV condition is shown to be almost identical between test points 2 and 3. However, it has already been observed in the polarisation curves, that this behaviour does not translate to better (or even equal) performance under polarisation. Again, this indicates rate-limiting behaviour as the fuel is consumed. Another notable observation with respect to the case where no contact paste is employed is the presence of some noise. This presents challenges with respect to analysing the data (i.e. conducting EIS modelling of the spectra). Based on the evidence and observations collected from these initial cell tests, the remaining tests in this chapter will employ the use of Au-contact paste on the oxygen electrode *only,* in addition with Ni and Ag contacting meshes on each side (Table 5.1). As was detailed

in Chapter 4, this is likely to offer greater benefit to certain materials (i.e. those with inferior electronic conductivity).

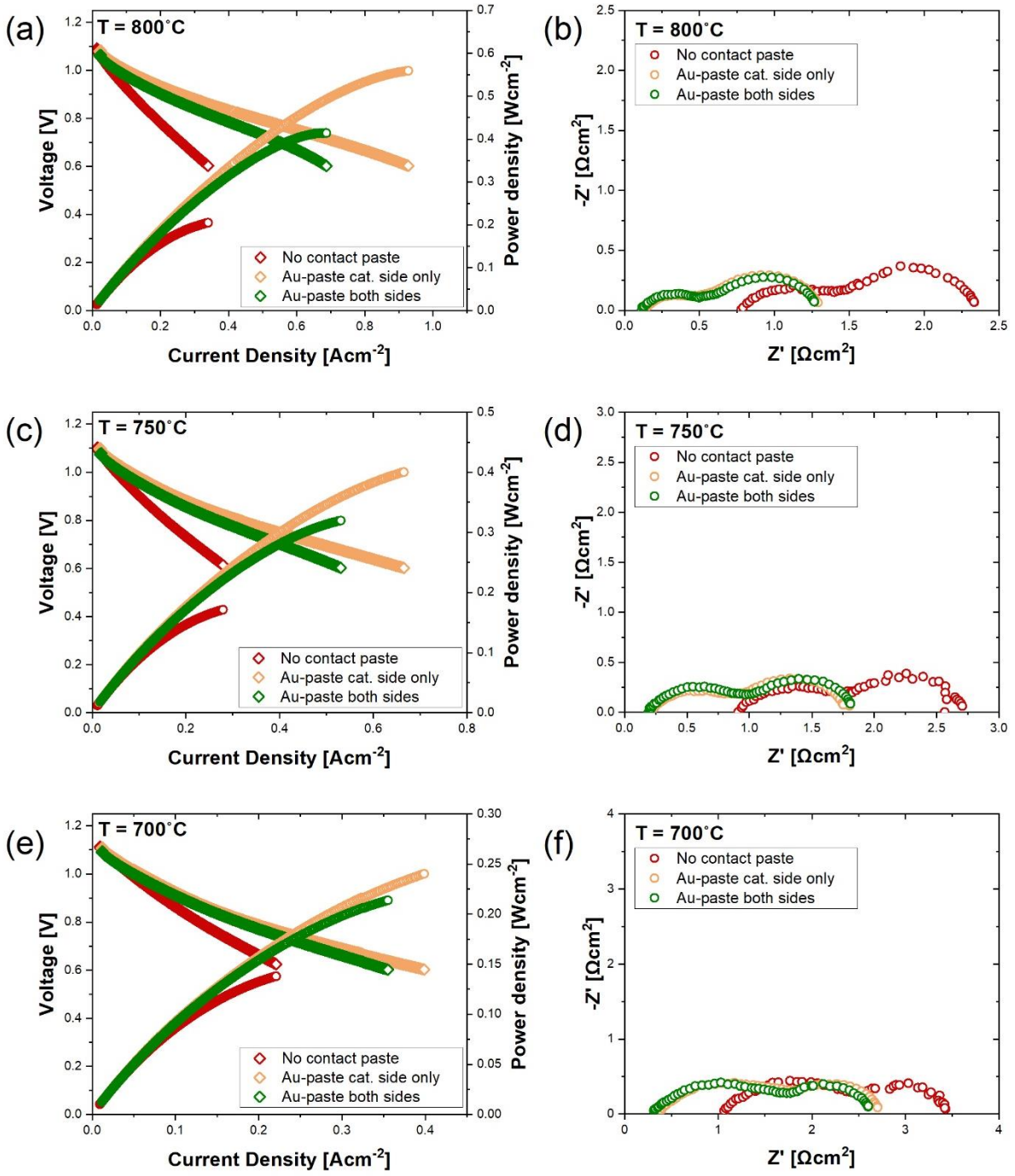


Figure 5.1 - Effect of contact configuration (i.e. use of Au contact paste) on cell performance; Effect of contact configuration on polarisation curves at (a) 800˚C, (b) 750˚C, (c) 700˚C and effect on the EIS spectra recorded at (d) 800˚C, (e) 750˚C and (f) 700˚C.

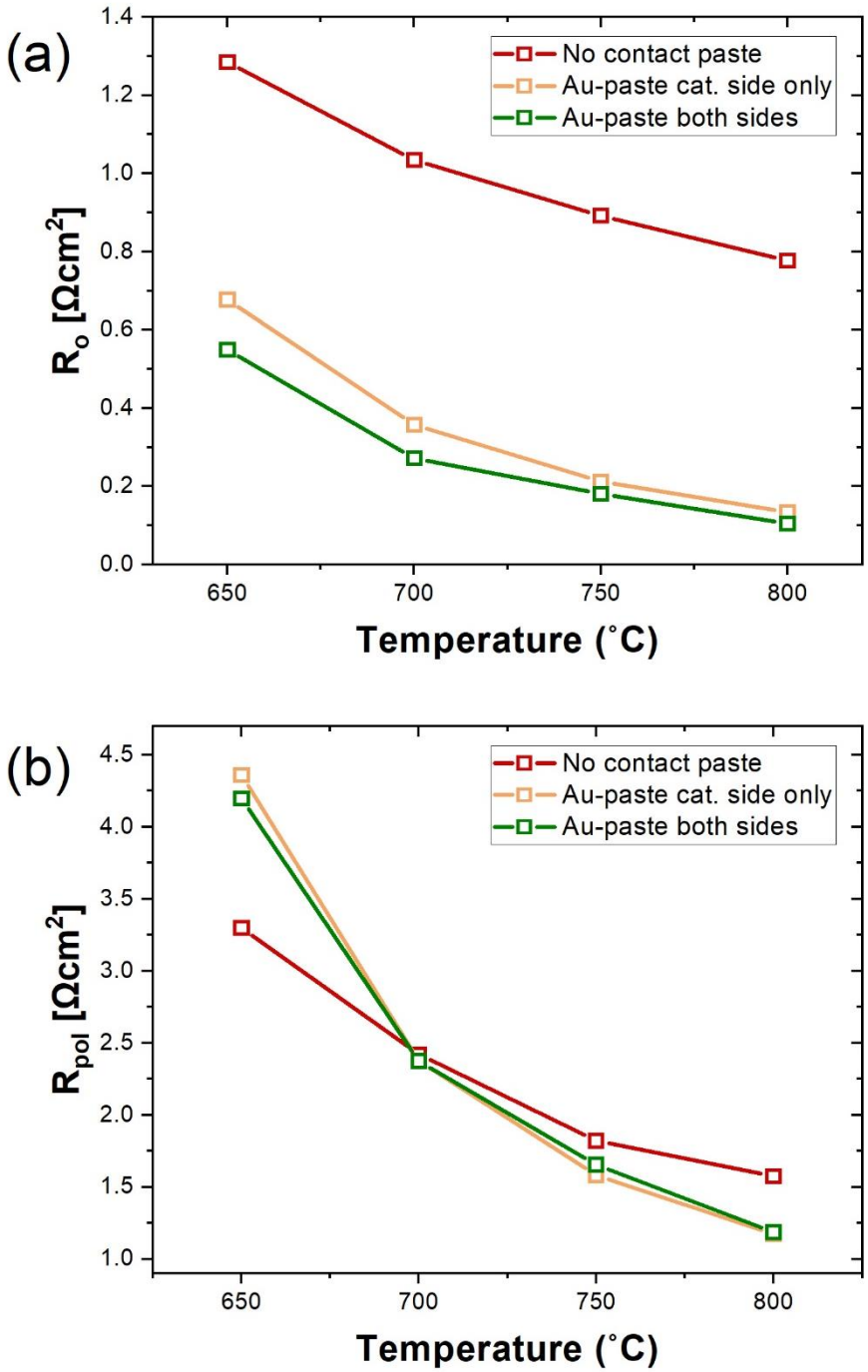


Figure 5.2 - Summary on the effects of contact paste on (a) ohmic resistance, R_o, and (b) polarisation resistance, R_{pol}, as measured from the EIS spectra taken at 'OCV-0.05V' condition.

5.2.1.2 The role of humidity in repeatable single cell testing

In order to understand the repeatability of the single-cell testing set-up (described in Chapter 3) and to ensure suitable comparisons can be drawn between tests, the performance of three identical commercial cells was compared under various conditions, i.e. different gas flow conditions and

operating temperatures. Both polarisation and EIS measurements were performed in order to develop an understanding of the behaviours seen.

In Figure 5.3a and Figure 5.3b, the performance of three commercial cells (A_{active}=16 cm^2) in dry H_2 is compared. It is apparent that there is a significant discrepancy between the impedance spectra measured at OCV (Figure 5.3a), despite the *apparently* identical nature of these three test points. This observation appears to present a significant issue with respect to assessing and comparing the relative performance of cells against one another. Moreover, and in the context of this thesis, this represents a barrier to comparing the performance of different electrode materials. Conveniently, however, this issue can be alleviated via the introduction of water in the fuel stream (i.e. the humidification of the hydrogen). The effect of hydrogen humidification can be appreciated in Figure 5.3c and Figure 5.3d.

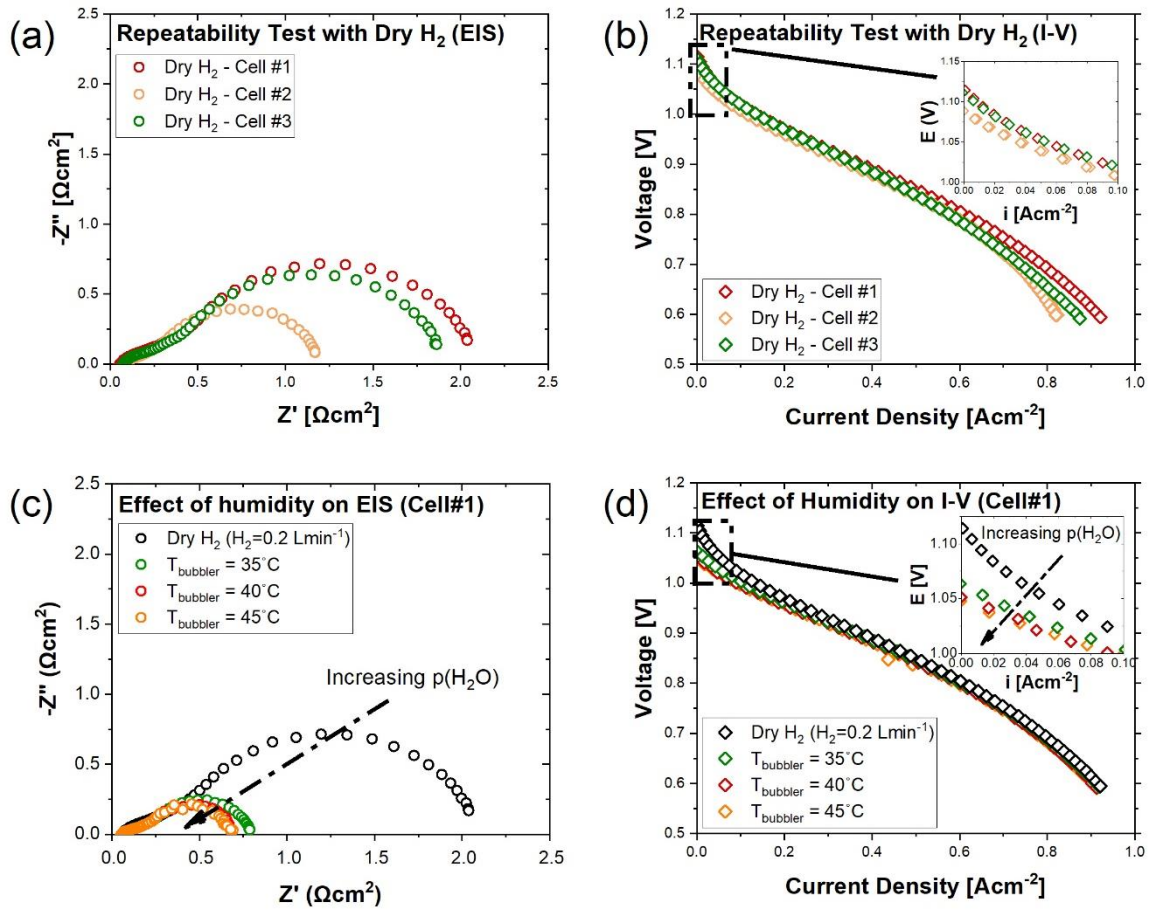


Figure 5.3 – (a, b) Repeatability test at 800˚C using dry hydrogen (c, d) effect of fuel humidity on impedance and i-V curves of a cell [H_2=0.2 $Lmin^{-1}$, Air=0.5 $Lmin^{-1}$, T_{Op}=800˚C].

To alter the working $p(H_2O)_{Fuel}$, a temperature-controlled water tank was employed. The ability to change the temperature of the tank offered control over the fuel condition regardless of atmospheric conditions (effectively setting a defined equilibrium water vapour pressure across all tests). By increasing the temperature of the bubbler, the quantity of water contained within the fuel stream could be increased. The resulting effect was a reduction in the open circuit voltage. Moreover, this led to a reduction of the "*tail*" at low current densities as displayed in the inset of Figure 5.3d. The effect is associated with a Nernstian effect (for the sake of discussion, this will be described here as a "*Nernstian tail*"). This can be further considered by an analysis of the Nernst equation:

$$E = E_o + \frac{RT}{nF} ln \frac{p(H_2).p(O_2)^{\frac{1}{2}}}{p(H_2O)} \quad (Eq. 5.1)$$

From Eq. 5.1 it is apparent that the use of dry hydrogen (on the anode side of the cell) leads to an increase in the cell voltage, theoretically to 'infinity'. The oxidation of hydrogen at the anode side of the SOFC leads to the formation of water. It can be anticipated therefore that, as the HOR proceeds and current is drawn from the cell, a drop in cell voltage is anticipated. When the cell is operated on dry hydrogen, therefore, a small increase in the water content of the gas stream can be anticipated to lead to a sizeable change in the voltage at low currents. As a result, the exponential decrease in voltage (towards the left hand side of the polarisation curve) can be anticipated. Similar effects are also described by Klotz and Weber [259]. However, in isolation the phenomena described thus far fail to explain the *variability* in the testing results for apparently identical cells (Figure 5.3a-b). To understand this further, a consideration of the real-life SOFC testing set-up is required and more specifically a consideration of the cell sealing and gas partial pressures. Imperfections in sealing (which are described in [259] as "*unavoidable*") can lead to small hydrogen leakages which, when combined with air at SOFC operating temperatures, lead to auto-combustion and, hence, the formation of water. This may also occur due to imperfections in the electrolyte substrate. In turn, this could allow fuel 'cross-over' and direct combustion of the hydrogen. As has already been described, the presence of water can lead to a reduction in cell voltage due to Nernstian effects. Any natural variation in sealing (and,

therefore, any variation in the partial pressure of water) can be anticipated to lead to variable degrees of the aforementioned effect. To further understand how this impacts on the impedance response of a cell, consider that the Z_{DC} (or "ASR") of a cell can be represented by the gradient of the polarisation curve [281] (i.e. $\Delta V/\Delta i$), in addition to its relationship with the impedance spectra. The previously described effect (i.e. the Nernstian tail) notably leads to an enlarged gradient (and hence an increased Z_{DC} value) at OCV. Indeed, this matches very well with that observed on the impedance spectra (i.e. the steeper the curve at OCV, the larger the corresponding impedance response of the given cell - as shown in Figure 5.3c-d).

The variation in fuel gas partial pressures offers a sizeable effect which is exposed when comparing the EIS responses at OCV. This has obvious implications when later comparing EIS results of different cell materials. In an attempt to demonstrate the impact that humidification has on experimental repeatability, the performance of three commercial cells is compared under humidified hydrogen (Figure 5.4). With the humidification temperature set at 35˚C it was observed that each cell provided a very similar performance at OCV (i.e. considering both the iV curve in the inset of Figure 5.4a and the impedance spectra in Figure 5.4b). The increase in the starting $p(H_2O)_{Fuel}$ corresponded to a flattening of the IV curve around the OCV point and a smaller (and more consistent) impedance spectrum. In summary, this can be further understood by the fact that any corresponding increase in H_2O leads to a relatively smaller percentage increase in $p(H_2O)_{Fuel}$ than when dry hydrogen is employed.

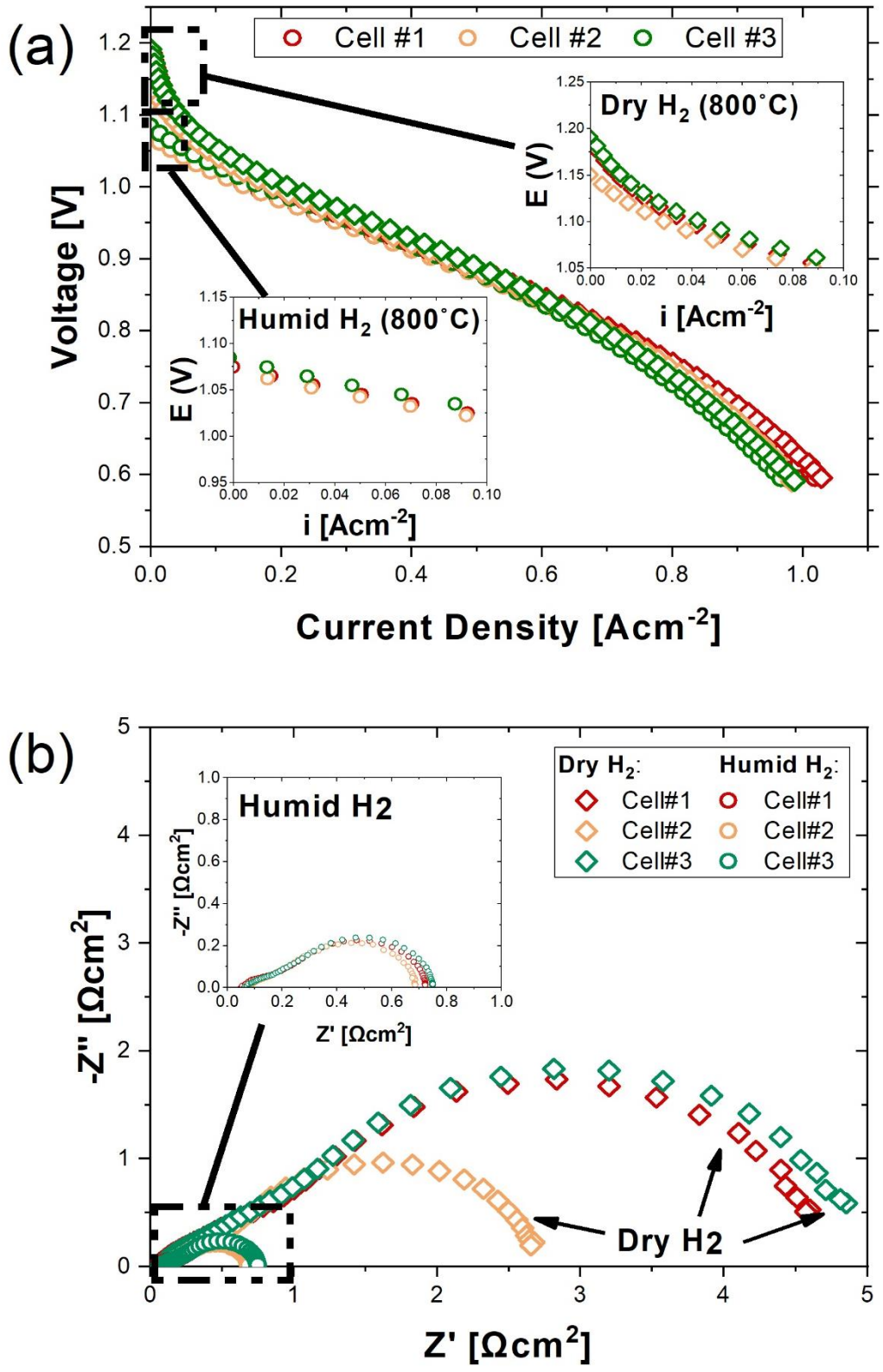


Figure 5.4 - Comparison of three commercial SOFC cell tests using dry and humidified hydrogen (0.5 Lmin^{-1}); effect of humidification on (a) the polarisation curve at 800˚C and (b) the OCV impedance responses at 800˚C.

Further understanding of this effect can also be gleaned via a simple modelling approach using the Nernst equation (eq. 5.1). Applying this equation to calculate cell voltage (and ignoring other losses such as activation, ohmic or mass flow losses) the effect of increasing the *initial* water content of the fuel can be readily observed (Figure 5.5). In all cases, water concentration in the anode compartment increases as the current density of the cell increases. By itself, this leads to a reduction in the cell voltage. However, it is only in the case where the initial water content in the fuel is low (<3vol%) that the issue of the *Nernstian tail* becomes evident.

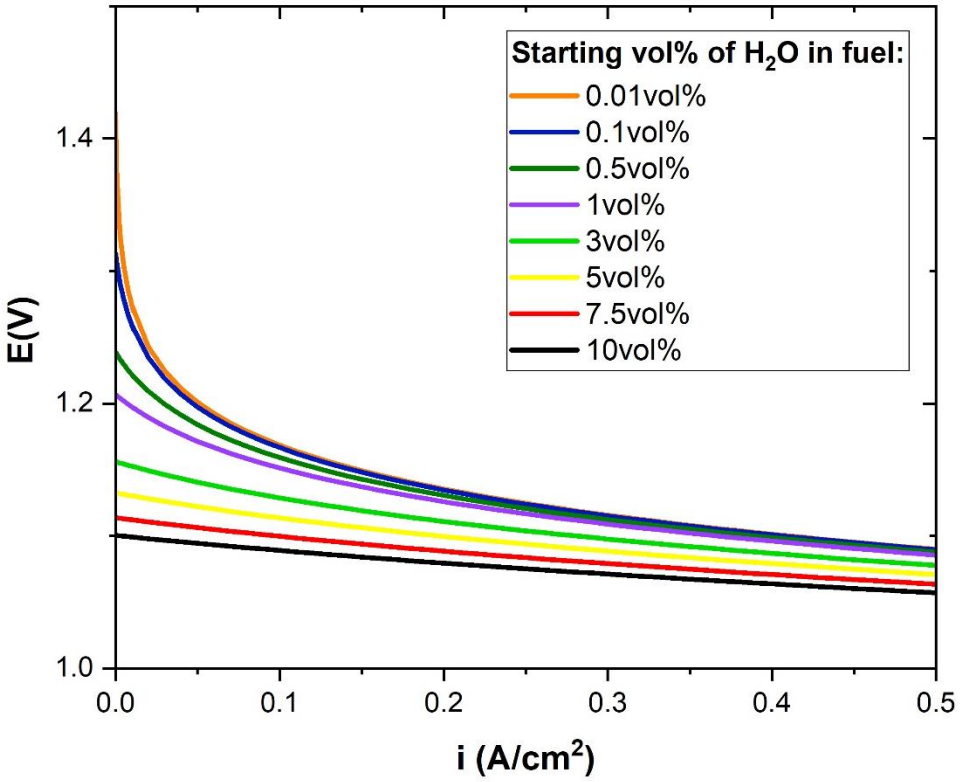


Figure 5.5 –Modelling the effect of humidifying hydrogen on the resulting current-voltage profile. Assumed conditions (T_{Op}=800˚C, $p(O_2)$=0.21 bar).

From the work described in this section, an appropriate set of conditions to conduct further testing has been identified. The use of a temperature-controlled humidifier (T_{bubb}=35˚C) enables a humidified gas stream (H_2=0.5 $Lmin^{-1}$) of sufficient consistency to achieve consistent results at SOFC operating conditions (700 to 800˚C). It was noted that setting the bubbler at higher temperature led to increased water concentration in the fuel but difficulties were also observed in maintaining voltage stability

under these conditions. This is likely a result of condensation forming within the pipelines, causing pressure fluctuations in the system. Table 5.2 summarises the conditions selected for the testing of single cells in the remaining tests described in this chapter.

Table 5.2 – Testing parameters employed to achieve repeatable results for bench-mark tests.

Anode Flow	**External Bubbler Temp (Fuel Side)**	**Cathode Flow**	**Operating Temp**	**Anode Contact config.**	**Cathode contact config.**
0.5 $Lmin^{-1}$ (H_2)	35˚C	0.5 $Lmin^{-1}$ (Air)	700 to 800˚C	Ni mesh	Ag mesh and Au contact paste

5.2.2 Bench-mark metrics for LSCF-containing Commercial Cells

With appropriate testing parameters now identified, it is possible to quantify a 'bench-mark standard'. In effect, this standard represents the performance-level that is achievable with the typical 'state-of-the-art' SOFC cells that are available on the commercial market. More specifically, it identifies the performance that is found to be readily achievable in the aforementioned testing configuration. This bench-mark takes on a new level of significance in subsequent sections where comparisons are drawn with the cathode materials, i.e. the La-Ni-O phases discussed in this thesis. Notably, such analysis may be based on metrics taken from either EIS *or* polarisation experiments. Indeed, the use of these metrics is common from within the literature and both will be considered here. Further, an analysis and discussion against the findings from Chapter 4 will also be offered. The polarisation curves and EIS spectra taken from three commercial cells are shown in Figure 5.6. A selection of bench-marks are identified for EIS measurements and polarisation curves in Table 5.3 and Table 5.4, respectively.

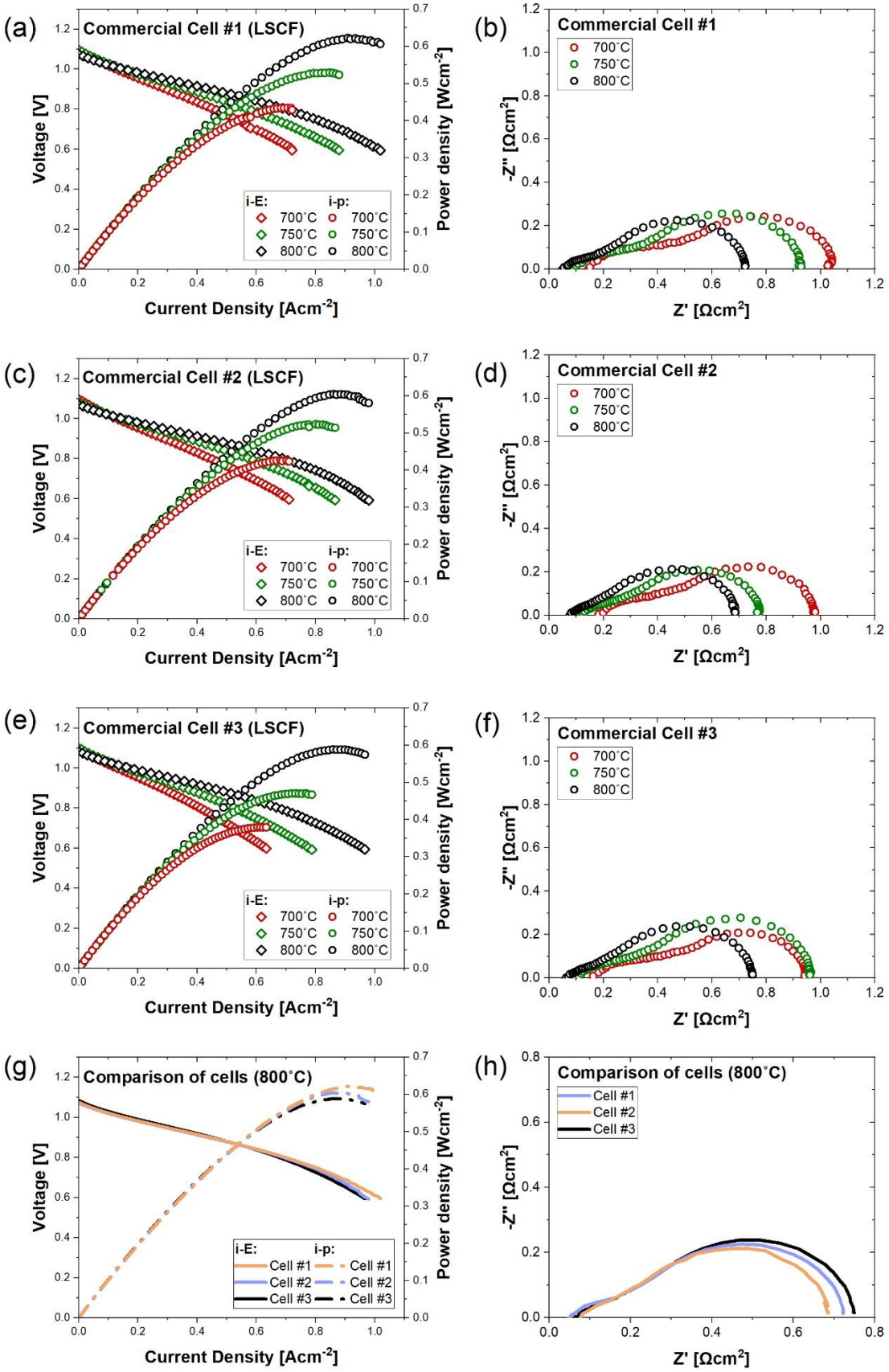


Figure 5.6 - Polarisation and EIS performance of three commercial cells (SOFCMan) containing LSCF cathodes; (a, c, d) polarisation curves, (b, d, e) EIS measurements conducted at OCV, (g, h) comparison of cells at an operating temperature of 800˚C.

Table 5.3 – EIS metrics for commercial cells tested at 800˚C OCV in accordance with conditions shown in Table 5.2

	EIS Metrics [Ωcm^2]		
	Z_{DC}	R_o	R_{pol}
Comm-Cell 1	0.72	0.05	0.67
Comm-Cell 2	0.69	0.07	0.62
Comm-Cell 3	0.75	0.06	0.69
Mean	0.72	0.06	0.66
Std Dev	0.03	0.01	0.04

Table 5.4 – Metrics taken from polarisation curves conducted on commercial cells at T_{Op} = 800˚C

	Current Density at various voltages (Acm^{-2})				
	i_{1V}	$i_{0.9V}$	$i_{0.8V}$	$i_{0.7V}$	$i_{0.6V}$
Comm-Cell 1	0.10	0.37	0.62	0.80	0.93
Comm-Cell 2	0.14	0.43	0.69	0.86	0.97
Comm-Cell 3	0.15	0.41	0.63	0.79	0.91
Mean	0.13	0.40	0.65	0.82	0.94
Std Dev	0.026	0.031	0.038	0.038	0.031

5.3 Assessing the performance of the La-Ni-O phases

With the achievable performance of commercial electrodes identified, it is now possible to develop a comparative understanding on the performance of lanthanum nickelate electrodes under polarisation. 16 cm^2 electrodes were applied to 25 cm^2 commercial half-cell substrates (Ni | Ni-YSZ | YSZ | GDC), procured from *SOFCMan* (as described in Chapter 3). This was with a view to minimising the potential impact of the remaining cell components on the performance variations observed (i.e. the avoidance/minimisation of variability that could conceivably originate from small-scale fabrication techniques). As a consequence, any resulting change in performance can be more reliably associated with the cathode material itself. For completeness, this methodology was also employed with a commercial LSCF powder (*Praxair*). The results of this test are shown in Figure 5.7. An enhancement in the maximum current density output was observed relative to the benchmark study with

commercial LSCF cells (see Figure 5.7a and Figure 5.7c). This highlights the impact of different starting materials and fabrication conditions in the performance of a cathode. These differences are acknowledged here and will be considered again later, in the context of the other cathode materials. For analysis of the EIS measurements (Figure 5.7b), DRT analysis was performed (Figure 5.7e) to identify a suitable equivalent circuit model[22] for modelling processes (the model is shown in the inset of the figure). Polarisation and ohmic resistance values were then determined from non-linear least squares fitting in ZView. The results are summarised against those of the commercial cells in Figure 5.7f. The same approach is applied to the other materials explored in the coming sections.

5.3.1 Lanthanum nickelate cathodes

For the tests conducted on lanthanum nickelate electrodes ($La_2NiO_{4+\delta}$, $La_3Ni_2O_{7-\delta}$, $La_4Ni_3O_{10-\delta}$, $LaNi_{0.6}Fe_{0.4}O_{3-\delta}$), cells were prepared using different cathode sintering temperatures. This reflects the corresponding study on symmetrical cell performance detailed in Chapter 4. The samples prepared are summarised in Table 5.5 and a selection of results are presented in Figure 5.8 to Figure 5.11. A comprehensive collection of data can be seen in Appendix G. As was the case for the tests conducted on the commercial cells, the conditions and contact configuration noted in Table 5.2 were maintained in order to ensure a consistent protocol was followed.

Table 5.5 – Overview of single cell test samples prepared for testing.

	Electrode Sintering Temperature			
Phase	**1000˚C**	**1050˚C**	**1100˚C**	**1150˚C**
$La_2NiO_{4+\delta}$	✓	✓	✓	✓
$La_3Ni_2O_{7-\delta}$	✓	-	✓	✓
$La_4Ni_3O_{10-\delta}$	✓	-	✓	✓
$LaNi_{0.6}Fe_{0.4}O_{3-\delta}$	✓	✓	✓	✓
LSCF-Praxair	✓	-	-	-

[22] Each peak shown in the DRT spectra shown is matched to an RQ element in the equivalent circuit for the modelling process. This is discussed further, later in this chapter. As will also be mentioned, DRT analysis in this thesis has been restricted due to difficulties in identifying the source of the different contributions/modelling elements, as is a typical approach (see Figure G.6 and Figure G.7 in Appendix G).

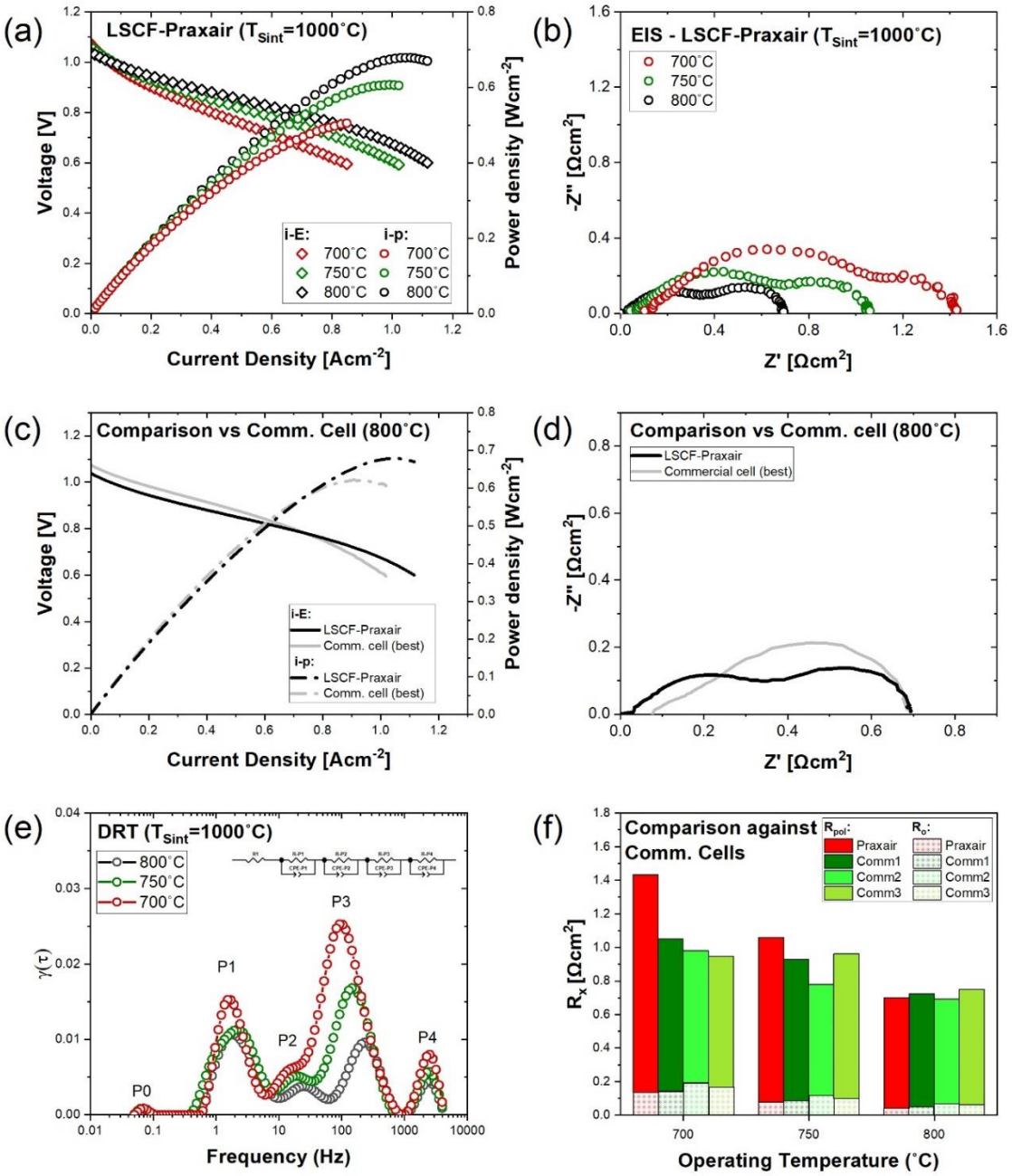


Figure 5.7 - Performance of a commercial LSCF6428 sample deposited onto a commercial half-cell; (a) polarisation curves and (b) EIS spectra recorded at 700, 750 and 800˚C, (c) iV and (d) EIS comparison with the best-performing commercial cell (T_{Op}=800˚C), (e) DRT spectrum (and resulting equivalent circuit model shown, inset) and (f)) performance comparison against full commercial cells (based on EIS measurements).

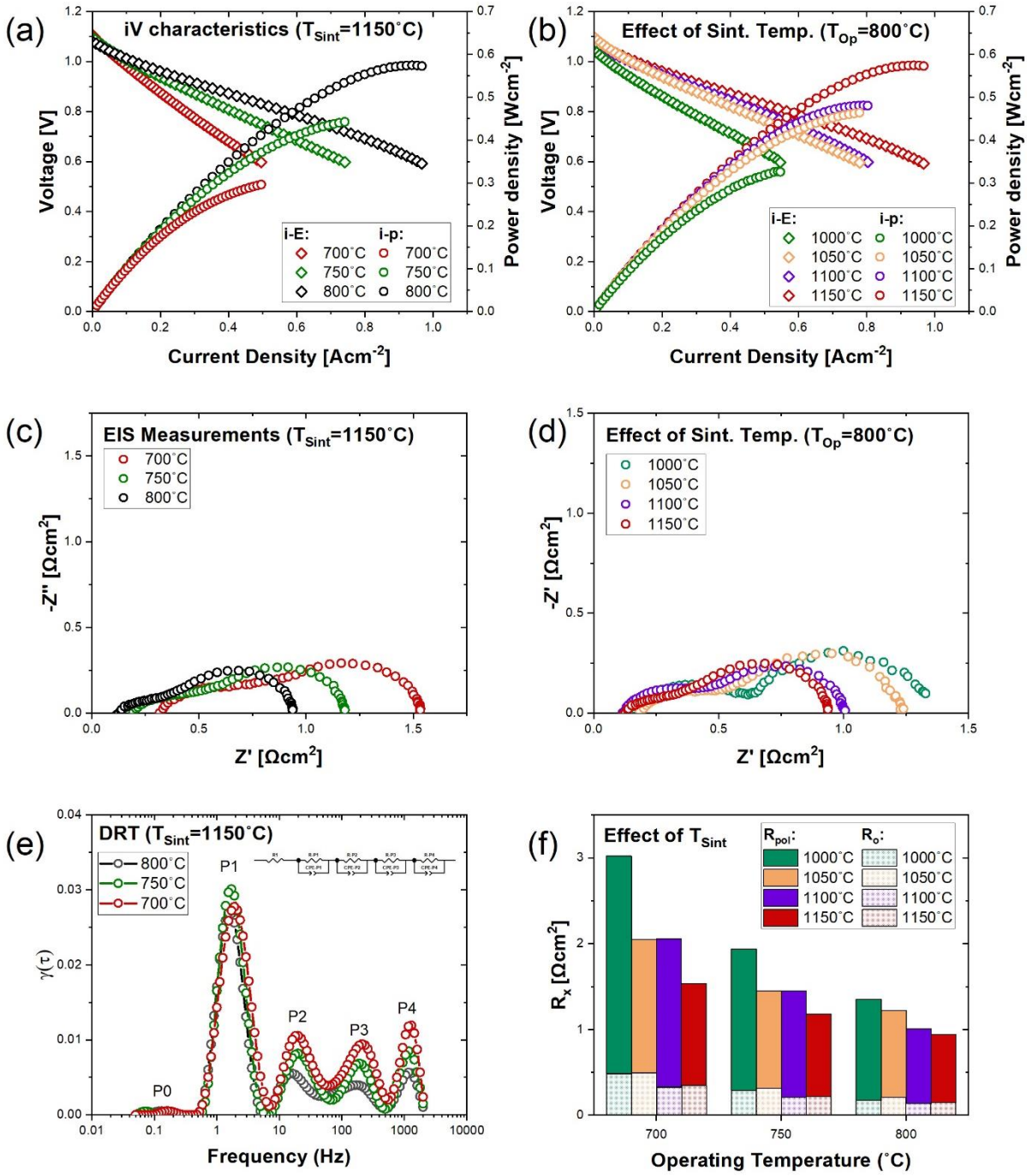


Figure 5.8 - Performance of $La_2NiO_{4+\delta}$ (LNO214) in single cell testing configuration. (a) Polarisation curves taken at 800, 750 and 700˚C for LNO214 electrode sintered at 1150˚C, (b) Effect of increasing sintering temperature on the observed polarisation curves recorded at 800˚C. (c) EIS spectra recorded at 800, 750 and 700˚C for LNO214 electrode sintered at 1150˚C, (d) effect of sintering temperature on EIS spectra recorded at 800˚C. (e) An example of DRT analysis performed on OCV-EIS measurements (LNO214-1150˚C) with the resulting equivalent circuit shown (inset) and (f) a comparison on modelled R_{pol} and R_o values for each electrode (and the effect of sintering temperature). A version of this figure is intended for publication [315].

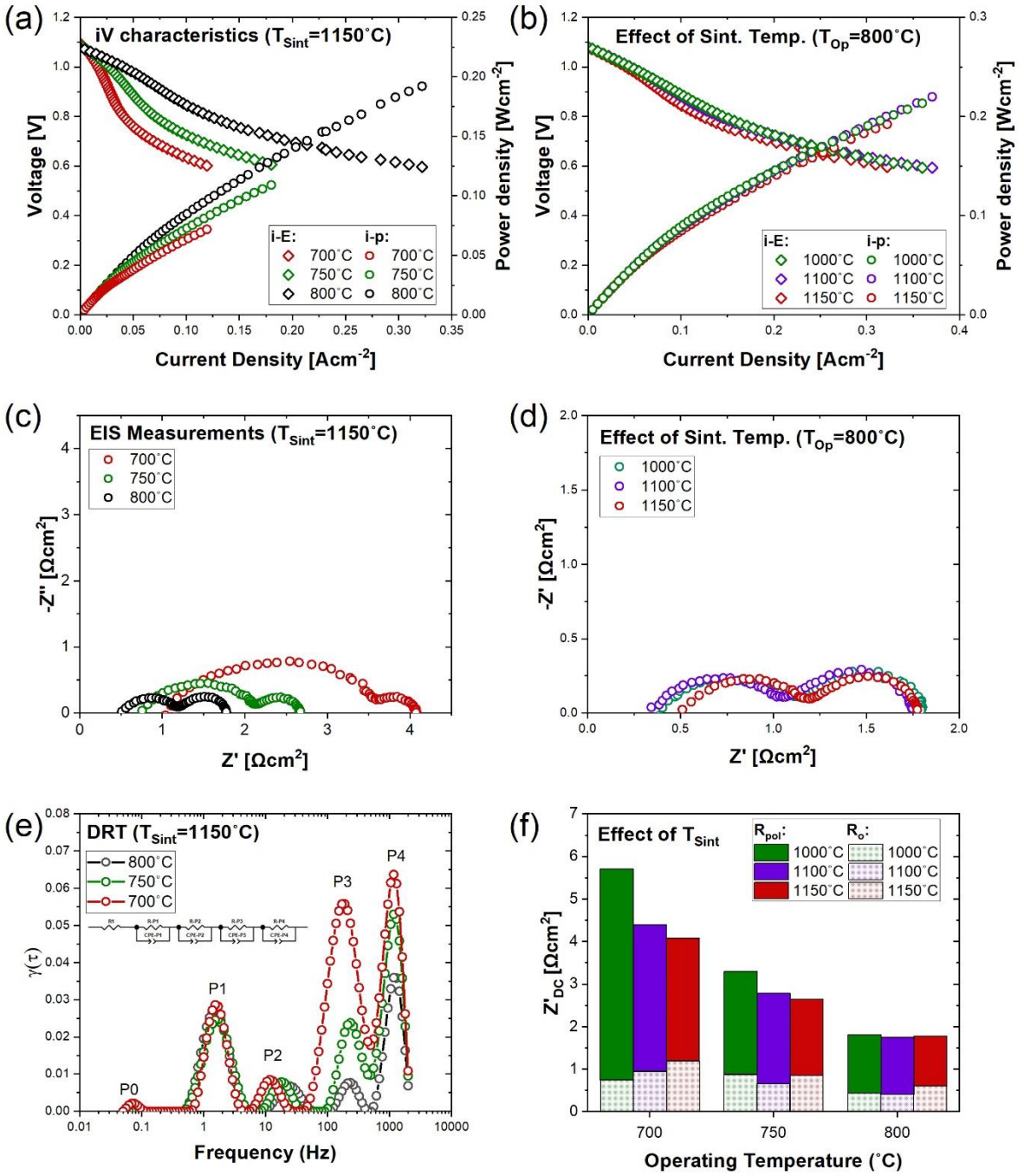


Figure 5.9 - Performance of $La_3Ni_2O_{7-\delta}$ (LNO327) in single cell testing configuration. (a) Polarisation curves taken at 800, 750 and 700˚C for LNO327 electrode sintered at 1150˚C, (b) Effect of increasing sintering temperature on the observed polarisation curves recorded at 800˚C. (c) EIS spectra recorded at 800, 750 and 700˚C for LNO327 electrode sintered at 1150˚C, (d) effect of sintering temperature on EIS spectra recorded at 800˚C. (e) An example of DRT analysis performed on OCV-EIS measurements (LNO327-1150˚C) with the resulting equivalent circuit shown (inset) and (f) a comparison on modelled R_{pol} and R_o values for each electrode (and the effect of sintering temperature).

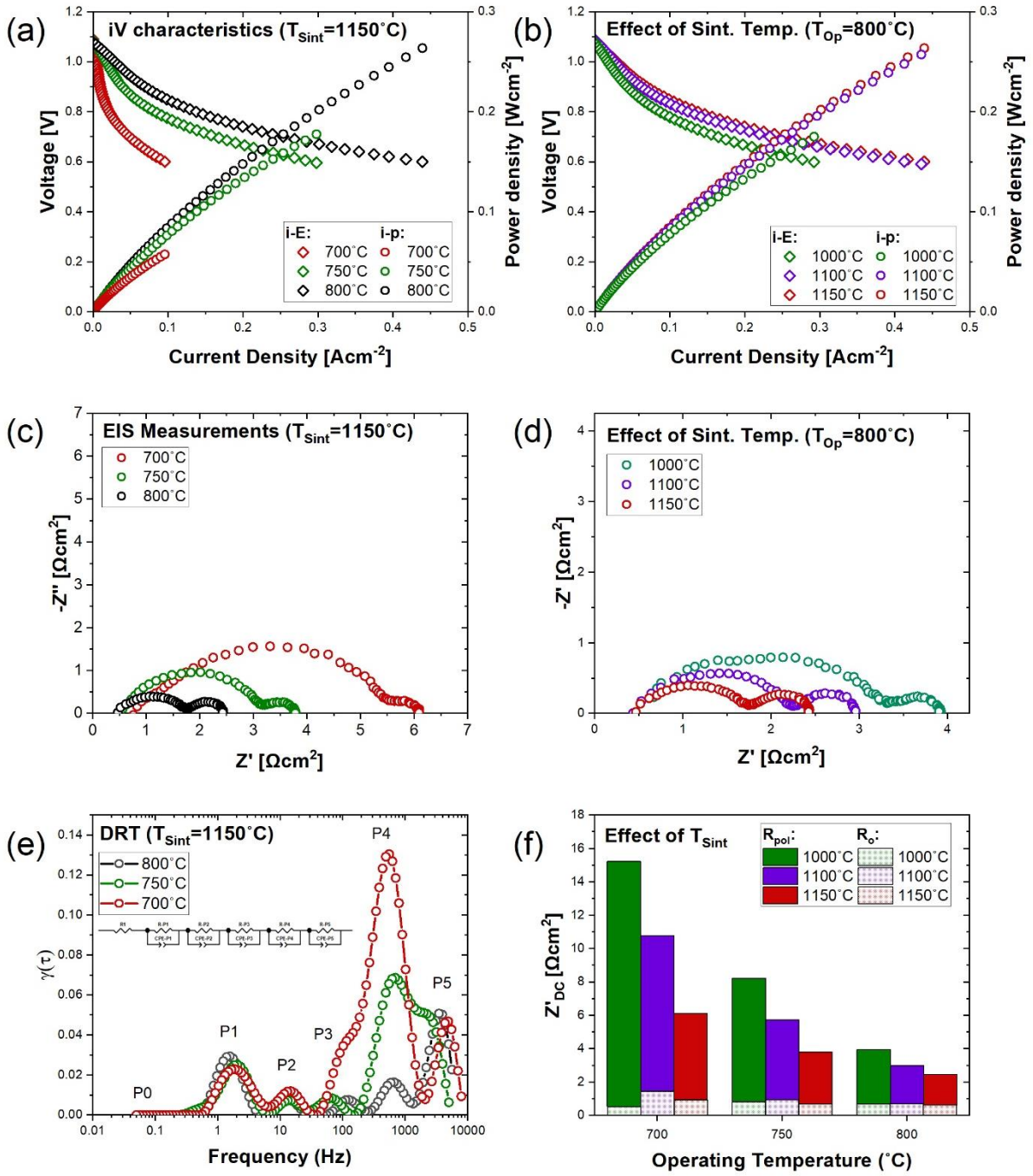


Figure 5.10 - Performance of $La_4Ni_3O_{10-\delta}$ (LNO4310) in single cell testing configuration. (a) Polarisation curves taken at 800, 750 and 700˚C for LNO4310 electrode sintered at 1150˚C, (b) Effect of increasing sintering temperature on the observed polarisation curves recorded at 800˚C. (c) EIS spectra recorded at 800, 750 and 700˚C for LNO4310 electrode sintered at 1150˚C, (d) effect of sintering temperature on EIS spectra recorded at 800˚C. (e) An example of DRT analysis performed on OCV-EIS measurements (LNO4310-1150˚C) with the resulting equivalent circuit shown (inset) and (f) a comparison on modelled R_{pol} and R_o values for each electrode (and the effect of sintering temperature).

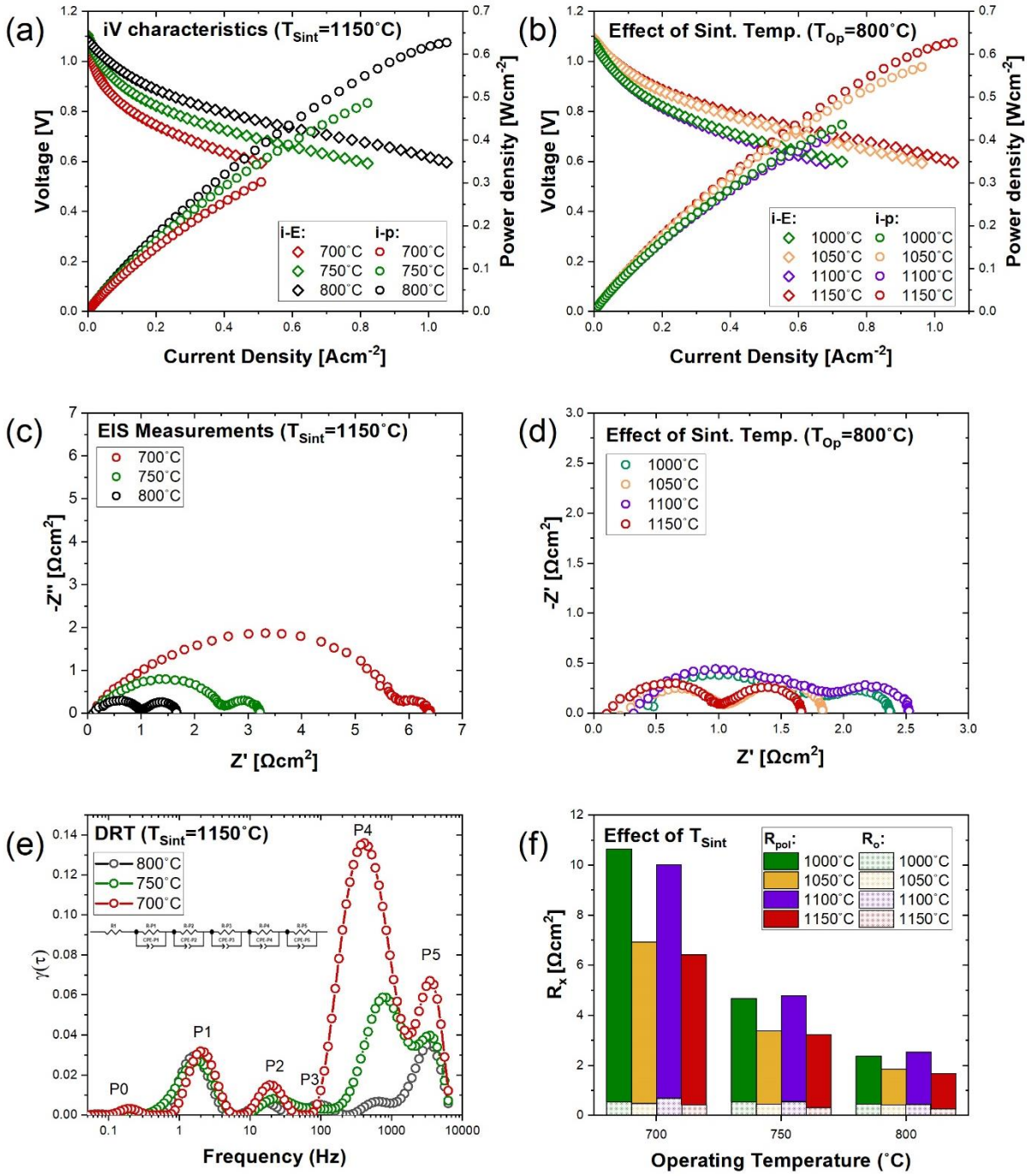


Figure 5.11 - Performance of $LaNi_{0.6}Fe_{0.4}O_{3-\delta}$ (LNF64) in single cell testing configuration. (a) Polarisation curves taken at 800, 750 and 700˚C for LNF64 electrode sintered at 1150˚C, (b) Effect of increasing sintering temperature on the observed polarisation curves recorded at 800 ˚C. (c) EIS spectra recorded at 800, 750 and 700˚C for LNF64 electrode sintered at 1150˚C, (d) effect of sintering temperature on EIS spectra recorded at 800˚C. (e) An example of DRT analysis performed on OCV-EIS measurements (LNF64-1150˚C) with the resulting equivalent circuit shown (inset) and (f) a comparison on modelled R_{pol} and R_o values for each electrode (and the effect of sintering temperature).

5.3.2 Analysis and Discussion

5.3.2.1 Polarisation Curves

Polarisation curves are shown in the (a) and (b) components of Figure 5.8 to Figure 5.11. In (a), an example (T_{Sint} = 1150˚C) of curves taken at 700, 750 and 800˚C is shown for each material. It is noted that the overall current densities that are achieved with the lanthanum nickelates are generally below those of LSCF (more in-depth comparisons are offered shortly). One striking feature about the polarisation curves is their general shape/profile; some materials (LNO327 and LNO4310) demonstrate very large activation losses at low current densities, suggesting very poor electrode behaviours. This is characteristic of the phase studied and is found to be consistent at different sintering temperatures (see (b) in the case of each figure). A comparison between a selection of these curves is shown in Figure 5.12. The relative performance of these cells is dependent on the operating voltage and temperature. In the 'activation region' (i.e. 1.1-1.0 V) some varied behaviours can be viewed. In the case of LNO327, and LNO4310 there is seen to be a sudden drop off in voltage at low current densities (i.e. a large initial activation loss). To a lesser extent, this is also seen for LNF64 – a similar activation behaviour is seen in work by other research groups considering this phase [323,324]. In the case of $La_2NiO_{4+\delta}$, however, a more linear polarisation curve is apparent (i.e. much lower activation losses). Similar behaviour can be appreciated in the literature [236,268]. In the lower voltage region (0.7 to 0.6 V), LNO214 demonstrates larger losses (i.e. a larger ASR or Z_{DC}) compared with the LNF64 phase. It seems likely that this relates to the underlying material properties of these phases. For instance, in the case of LNO214, which possesses excellent oxygen exchange and transport properties [208], impressive performance at high-to-intermediate voltages is noted. This likely suggests facile oxygen exchange kinetics. LNF64, on the other hand, offers the best performance at lower operating voltages where ohmic losses are likely more prominent and hence the excellent electronic conductivity of this phase (e.g. [198,325]) becomes of greater significance. These observations indicate that these two materials appear to show somewhat complimentary behaviour. With the exception of perhaps the LSCF-Praxair electrode (around 0.65 V), it does not appear that any

of the cells enter into a transport-limiting regime within the studied voltage range. This is a result of the poorer reaction kinetics of the lanthanum nickelates.

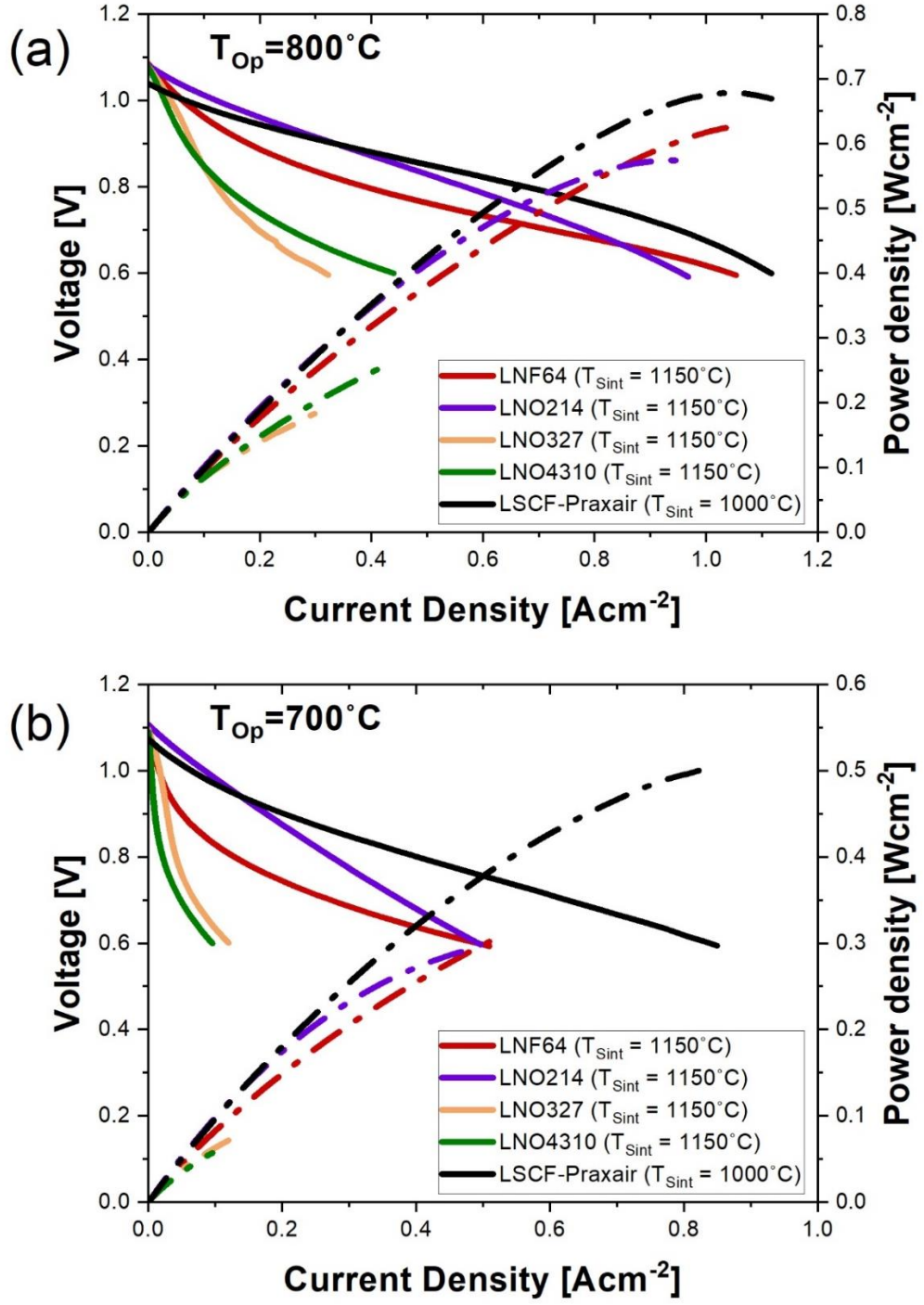


Figure 5.12 - Comparison of polarisation curves recorded for the different cathode materials as obtained at (a) 800˚C and (b) 700˚C. It can be noted that the OCV of the LSCF-Praxair cell is below that of the other cells; this is likely a result of greater hydrogen leakage for this cell (e.g. from sealing or micro-cracks in the electrolyte) in comparison with the other tested cells. Regardless of this, the LSCF-Praxair cell shows the most superior performance of all the shown cells and similar to that of the full commercial LSCF-cells discussed previously.

5.3.2.2 Observations on the effects of sintering temperature

The effect of sintering temperature on the polarisation curves is shown in the (b) component of Figure 5.8 to Figure 5.11. The curves are generally seen to be translated upwards with higher sintering temperatures (i.e. more favourable current output is achieved). In some cases, the effect is shown to be profound; a seemingly dramatic increase in the achievable current output is observed (see Figure 5.13). This is largely supportive of the findings from the symmetrical cell testing (i.e. improved adhesion and particle coalescence leading to better electrode performance). In the case of $La_3Ni_2O_{7-\delta}$, the improvement is shown to be very minimal. Indeed, the performances of the n=2 and n=3 phases (in terms of current output) are generally poor when compared to $La_2NiO_{4+\delta}$ and $LaNi_{0.6}Fe_{0.4}O_{3-\delta}$. Moreover, the former materials fall well short of the LSCF bench-mark. The latter two nickelates, however, are shown to offer comparable performance when electrodes are fabricated at higher temperatures. However, as is shown in Figure 5.12, this 'competitiveness' with LSCF increasingly diminishes as the operating temperature is reduced.

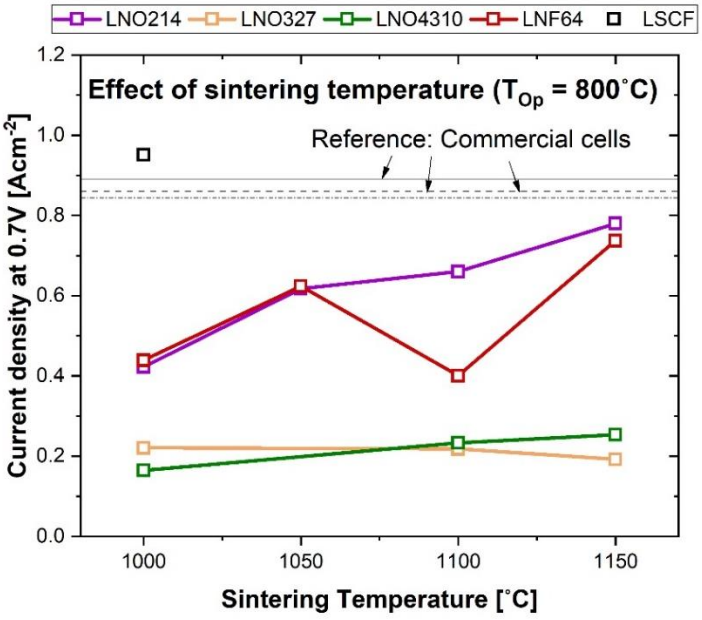


Figure 5.13 – Effect of sintering temperature on the current density at 0.7 V for different phases

The effect of sintering temperature on the EIS performance of each of the materials can be further seen in Figure 5.8 to Figure 5.11 (d and f). A corresponding shrinkage of the EIS curves is also seen, indicating improved species conversion around OCV (i.e. low activation losses, as was also indicated

by the symmetrical cell tests described in Chapter 4). As previously mentioned, and as was discussed in Chapter 4, these effects are likely a result of the improved electrode morphology and the associated improvement in charge transfer. Further to the evidence described in Chapter 4, it has also been noted in these tests that at lower sintering temperatures (T_{Sint}=1000˚C) a complete de-lamination of the electrode was seen during tear-down (see Figure 5.14a and Figure 5.15b). This would appear to be a consequence of a strengthened adhesion between the Ag-mesh and the electrode. Effectively, the disassembly of the cell set-up caused a shearing effect that de-laminated the electrode. At higher sintering temperatures this issue was significantly reduced (Figure 5.14b). These observations would appear to demonstrate the improvement in adhesion between the electrode and electrolyte that is achieved at the higher sintering temperatures. In contrast, the LSCF cathode sintered at 1000˚C was found to retain its integrity upon cell-teardown (Figure 5.14c and Figure 5.15a) despite the cell itself cracking on disassembly. Again, this would suggest that higher sintering temperatures are necessary for the lanthanum nickelate phases even though there is likely to be some reaction (however limited) with the GDC layer at such temperatures.

It is notable that many authors [212,227,237,240,301,326] prefer to employ lower sintering temperatures (~1000˚C) when fabricating lanthanum nickelate electrodes. Partly, this is a means to avoid major reactions with the underlying electrolyte. Indeed, several researchers have attempted to develop novel methods of lower-temperature fabrication routes [327,328]. Whilst powder-reaction testing detailed in Chapter 4 confirmed the reactivity between GDC and La-Ni-O electrodes, this has not been observed to lead to a worsening of electrode performance in the majority of cases. Or, at the very least, the benefits of improved particle connectivity and electrode adhesion far outweigh any negative impacts that may result from interactions. Of course, the optimised sintering temperature may be anticipated to change dependent on particle size (amongst other factors). Nevertheless, care should be taken with the assumption that high temperature sintering regimes should always be avoided with these phases as performance can be significantly improved in at least some cases (Figure 5.13).

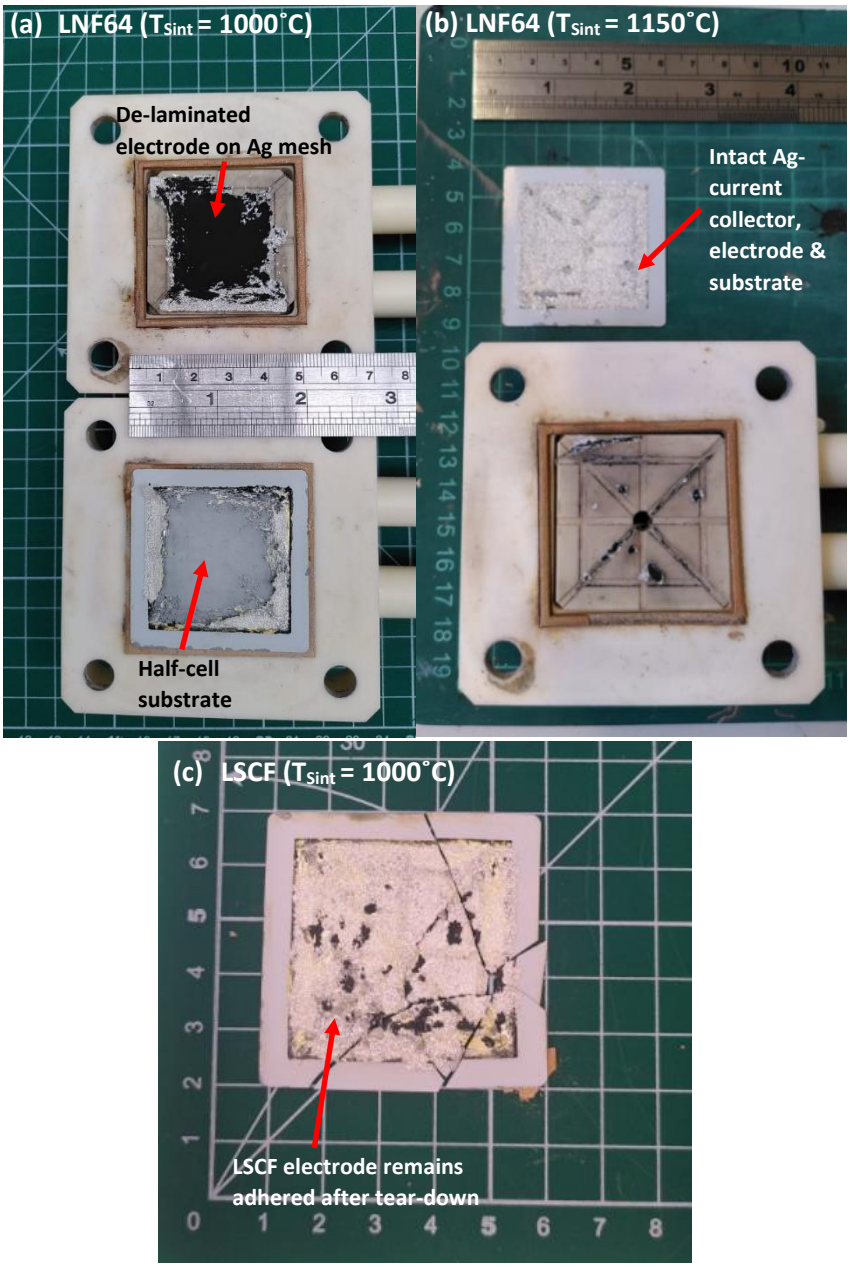


Figure 5.14 – Images taken of SOFC cells on tear-down; (a) LNF64-1000˚C, (b) LNF64-1150˚C and (c) LSCF-1000˚C.

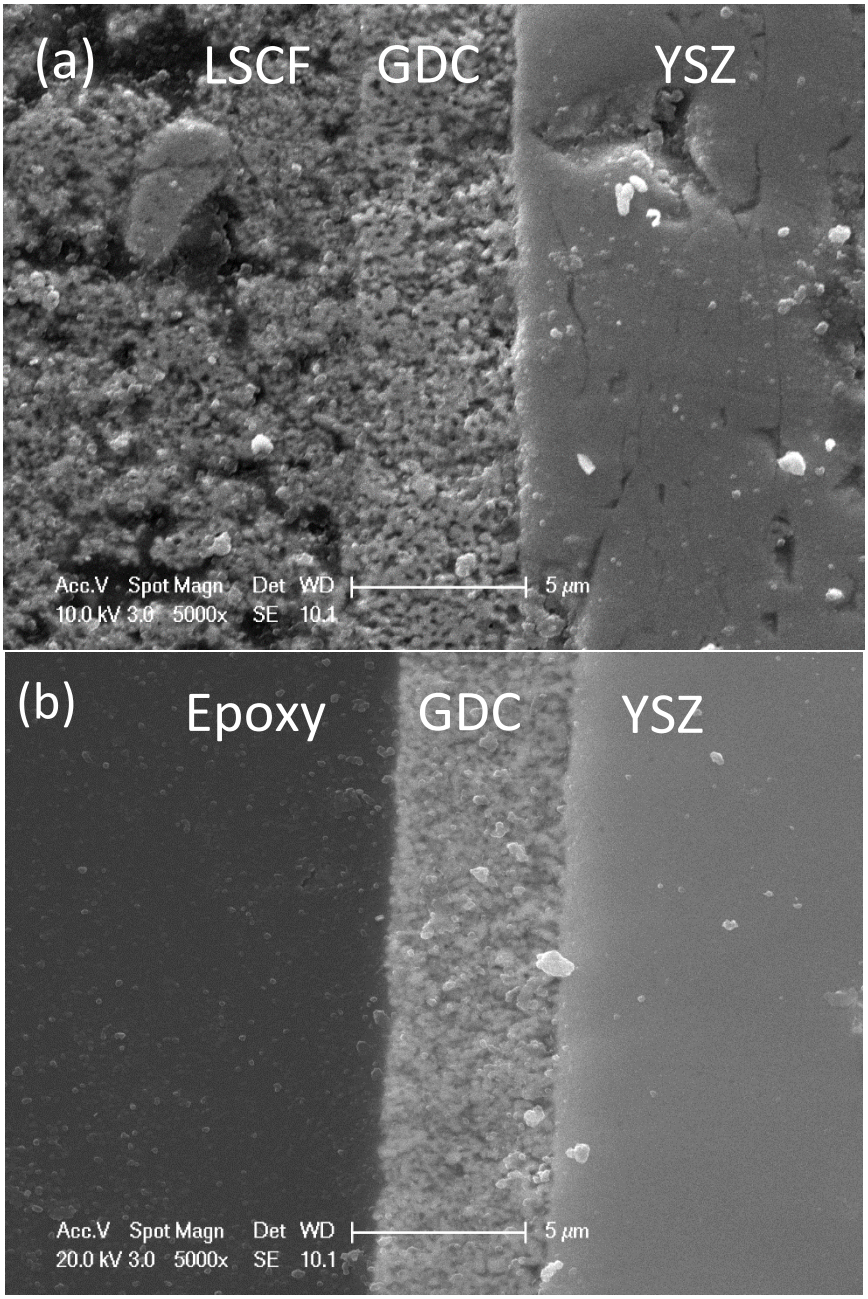


Figure 5.15 – Post-test SEM images of (a, top) in-tact LSCF cathode (T_{Sint}=1000˚C) and (b, bottom) the La-nickelate cathode (T_{Sint} = 1000˚C) was found to be completely delaminated, leaving the GDC layer.

5.3.2.3 EIS observations and comparing material performance

The EIS behaviour of the electrodes studied in this chapter show a sizeable level of variation. In each instance, the EIS spectra appear to be comprised of two arcs or 'contributions' (one at high-medium frequency and a second towards a lower frequency range). In fact, the more in-focus EIS literature [329,330] indicates that these spectra are more likely comprised of around 5 separate contributions associated with the anode and cathode. Indeed, the DRT measurements (see Figure 5.8e to Figure

5.11e) indicate a similar finding where 4 to 5 peaks can be seen in each instance. It is generally agreed that each 'peak' in the DRT spectrum corresponds to an individual electrode process (which has been modelled here using an RQ element; the resulting equivalent circuits are shown in the inset of Figure 5.8e to Figure 5.11e). Unfortunately attempts at further identifying these components by modelling measurements under a range of gas compositions and temperatures was unsuccessful[23] (see Appendix G for these data). The modelled processes cannot, therefore, be reliably assigned to specific components to allow for further insight. As a result of this, a focus must be placed on the total cell polarisation resistance. Overall, this would appear to be an acceptable approach given that the anode contribution can be considered to be the same in each case (i.e. commercial electrode tested under same conditions).

Figure 5.16a shows a summary of the measured polarisation resistance values for each electrode material, across various sintering temperatures. Figure 5.16b summarises the achievable current density at an operating voltage of 0.7 V ($i_{0.7V}$). By both measures, the data available here suggests that lanthanum nickelate performance is below that of the state-of-the-art LSCF. This is largely consistent with observations from literature (see Chapter 2). LNF64, which can be considered to be one of the better performing materials in terms of the achievable current output (Figure 5.16b), shows a comparably large polarisation resistance (R_{pol}) at OCV. $La_3Ni_2O_{7-\delta}$, on the other hand, shows the inverse behaviour. Importantly, therefore, the manner in which a material is categorised as a 'strong performer' is heavily dependent on the metric under consideration. These observations open an interesting avenue of discussion in relation to the correlation between electrodes that show good 'polarisation resistance' (R_{pol}) and those that demonstrate suitable current output. This will be discussed in further detail later.

[23] In the approach trialled, systematically changing the fuel and oxidant partial pressure was intended to identify the processes that were influenced by which variables (and thus identify which processes could be associated with which electrode) – this is in accordance with similar approaches applied in the literature. However, as is shown in Appendix G, the relationships between the processes and the gas pressures were ambiguous. As such, no further analysis was possible.

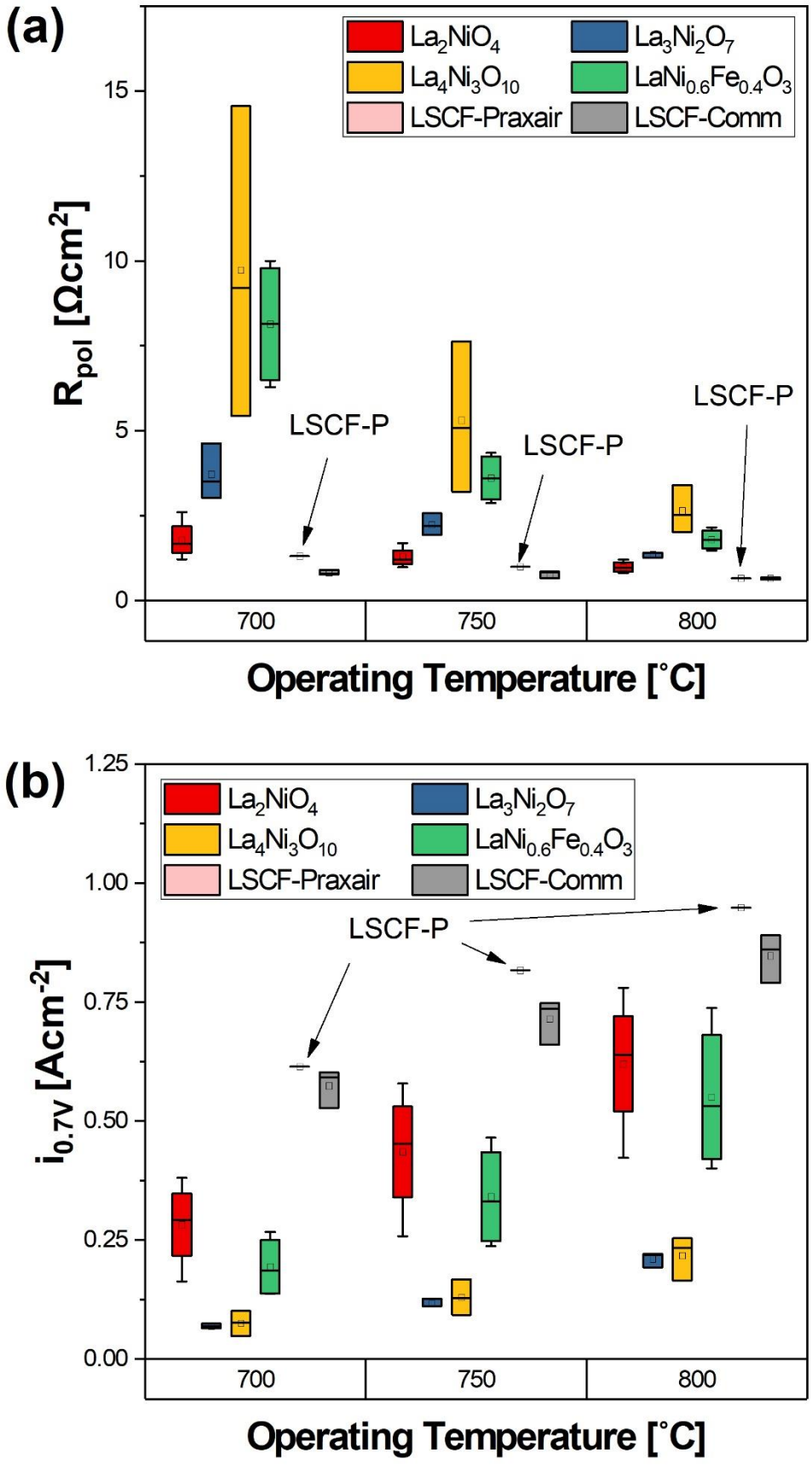


Figure 5.16 – Summary of (a) R_{pol} values measured from single cell tests (various sintering temperatures) and (b) $i_{0.7V}$ values measured from single cell tests (various sintering temperatures).

5.3.2.4 *Comparing single cell test data with symmetrical cell testing data*

Having now considered EIS measurements for a number of materials under both single cell (this chapter) and symmetrical cell (Chapter 4) conditions, it is possible to consider how well the results from these respective experiments correlate. Importantly, the R_{pol} values are not anticipated to be identical given the different cell configurations (i.e. the single cell measurements also contain an anode contribution). However, given that the anode contribution should be the same in each case, these values should remain relatable. A comparison between the polarisation resistance measurements taken from these experiments is shown in Figure 5.17. The displayed data are limited to those test points where Au-contact paste has been applied to the electrodes to ensure a 'like-for-like' comparison. Generally, a correlation is observed between these metrics. This appears to support the notion that the symmetrical cell testing approach suitably represents the EIS behaviour of these electrodes at OCV in the single cell configuration (i.e. the 'real-life' configuration). The overall relevance of these measurements is now discussed.

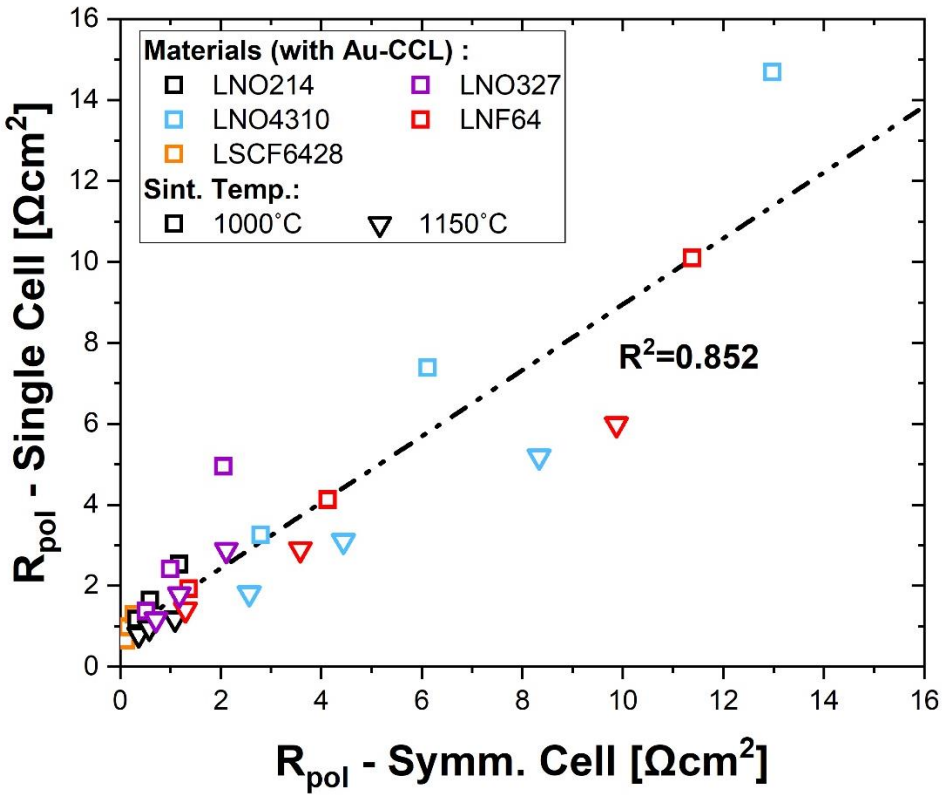


Figure 5.17 - Comparison of polarisation resistances measured in symmetrical cell and single cell testing configurations (Note: comparisons are only drawn with those electrodes where Au-contact paste is applied).

5.3.2.5 Comments on testing methodology: EIS vs current-voltage curves

As has been mentioned, there are some discrepancies with respect to the conclusions that might be drawn from EIS measurements and those drawn from polarisation experiments. A common perception might be that those materials that 'perform well' in the first experiment, do so in the second. Indeed, as has already been mentioned, a number of studies in the literature were found to focus solely on EIS results from symmetrical cell testing when assessing electrode or material performance. There is also a prominence for review papers to reference R_{pol} values, often taken from symmetrical cell tests, as a 'measure of success' [331,332]. In effect, such an approach assumes these results correlate with current output in single cell configurations. But how appropriate is this assumption? Certainly, this correlation might be expected if the iV curves were perfectly linear in all cases (i.e. if $\Delta V/\Delta i$ is constant). However, the non-linearity of iV curves when certain electrode materials are employed has already been noted. A comparison between the inverse of the polarisation resistances (1/R) measured at OCV in the single cell testing configuration and the measured values of current density at 0.7 V ($i_{0.7V}$) is seen in Figure 5.18b. This data covers many operating temperatures, electrode materials and sintering temperatures. The *general* trend observed is that lower polarisation resistances *typically* lead to higher measured current densities. However, this is by no means a '*hard-and-fast'* rule across the various materials (compare the data points of LNF64 and those of LNO327 as an example of this). The trend between ($1/R_{pol}$) values measured at OCV and the current values recorded at 1 V (Figure 5.18a) offers an improved linear[24] relationship as demonstrated by the R^2 values shown in the figures. That is to say that those materials that show low polarisation resistances at OCV also typically show the larger current densities around 1 V. Given that the i_{1V} measurement is closer to the condition under which the EIS spectra are measured, this is perhaps not surprising. However, this observation does highlight the difficulty of drawing certain conclusions about the

[24] The linear relationship of the plots alludes to Ohm's law (V=IR)

performance of a given electrode material in the lower voltage region, based on EIS results recorded at OCV.

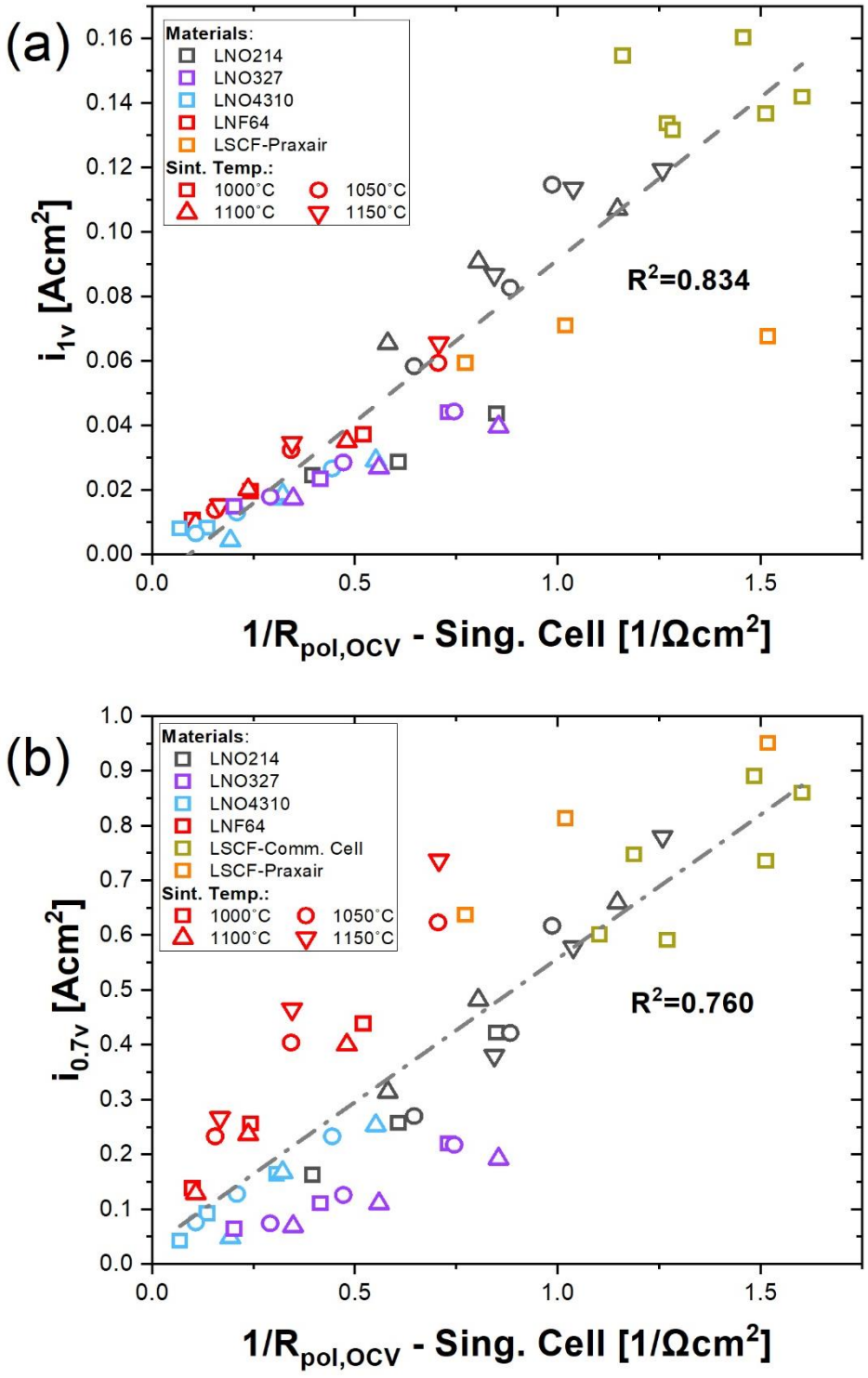


Figure 5.18 - Comparison of measured current density at (a) 1 V and (b) 0.7 V vs the inverse of polarisation resistance measured at open circuit (single cell configuration) across various cells and operating temperatures.

The aforementioned discussion has shown some difficulties in interpreting the various experimental results from a collection of different electrodes. The breadth of materials studied in this thesis, which show a great variety of properties, exposes this issue (as opposed to common literature studies looking at (a) fewer materials, (b) materials with similar properties, or (c) a series of materials with more subtle changes such as doping concentration). This observation can be understood by further study of the polarisation curves. The larger EIS spectra values belong to those materials that possess large activation losses (i.e. those that show steep gradients, $\Delta V/\Delta i$, on the polarisation curves around OCV). Indeed, the gradient at a specific point along the iV curve (e.g. at a given operating voltage) is another approach to calculating ASR values described within the literature [281]. However, these EIS spectra do not account for, or predict, the 'flattening' of the iV curve that is observed with some materials. Most prominently it is seen in the case of the LNF64 electrode, i.e. the material with the best electrical conductivity. The manner in which LNF64 eventually '*catches up'* with the performance of LNO214 in this low voltage region is most likely a result of the increasing ohmic losses in this region and the increasing role of facile electron transport. In that case, therefore, it seems that the EIS measurements at OCV effectively "*under-value*" the importance of electronic conductivity in achieving a truly well-performing cathode material. An alternative theory in this regard, is that the reduction of oxygen in the cathode chamber (as it is consumed and the polarisation curve proceeds to the right) could lead to changes in the phase stoichiometry. In other words, such a condition could lead to an increase in oxygen vacancies and consequently lead to an improvement in oxygen transport at the higher current densities. Considering this further, this effect could be anticipated to be dependent on the material itself. For example, LNF64, LNO327 and LNO4310 are oxygen deficient materials, relying on oxygen vacancies to transport oxygen through their crystal structure. In such cases, a reduction in the partial pressure of oxygen and a corresponding increase in oxygen vacancies would be anticipated to increase oxygen transport (or, at least, lead to an increase in electron holes due to charge compensation) and thus improve electrode performance. Indeed, Sereda et al. [333] have shown the increase in the electrical conductivity of LN64 when oxygen pressure is reduced. In the case of LNO214,

possessing an oxygen surplus, a reduction in oxygen partial pressure and a loss of oxygen interstitials could be anticipated to lead to a loss in the oxygen transport behaviours. This could thus then lead to a relative loss in electrode performance (relative to the case where the oxygen pressure was higher (e.g. at the OCV condition). Indeed, the strong influence of oxygen partial pressure on the oxygen stoichiometry and conductivity of LNO214 can be seen in work by Song et al. [208]; both are shown to increase in oxygen-rich atmospheres. It is interesting however, to consider that in that particular study, whilst the oxygen content of the LNO327 and LNO4310 phase reduces with a decreasing oxygen pressure (as expected), the electrical conductivity *also* slightly reduces (for the aforementioned reasons it might be anticipated to increase with increasing oxygen vacancy content of these phases). Regardless of the cause of the different behaviours shown in Figure 5.12, it should be noted that the behaviour at lower voltage can only be appreciated in the polarisation tests (i.e. symmetrical testing does not offer this insight).

For those electrodes sintered at 1150˚C, further EIS measurements were taken at different operating voltages, effectively exploring performance along the iV curve. The results are shown in Figure 5.19. Observations supporting the previous discussion points can be drawn. Notably, the EIS spectra show that the cells perform differently (with respect to R_{pol} values) at different operating voltages. Interestingly, in the case of LNF64 and LNO214, there is seen to be an increase in R_{pol} values at an operating voltage of 0.6 V (relative to that taken at 0.8 V). This can be explained by consideration of the change in gas conditions as the cell is biased towards lower voltages/higher current densities. This is possibly a result of the reduced quantities of reactant species at these higher current densities. Notably, $La_3Ni_2O_{7-\delta}$ and $La_4Ni_3O_{10-\delta}$ do not observe similar increases in R_{pol} at 0.6 V. Referring back to Figure 5.9a and Figure 5.10a, of course, offers a reminder that at this condition, the current density remains relatively low for these materials and hence H_2-depletion and/or O_2 reduction is lessened. This highlights a key issue with conducting EIS measurements at different operating voltages. That is to say that the different iV characteristics lead to different conditions within the cell components which will heavily influence the resulting EIS spectra. As discussed previously, such a change in gas

conditions could also lead to a change in phase stoichiometry which could also influence performance. This effect is also not ruled out here.

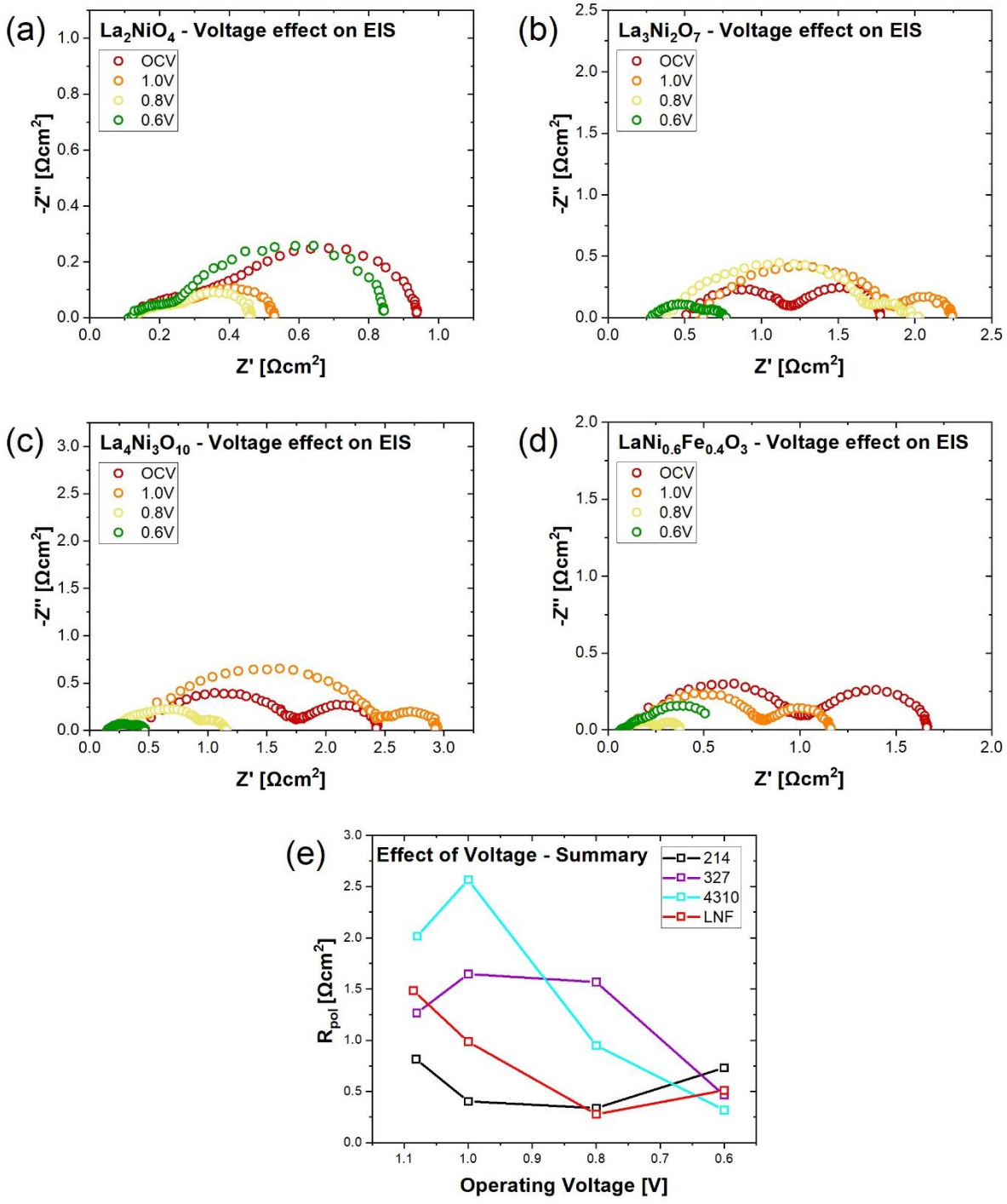


Figure 5.19 - EIS measurements taken at 700˚C with various operating voltages for (a) $La_2NiO_{4+\delta}$, (b) $La_3Ni_2O_{7-\delta}$, (c) $La_4Ni_3O_{10-\delta}$, (d) $LaNi_{0.6}Fe_{0.4}O_{3-\delta}$ and (e) a summary of R_{pol} values against operating voltage for these materials.

At this stage, a rather controversial question can be asked in relation to the relevance of EIS measurements at OCV (symmetrical cell or single cell configuration). Ultimately, the main metric of interest for an SOFC is the current output. EIS measurements are widely performed and their relevance is said to lie in the de-convolution of the impact of various components. However, if the performance at OCV does not correctly reflect the true measure of performance (i.e. current output), what purpose does such analysis serve? However, it is also important to recognise that well performing electrodes will offer optimised current output along the whole breadth of the polarisation curve and not at a single operating point. As such, a more idealised behaviour will likely be achieved with an electrode that performs well in *both* EIS experiments and in polarisation experiments. Certainly, this was found to be the case with the LSCF cathodes which demonstrated favourable performance around OCV and in the lower voltage region (Figure 5.16). Further attempts to identify a suitable lanthanum nickelate electrode that can achieve both of these performance metrics are detailed in Chapter 6. In that chapter, symmetrical cell testing will be employed as an initial approach to 'screen' electrodes. Such a methodology is simple and can aid with the identification of electrodes that will likely perform well in the higher voltage range (or, in other words, around OCV). Since the attention turns to optimising an electrode with promising behaviour in all regions, this is deemed to be a suitable approach. The single cell testing method has already been shown to be vital in confirming that suitable performance is achievable in the intermediate-to-lower voltage region. As such, those electrodes that are identified as offering promise will be further analysed in the second configuration.

5.4 Conclusions from single cell tests

5.4.1 Main observations

In this chapter a series of single cell tests have been detailed. A number of major observations can be made. Firstly, in relation to developing a repeatable test with good quality results:

- Contact paste has been found to be necessary on the oxygen electrode – this has been shown to reduce the contact resistance and thus reduce the ohmic contribution in the EIS spectra

considerably. In turn, this appears to indicate the difficulties with a solid-on-solid electrical contact on the cathode side of the cell. Attempts to avoid the use of contact paste have demonstrated noisy EIS data in addition to low current outputs.

- On the other hand, the use of such contact paste on the anode has been found to have no beneficial impact and, in fact, appears to offer an inhibiting factor with respect to the current density that is achievable. This is likely due concentration losses, with the Au-layer acting to inhibit species transport to some extent.
- The use of a humidified stream of hydrogen has been found to offer more repeatable results with respect to impedance measurements at OCV – fundamentally, this relates to variable leakage rates and the effects of $p(H_2O)$ on cell voltage, specifically at $p(H_2O)=0$, as described by the Nernst equation.
- Bench-mark performance metrics were determined for commercial cells with key metrics at 800˚C shown in Table 5.3 and Table 5.4.

In relation to the lanthanum nickelate electrodes, the following key points were observed:

- In general, the performance of all of the studied lanthanum nickelates is below that of the state-of-the-art material LSCF – this is shown to be true in consideration of both the considered metrics ($i_{0.7V}$ and R_{pol}).
- Whilst the performance of the materials has been shown to be generally inferior to LSCF, the data here indicate that $La_2NiO_{4+\delta}$ and $LaNi_{0.6}Fe_{0.4}O_{3-\delta}$ (and not the higher order Ruddlesden-Popper phases as suggested by some literature) can offer the most competitive outputs.
- In particular, this has been shown to be the case for electrodes sintered at higher temperatures which offer higher current densities and lower R_{pol} values. This supports the observations in Chapter 4 where similar trends were seen and associated with improvements in particle coalescence and electrode adhesion.

- Each of the considered materials appears to show a characteristic iV curve with a defined profile specifically with regards to activation and ohmic behaviours. This shape is consistent across the various sintering temperatures that have been adopted and would appear to relate to the underlying properties of the electrode materials that are well-described in literature.
- $La_2NiO_{4+\delta}$, for instance, has a very linear-like IV curve whereas $LaNi_{0.6}Fe_{0.4}O_{3-\delta}$ has a very pronounced 'activation region' but improved ASR in the lower voltage regime.
- This behaviour was also found to be reflected in the EIS measurements taken at OCV.

Due to the range of materials that have been considered in this chapter, several notable points in relation to the testing of SOFCs can be made:

- Conclusions that may be drawn based on EIS measurements at OCV in relation to the performance of a given cell may not *necessarily* reflect the conclusions that are drawn from current density measurements at standard operating voltage, e.g. $i_{0.7V}$. For example, based on the EIS results in this study, it may be considered that LNF64 is one of the worst performing nickelates and yet, at an operating voltage of 0.6 V, the largest current density of all the nickelate materials is seen (i.e. it is the 'best performer' at high currents with a low ASR).
- This supports a conclusion that studies on material selection or optimisation should not solely focus on EIS results as a single means by which an electrode performance can be determined – in turn, this could lead to a questioning of the symmetrical cell testing approach, which broadly reflects the behaviour seen in single cell EIS test data at OCV.
- However, an optimal SOFC electrode is likely to show excellent behaviour at both high and low voltage regions (i.e. low activation losses and ASR, as LSCF has been found to achieve) and, as such, EIS behaviour at OCV remains of significance in developing an electrode to '*rival*' the state-of-the-art.

5.4.2 Next Steps

Based on the observations on lanthanum nickelate electrode performance detailed in this chapter, a series of further questions remain that can be explored in Chapter 6:

- It has been shown that, to some extent at least, the performance of electrodes can be optimised via appropriate strategies in relation to cell fabrication (e.g. optimising sintering temperature) – further optimisation via the fabrication of composite electrodes can provide the opportunity for an additional improvement to be obtained. For example, can a combination of materials be found that show superior properties to the state-of-the-art electrodes?
- An understanding on the properties of the La-Ni-O materials would suggest that different effects can be anticipated when combining each with different phases that show contrasting behaviour. For example, the combination of an ionic-conducting phase (e.g. GDC) with $LaNi_{0.6}Fe_{0.4}O_{3-\delta}$ may provide an optimal solution for that material whereas it may be preferable to mix $La_2NiO_{4+\delta}$ with a phase with better electronic conducting properties. Many authors [236,270,334] have sought to combine the $La_2NiO_{4+\delta}$ phase with ionic-conducting phases but this appears to neglect observations that the poor electronic conductivity is the limiting factor for this phase.
- Further, the evidence from the literature and from Chapters 4 and 5 would suggest that the family of lanthanum nickelate materials explored in this study offers complimentary properties and behaviour – does a mixture of appropriate phases offer any significant performance improvement?
- It has been acknowledged that La-Ni-O phases have some reactivity with CeO_2 phases but it has been observed that higher sintering temperatures improve (rather than hamper) cell performance. This may indicate that the "impurity" phase offers suitable conductivity (and/or some alternative beneficial effect). Alternatively, any 'negative' impact such phase formation may have may simply be heavily outweighed by improvements to particle connectivity (and

hence transport properties). A further study is conducted on an alternative interlayer material to see if it is possible to offer a further improvement. Also, longer-term measurements would need to confirm that ongoing reactions do not decrease the cathode properties with time.

6 Strategies for the optimisation of composite lanthanum electrode performance via appropriate material selection

6.1 Overview of chapter

In the previous experimental chapters of this thesis, the focus was on defining the performance of single-phase SOFC cathodes. In this chapter, similar techniques will be utilised to explore the advantages of employing composite electrodes (i.e. electrodes consisting of multiple phases). This is with a view to further optimising the performance of the lanthanum nickelates beyond what was achieved in previous chapters. The findings in this chapter are intended to inform future research directions for the optimisation of alternative electrode materials.

As was described in the literature review of this thesis, composite lanthanum nickelate electrodes are not, in isolation, a novel concept and, indeed, have already been studied by a number of researchers. However, it is notable that there is often very little discussion around what might be the most appropriate strategy (or strategies) to selecting a suitable combination of materials with complimentary properties. For instance, a selection of studies pair $La_2NiO_{4+\delta}$ with excellent ionic-conducting phases such as doped ceria (e.g. [236,270]). This approach would appear to overlook a rather fundamental truth that has been noted earlier in this work; the performance of $La_2NiO_{4+\delta}$ is limited by poor electronic transport, rather than by oxygen transport. Therefore, it would be expected to be a more suitable strategy to combine this particular material with a predominantly electronic conducting material. Alternatively, a mixture of the electronic conducting properties of LNF64 and the oxygen transport properties of GDC10 ($Gd_{0.1}Ce_{0.9}O_2$) might provide a more credible option. A further question is, can the performance of the n=2 and n=3 Ruddlesden-Popper phases be significantly improved by combination with additional phases? Whilst some of these described composites have been explored individually (e.g. LNO214-LNF composites [335]) in the literature (and indeed these have been shown to offer promise in promoting performance over single-phase electrodes) a wider survey of different composites is lacking. As such, it is difficult to identify *which* approaches are likely to be the most promising. A broad study of different lanthanum nickelate-based composite electrodes

would make it possible to garner a more comprehensive understanding on this matter and comment on future directions for electrode development. In this chapter, three types of composite are studied; (1) GDC-lanthanum nickelate, (2) LNF64-Ruddlesden-Popper, (3) LDC45-lanthanum nickelate. This is with a view to combine the lanthanum nickelates with phases that can provide different benefits (e.g. improved electronic conductivity or oxygen transport). LNF64 was selected as a material that demonstrates excellent electronic properties whereas GDC was selected as a material with excellent oxygen transport properties. LDC45 ($La_{0.45}Ce_{0.55}O_{2-\delta}$) was selected with a view to identifying an oxide conducting CeO_2-phase which, as will be shown later, could avoid the reaction between the lanthanum nickelate and the CeO_2-phase.

As has already been acknowledged earlier in this thesis, defining the performance of a given electrode can be complex and one of the simplest and most widely used routes (i.e. symmetrical cell testing) does not necessarily identify those electrodes that can provide maximum power output. However, as was discussed in the previous chapter, symmetrical cell testing is a simple and effective means of scoping how an electrode will behave in the low current density/high voltage region. Given that the state-of-the-art materials have been shown to offer excellent performance at both high and low voltages (and in both symmetrical cell and single cell tests), it seems fair to suggest that a competing electrode must do the same. As such, in this chapter, symmetrical cell testing is employed (in combination with the intelligence gained from previous chapters) as an approach to perform an initial screening of electrodes. This is with a view to identify promising material combinations that are then further assessed via single cell testing. As per previous chapters, an emphasis will be placed on providing a benchmark against state-of-the-art materials and against achievements reported in the literature.

6.2 Screening Electrodes (Symmetrical Cell Testing)

6.2.1 Overview of tests

To assess the potential of composite electrodes in promoting the performance of the lanthanum nickelate materials, a series of electrodes were prepared. These are summarised in Table 6.1. As in Chapter 4, these tests were performed both with and without the use of a gold current collector layer (Au-CCL). This was, again, to study its effect on these different combinations of materials. In each instance, the lanthanum nickelate materials were combined in a 1:1 volume ratio with a secondary phase and added to an ink vehicle prior to deposition via hand-painting. In addition to the use of GDC10 (*Fuel Cell Materials*), which was introduced with a view to improving oxide ion transport in the cathodes, these tests also considered the effects obtained by the use of lanthanum doped ceria ($La_{1-x}Ce_xO_2$). This phase has been explored in a limited number of reports (e.g. [336]) in an attempt to overcome the potential deleterious impact of the reaction between the lanthanum nickelate phases and GDC materials. As has already been described, the experimental analysis conducted so far in this thesis indicated that this effect is relatively minor (i.e. significantly improved performance was noted even at higher sintering temperatures). However, it is also noted that any such reactions in the case of those previously discussed single-phase electrodes would be limited to the electrode-electrolyte interface. As such, it could be anticipated that degradative effects might become more pronounced in a composite nickelate-GDC electrode where the number of contact points were increased and, hence, the extent of impurity formation increased. To further assess this, a comparison with LDC45 is offered. Details on the preparation of LDC compositions and a study on reactivity are described in Section 6.2.2. The final group of composites described in this initial work are the combination of LNF (shown in previous chapters to display very good electronic conduction properties) with the remaining lanthanum nickelate materials (i.e. Ruddlesden-Popper phases). In this case, the aim of secondary phase addition is to enhance electronic transport through the cathode layer.

Table 6.1 – Overview of symmetrical cell tests conducted in this chapter. Materials were mixed in 1:1 volume ratio.

	GDC (1000˚C)	GDC-Au (1000˚C)	LNF (1000˚C)	LNF-Au (1000˚C)	LDC45 (1150˚C)	LDC45-Au (1150˚C)
$La_2NiO_{4+\delta}$	✓	✓	✓	✓	✓	✓
$La_3Ni_2O_{7-\delta}$	✓	✓	✓	✓	-	-
$La_4Ni_3O_{10-\delta}$	✓	✓	✓	✓	-	-
$LaNi_{0.6}Fe_{0.4}O_{3-\delta}$	✓	✓	-	-	✓	✓

6.2.2 LDC synthesis, reactivity and layer preparation

The synthesis of $La_xCe_{1-x}O_2$ materials (this general form herein denoted LDCX) was found to be possible via the same Pechini route detailed earlier in this thesis. In line with the previously described approach, reagents of $La(NO_3)_3.(6H_2O)$ (*Merck, 99.99%*) and $Ce(NO_3)_3.(6H_2O)$ (*Sigma-Aldrich, 99%*) were dissolved in water at 80˚C. Citric acid (*Sigma Aldrich, 99%*) and ethylene glycol (*VWR*) were then added in stoichiometric ratios (1.5 CA: 1.5 EG: 1 total metal ions). The resulting gel was then heated to 350˚C and the subsequent ash-like material was ground and annealed at 1000˚C for 12 hours. To identify an optimum $La_xCe_{1-x}O_2$ phase that could avoid reactivity with the lanthanum nickelate materials, a series of materials were prepared ($La_{0.1}Ce_{0.9}O_2$, $La_{0.3}Ce_{0.7}O_2$, $La_{0.35}Ce_{0.65}O_2$, $La_{0.4}Ce_{0.6}O_2$, $La_{0.45}Ce_{0.55}O_2$ $La_{0.5}Ce_{0.5}O_2$ herein denoted LDC10, LDC30, LDC35, LDC40, LDC45 and LDC50, respectively). The XRD scans taken from these materials can be seen in Figure 6.1 where they are additionally compared with a commercial CeO_2 material (*VWR International; ≥ 99.5%*); the relative shift in the spectra can be seen as the lanthanum dopant concentration is increased.

After synthesis of the LDCX phases, a reactivity study was conducted between these materials and the lanthanum nickelate phases to identify a compatible combination of materials. A selection of the LDCX phases were mixed with the lanthanum nickelates in a 1:1 mass ratio and heated to 1100˚C. The results of reaction between LDCX phases and LNO214 can be seen in Appendix H. It is apparent from those tests that at low lanthanum dopant concentrations some reaction remained apparent. However, this was seemingly minor in comparison with similar compatibility tests conducted with GDC10 (see

Chapter 4). As the lanthanum concentration was increased, the level of reactivity was found to decrease. No impurity phases were observed after heating with a composition of $La_{0.45}Ce_{0.55}O_2$ at 1100˚C. Reactivity between LDC45 and the LNO214 and LNF64 phases was also avoided when the phases were heated to 1150˚C, as is shown in Figure 6.2 and Figure 6.3. Given previous observations of lanthanum migration from the cathode phase into the electrolyte phase, the observations here seem logical. An increase in the La-concentration is likely to limit any cation diffusion. Given the results of the reactivity tests detailed in this section, LDC45 phase was identified as a phase of further interest for combination with the nickelate phases. It is stressed here that LDC45 has been identified purely on the grounds of compatibility. In part, this is to see whether or not the avoidance of secondary phase formation during fabrication is significantly beneficial or not. Given higher La-dopant concentrations (x>~0.2) have been shown [337,338] to offer inferior conductivity properties to those materials with lower concentrations, it is plausible that LDC45 may not offer optimum performance. However, as described, this material was selected on the grounds of electrolyte-electrode compatibility.

In advance of LNO214-LDC45 and LNF64-LDC45 electrode deposition, an LDC45 barrier layer was first applied to the electrolyte substrates. These layers were applied to commercial 5 x 5cm^2 YSZ substrates for symmetrical cell testing and, later, to commercial half-cells (Ni-YSZ | YSZ). In order to achieve this, an LDC45 ink was prepared. The synthesised materials were added to deionised water alongside a series of additives (see Table 6.2). The constituents were measured out and mixed on a roller-mill for around 24 hours. The resulting ink was then placed under a vacuum to remove any air. The ink was subsequently applied to the exposed surface of the substrates using a pipette and a thin layer achieved via spin coating. The resulting samples were then dried and sintered at 1200˚C. An image of a resulting layer is shown in Figure 6.4. It was observed that there was some small leakage of the ink around the masking (highlighted in Figure 6.4). This was found to be difficult to avoid using spin coating but any areas of leakage (i.e. around the masking) were gently sanded to prevent a short-circuit between the anode and cathode.

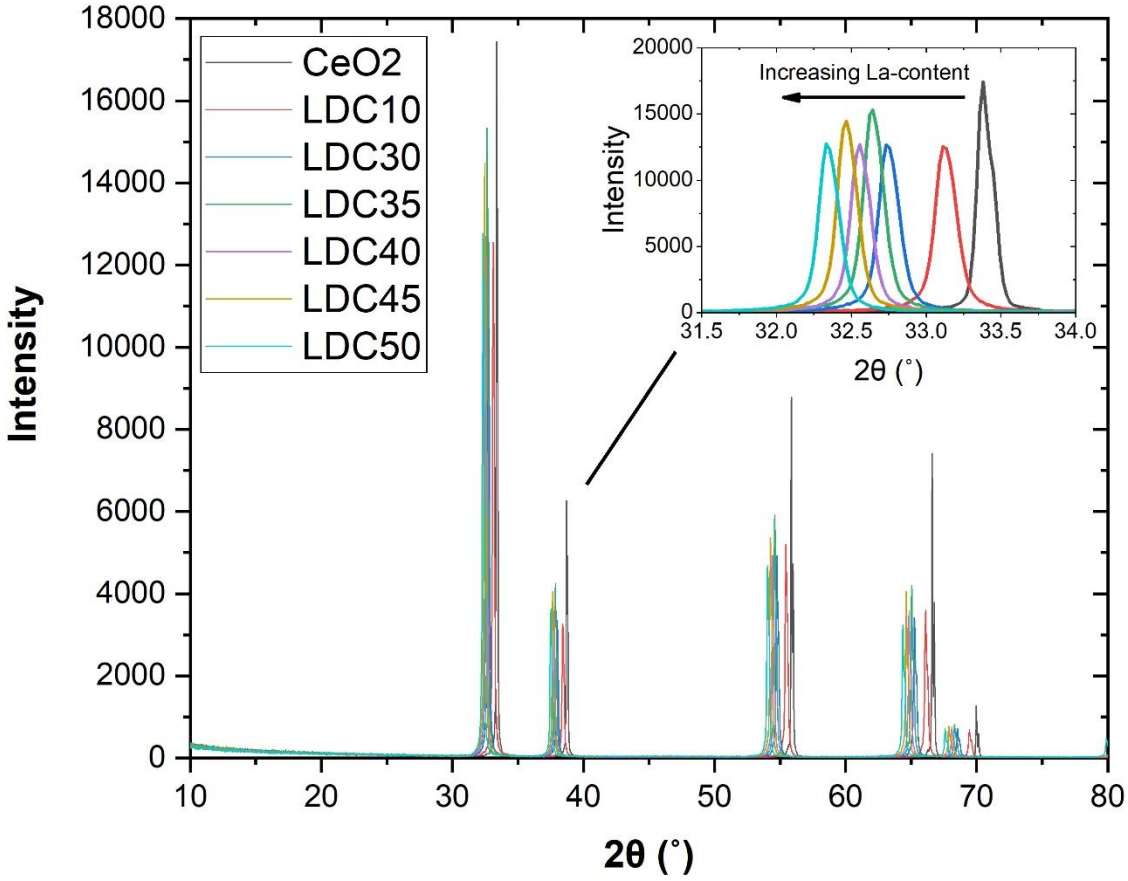


Figure 6.1 – XRD pattern of LDCX compositions against commercial CeO_2 material.

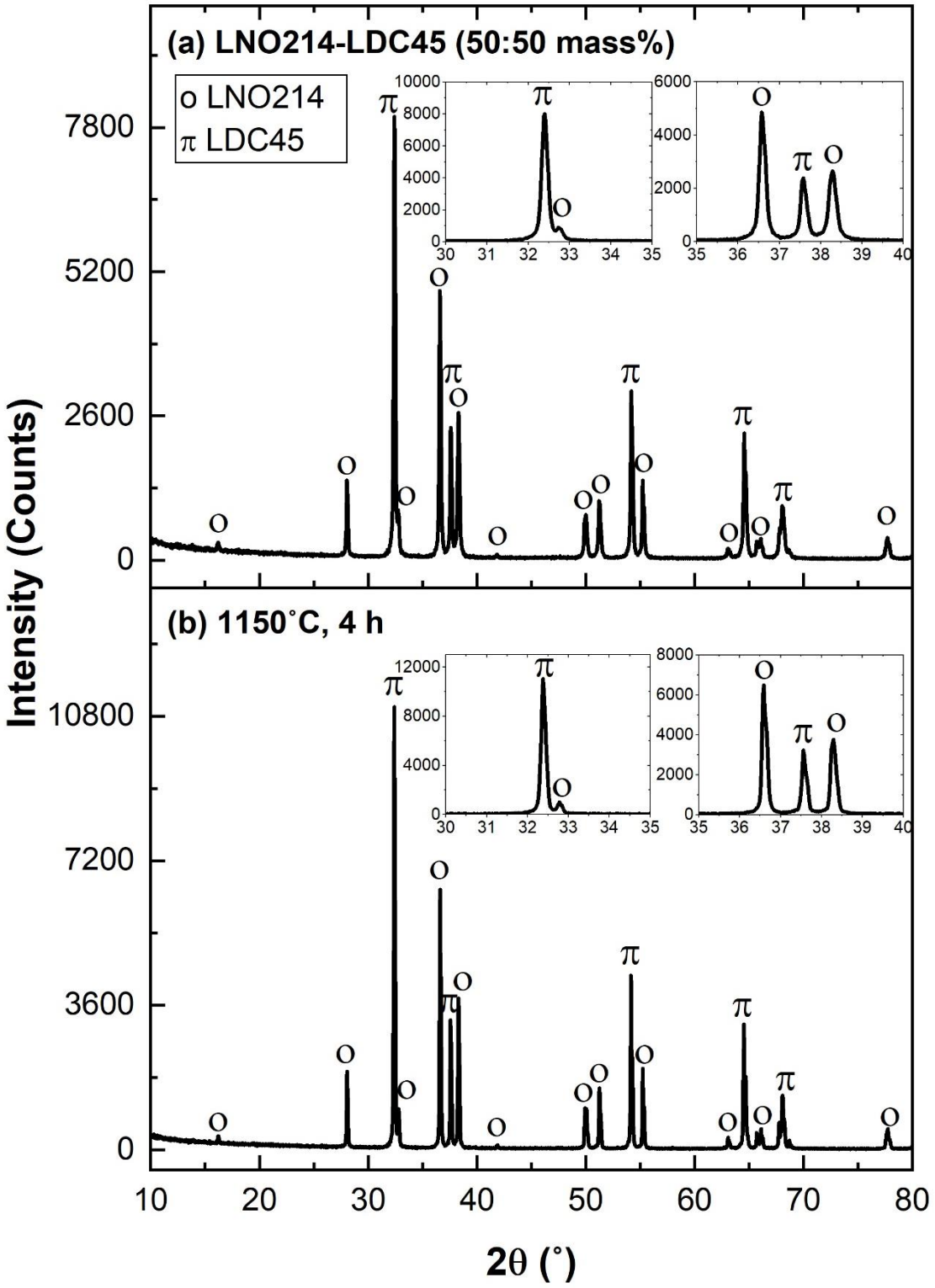


Figure 6.2 – Reactivity test of $La_2NiO_{4+\delta}$ and $La_{0.45}Ce_{0.55}O_2$; XRD results for (a) 50:50 mass% mix of materials prior to heating and (b) after heating to 1150˚C for 4 hours.

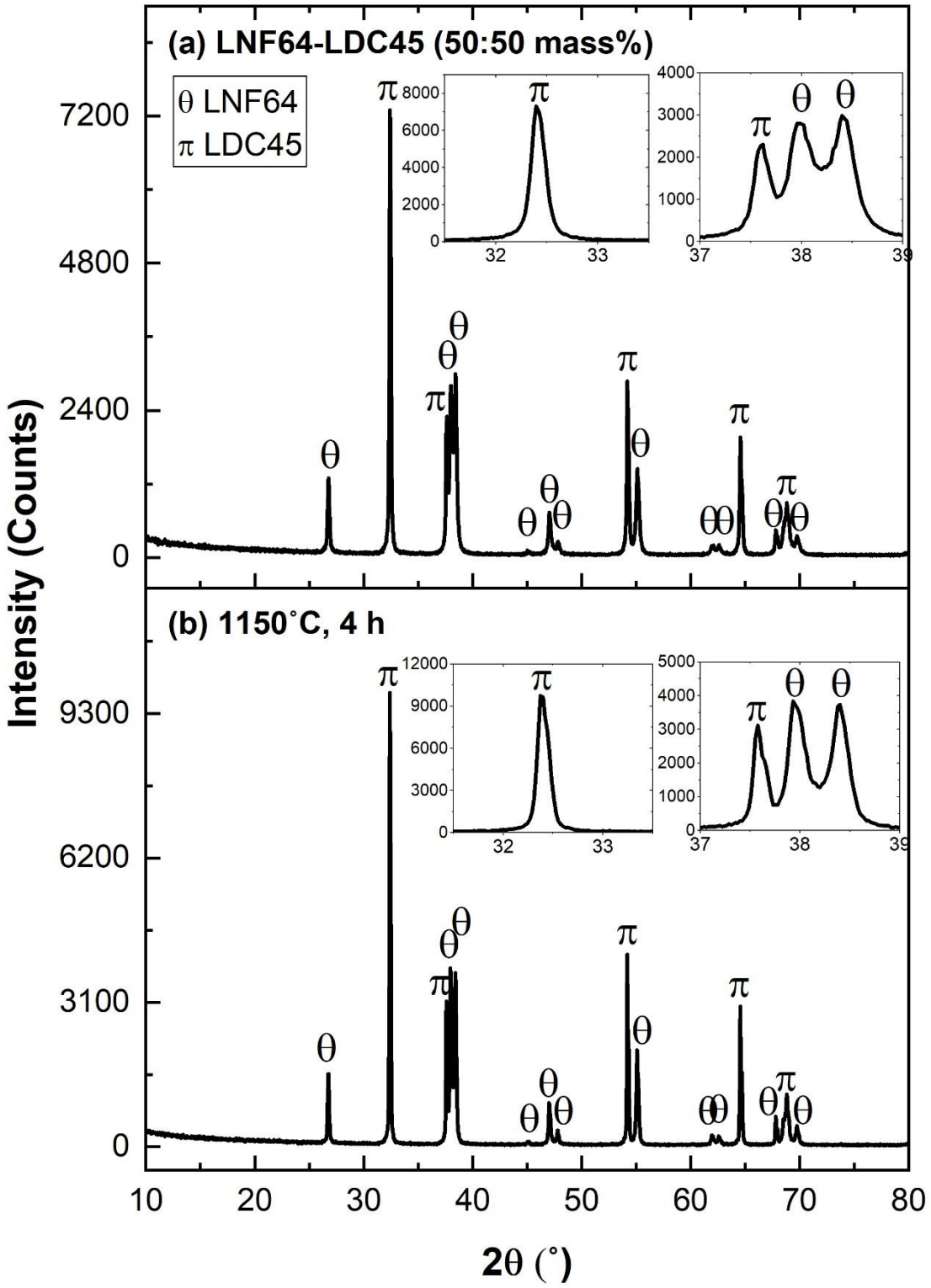


Figure 6.3 - Reactivity test of $LaNi_{0.6}Fe_{0.4}O_{3-\delta}$ and $La_{0.45}Ce_{0.55}O_2$; XRD results for (a) 50:50 mass% mix of materials prior to heating and (b) after heating to 1150˚C for 4 hours.

Table 6.2 – Composition of LDC45 ink prepared for spin-coating process

Material	Content (wt%)
LDC45	50
H_2O (Deionised)	30
DS001	1
WB4101	18
PL005	0.5
DF002	0.5

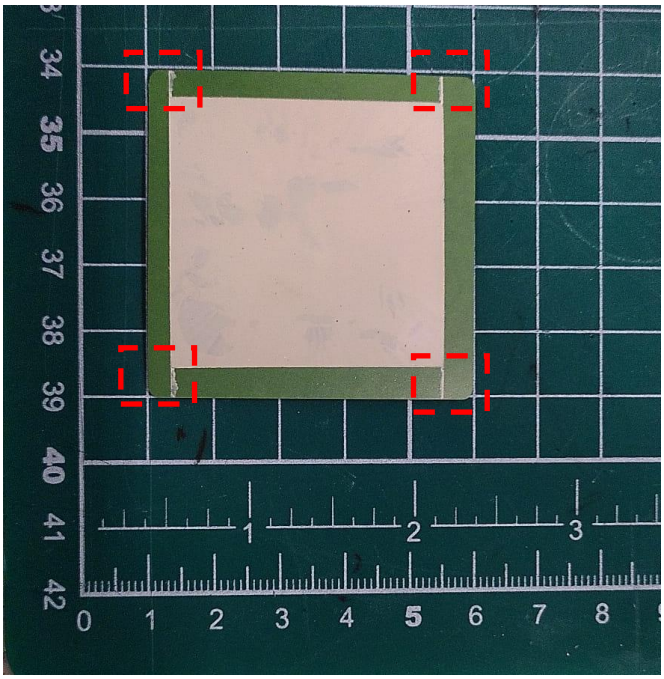


Figure 6.4 - LDC45 layer applied to a commercial half-cell by spin-coating. The leakage around the masking is highlighted.

6.2.3 Symmetrical Cell Test Results

For illustrative purposes, Nyquist plots of LNF and LNO214-based composites are shown in Figure 6.5, as recorded at an operating temperature of 800˚C. Results of the wider body of tests are summarised in Figure 6.6 to Figure 6.9. The data show that picking a 'best-performer' (i.e. a "winner") amongst these electrodes is highly temperature-dependent and also significantly influenced by the role of the Au-CCL (this effect was previously explored in Chapter 4). Although it was shown in Chapter 5 that the use of the current collector was necessary in the single cell testing set-up, both cases (with and without the gold current collector) are discussed here as they offer complimentary insight (e.g. effect on R_o

properties and the relative need for current collector layers). A number of trends can be summarised and are discussed in the following.

The addition of GDC leads to very large R_o and R_{pol} values in the absence of the current collector layer. In effect, such composites are the worst performing electrode configuration of those studied. However, the addition of the Au-CCL results in a sizeable reduction in these values. This effect was also seen in certain instances in Chapter 4. In this testing configuration, the GDC-containing composites are shown to offer the lowest resistance values in all cases. It is evident that the oxygen transport properties of GDC10 enable a promotion of the performance but *only* when measures to ensure electronic transport (which is clearly worsened by the addition of the GDC) is suitably supplemented for, via the employment of a contact layer.

In the absence of the Au-CCL, **the addition of LNF64** has the effect of reducing R_o values in all cases. The effect is most pronounced when combined with the $La_2NiO_{4+\delta}$ phase (see Figure 6.6b) and least for $La_4Ni_3O_{10-\delta}$ (see Figure 6.8b) which is logical given the relative electronic conductivity of these materials (poor for the former, good for the latter; see Figure 2.5 in Chapter 2) and given the results that were described in Chapter 4. In the presence of the Au-CCL, the LNF-type composites (i.e. LNO214-LNF, LNO327-LNF, LNO4310-LNF) are inferior to these other composites studied here. However, evidence from Chapter 5 indicates that the improved electron transport behaviours of these composites may offer a point of further interest (i.e. the relative benefit of LNF64 may become more apparent under polarisation testing). Further consideration of the LNF64-based composites **with the Au-CCL** (Figure 6.9f) shows that polarisation performance can be appreciably improved by a combination with materials that possess favourable oxygen exchange behaviour under the condition that a suitable CCL is applied. The R_{pol} values decreased in the order: LNO4310-LNF>LNO327-LNF>LNF-LNO214>LNF-LDC45>LNF-GDC.

Interestingly, **the LDC45 composites** (LNO214-LDC45 and LNF64-LDC45) showed lower R_o values than the GDC composites that have already been discussed. This likely alluded to a higher electronic

conductivity of this material, whilst the higher R_{pol} values that are seen in the presence of an Au-CCL were likely a result of inferior oxygen transport properties relative to GDC10.

A key conclusion from symmetrical cell tests is that the performance of lanthanum nickelate electrodes can be significantly altered via a number of different approaches to forming composite electrodes. Based on the results from symmetrical cell tests, five composite electrodes were identified for further consideration under polarisation. These were (1) LNF-GDC, (2) LNF-LNO214, (3) LNF-LDC45, (4) LNO214-GDC and (5) LNO214-LDC45.

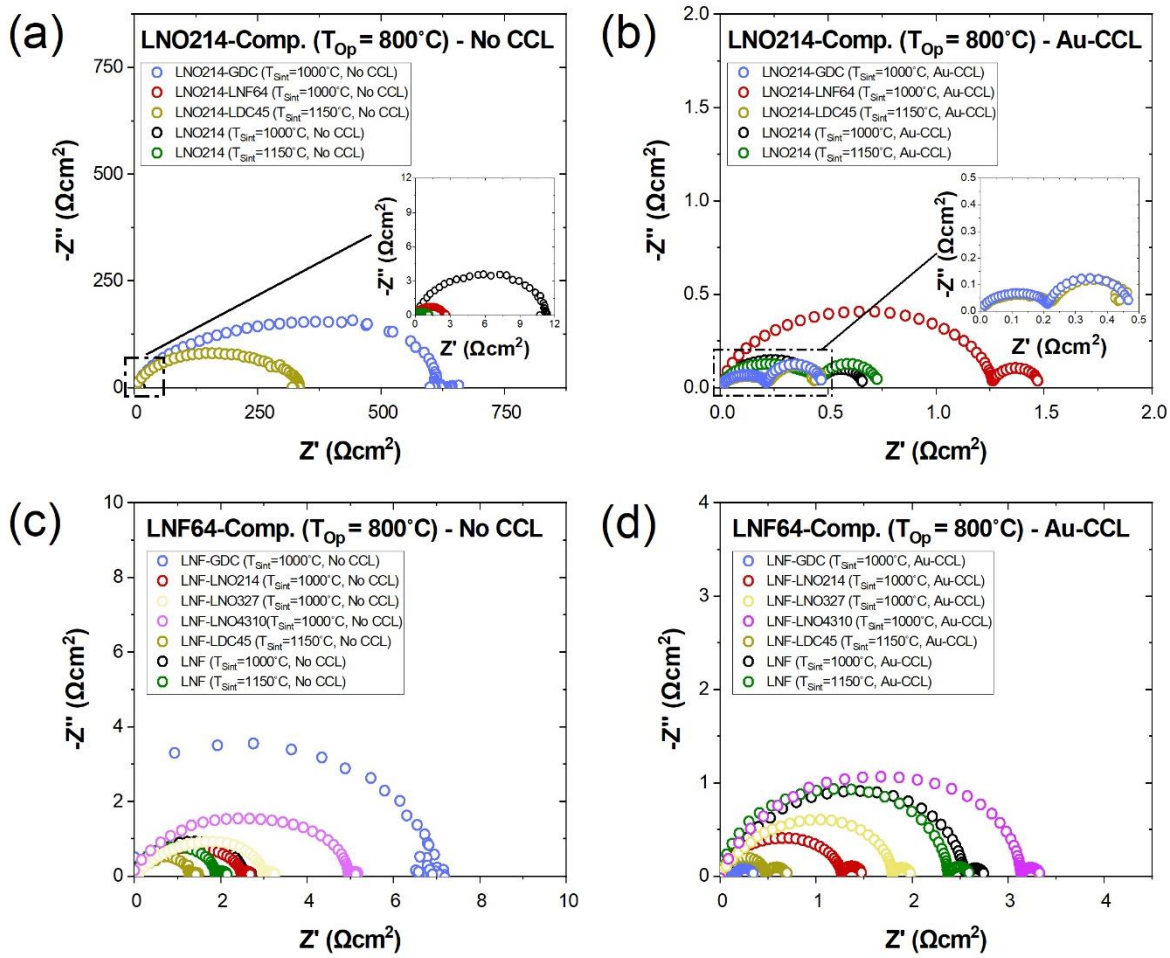


Figure 6.5 - Nyquist plots of composites; LNO214-based composites (a) without CCL and (b) with CCL. LNF64-based composites (c) without CCL and (d) with CCL. All composites were mixed in a 1:1 volume ratio. Electrode sintering temperatures are shown in brackets in the legend.

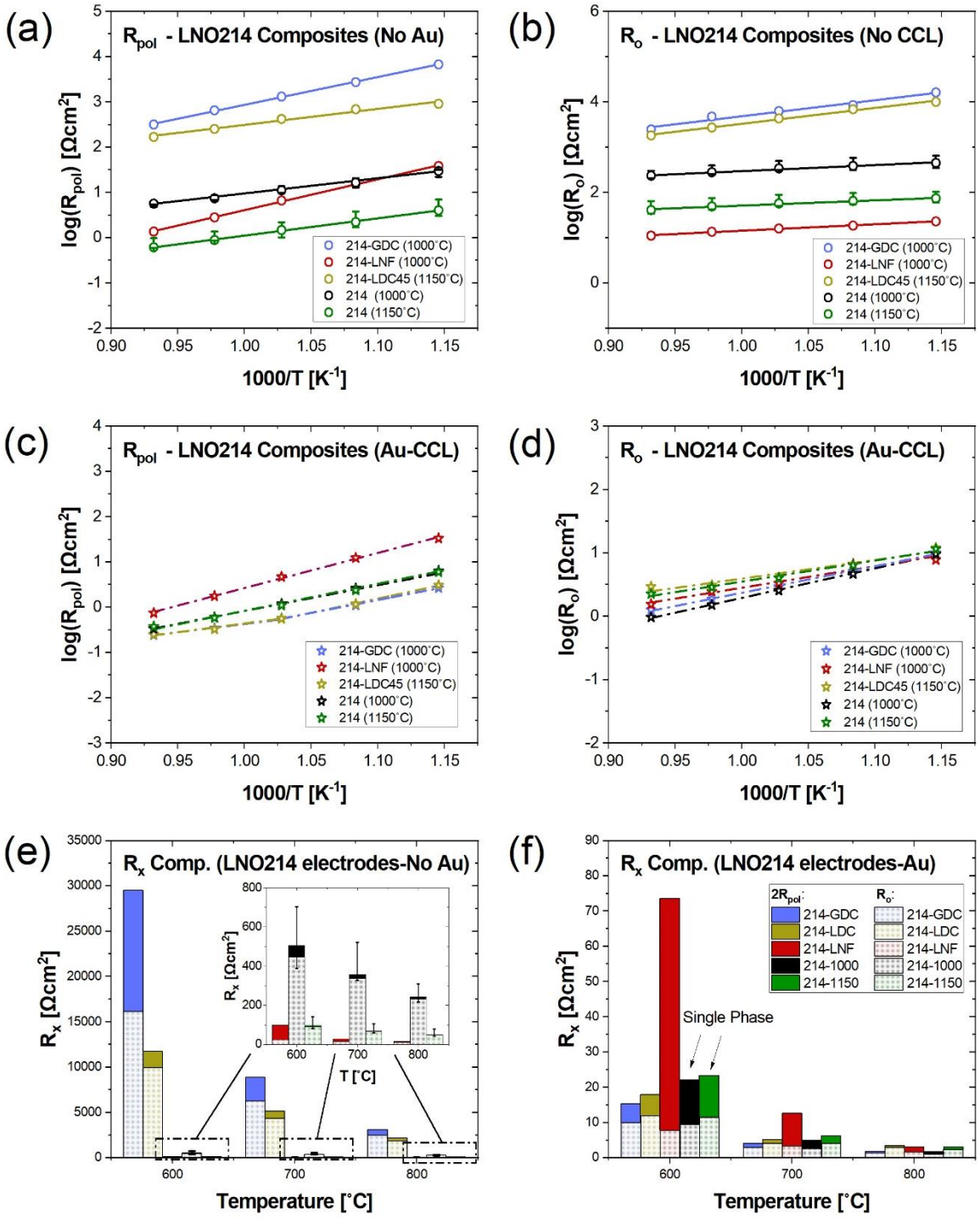


Figure 6.6 – Symmetrical cell performance of $La_2NiO_{4+\delta}$ composite electrodes (1:1 volume ratio of 214-to-composite phase); (a) Arrenhius plot (600-800˚C; 50˚C intervals) showing polarisation resistance of different LNO214-composite electrodes in the absence of a current collector, (b) Arrenhius plot showing ohmic resistance of the electrodes in the absence of the current collector and (c, d) the R_{pol} and R_o Arrenhius plots (respectively) in the presence of a current collector layer. Total impedance values in (e) absence of the Au-CCL and (f) the presence of the Au-CCL. Electrode sintering temperatures are shown in brackets in the legend.

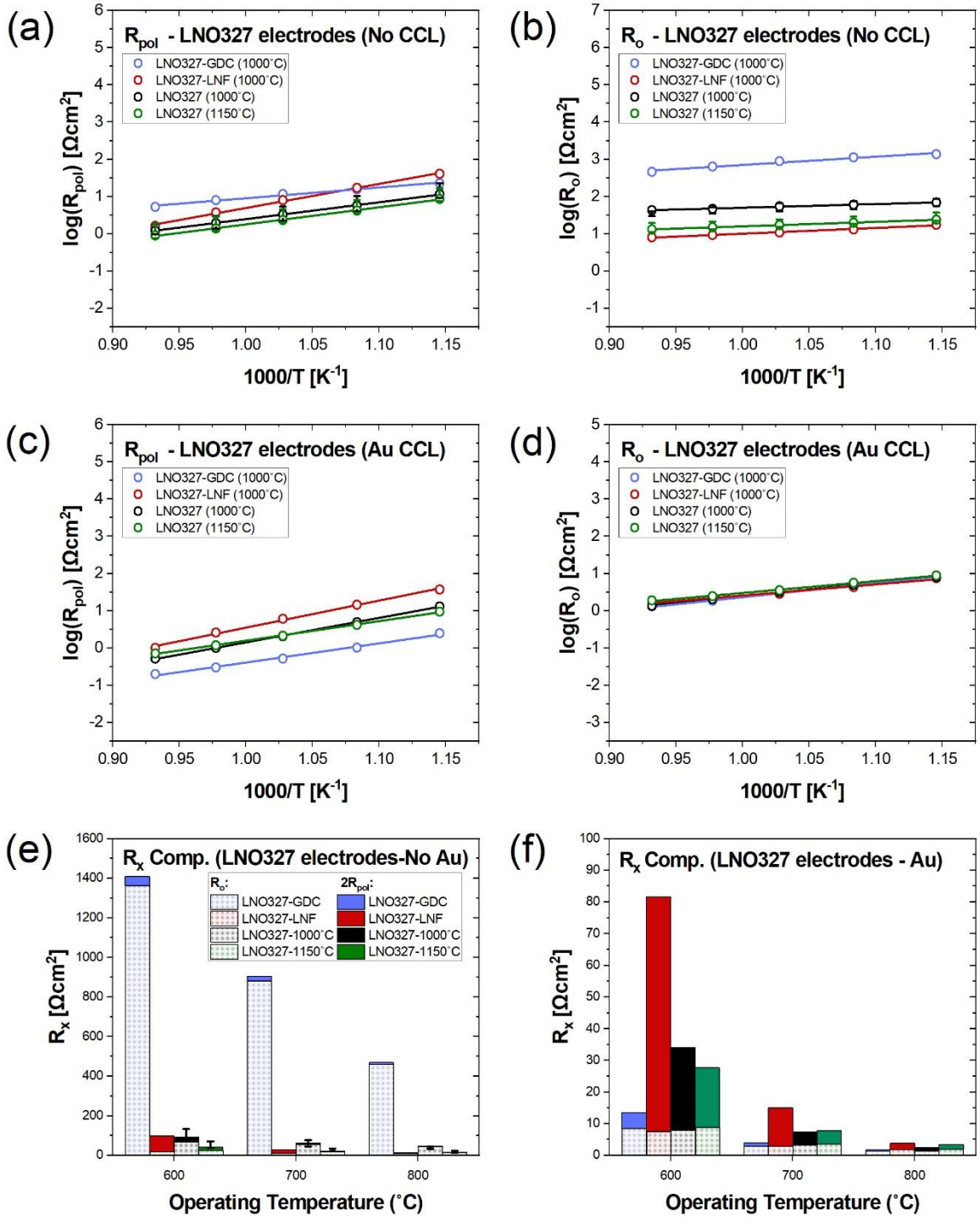


Figure 6.7 – Symmetrical cell performance of $La_3Ni_2O_{7-\delta}$ composite electrodes (1:1 volume ratio of 327-to-composite phase); (a) Arrenhius plot (600-800˚C; 50˚C intervals) showing polarisation resistance of different LNO327-composite electrodes in the absence of a current collector, (b) Arrenhius plot showing ohmic resistance of the electrodes in the absence of the current collector and (c, d) the R_{pol} and R_o Arrenhius plots (respectively) in the presence of a current collector layer. Total impedance values in (e) absence of the Au-CCL and (f) the presence of the Au-CCL. Electrode sintering temperatures are shown in brackets in the legend.

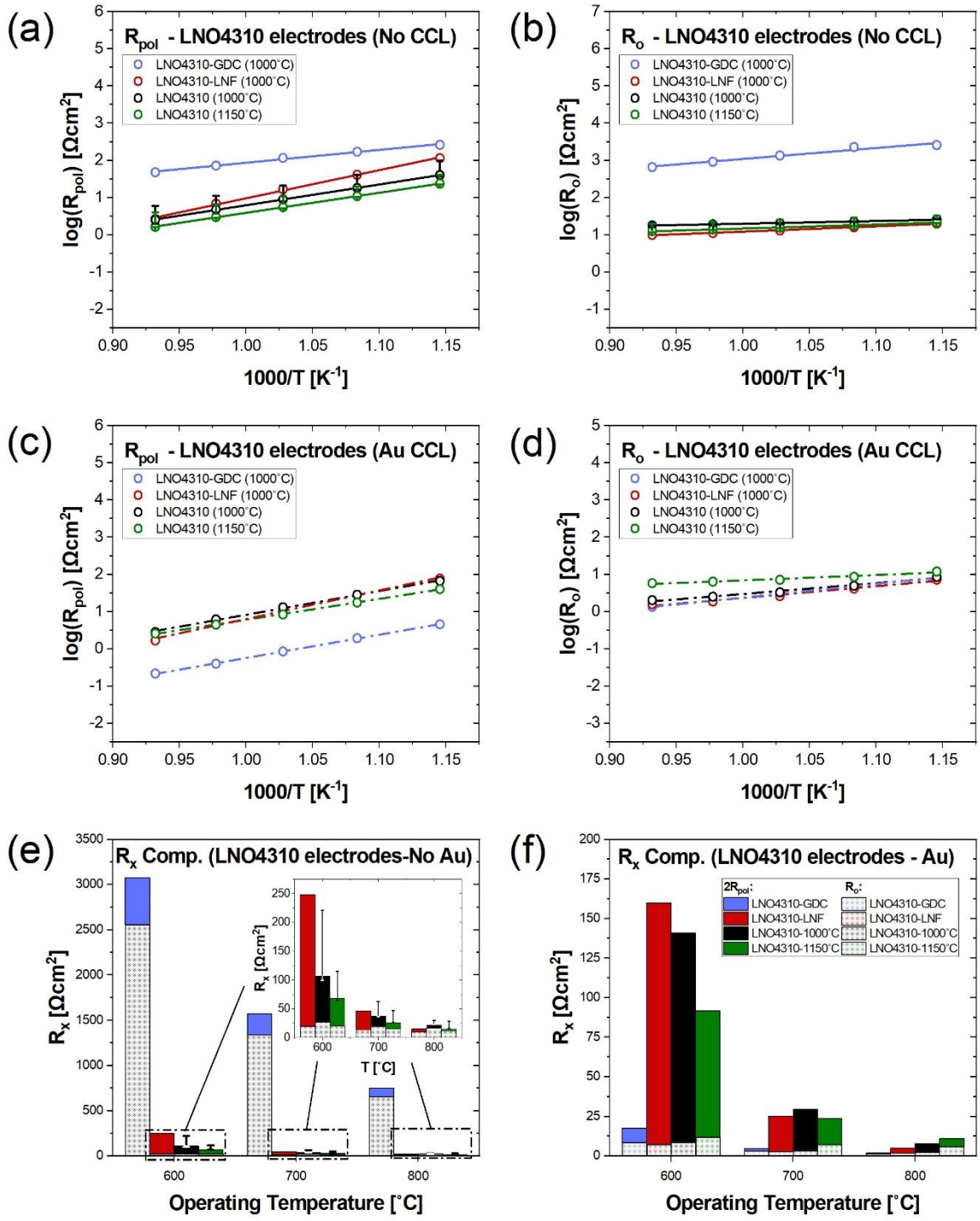


Figure 6.8 – Symmetrical cell performance of $La_4Ni_3O_{10-\delta}$ composite electrodes (1:1 volume ratio of 4310-to-composite phase); (a) Arrenhius plot (600-800˚C; 50˚C intervals) showing polarisation resistance of different LNO4310-composite electrodes in the absence of a current collector, (b) Arrenhius plot showing ohmic resistance of the electrodes in the absence of the current collector and (c, d) the R_{pol} and R_o Arrenhius plots (respectively) in the presence of a current collector layer. Total impedance values in (e) absence of the Au-CCL and (f) the presence of the Au-CCL. Electrode sintering temperatures are shown in brackets in the legend.

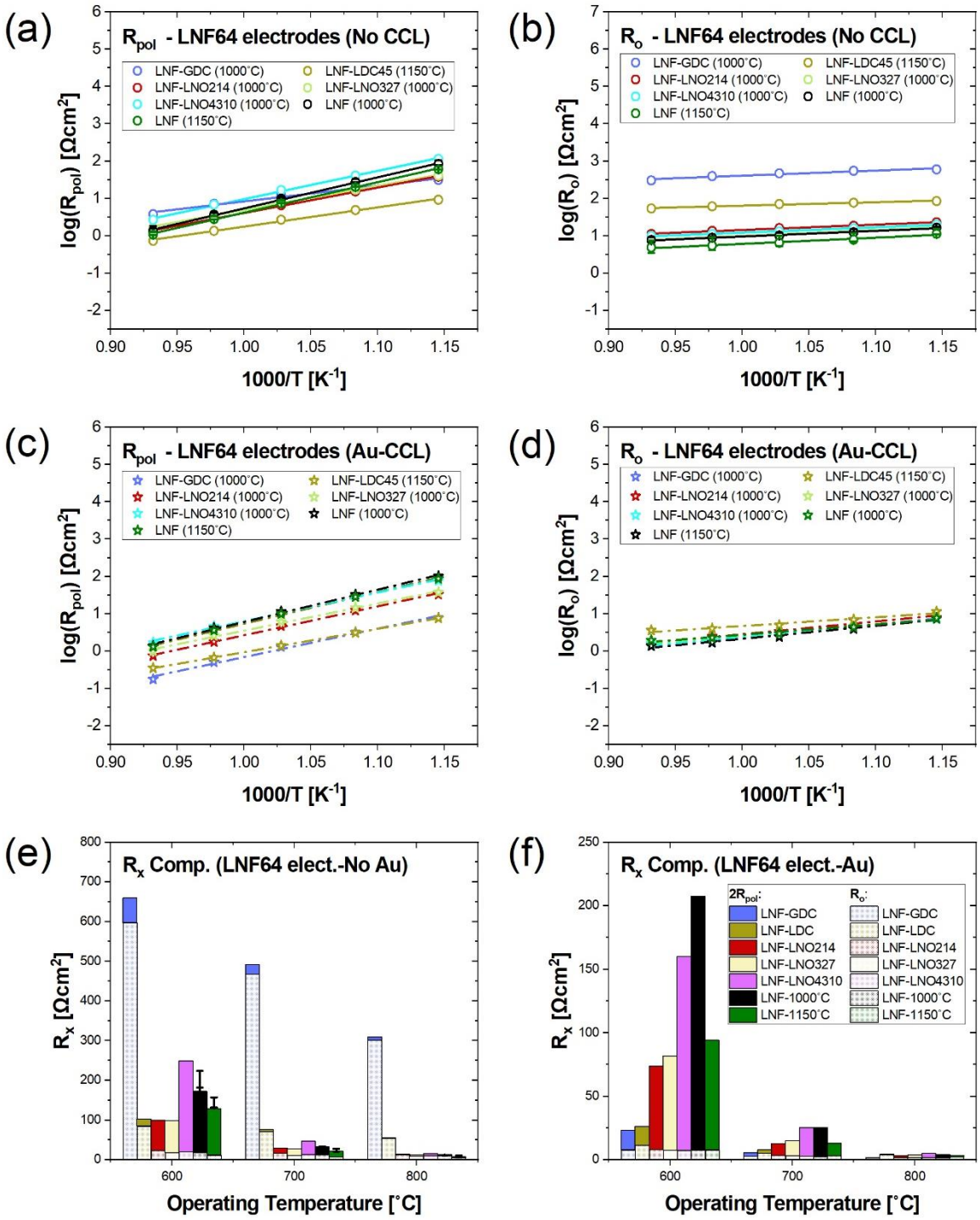


Figure 6.9 – Symmetrical cell performance of $LaNi_{0.6}Fe_{0.4}O_{3-\delta}$ composite electrodes (1:1 volume ratio of LNF64-to-composite phase); (a) Arrenhius plot (600-800˚C; 50˚C intervals) showing polarisation resistance of different LNF64-composite electrodes in the absence of a current collector, (b) Arrenhius plot showing ohmic resistance of the electrodes in the abscence of the current collector and (c, d) the R_{pol} and R_o Arrenhius plots (respectively) in the presence of a current collector layer. Total impedance values in (e) absence of the Au-CCL and (f) the presence of the Au-CCL. Electrode sintering temperatures are shown in brackets in the legend.

6.3 Single Cell Testing

To further assess the performance of the identified electrode configurations, single cell tests were conducted, akin to those reported in Chapter 5. Again, the electrodes were applied to commercial half-cell substrates as a means of maintaining consistent anode and electrolyte performance. The iV-results and corresponding EIS data (recorded at OCV) from these tests are summarised in Figure 6.10 and Figure 6.11, respectively. In Figure 6.10f and Figure 6.11f, $i_{0.7V}$ and R_{pol} values (respectively) are compared against the single phase electrodes previously tested. As was also evident in the symmetrical cell tests, it is shown that improvements can be garnered via combination with the secondary phases which, again, highlights the beneficial effect of combining materials with different fundamental properties.

The most notable electrode performance obtained in this study was that from the LNF-GDC electrode (Figure 6.10c), demonstrating the importance of selecting materials with complimentary properties. The improvement in performance can perhaps be most appreciably noticed by consideration of the profile of the polarisation curve which is shown to be much more linear than that which was shown in Chapter 5 for the single phase LNF electrode. In those cases, large losses were seen in the activation region of the iV curve. The change in behaviour of the composite electrode is seemingly achieved by an improvement in the reaction kinetics in the low current-high voltage regime where oxygen exchange is likely to be the rate-limiting process (rather than electron transport). In this case, the oxygen transport of the doped CeO_2-phase are well suited to a combination with the electronic transport properties of the LNF phase. As was the case in Chapter 5, it can again be noted that this electrode did not appear to demonstrate the most favourable symmetrical cell performance in comparison with those other electrodes in Section 6.2.3. Once more, this highlights a serious limitation of that particular approach in assessing performance.

The LNF-LNO214 composite offered a particularly interesting case-study for a specific consideration and discussion. When compared against the single phase LNF64 and LNO214 electrodes that were

analysed in Chapter 5, the effect of combining the two materials becomes apparent. This comparison can be viewed in Figure 6.12, in which the behaviour of electrodes (each sintered at 1000˚C) is compared. At an operating temperature of 800˚C, the performance enhancement is unmistakable and the current output is improved across the entire voltage range studied (Figure 6.12a). It might be anticipated that the current density values would represent an approximate average of those recorded for the single-phase electrodes, at all points over the studied voltage range. This is shown not to be the case and, instead, a synergistic effect is apparent. At the lower operating temperature of 700˚C, the behaviour is slightly different. Whilst the performance at lower voltages remained marked, the behaviour around OCV appeared to represent more of an average of that recorded for LNF64 and LNO214. A variation in the relative compositions of these materials may lead to different behaviour and it seems likely that the optimum ratio is different at each operating temperature (e.g. a higher LNO214 content may be beneficial at lower temperatures).

Comparing the $i_{0.7V}$ values of the LNF-LNO214 electrode against that of the LNO214-GDC electrode (at T_{Op}=800˚C) would appear to confirm that the performance of an LNO214-based electrode can be most appreciably improved via its combination with an electronic conducting phase. However, further comparison of the $i_{0.7V}$ values at lower temperature shows that this behaviour does not necessarily hold under all conditions. However, the maximum current density recorded ($i_{0.6V}$ – see the far right of the polarisation curves) demonstrates that the LNO214-LNF64 electrode performs more favourably in this region. Given the relatively non-linear nature of the polarisation curve of the LNO214-LNF (see Figure 6.10e) in comparison to the LNO214-GDC electrode (see Figure 6.10a), it may be possible to further enhance the cell output by an optimisation of the LNO214-LNF ratio.

The polarisation curves of the LNF-LDC45 (Figure 6.10b) and LNO214-LDC45 (Figure 6.10d) electrodes were found to be very similar in both cases. However, the use of the LDC45 material did not show any benefit in comparison with the GDC10 composite – this, despite the use of higher sintering temperatures (and the lower reactivity previously reported). This could plausibly be a result of the

inferior transport behaviour of LDC45 in comparison with GDC10. The postulate here is that, whilst authors have looked to avoid reactivity with CeO_2, the excellent behaviour of GDC10 means that such a strategy is unlikely to reap major improvements in performance (although this could feasibly offer a more long-term benefit with respect to reduced degradation rates). However, another alternative here could be interactions between the LDC45 and the underlying 8YSZ phase leading to a rate-limiting insulating layer. Indeed, further subsequent XRD analysis has shown that the introduction of lanthanum into the CeO_2 phase causes this effect (see Figure 6.13). It is notable that this apparent incompatibility is not observed between GDC10 and 8YSZ under the same conditions (see Figure 6.14). As such, despite efforts to avoid reaction between the cathode and the barrier layer, a new incompatibility issue is introduced at the electrolyte-barrier layer. Given this observation, and given also the relative performance of the LDC45-type composites, the use of LDCX is not recommended as a route of boosting the performance of lanthanum nickelate electrodes.

Despite the improvements that have been noted in this study, a clear observation remains, namely that is that the $i_{0.7V}$ performance of the cells remains below that of the commercial single-phase LSCF material. This is increasingly evident as the operating temperature is reduced. It is further noted that there has been no real attempt in this work to optimise the LSCF performance (via the use of composite layers) and, for instance, the addition of LSCF with other phases such as GDC may make an even more difficult case for the lanthanum electrodes to compete with. Further optimisation of the lanthanum nickelates has not been explored here and may result in further improved performance. In this chapter there has been no attempt to optimise sintering temperatures or, going further, to optimise the ratios of materials used in each case. This could represent an area of interest for the future. Use of existing electrode models (e.g. the Adler Steele Lane model [339]) may also help to support optimisation attempts.

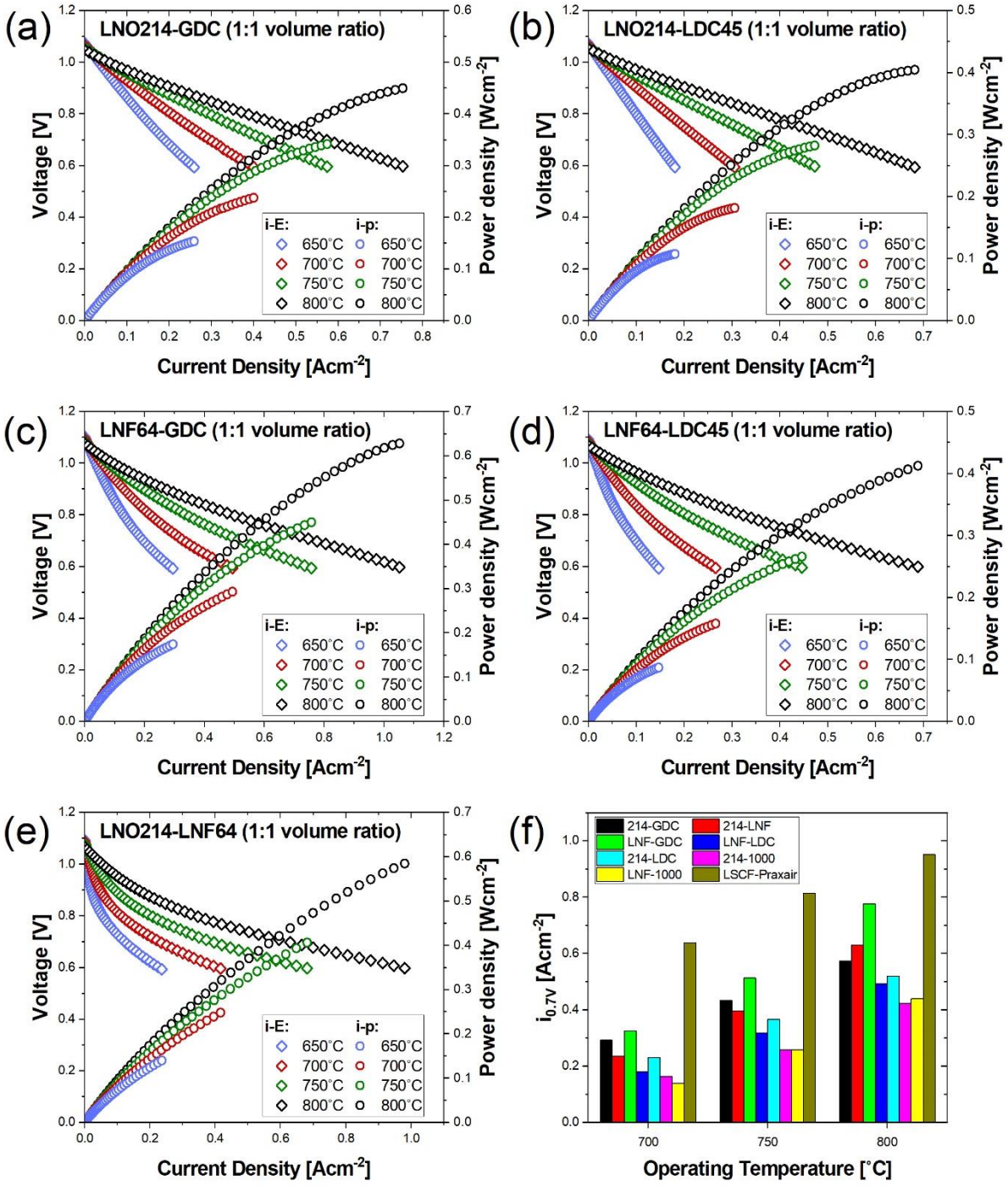


Figure 6.10 – Polarisation curves of composite electrodes; (a) LNO214-GDC (T_{Sint}=1000˚C), (b) LNO214-LDC45 (T_{Sint}=1150˚C), (c) LNF64-GDC (T_{Sint}=1000˚C), (d) LNF64-LDC45 (T_{Sint}=1150˚C), (e) LNO214-LNF64 (T_{Sint}=1000˚C) and (f) a comparison of $i_{0.7V}$ values compared against single phase electrodes (LNO214, LNF64 and LSCF) sintered at 1000˚C.

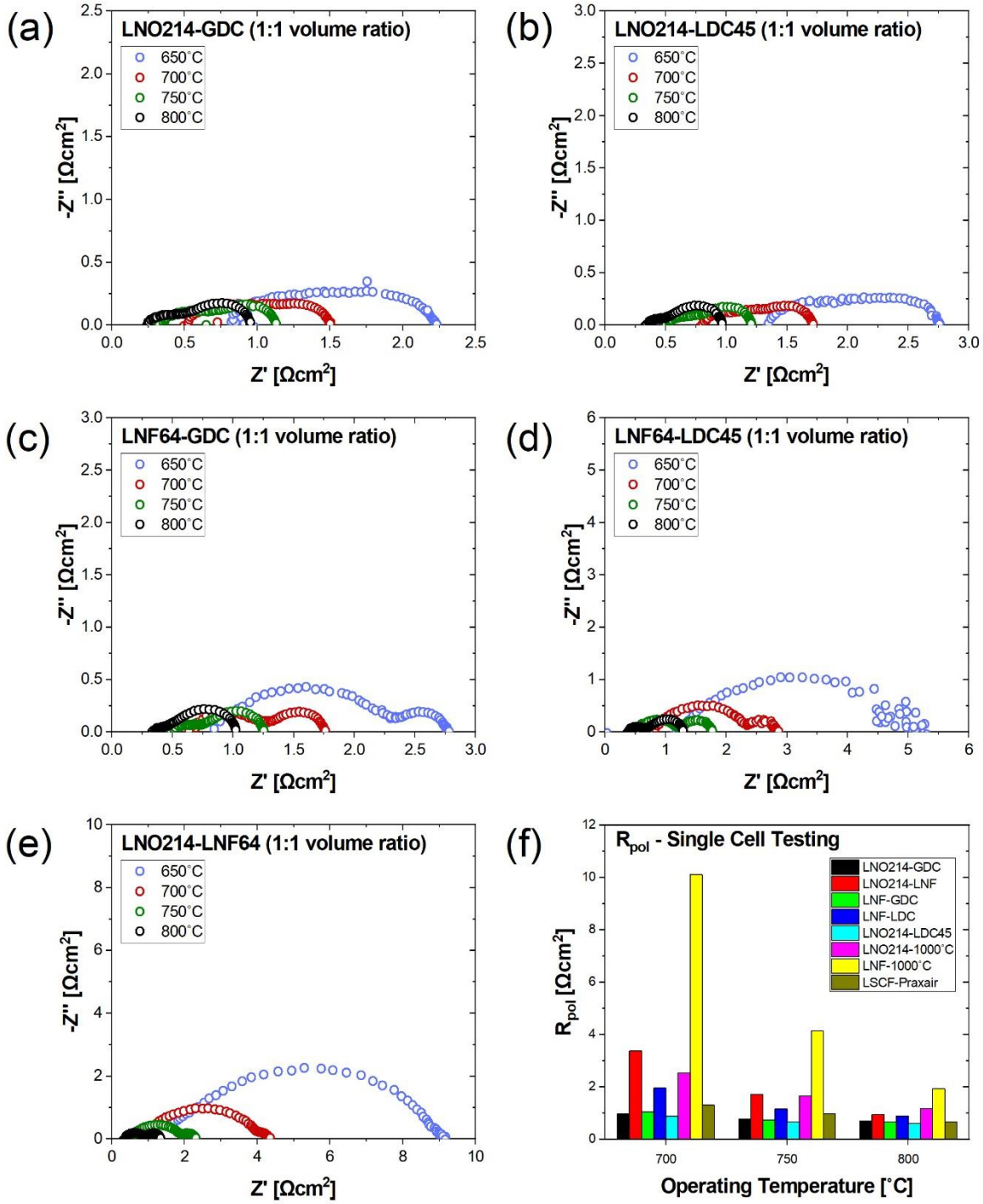


Figure 6.11 – EIS measurements recorded at OCV for composite electrodes; (a) LNO214-GDC (T_{Sint}=1000˚C), (b) LNO214-LDC45 (T_{Sint}=1150˚C), (c) LNF64-GDC (T_{Sint}=1000˚C), (d) LNF64-LDC45 (T_{Sint}=1150˚C), (e) LNO214-LNF64 (T_{Sint}=1000˚C) and (f) a comparison of R_{pol} values compared against single phase electrodes (LNO214, LNF64 and LSCF) sintered at 1000˚C.

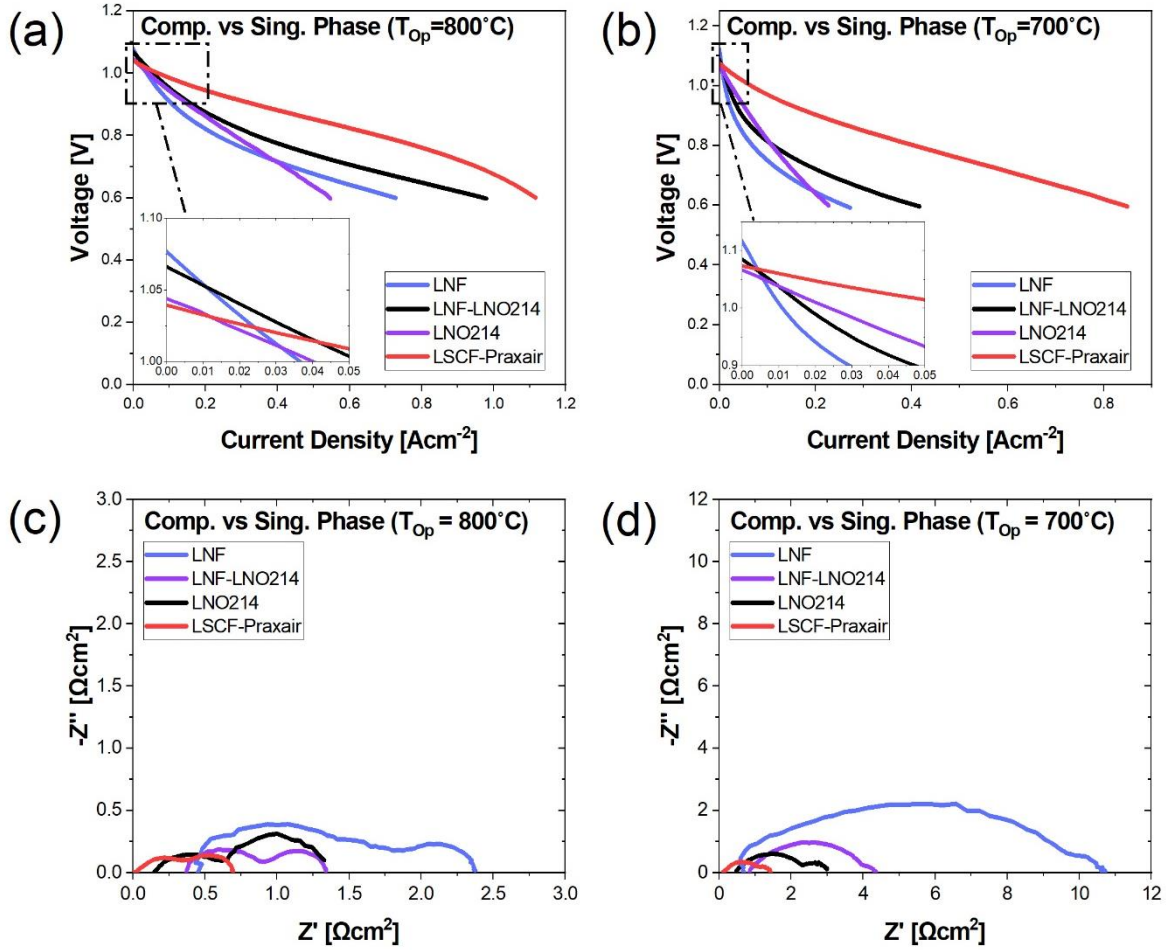


Figure 6.12 – Comparison of polarisation curves of single phase and composite phase electrodes (LNF, LNO214, LNF-LNO214) at an operating temperature of 800˚C with Au-CCL.

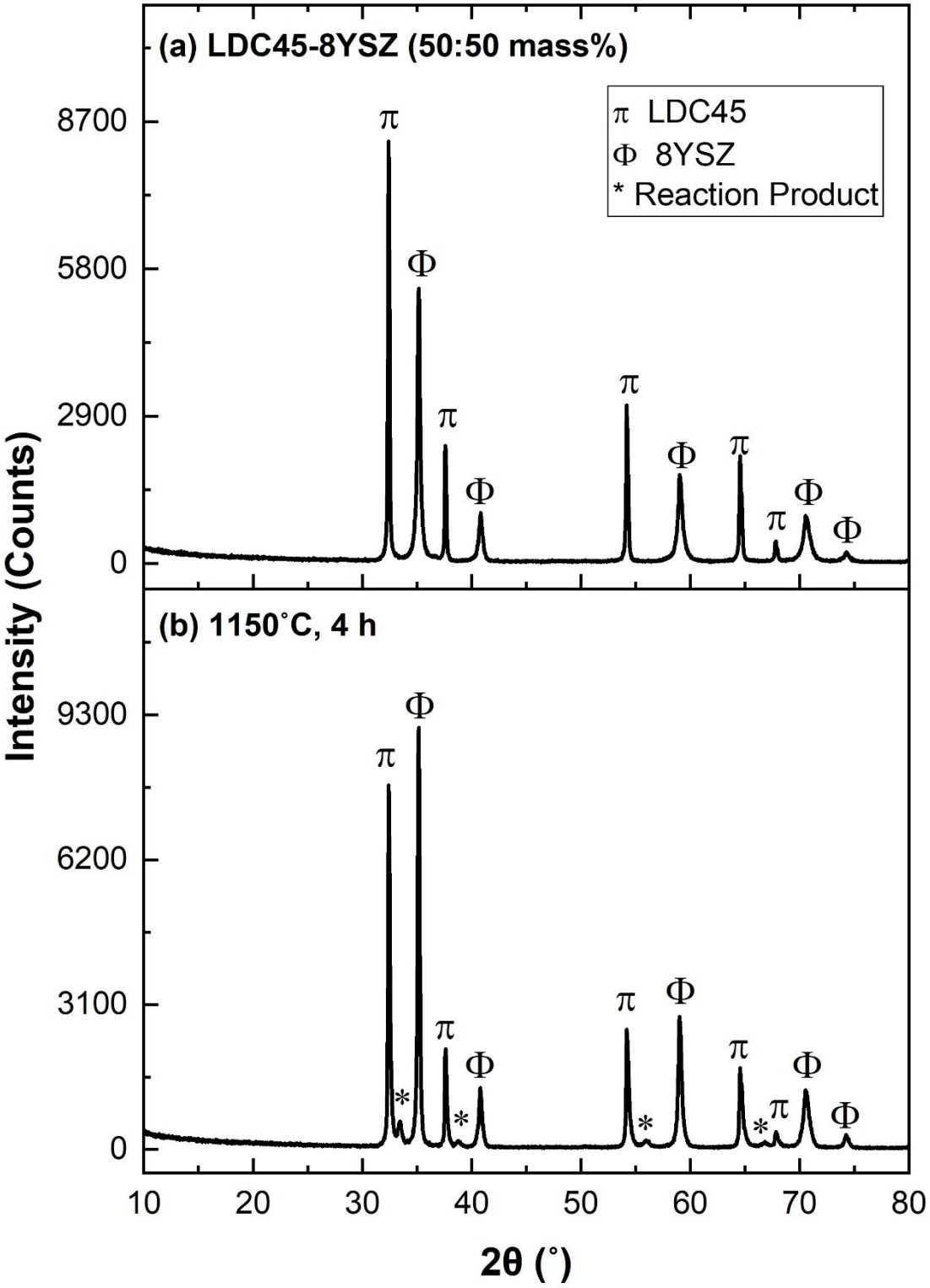


Figure 6.13 – XRD showing reactivity between LDC45 and 8YSZ.

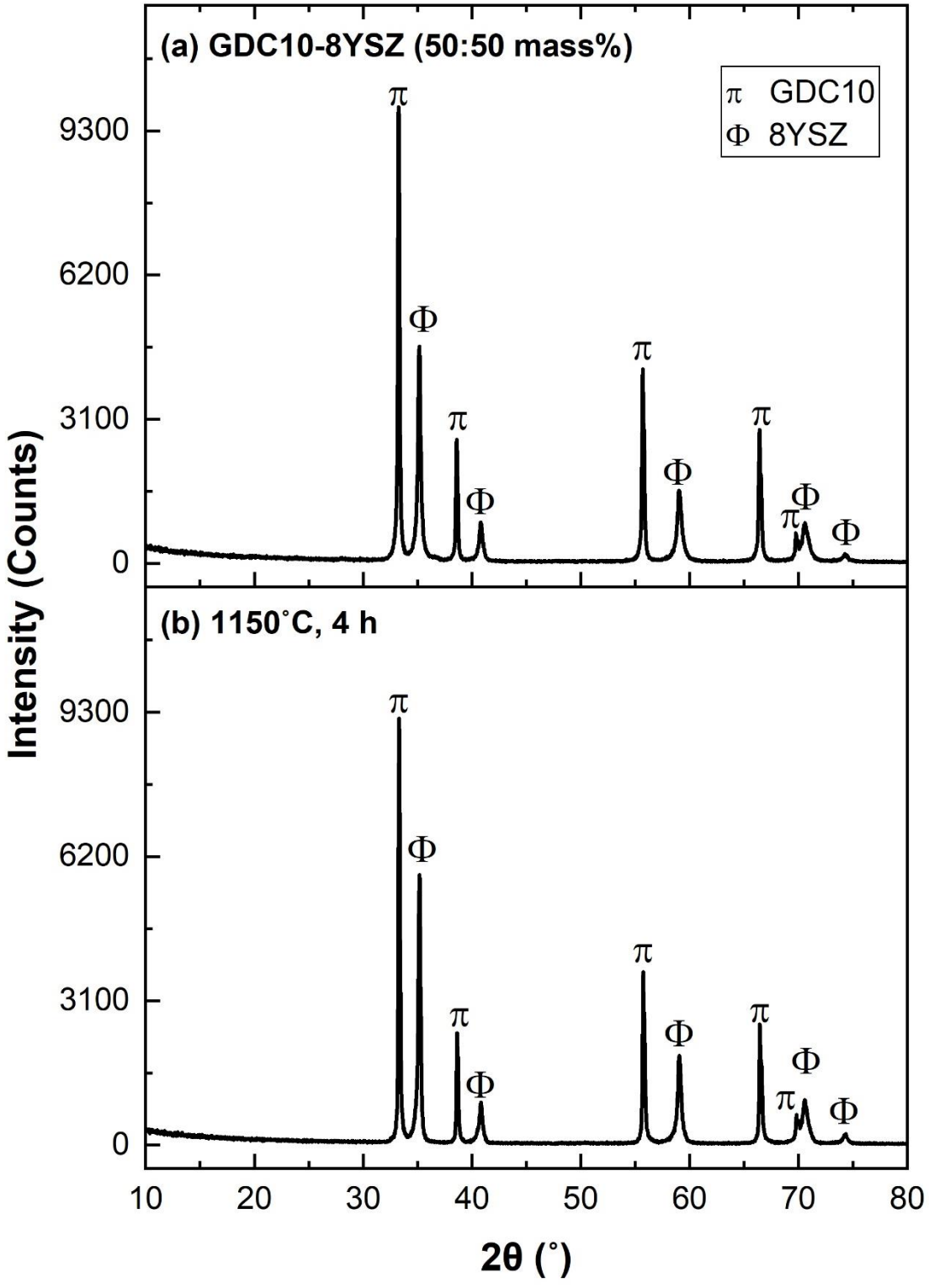


Figure 6.14 – XRD showing the compatibility of GDC10 and 8YSZ.

6.4 Comparisons with literature data

To identify possible further routes for the development of lanthanum nickelate electrodes, it is of interest to consider the results recorded in this chapter against the literature data. This not only provides context for the performance that has been achieved in this study but also enables an assessment of other author's work and helps to identify those studies that have been particularly successful in developing novel electrodes. In turn, this can offer further insight into the most suitable strategies for promoting cell performance. A comparison of data recorded in this work and those seen in the literature is shown in Figure 6.15. There are a number of lanthanum nickelate electrodes that have been studied by other authors that have exceeded the performance that has been achieved in the work described in this chapter.

Starting with a consideration of those $La_2NiO_{4+\delta}$ electrodes that have out-performed those considered in this work (see Figure 6.15a), a number of important studies can be identified. Of those considered, there are two reports that indicate current density ($i_{0.7V}$) of over 2 Acm^{-2} is possible at an operating temperature of 800˚C [222,236]. It is noticeable that in both of these studies (conducted by two different research groups) a layered configuration is employed to promote performance. The approach involves improving the oxygen exchange towards the electrolyte-interface and improving the electronic conductivity towards the current collection part of the cell. It is interesting to note that, in addition to developing a highly active functional layer comprised of LNO214 and a doped ceria phase (GDC or SDC [236]), both of the aforementioned works employ a further $La_{1-x}Sr_xCoO_3$ (LSC) layer to maximise the cell output. Whilst this appears to suggest such an approach offers promise, it is a wonder if the introduction of a cobaltite phase re-introduces the problems that the lanthanum nickelates are intended to resolve (i.e. Cr-poisoning, TEC mismatch issues). In other words, does the lanthanum nickelate serve an important purpose or would it be better to replace this entirely with the better-performing LSC and, effectively, accept/manage the anticipated issues with this material? The remaining two studies [335,340] that have reported electrodes with better performance better are LNO214-LNF64 electrodes. There are a number of studies [236,270,334,336,341,342] that report

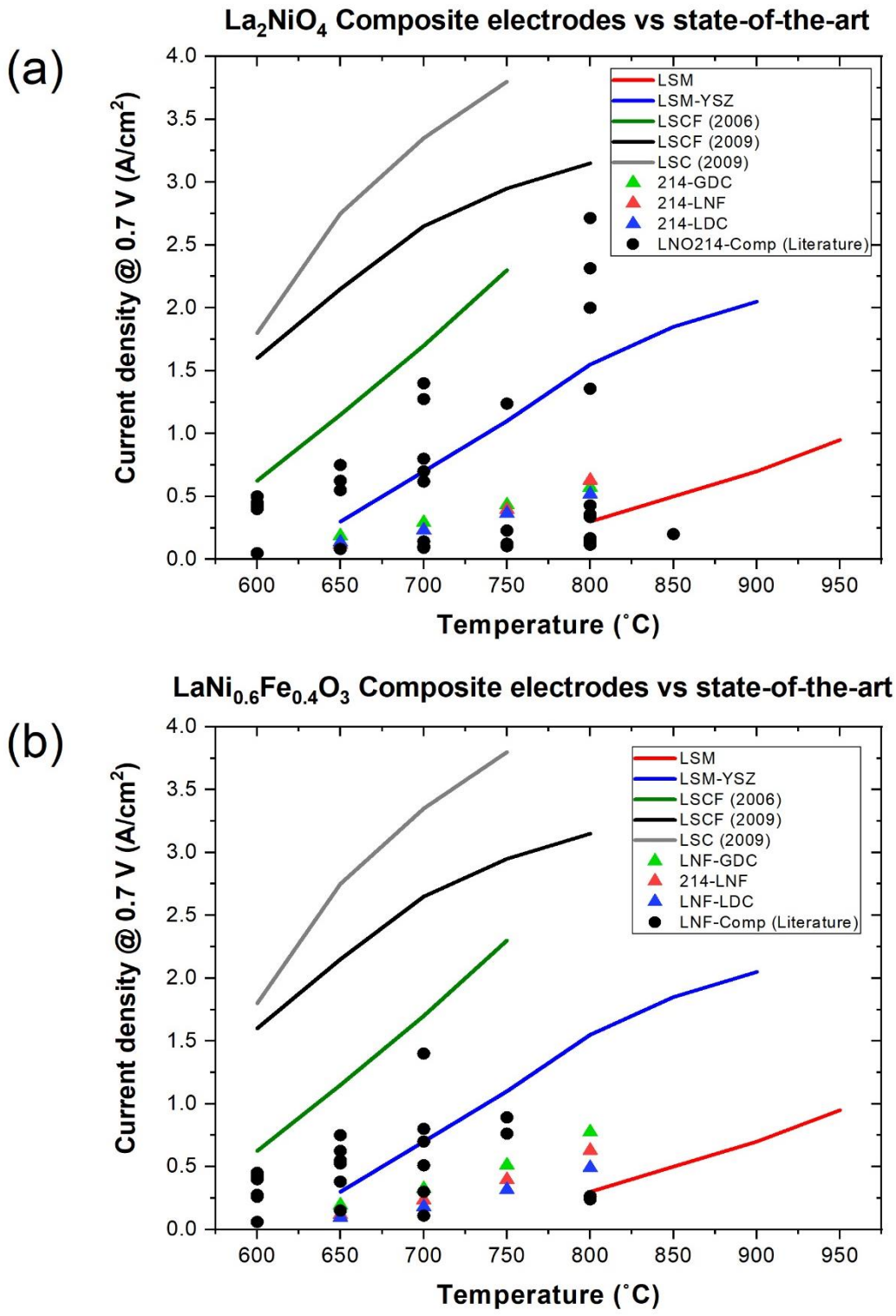


Figure 6.15 – Comparison of $i_{0.7V}$ measured in this study and those measured in other studies; (a) LNO214 composites and (b) LN64 composites.

composite electrodes with relatively inferior performance when compared with the results reported in this thesis. These electrodes consist of a combination of LNO214 with doped ceria phases. These observations appear to support earlier suggestions that this material, possessing excellent oxygen transport properties, is most suitably improved via combination with electronic conductors rather than other oxygen conducting materials. Conducting a similar analysis on LNF64 suggests a more fragmented approach has been conducted by authors with a broad variety of different materials employed in combination with the electronic conductor [243,335,340,343–345]. As such, it is difficult to identify any major trends but the highest performing electrodes employ more novel materials including BZCY [344] and EDB [343]. This possibly alludes to the promise of developing new electrolyte phases for use with the lanthanum nickelates. A combination of LNO214 and LNF64 (1:1 volume ratio) is, again, shown to be a strong performer [340].

6.5 Conclusions

The study of composite electrodes in this chapter has provided a number of notable findings which can be summarised as follows:

- Symmetrical cell testing in this chapter has been shown to have fairly limited relevance in predicting the behaviour of electrodes at lower operating voltages. However, it has been shown that the use of this testing approach can offer a quick and simple means by which improvements for a given class of materials can be identified. Importantly, valuable information can be obtained on how the addition of new phases influences the ohmic and polarisation properties of an electrode. However, we advise upmost care when equating the outcomes of these results with those from single cell testing.
- Efforts to optimise electrode materials should consider the fundamental properties of the selected phases (what is the drawback of a given phase when used as an electrode? An ‘enhancement’ in which property or behaviour would likely offer the most appreciable improvement?). Such considerations do not appear to be universally applied within the

literature. A more robust assessment of material performance via direct comparison with state-of-the-art materials should be generally performed. This offers a benchmark against which materials can truly be assessed. Often, academic studies in this area fail to provide such context and this can make interpretation difficult, particularly for differing materials.

- It has been shown that cathodes can be improved quite significantly via the use of composites. It has been shown that a combination of two electrode phases can out-perform those of the single phases, showing a certain synergistic effect. This was most clearly highlighted in the case of the LNO214-LNF64 electrode.
- The addition of oxygen conducting materials (such as GDC10) can help to improve the polarisation performance of electrodes but this approach also requires appreciation of the loss in conductivity. This can be offset by the use of contacting layers. In this study this has been provided by an Au-CCL but, in a commercial set-up, this role could be taken up by a lower cost alternative (e.g. LNF64 or LSM).
- Whilst it is apparent that enhanced performance can be achieved via a combination of different phases, developing a lanthanum nickelate electrode that can clearly rival the state-of-the-art LSCF material has proven more difficult. In this study, this observation has been particularly evident as operating temperatures are lowered from 800˚C. It is notable that LSCF maintains superior performance in the lower temperature range. It is also worth noting that, in this study, development and testing has been limited to that of lanthanum nickelate electrodes. Very little effort has been applied to optimising LSCF, itself. It is, therefore, inevitable that the performance of the LSCF material could be further enhanced and, indeed, this is what the literature would appear to suggest. This highlights the difficulty that materials researchers face in replacing the incumbent phases.

This chapter has detailed a simple means by which La-Ni-O cathodes for SOFC can be explored. Further optimisation is no doubt possible with the lanthanum nickelates. This could include:

- Changing the ratio of materials in the composite electrode to find an optimum composition that offers enhanced current output.
- Use of more advanced electrode structures and/or use of nano-materials to increase the catalytic area – this could include layered structures, employing a highly active functional layer (e.g. LNO214-GDC) with a highly conducting CCL (e.g. LNF). In some works, more than two layers are used with a gradual changing of the electrode properties through the structure.
- Optimisation of sintering temperatures– evidence from previous chapters in this thesis shows that improvements to particle connectivity can lead to a boost in electrode performance. Whereas in that case, interaction between the cathode and electrolyte was limited to the interface between the components, this effect is likely to be complicated by increased reactivity with intimately mixed phases.
- This issue may be offset by the development and consideration of alternative electrolyte materials

7 Conclusions and outlook

7.1 Overview

The work documented in this thesis has analysed the performance of lanthanum nickelate electrodes from a number of perspectives. This has covered an assessment of data from the wider literature, and involved a comprehensive testing programme carried out in the Fuel Cells and Hydrogen laboratory at the University of Birmingham. A broad selection of materials was studied, including synthesised materials ($La_2NiO_{4+\delta}$, $La_3Ni_2O_{7-\delta}$, $La_4Ni_3O_{10-\delta}$, $LaNi_{0.6}Fe_{0.4}O_{3-\delta}$, $La_{0.6}Sr_{0.4}Co_{0.2}Fe_{0.8}O_{3-\delta}$) in addition to state-of-the-art commercial alternatives ($La_{0.6}Sr_{0.4}Co_{0.2}Fe_{0.8}O_{3-\delta}$). This assortment of materials offers a diverse mix of properties; from those possessing predominantly oxygen transport behaviour, to those that demonstrate predominantly electronic transport (and, additionally, those with intermediate behaviour). This study is of particular interest in developing a contextualised understanding of the lanthanum nickelate materials; it is differentiated from many other studies detailed in the literature by its breadth and systematic approach to ensure each material is similarly characterised. It is also notable that the number and type of materials studied allows for comment on potential issues with common approaches to SOFC testing. Further, a study of fabrication and testing considerations (sintering temperature, material selection, use of noble metal contact layers) has provided some insight into the possible influence of different parameters on the conclusions that might be drawn from experimental work. In the final chapter of this work, the findings from this study are summarised and possible future research directions are identified.

7.2 The performance of lanthanum nickelate electrodes

In very general terms, the work that has been conducted in this thesis shows that the lanthanum nickelates offer relatively inferior performance when compared to the state-of-the-art oxygen electrode material (LSCF6428). This was already initially evident from considerations of the literature data. It was acknowledged, however, that any literature-based analysis (like that performed in Chapter 2) can be complicated by a need to draw comparisons across a range of studies conducted by different

research groups. Such analysis will neglect the role of many different approaches to material synthesis, and to cell and electrode fabrication. Further, the effects of various approaches to testing (i.e. different bench set-ups) are likely to additionally complicate attempts to perform any such comparisons. To generate a bench-mark of electrode materials, a series of tests were performed on single-phase electrodes. This covered both the symmetrical-cell and single-cell testing approaches that were described in Chapters 4 and 5, respectively. A number of factors relating to electrode performance were observed and are summarised here.

Relative to state-of-the-art commercial LSCF6428, each of the lanthanum nickelate phases displayed inferior performance. This was clearly apparent in the R_o, R_{pol} and Z_{DC} values recorded during symmetrical cell testing (Chapter 4); in certain scenarios, impedance values were found to be orders of magnitude larger than commercial materials. The addition of improved contact layers had, in some cases, an extraordinary effect on the measured performance. For obvious reasons, this effect was most heavily apparent in the case of the poorer conducting phases. In the case of the symmetrical cell testing of LNO214 electrodes, for instance, Z_{DC} values (T_{Op}=800˚C) were reduced from 309.5 Ωcm^2 to 1.3 Ωcm^2. Comparatively, the addition of Au-paste to LSCF6428 was relatively minor (from 7.2 Ωcm^2 to 0.75 Ωcm^2). These observations highlight that different effects should be anticipated for materials with dissimilar properties. Such conclusions have some important consequences for SOFC testing. These will be considered in further detail in Section 7.3.

Attempts to conduct testing on electrodes in the single-cell configuration (Chapter 5) brought an improved understanding of the performance of the lanthanum nickelates when placed under polarisation. First considering the polarisation curves measured with the different materials, it was apparent that each phase possessed a characteristic profile or shape. This is believed to be related to the relative properties of the electrode materials. In one case, LNO214 (which possesses very good oxygen exchange behaviour) displayed a rather linear iV-behaviour. In another case, LNF64 which can be considered as the antithesis of LNO214 (i.e. good electronic conductivity, relatively poor oxygen

exchange) showed a very activation-heavy profile but offered much more favourable behaviour in the ohmic region of the curve.

Overall, it was apparent that the studied materials demonstrated relatively limited potential in replacing commercial materials. An initial bench-mark of a commercial cell found that a current density between 0.79 and 0.86 Acm^{-2} was possible at an operating temperature of 800˚C and 0.7 V, respectively. In the majority of cases, the current density achieved from the lanthanum nickelates was below this and, in some cases, well below this. The poor performance could also be observed in the EIS spectra that were recorded at open circuit. DRT analysis indicated additional cell processes were present, suggesting sluggish kinetics.

Although the single-phase lanthanum nickelate electrodes were shown to offer relatively mediocre output, it was highlighted that there exist a number of approaches that can be used to enhance electrode performance. Increased sintering temperatures have proven, in many cases, to lead to a sizeable performance enhancement. In the case of LNO214, symmetrical cell Z_{DC} values (T_{Op}=800˚C) were reduced from 309.5 Ωcm^2 to 79.4 Ωcm^2. Post-test analysis indicated that this was a result of improved particle connectivity and, as a result, an improvement in charge transfer processes. The improvement in performance that was noted appeared to overcome any issues associated with incompatibility with the GDC barrier layer under fabrication conditions. This somewhat challenged the perception that lower sintering temperatures are favourable due to the issue of reactivity between the materials. Notably, the effect of T_{sint} on LNO214 appeared to be more pronounced than that seen for the other materials and this is thought to be a result of the underlying properties of this phase (i.e. lower electronic conductivity). Importantly, this highlights the need to approach the optimisation of materials on a case-by-case basis. Indeed, an increase in electrode sintering temperatures was shown to worsen the performance of the commercial LSCF6428 phase; this likely leads to changes in electrode morphology.

Another important route for improving the performance of electrodes is to combine with additional phases (e.g. GDC10) to form composite electrodes. In Chapter 6 of this thesis, a number of different combinations of materials were analysed in both symmetrical cell and single cell testing configuration. The most promising combination of materials was found to be LNF64-GDC although, by some measures at least, this still fell short of the performance achieved with the commercial LSCF. It is noted that this combination of materials combined the material with the most superior oxygen transport behaviour (GDC10) with the material with the most favourable electronic conduction properties. The effect that this had on the LNF64 electrode could be appreciated from the polarisation curves which became significantly more 'linear' (i.e. lower activation losses) with the addition of GDC10. Elsewhere, it was observed that the combination of LNO214 with LNF64 showed a synergistic effect, promoting the cell performance beyond that achieved with either of the single-phase electrodes. At the higher operating temperatures, LNO214 was found to be most favourably promoted with LNF64 whereas, as the temperature was lowered, LNO214-GDC became a more attractive proposition. This potentially alludes to the increasing necessity to aid oxygen exchange as the temperatures are lowered (i.e. this becomes the limiting factor rather than electronic transport). Further, it suggests that the optimum combination of phases is likely to be influenced by the operating temperatures that may be favoured at a system-level.

A crucial observation from this work is the difficulty that was found in obtaining a material (or combination of materials) that could compete with LSCF. This is particularly apparent at lower operating temperatures where LSCF retains excellent behaviour due to its favourable combination of electronic and ionic conductivity. An impressive level of performance was achieved in both the symmetrical cell and single cell testing configurations and was found to be evident in almost all metrics and in all conditions that were studied. Such observations offer a rather inconvenient truth for advocates of the lanthanum nickelate materials. Given degradation rates of LSCF-containing cells have been significantly reduced in the last 10 to 15 years (e.g. via the engineering of new Cr-transport inhibiting layers), it is rather difficult to build a case for the replacement of LSCF with the La-Ni-O

phases based on the results from this thesis. This is not, of course, to suggest that a high-performance lanthanum nickelate electrode *can't* be engineered via a careful combination of factors (e.g. layered electrode configurations, nano-structures, composite ratio optimisation). Indeed, examples of impressive electrodes comprising these materials exist within the literature. However, it should be stated that, based on the evidence from this thesis, such materials will necessitate a much greater (and, therefore, likely more costly) attention to such parameters of optimisation.

7.3 Comments on SOFC testing approaches

In addition to the comments on the performance of the various materials studied in this work, the observations from this thesis also have implications towards SOFC testing approaches that are seen in the literature. Due to the variety of materials studied, it was possible to assess the role of various testing approaches and elucidate how different phases (or fundamental properties) might influence the observations and conclusions that were drawn within each. Firstly, with regard to the use of noble metal contact layers, it became apparent that the electrical contact configuration seriously impacted the performance of the electrodes to which they are applied. Perhaps more pertinently, the *extent* to which such layers impact the performance of the underlying electrode was heavily influenced by the underlying properties of that material itself. The symmetrical cell behaviour (R_{pol}, $R_{o,}$ Z_{DC}) of LNO214, for instance, was found to be much more heavily improved by the addition of the Au-contact layer than was seen to be the case for LNF64 and LSCF6428. Indeed, to some extent, this could even influence the conclusions that might be drawn from a given study (i.e. in certain scenarios the presence of an Au-CCL LNO214 was shown to out-perform LNF64 but in the absence of the layer, the reverse was shown to be true). This has implications for studies in which optimisation or comparisons between materials are drawn. In particular, this confirms the difficulty of conducting like-for-like comparisons across studies with different approaches to contact configurations. Researchers should be aware of these effects and determine which approach is likely to be most beneficial to their application. There is an argument to suggest both approaches could offer benefit.

Another key observation that was made towards SOFC testing in this thesis is the relevance of symmetrical cell testing. The perceived benefit of this testing approach is that it can remove the influence of the fuel electrode and isolate the performance of the air electrode (i.e. the electrode of interest in this case). The drawback is that the approach limits study of the behaviour to open circuit conditions. Symmetrical cell testing is widespread and often conducted as a sole means of assessing the performance of a given material or electrode (i.e. without further consideration of polarisation testing). If the performance of all (or, at least, the studied) electrodes in this testing configuration correlates well with their corresponding performance under polarisation (i.e. lower voltages) then this represents an acceptable approach. However, it has been shown that, with certain materials (e.g. LNF64), polarisation curves are non-linear and strong activation losses can be seen even at relatively high operating temperatures. Moreover, these polarisation curves can 'flatten' at lower operating voltages where electronic conductivity becomes a much greater consideration (i.e., the relative voltage losses are reduced). This creates a situation where electrodes that do not appear to perform well at OCV (and hence have large EIS values in symmetrical cell testing) can conversely achieve high current densities at lower operating voltages and even out-perform those materials which behave more favourably at OCV. Given the ultimate goal of electrode development should be aimed at optimising current output, the role of symmetrical cell testing can therefore be questioned. This issue becomes particularly apparent when comparing dissimilar materials. However, it is worth noting that the findings in this thesis do appear to show that symmetrical cell testing correlates with single cell performance at OCV. In the case of LNF64, for instance, the large activation loss found via procurement of the polarisation curve is predicted by the sizeable symmetrical cell impedance. The need to develop electrodes that perform well across the entire voltage range also means that this technique can be used to de-select materials that do not meet this criteria in at least one part of the operating voltage range. Further, the use of the symmetrical cell testing approach brings an appreciation of the material when operated as an electrode and can help develop understanding towards likely behaviour with respect to R_o and R_{pol}. Finally, the use of symmetrical cell testing

becomes more favourable when comparing electrodes with similar properties (this might cover small changes in composition or different microstructures). Researchers should therefore be aware of the limitations of symmetrical cell testing, especially given that such considerations are not particularly well-documented.

7.4 Future Work

Whilst the difficulty in achieving a high-performance lanthanum nickelate electrode has been apparent in this work, it is acknowledged that further optimisation is no doubt possible. Indeed, as part of the previously discussed analysis, it has been shown that other authors have utilised these materials to out-perform that which has been achieved here. Some of these studies have involved the combination of lanthanum nickelates with materials such as LSC or LSCF. This is an interesting approach when considering that the common objective (described in Chapter 2) is to remove the use of Co- and alkaline-earth-doping. A better understanding will be required as to how these electrode designs perform in long-term operation and whether or not the overall benefit is sufficient to justify the replacement of conventional electrodes. Other options for optimisation may include the role of layered lanthanum nickelate electrodes, for instance, combining the excellent oxygen transport properties of LNO214 with the impressive electronic conductivity of LNF64. The performance of different ratios of composite phases is also an area of interest. Given the evidence in Chapter 6 of this thesis, investigating how different operating temperatures influence the selection of optimum material mix ratios is of interest. Another area of interest is the understanding of how the different approaches to optimising performance influence long-term degradation rates. Does the addition of GDC10, for instance, lead to greater degradation rates in long-term testing (given its apparent reactivity with the lanthanum nickelate phases)? In turn, does this negate any such benefit that can be garnered from composites of such materials? The potential of introducing dopants into the Ruddlesden-Popper phases has not been explored in this thesis but there is significant work in this area. A comprehensive consideration of the literature data for doped systems may be revealing. A key

challenge in this regard is to avoid introducing issues such as alkaline-earth segregation as a result of the choice of dopants.

From an SOFC testing perspectives, the insight that has been achieved towards symmetrical cell testing opens up an interesting line of enquiry. It has been shown that useful information on both polarisation resistance and ohmic resistance can support an understanding of electrode behaviour. However, the use of measurements in predicting behaviour under polarisation (perhaps a more realistic reflection of performance) is limited. However, a question remains as to whether the results from symmetrical cell testing be utilised to develop a model that can effectively describe electrode behaviour under polarisation? It could be envisaged that information of ohmic resistance (R_O) might be used to develop an idea or prediction of cell output at the extremities of the polarisation curve (i.e. medium-to-low operating voltages). In the long-term, such an analysis could improve the benefit of performing these measurements. Certainly, electrode performance models exist (e.g. Adler Lane Steele [339]) based on fundamental material properties such as surface exchange and bulk diffusion properties. However, it may be interesting to understand if polarisation performance (i.e. that seen in iV curve experiments) can be modelled based on the more straight-forward symmetrical cell testing approach.

Part of the difficulty that remains in electrode development is in understanding the bench-mark of 'what is good' and 'what is not'. Moreover, there is a need for further information on what sort of performance must be achieved for materials to be truly considered as promising alternatives. A wider question for the SOFC community surrounds, therefore, the targeted performance that researchers should be seeking from their work (and in what conditions they must be achieved to penetrate the commercial market). In this thesis, comparisons have been drawn with tests conducted on state-of-the-art materials and additionally with data taken from the literature. It remains difficult to assess, however, how the suitability of such an approach and strategies for a more universally agreed methodology could help identify the best performing materials for the next generation of SOFC cells.

Appendix A - Fuel cell thermodynamics: the effect of operating temperature

For a fuel cell operated with hydrogen and oxygen, the total reaction can be represented by:

$$H_2 + \frac{1}{2}O_2 \rightarrow H_2O \; [Eq.A1]$$

The maximum thermodynamic efficiency ($\eta_{thermodynamic}$) and voltage (E_o) of this reaction are calculated from:

$$\eta_{thermodynamic} = \frac{w_{electrical}}{w_{total}} = \frac{\Delta g_T}{\Delta h_T} = \frac{\Delta h_T - T\Delta s_T}{\Delta h_T} = 1 - \frac{T\Delta s_T}{\Delta h_T} \; [Eq.A2]$$

$$E_o = -\frac{\Delta g_T}{nF} == -\frac{\Delta h_T - T\Delta s_T}{nF} \; [Eq.A3]$$

Where $w_{electrical}$, w_{total}, Δg_T, h_T, T, Δs_T, n and F are the electrical work, total work, Gibbs free energy of reaction, enthalpy of reaction, specific entropy of reaction, the number of electrons transferred in the reaction and Faraday's constant. A lower case letter has been employed to denote that intensive properties are employed (i.e., values are on a per unit mole basis). The subscript T is used to denote that values are taken for a given temperature and pressure. The specific enthalpy and entropy at a given temperature are calculated by the difference between product and reactant states:

$$\Delta h_T = \sum h_{fprod} - \sum h_{react} \; [Eq.A4]$$

$$\Delta s_T = \sum s_{prod} - \sum s_{react} \; [Eq.A5]$$

Where Σh_{prod}, Σh_{react}, Σs_{prod} and Σs_{react} are the sum of the enthalpies and entropies of formation for the products and reactants, respectively. At room temperature (T=298K) and under standard conditions (pressure=1 bar), the enthalpy and entropy of formation of each reactants and products are as shown in Table A.1.

Table A.1 – standard values of the enthalpy and entropy of reaction at room temperature and standard pressure

Molecule	$h^o_{f,298}$ **(kJmol^{-1})**	$s^o_{f,298}$ **(kJmol^{-1}C^{-1})**
H_2	0	130.59
O_2	0	205.14
H_2O (gas) – LHV	-241.83	188.83
H_2O (liquid) - HHV	-285.84	70.05

The values can be used to calculate the enthalpy of reaction (Δh^o_{298}), entropy of reaction (Δs^o_{298}) at room temperature and standard pressure. These values are then used to calculate the Gibbs free energy of reaction (Δg^o_{298}), thermodynamic voltage (E_o) and thermodynamic efficiency ($\eta_{thermodynamic}$) under these same conditions. These values are shown in Table A.2.

Table A.2 – calculated values based on standard conditions and room temperature.

Temperature , T	298K
$\sum \boldsymbol{h_{prod}}$	-285.84 kJmol^{-1}
$\sum \boldsymbol{h_{react}}$	0 kJmol^{-1}
$\Delta \boldsymbol{h_T}$ **(=** $\boldsymbol{h^o_{298}}$ **when T=298K and p=1bar)**	-285.84 kJmol^{-1}
$\sum \boldsymbol{s_{prod}}$	70.05 kJmol^{-1}C^{-1}
$\sum \boldsymbol{s_{react}}$	233.16 kJmol^{-1}C^{-1}
$\Delta \boldsymbol{s_T}$ **(=** $\boldsymbol{s^o_{298}}$ **when T=298K and p=1bar)**	-163.11 kJmol^{-1}
$\Delta \boldsymbol{g^o_{298}}$	-237.2 kJmol^{-1}
$\mathbf{E_o}$	1.23 V
$\boldsymbol{\eta_{thermodynamic}}$	83%

This analysis can be extended for different operating temperature and pressures but requires consideration on the effect of temperature on the enthalpies of formation. These can be calculated using the following equations:

$$\Delta g_T = g^o_{298} + RTln(K)\ [Eq.A6]$$

$$\Delta h_T = h^o_{f,298} + \int_{298}^{T} C_p dT \ [Eq. A7]$$

$$\Delta s_T = s^o_{f,298} + \int_{298}^{T} \frac{1}{T} C_p dT \ [Eq. A8]$$

Where K is the reaction quotient and C_p is the specific heat capacity which is itself temperature-dependent as well as being substance dependent:

$$(C_p)_{H_2} = 56.505 - 22{,}222.6T^{-0.75} + 116{,}500T^{-1} - 560{,}700T^{-1.5} \ [Eq. A9]$$

$$(C_p)_{H_2O(g)} = 143.05 - 58.040T^{0.25} + 8.2751T^{0.5} - 560{,}700T^{-1.5} \ [Eq. A10]$$

$$(C_p)_{O_2} = 37.432 + (2010{,}2 \times 10^{-5}T^{1.5}) + 178{,}570T^{-1.5} + 2{,}368{,}800T^{-2} \ [Eq. A11]$$

From these equations it is possible to equate the relative values of Δg_T, Δh_T, Δs_T, E_o and $\eta_{thermodynamic}$. The results are shown in Figure A.1.

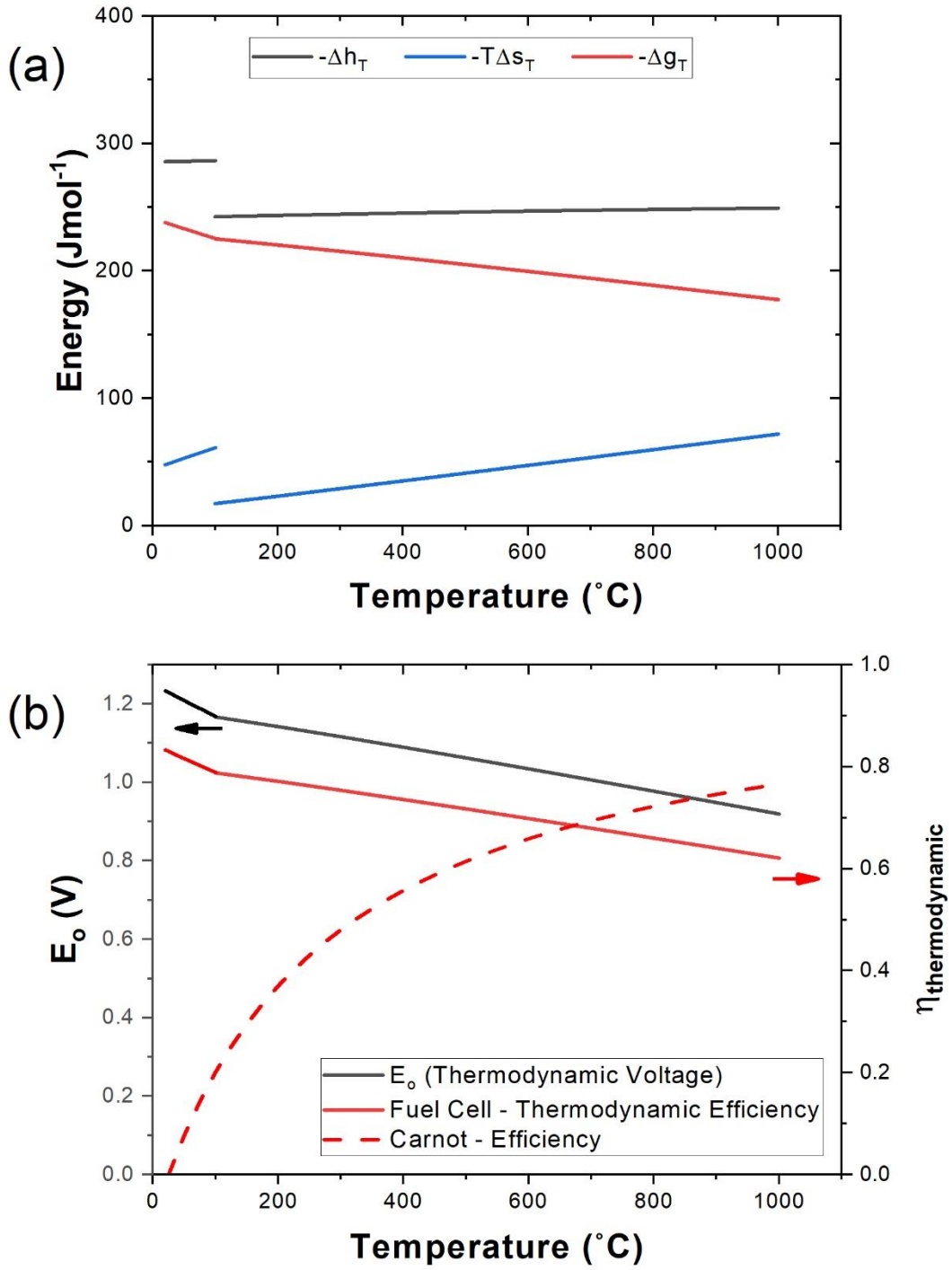


Figure A.1 – (a) effect of operating temperature on Δg_T, Δh_T, $T\Delta s_T$ and (b) E_o and $\eta_{thermodymaic}$.

Appendix B - Conductivity and thermal expansion data

Table B.1 – Electrical conductivity data taken from literature sources. Originally presented in [95].

Number in superscript denotes pellet sintering temp in degrees celcius. All values measured in air (or P_{O2}=0.21 bar) unless otherwise specified, S=Solid State , P=Pechini, C=Combustion, Cx=Complexing Method, GN=Glycine Nitrate, CP=coprecipitation, SG=Sol gel, Com.=Commercial, F.D.=Freeze Drying, Ci=Citrate, Ni-Ac=Nitrate/Acetate, Ct=Citric Acid Method, pyn=pyrolysis of nitrates, pre=precipitation, U=Urea route

~ = estimated from graphical data, # = data is recorded in tabulated form in source, @ = composition is A-site sub-stoichiometric. Note: some of the phase abbreviations (e.g. LNF64) are represented differently in the literature.

Material	**Electrical Conductivity**			**TEC**
	600˚C	**700˚C**	**800˚C**	**(x10^{-6}°C^{-1})**
La_2NiO_4 (**LNO214**)	~9.8 [197]$^{Ci\ /\ 1100}$	~8.9 [197]$^{Ci\ /\ 1100}$	~8.1 [197]$^{Ci\ /\ 1100}$	11.9 (30-1000˚C) [355]
	~40 [239]$^{S\ /\ 1200}$	~35 [239]$^{S\ /\ 1200}$	~30 [239]$^{S\ /\ 1200}$	13.1 (50-900˚C) [356]
	~57 [346]$^{NC\ /\ 1350}$	~50 [346]$^{NC\ /\ 1350}$	~46 [346]$^{NC\ /\ 1350}$	12.6 (50-1000˚C) [293]
	~59 [293]^{NC}	~53 [293]^{SG}	~50 [293]^{SG}	12.6 (50-800˚C) [293]
	~60 [342]^{S}	~55 [342]^{S}	~51 [342]^{S}	12.1 (50-600˚C) [293]
	~61 [347]$^{SG\ /\ 1350}$	~57 [347]$^{SG\ /\ 1350}$	-	13.0 (r.t.-1400˚C) [357]
	~62.5 [348]$^{CP\ /\ 1450}$	~57 [348]$^{CP\ /\ 1450}$	~50 [348]$^{CP\ /\ 1450}$	13.0 (27-1000˚C) [201]
	~63 [349]$^{FP\ /\ 1500}$	~58 [349]$^{FP\ /\ 1500}$	~52 [349]$^{FP\ /\ 1500}$	14-15.5 (20-1100˚C)
	~68 [241]$^{S\ /\ 1400}$	~61 [241]$^{S\ /\ 1400}$	~54 [241]$^{S\ /\ 1400}$	[194]
	~68 [335]$^{SG\ /\ 1400}$	~60 [335]$^{SG\ /\ 1400}$	~52 [335]$^{SG\ /\ 1400}$	13.7 (20-900˚C) [202]
	~74 [350]$^{S\ /\ 1300}$	~71 [350]$^{S\ /\ 1300}$	~66 [350]$^{S\ /\ 1300}$	12.6 (50-1000˚C) [353]
	~77.5 [206]$^{P\ /\ 1150}$	~67.5 [206]$^{P\ /\ 1150}$	~60 [206]$^{P\ /\ 1150}$	13.5 (30-1000˚C) [251]
	~80 [351]$^{LE\ /\ 1400}$	~70 [351]$^{LE\ /\ 1400}$	~65 [351]$^{LE\ /\ 1400}$	13.3 (25-800˚C) [239]
	~85 [294]$^{SG\ /\ 1400}$	~77 [294]$^{SG\ /\ 1400}$	~70 [294]$^{SG\ /\ 1400}$	14.6 (50-400˚C) [294]
	-	~86 [208]$^{P\ /\ 1300}$	~77 [208]$^{P\ /\ 1300}$	11.2 (400-800˚C) [294]
	~93 [255]$^{GN\ /\ 1300}$	~88 [255]$^{GN\ /\ 1300}$	~83 [255]$^{GN\ /\ 1300}$	14.9 (200-850˚C) [336]
	~94 [352]$^{GN/\ 1320\text{-}1450}$	~85 [352]$^{GN/\ 1320\text{-}1450}$	~76 [352]$^{GN\ /\ 1320\text{-}1450}$	12.9 (25-700˚C) [255]
	~95 [353]$^{PCP\ /\ 1250}$	~84 [353]$^{PCP\ /\ 1250}$	~75 [353]$^{PCP\ /\ 1250}$	
	~96 [354]$^{SG\ /\ 1300}$	~85 [354]$^{SG\ /\ 1300}$	~76 [354]$^{SG\ /\ 1300}$	
$La_3Ni_2O_7$ (**LNO327**)	53 [197]$^{Ci\ /\ 1100}$	51 [197]$^{Ci\ /\ 1100}$	50 [197]$^{Ci\ /\ 1100}$	12.9 (40-800˚C) [311]
	~60 [206]$^{P\ /\ 1100}$	~57.5 [206]$^{P\ /\ 1100}$	~52.5 [206]$^{P\ /\ 1100}$	11.0 (250-800˚C) [233]
	~62 [311]$^{SG\ /\ 1100?}$	~61 [311]$^{SG\ /\ 1100?}$	~59 [311]$^{SG\ /\ 1100?}$	14.5 (200-800˚C) [336]
	~100 [350]$^{S\ /\ 1300}$	~93 [350]$^{S\ /\ 1300}$	~85 [350]$^{S\ /\ 1300}$	
	-	~250 [208]$^{P\ /\ 1300}$	~239 [208]$^{P\ /\ 1300}$	
$La_4Ni_3O_{10}$ (**LNO4310**)	~97.7 [197]$^{Ci\ /\ 1100}$	~89.1 [197]$^{Ci\ /\ 1100}$	~87.1 [197]$^{Ci\ /\ 1100}$	12.6 (40-800˚C) [358]
	~100 [206]$^{P\ /\ 1050}$	~92.5 [206]$^{P\ /\ 1100}$	~87.5 [206]$^{P\ /\ 1050}$	11.5 (250-800˚C) [233]
	~100 [358]$^{SG\ /\ 1000}$	~96 [358]$^{SG\ /\ 1000}$	~89 [358]$^{SG\ /\ 1000}$	
	~138 [230]^{SG}	~129 [230]^{SG}	-	
	~235 [350]$^{S\ /\ 1350}$	~195 [350]$^{S\ /\ 1350}$	~168 [350]$^{S\ /\ 1350}$	
	-	~435 [208]$^{P\ /\ 1300}$	~400 [208]$^{P\ /\ 1300}$	

$LaNiO_3$ (**LNO113**)	~119 [239]$^{S/1200}$	~111 [239]$^{S/1200}$	~115 [239]$^{S/1200}$	10.0 (0-1100˚C) [361]
	~150 [197]$^{800\ /\ Ci}$	~105 [197]$^{800/Ci}$	~100 [197]$^{800/Ci}$	
	~393 [359]^{Ct}	~355 [359]^{Ct}	~309 [359]^{Ct}	
	~700 [360]$^{1050/Ni\text{-}Ac}$	~750 [360]$^{1050/Ni\text{-}Ac}$	~800 [360]$^{1050/Ni\text{-}Ac}$	
$LaNi_{0.6}Fe_{0.4}O_3$ (**LNF64**)	-	#33.9 [366]$^{1000\ /\ Ci}$	#32.4 [366]$^{1000\ /\ Ci}$	11.1 (30-800˚C) [198]
	-	#71.3 [366]$^{1000\ /\ U}$	#71.5 [366]$^{1000\ /\ Ci}$	11.4 (30-1000˚C) [198]
	#93 [362]^{GN}	#87 [362]^{GN}	#82 [362]^{GN}	11.6 (20-850˚C) [361]
	~115 [313]^{1300}	~110 [313]^{1300}	~105 [313]^{1300}	11.93-12.52 (600-
	~148.4 [333]$^{1200/GN}$	~141.7 [333]$^{1200/GN}$	~135.3 [333]$^{1200/GN}$	1000˚C) [365]
	-	#172.7[366]$^{1200\ /\ Ci}$	#166.6 [366]$^{1200\ /\ Ci}$	12.3 (r.t.-1000˚C) [368]
	~182 [363]$^{1200\ /\ Cx}$	~178 [363]$^{1200\ /\ Cx}$	~171 [363]$^{1200\ /\ Cx}$	12.4 (r.t.-1000˚C) [306]
	-	#140.8 [366]$^{1200\ /\ U}$	#135.7 [366]$^{1200\ /\ U}$	12.5 (50-900˚C) [356]
	~218 [198]$^{1250\ /\ S}$	~216 [198]$^{1250\ /\ S}$	#212 [198]$^{1250\ /\ S}$	12.7 (200-750˚C) [333]
	~225 [313]^{1400}	~220 [313]^{1400}	~215 [313]^{1400}	14.5 (50-1000˚C) [344]
	-	~236 [367]$^{1000\ /\ P}$	-	14.8 (200-800˚C) [362]
	~260 [364]$^{1200\ /\ GN}$	~250 [364] $^{1200\ /\ GN}$	#304.5 [366]$^{1400\ /\ Ci}$	15.26-17.22 (200-600˚C)
	-	#313 [366]$^{1400\ /\ Ci}$	#333.5 [366]$^{1400\ /\ U}$	[365]
	-	~313 [367]$^{1100\ /\ P}$	-	16.1 (30-800˚C) [325]
	-	#343.5 [366]$^{1400\ /\ U}$	-	16.0 (30-1000˚C) [325]
	~385 [364]$^{1200\ /\ GN}$	~375 [364]$^{1200\ /\ GN}$	-	
	#387 [365]$^{1050\ /\ GN}$	#373 [365]$^{1050\ /\ GN}$	#360 [365]$^{1050\ /\ GN}$	
	~400 [364]$^{1400\ /\ GN}$	~385 [364]$^{1400\ /\ GN}$	-	
	~450 [364]$^{1400\ /\ GN}$	~435 [364]$^{1400\ /\ GN}$	-	
	~490 [364]$^{1200\ /\ CP}$	~475 [364]$^{1200\ /\ CP}$	-	
	~545 [324]^{SG}	~530 [324]^{SG}	~512 [324]^{SG}	
	-	~571 [367]$^{1200\ /\ P}$	-	
	~612 [198]$^{1400\ /\ S}$	~597 [198]$^{1400\ /\ S}$	~582 [198]$^{1400\ /\ S}$	
	~740 [325]$^{1350\ /\ Com.}$	~710 [325] $^{1350\ /\ Com.}$	#685 [325] $^{1350\ /\ Com.}$	
$LaNi_{0.2}Fe_{0.8}O_3$ **(LNF28)**	~17 [198]$^{1250\ /\ S}$	~21 [198]$^{1250\ /\ S}$	~22 [198]$^{1250\ /\ S}$	-
$LaNi_{0.4}Fe_{0.6}O_3$ **(LNF46)**	~100 [198]$^{1250\ /\ S}$	~107 [198]$^{1250\ /\ S}$	~111 [198]$^{1250\ /\ S}$	11.5 (30-1000˚C) [306]
$LaNi_{0.7}Fe_{0.3}O_3$ **(LNF73)**	~162 [198]$^{1250\ /\ S}$	~173 [198]$^{1250\ /\ S}$	~171 [198]$^{1250\ /\ S}$	11.7 (30-1000˚C) [306]
$LaNi_{0.8}Fe_{0.2}O_3$ **(LNF82)**	~80 [198]$^{1250\ /\ S}$	~76 [198]$^{1250\ /\ S}$	~75 [198]$^{1250\ /\ S}$	-
$LaNi_{0.6}Co_{0.4}O_3$ **(LNC64)**	~369 [198]$^{1250\ /\ S}$	~356 [198]$^{1250\ /\ S}$	#345 [198]$^{1250\ /\ S}$	11.9(r.t.-1000˚C) [199]
	~485 [324]^{SG}	~460 [324]^{SG}	~431 [324]^{SG}	14.3 (r.t.- 800˚C) [198]
	~624 [361]$^{1150\text{-}1250/P}$	~602 [361]$^{1150\text{-}1250/P}$	~596 [361]$^{1150\text{-}1250/P}$	15.0 (r.t.-1000˚C) [198]
	~1225 [325]$^{1200/Com.}$	~1225 [325]$^{1200/Com.}$	#1229 [325]$^{1200/Com.}$	15.9 (20-850˚C) [361]
	~@1410	~@1350[257]$^{1200/GN}$	~@1300[257]$^{1200/GN}$	17.9 (30-800˚C) [325]
	[257]$^{1200/GN}$			17.5 (30-1000˚C) [325]

$LaNi_{0.4}Co_{0.6}O_3$ **(LNC46)**	~933 [361][1150-1250/P] ~@1407 [369][1100/GN] ~@1580 [257][1250/GN]	~861 [361][1150-1250/P] ~@1344[369][1100/GN] ~@1500 [257][1250/GN]	~818 [361][1150-1250/P] ~@1273[369][1100/GN] ~@1420 [257][1250/GN]	14.3 (20-850˚C) [361]
$LaNi_{0.3}Co_{0.7}O_3$ **(LNC37)**	~832 [370][1327-1397/ S]	-	~794 [370] [1327-1397/ S]	17.3 x 10^{-6} (27-827˚C) [370]
$LaNi_{0.1}Co_{0.9}O_3$ **(LNC19)**	~977 [370][1327-1397/ S]	-	~1000 [370][1327-1397/ S]	19.6 x 10^{-6} (27-827˚C) [370]
$LaNi_{0.6}Cr_{0.4}O_3$ **(LNCr64)**	~32.6 [198][1250 / S]	~32 [198][1250 / S]	~30 [198][1250 / S]	9.8 (r.t.-800˚C) [198] 11.7 (r.t.-1000˚C) [198]
$LaNi_{0.6}Al_{0.4}O_3$ **(LNA64)**	~4.26 [198][1250 / S]	~4.35 [198][1250 / S]	~4.17 [198][1250 / S]	10.8 (r.t.-800˚C) [198] 11.4 (r.t.-1000˚C) [198]
$LaNi_{0.6}Mn_{0.4}O_3$ **(LNM64)**	~9.2 [198][1250 / S]	~10.3 [198][1250 / S]	~11.1 [198][1250 / S]	10.2 (r.t.-800˚C) [198] 10.8 (r.t.-1000˚C) [198]
$LaNi_{0.6}Ga_{0.4}O_3$ **(LNG64)**	~21.1 [198][1250 / S]	~17.3 [198][1250 / S]	~12 [198][1250 / S]	10.8 (r.t.-800˚C) [198] 11.7 (r.t.-1000˚C) [198]
$La_{0.9}Sr_{0.1}Fe_{0.9}Ni_{0.1}O_3$ **(LSFN9191)**	~33 [361][1400/S]	~41 [361][1400/S]	~45 [361][1400/S]	11.7 (20-850˚C) [361]
$La_{0.9}Sr_{0.1}Fe_{0.8}Ni_{0.2}O_3$ **(LSFN9182)**	~138 [361][1400/S]	~152 [361][1400/S]	~173 [361][1400/S]	12.6 (20-850˚C) [361]
$La_{0.8}Sr_{0.2}Fe_{0.8}Ni_{0.2}O_3$ **(LSFN9182)**	~244 [361][1400/S]	~240 [361][1400/S]	~234 [361][1400/S]	12.8 (20-850˚C) [361]
$La_{0.8}Sr_{0.2}Fe_{0.7}Ni_{0.3}O_3$ **(LSFN8273)**	-	#200 [371][1200/F.D.]	-	-
$La_{0.7}Sr_{0.3}Fe_{0.8}Ni_{0.2}O_3$ **(LSFN7382)**	~426 [361][1400/S]	~419 [361][1400/S] 290 (750˚C) [372]	~399 [361][1400/S]	13.7 (30-1000˚C) [372]
$LaCo_{0.8}Fe_{0.1}Ni_{0.1}O_3$ **(LCFN10811)**	~513 [373][1397-1627/S] ~450 [374][1300/P]	- ~500 [374][1300/P]	~631 [373][1397-1627/S] ~737.3 [374][1300/P]	20.8 (r.t-827˚C) [373] 21.83 (r.t-900˚C) [374]
$LaCo_{0.7}Fe_{0.1}Ni_{0.2}O_3$ **(LCFN10712)**	~708 [373][1397-1627/S]	-	~759 [373][1397-1627/S]	18.6 (r.t-827˚C) [373]
$LaCo_{0.6}Fe_{0.2}Ni_{0.2}O_3$ **(LNCF10262)**	~476 [373][1397-1627/S]	-	~550 [373][1397-1627/S]	19.2 (r.t-827˚C) [373]
$LaCo_{0.5}Fe_{0.2}Ni_{0.3}O_3$ **(LNCF10352)**	~447 [373][1397-1627/S]	-	~473 [373][1397-1627/S]	-
$LaFe_{0.8}Co_{0.1}Ni_{0.1}O_3$ **(LFCN10811)**	~30 [374] [1300/P]	~40 [374][1300/P]	~55.6 [374][1300/P]	13.42 (r.t.-900˚C) [374]
$LaNi_{0.8}Co_{0.1}Fe_{0.1}O_3$ **(LNCF10811)**	~205 [374] [1300/P]	~190 [374] [1300/P]	~185 [374] [1300/P]	21.69 (r.t.-900˚C) [374]
$(La_{0.9}Sr_{0.1})Co_{0.9}Ni_{0.1}O_3$ **(LSNC9191)**	~966 [361][1150-1250/P]	~926 [361][1150-1250/P]	~866 [361][1150-1250/P]	17.6 (20-850˚C) [361]
$(La_{0.9}Sr_{0.1})Co_{0.7}Ni_{0.3}O_3$ **(LSNC9173)**	~@1621 [369][1100/GN]	~@1500[369][1100/GN]	~@1417 [369][1100/GN]	-

$(La_{0.8}Sr_{0.2})Co_{0.8}Ni_{0.2}O_3$ **(LSNC8282)**	~2270 [361]$^{1150-1250/P}$ ~@2077 [369]$^{1100/GN}$	~1819 [361]$^{1150-1250/P}$ ~@1923[369]$^{1100/GN}$	~1634 [361]$^{1150-1250/P}$ ~@1791 [369]$^{1100/GN}$	16.1 (20-850˚C) [361]
$(La_{0.8}Sr_{0.2})Co_{0.9}Ni_{0.1}O_3$ **(LSNC8291)**	~1470 [361]$^{1150-1250/P}$	~1388 [361]$^{1150-1250/P}$	~1263 [361]$^{1150-1250/P}$	16.1 (20-850˚C) [361]
$La_{0.7}Sr_{0.3}Ni_{0.1}Co_{0.9}O_3$ **(LSNC7319)**	~2203 [361]$^{1150-1250/P}$ ~@2182 [369]$^{1100/GN}$	~2011 [361] $^{1150-1250/P}$ ~@1931[369]$^{1100/GN}$	~1734 [361] $^{1150-1250/P}$ ~@1717 [369]$^{1100/GN}$	16.3 (20-850˚C) [361]
$La_{0.6}Sr_{0.4}Co_{0.2}Fe_{0.8}O_3$ (LSCF6428)	~ 330 [375]^{1325}	~ 320 [375]^{1325}	~ 280 [375]^{1325}	17.5 (30-1000˚C) [126] 16.8 (100-900˚C) [376] 15.2 (100-600˚C) [375] 17.5 (r.t -1000˚C) [126]
$La_{0.8}Sr_{0.2}CoO_3$ (LSC82)	~1375 [377]^{1250}	~1300 [377]^{1250}	~1240 [377]^{1250}	19.1 (30-1000˚C) [378]
$La_{0.6}Sr_{0.4}CoO_3$ (LSC64)	~2200 [379]^{1250}	~1950 [379]^{1250}	~1870 [379]^{1250}	~19.6 (25-1000 ˚C) [380] 20.5 (30-1000˚C) [126]

Table C.1 – Symmetrical cell performance of different lanthanum nickelate electrodes studied by various researchers. Partially presented in [95].

Cathode Config.	**Electrolyte Layers**	**Cathode Sintering Temp (˚C)**	**Current Collector**	**R_{pol}** (*Denotes where values have been estimated from graphical data, **bold** text denotes were values are reference in text in the original work) [Ωcm^2]							**Ref.**
				500˚C	**550˚C**	**600˚C**	**650˚C**	**700˚C**	**750˚C**	**800˚C**	
LNF64-SDC	SDC	1000	Ag paste	-	-	*17	*7	**2.8**	*1	**0.48**	[301]
LNF64	SDC	1000	Ag paste			*28.14	*13.3	*6.3	*2.82	**1.3**	
LNF64	YSZ	1000	Ag paste			*84.5	*36.1	*17.07	*9.36	**4.6**	
LNF64-GDC (70:30)	SSZ	1050	Pt mesh	-	-	-	-	*1.363	-	*0.242	[249]
LNF64-GDC (60:40) | LNF64-GDC (70:30) | LNF64	SSZ	1050	Pt mesh	-	-	-	-	*1.009	-	*0.202	
GDC-infil.-into LNF64	SSZ	1050	Pt mesh	-	-	-	-	*0.285	-	*0.054	
Ag-infil.-into LNF64-SDC	SDC	1000	Ag paste	-	-	*1	-	*0.18	-	-	[237]
LNF64-SDC (50:50)	SDC	1000	Ag paste			*5		*0.92	-	*0.2	
LNF64	SDC	1000	Ag paste			*10.2		*2.4		*0.6	
LNO214-LNF64 (70:30)	BZCY	1000	Unclear	-	*37.5	*13	*5	*2.1	-	-	[335]
LNO214-LNF64 (50:50)	BZCY	1000	Unclear	-	*42	*15	*6	*2.4	-	-	
LNO214-LNF64 (30:70)	BZCY	1000	Unclear	-	*55	*20	*7	*3	-	-	

LNO214-LNF64 (50:50)	BZCY	1000	Unclear	-	*24	*11	*4	*2	-	-	[340]
SDC-LNF64 (50:50)	BZCY	1000	Unclear	-	*38	*14	*6	*2.500	-	-	
LNF64 | LNF64 Dense Interlayer	GDC	1100	Pt paste	-	-	*7	*2.500	*0.900	*0.380	*0.170	[245]
LNF64 | LSCF6428 Dense Interlayer	GDC	1100	Pt paste	-	-	*5.1	*1.900	*0.800	*0.300	0.140	
LNF64 | STF ($SrTi_{0.65}Fe_{0.35}O_3$) Dense Interlayer	GDC	1100	Pt paste	-	-	*14	*5.100	*1.700	*0.600	*0.280	
LNF64	GDC	1100	Pt paste	-	-	*8.000	*2.700	*1.00	*0.400	**0.200**	
LNF64	SDC	950	Pt grids	-	-	*457.1	-	**34.29**	-	*10	[343]
LNF64-SDC | LNF-EDB-CuO	SDC	1100 900	Pt grids	-	-	*0.66	-	*0.11	-	*0.03	
LNF-SDC | LNF-CuO	SDC	1000 900	-	-	-	**3.52**	-	**0.48**	-	-	[381]
LNF-SDC-CuO | LNF-CuO	SDC	1000 950	-	-	-	**2.36**	-	**0.38**	-	-	
LNF-SDC | LNF-YDB-CuO	SDC	1000 900	-	-	-	**0.67**	-	**0.16**	-	-	
LNF-SDC-CuO | LNF-EDB-CuO	SDC	900 900	-	-	-	**0.77**	-	**0.15**	-	-	
LNF-SDC | LNF-EDB-CuO	SDC	1000 900	-	-	-	**0.60**	-	**0.13**	-	-	
LNF-SDC | LNF-YBD	SDC	1000 900	-	-	-	**0.96**	-	**0.18**	-	-	
LNO214 | LNF64	SDC	1200	Pt mesh	-	-	**1.46**	**-**	**0.39**	**-**	**0.13**	[244]

		1200									
LNO214 |LNF64	SDC	1300 1250	Pt mesh	-	-	**0.80**	**-**	**0.18**	**-**	**0.06**	
LNF64	YSZ	900	Pt mesh	-	-	*12	*10	*4	*2	*1	[243]
LNF64 porous | LNF64 dense	YSZ	900	Pt mesh	-	-	*1.8	*0.55	*0.25	*0.1	*0.05	
LNF64 porous | LNF64 dense	GDC | YSZ	900	Pt mesh	-	-	*1.9	*0.5	*0.2	*0.08	0.03	
LNF64	LSGM	800	Pt gauze & paste	-	-	-	-	**3.19**	**1.22**	**0.51**	[324]
LNC64	LSGM	800	Pt gauze & paste	-	-	-	-	**2.88**	**0.94**	**0.34**	
LNF64	GDC | YSZ	850	Ag mesh	-	-	-	-	**2.60**	-	-	[382]
LSCF-infil.-into-LNF64	GDC | YSZ	850	Ag mesh	-	-	-	-	*0.1	-	-	
LNF64-infil.-into-LNF64	GDC | YSZ	850	Ag mesh	-	-	-	-	**0.15**	-	-	
GDC-infil.-into-LNF64	GDC | YSZ	850	Ag mesh	-	-	-	-	*0.1	-	-	
LSM-infil.-into-LNF64	GDC | YSZ	850	Ag mesh	-	-	-	-	*0.575	-	-	
Pr_6O_{11}-infil.-into-LNF64	GDC | YSZ	850	Ag mesh	-	-	-	-	*0.06	-	-	
LNF64-GDC (35:65)	GDC	1000	Pt paste + Au grid	-	-	**22.694**	**7.575**	*2.7	*1.1	*0.4	[383]
Cu-infil.-into-LNF64-GDC (35:65)	GDC	1000 600	Pt paste + Au grid	**5.774**	**2.08**	**0.839**	-	-	-	-	
Cu-infil.-into-LNF64-GDC (35:65)	GDC	1000 650	Pt paste + Au grid	**6.370**	**1.991**	**0.736**	**0.312**	-	-	--	

Pr-infil.-into-LNF64-GDC (35:65)	GDC	1000 600	Pt paste + Au grid	**0.724**	**0.210**	**0.081**	-	-	-	-	
Pr-infil.-into-LNF64-GDC (35:65)	GDC	1000 650	Pt paste + Au grid	**0.684**	**0.205**	**0.092**	**0.058**	-	-	-	
LNC64	GDC	950	Pt paste	-	-	*398.1	-	*55.0	-	*6.8	[369]
LSCN9173	GDC	950	Pt paste	-	-	*75.9	-	*10.0	-	*1.1	
LSCN8282	GDC	950	Pt paste	-	-	*26.9	-	*2.7	-	*0.32	
LNC64-GDC	GDC	1000	Not spec.	-	-	*0.45 (595 ˚C)	*0.21 (645 ˚C)	*0.15 (695 ˚C)	*0.08 (745 ˚C)	*0.05 (795 ˚C)	[257]
LSC64-infil.-into-LNC64-GDC	GDC	1000	Not spec.	-	-	*0.29	*0.15	*0.07	-	-	
LFCN10811	GDC | YSZ	Not spec.	Ag paste	-	-	-	*0.21	*0.16	**0.14**	-	[374]
LNCF10811	GDC | YSZ	Not spec.	Ag paste	-	-	-	*0.85	*0.63	*0.48	-	
LCFN10811	GDC | YSZ	Not spec.	Ag paste	-	-	-	*0.42	*0.32	*0.23	-	
LNC64-and-GDC-infil.-into-YSZ	YSZ	600	Pt paste + Pt grids	-	-	**0.053**	-	-	-	-	[384]
LNO214	YSZ	1000	Pt plates	-	*148.413	*60.340	*24.533	*14.154	*7.389	*4.263	[293]
LNO214	GDC	1000	Pt plates	-	*18.174	*10.486	*6.360	*4.055	*2.586	*2.014	
LNO214	YSZ | GDC	1150	Not spec.	-	-	**1.300**	*0.650	*0.260	*0.140	-	[251]
LNO214	SDC	1100	Pt paste.	-	-	-	-	**3.820**	-	-	[239]
LNO214	LSGM	1000	Ag paste	-	-	-	*0.446	*0.215	*0.121	*0.077	[294]
LNO214	YSZ	1000	Pt plates	-	-	**54.11**	**30.72**	**15.27**	**7.88**	**2.48**	[295]
LNO214	SDC	1000	Pt paste	-	-	*40.851	-	*6.380	-	**1.640**	[224]
LNO214	SDC (2%Co)	1000	Pt paste	-	-	*12.023	-	*1.687	-	**0.400**	
LNO214	YSZ	1100	Pt grids	-	-	*15	*5	*1.5	*0.5	**0.200**	[252]
LNO214	YSZ | GDC	1150	Pt paste	-	-	-	-	-	-	**0.110**	[246]
LNO214	GDC	1100	Pt mesh	-	-	*17.783	10.830	**7.400**	5.623	5.012	[247]

LNO214	GDC	1100	Pt mesh + Pt paint	-	-	*3.162	*1.613	**1.000**	*0.689	*0.510	[247]
LNO214 Dense layer | LNO214	GDC	1100	Pt mesh	-	-	*5.101	*2.320	**1.000**	*0.479	*0.222	
LNO214	SDC	900	Pt mesh	-	-	**5.77**	**2.46**	**1.14**	**0.59**	**0.28**	[297]
LNO214	SDC	950	Pt mesh	-	-	**16.61**	**6.7**	**2.46**	**1.02**	**0.4**	
LNO214	SDC	1000	Pt mesh	-	-	**11.63**	**5.19**	**2.13**	**1.12**	**0.57**	
LNO214	SDC	1050	Pt mesh	-	-	**20.16**	**8.2**	**3.47**	**1.65**	**0.79**	
LNO214	SDC	1100	Pt mesh	-	-	**23.4**	**7.33**	**2.71**	**1.34**	**0.69**	
LNO214 (A-site deficient)	GDC	900	Not spec.	-	-	*71.421	*42.424	*27.743	*19.189	*14.968	[298]
LNO214 (A-site deficient)	YSZ	900	Not spec.	-	-	*133.441	*43.109	*20.958	*9.404	*6.401	
LNO214	LSGM	1000	Not spec.	-	-	*4.746	*1.980	*0.958	-	-	
LNO214	GDC	1100	Not spec.	-	-	**2.2**	-	**0.55**	-		[226]
LNO214	GDC	1150	Not spec.	-	-	**2**	-	**0.42**	-	*0.15	
LNO214	LSGM	1100	Not spec.	-	-	**4.5**	-	**1.42**	-	-	
LNO214	LSGM	1150	Not spec.	-	-	**3.7**	-	**1.03**	-	*0.5	[226]
LNO214	LSSO	1100	Not spec.	-	-	**4.4**	-	**0.79**	-	*0.2	
LNO214	LSSO	1150	Not spec.	-	-	**9.3**	-	**1.73**	-	-	
LNO214	LWO ($La_{5.5}WO_{11.25}$)	1150	Pt mesh	-	-		*30	*11	**5.03**	*2.5	[299]
LNO214	LSGM	1300	None	-	-	*6.653	*5.084	*4.297	-	-	[250]

LNO214 | LNO214	SDC	1300 (both layers)	Pt mesh	-	-	**4.910**	-	**1.050**	-	**0.300**	[244]
LNO214 (ESD EtOH)	GDC	950	Au grids	-	-	**40.730**	-	**20.300**	-	-	[242]
LNO214 (ESD EtOH + H_2O)	GDC	950	Au grids	-	-	**3.330**	-	**1.260**	-	-	
LNO214 (screen-printed)	GDC	1050 1100	Au grids	-	-	**3.530**	-	**0.580**	-	-	
LNO214 (ESD EtOH + H2O) | LNO214 (Screen Printed)	GDC	950 (ESD) 1050 1100	Au grids	-	-	**0.420**	-	**0.080**	-	-	
LNO214	SDC	1100	Pt paste	-	-	*1.375	*0.415	*0.210	*0.100	*0.054	[255]
LNO214	GDC	900	Au grid	-	-	*1398	*950	*400	*200	*56.234	[254]
LNO214	YSZ	900	Au grid	-	-	*177.828	*54.600	*39.500	*16.750	*7.526	[254]
LNO214	LSGM	900	Not spec.	-	-	*31.623	*14.135	*6.780	*3.913	*2.150	[205]
LNO214: LNO113 (60:40)	SDC	1100	Pt paste and current collector	-	-	-	-	**3.280**	-	-	[239]
LNO214: LNO113 (50:50)	SDC	1100	Pt paste and current collector	-	-	-		**3.840**	-	-	[239]
LNO214-GDC	YSZ	900	Not spec.	-	-	-	-	-	**0.244**	-	[222]
LNO214-GDC	YSZ	1000	Not spec.	-	-	-	-	-	**0.344**	-	[222]
LNO214-GDC	YSZ	1100	Not spec.	-	-	-	-	-	**0.698**	-	[222]

LN0214-LNO327-LDC (0.3:2.2:2.5)	SDC	1100	Not clear - Ag paste?	-	-	**1.110**	*0.460	**0.220**	*0.110	**0.060**	[336]
LNO214:LNO4310 (50:50)	LSGM	1000	Not spec.	**38.1**	**10.3**	**3.450**	**1.370**	**0.620**	-	-	[240]
LNO214 | 50:50 (LNO214:LNO4310)	LSGM	1300 (Compact 214 layer) 1000 (Composite)	None	-	-	*2.651	*1.178	*0.630	-	-	[250]
LNO214 | 50:50 (LNO214:LNO4310) | LNO4310	LSGM	1300 (Compact 214 layer) 1000 (Composite)	None	-	-	**2.290**	**1.060**	**0.530**	-	-	[250]
LNO214 | LNF64	SDC	1473-1673K (FL) 1473-1523K (CCL)	-	-	-	*3.500	-	*0.700	-	*0.200	[241]
LNO214 (Solid State) | LNF64 (Pechini)	SDC	1200	Pt mesh	-	-	**3.650**	-	**0.740**	-	**0.200**	[244]
LNO214 (Solid State) | LNF64 (Pechini)	SDC	1300 1250	Pt mesh	-	-	**2.830**	-	**0.570**	-	**0.170**	
LNO214 (Pechini) | LNF64 (Pechini)	SDC	1200 1200	Pt mesh	-	-	**2.780**	-	**0.530**	-	**0.150**	
LNO214 (Pechini) | LNF64 (Pechini)	SDC	1300 1250	Pt mesh	-	-	**1.230**	-	**0.260**	-	**0.080**	

LNO214 (Nitrate Combustion) | LNF64 (Pechini)	SDC	1200 1200	Pt mesh	-	-	**1.760**	-	**0.390**	-	**0.120**	
LNO214 (Nitrate Combustion) | LNF64 (Pechini)	SDC	1300 1250	Pt mesh	-	-	**1.000**	-	**0.230**	-	**0.080**	
LNO214 (Nitrate Combustion) | LNF64 (Combustion)	SDC	1200 1200	Pt mesh	-	-	**1.460**	-	**0.390**	-	**0.130**	
LNO214 (Nitrate Combustion) | LNF64 (Combustion)	SDC	1300 1250	Pt mesh	-	-	**0.800**	-	**0.180**	-	**0.060**	
LNO214:LNO4310 (75:25)	GDC	1000	Au mesh	-	-	**1.180**	*0.447	*0.211	-	-	[385]
LNO214:LNO4310 (50:50)	GDC	1000	Au mesh	-	-	**0.620**	*0.316	*0.178	-	-	
LNO214:LNO4310 (25:75)	GDC	1000	Au mesh	-	-	**2.630**	*1.122	*0.501	-	-	
LNO214:LNO327 (50:50)	GDC	1000	Au mesh	-	-	**1.090**	*0.482	*0.240	-	-	
LNO214:LNO4310 (ESD) | LNO214:LNO4310 (50:50)	GDC	1100 1000	Au mesh	-	-	**0.500**	*0.316	*0.145	-	-	
LNO214 (ESD) | LNO327 (Screen Printed)	GDC	950 1000	Au mesh	-	-	**0.210**	*0.110	*0.049	-	-	
LNO214 (ESD) | LNO4310 (Screen Printed)	GDC	950 1000	Au mesh	-	-	**0.220**	*0.110	*0.050	-	-	

LNO214/GDC (Thin dense layer) | LNO214 (ESD FL) | LNO214 (CCL) Screen printed	GDC	900	"Grid"	-	-	*0.157	*0.080	*0.040	-	-	[300]
LNO-SDC | LNF64 + 2wt% CuO	Triple layer SSZ	1100 (FL) 1050 (CCL)	Pt paste	-	-	-	-	-	-	**0.16**	[341]
LNO214-LSCF (80:20)	SDC	1150	Pt paste	-	-	*1.250	*0.372	*0.163	*0.086	*0.048	[255]
LNO214-LSCF (70:30)	SDC	1150	Pt paste	-	-	*1.000	*0.286	*0.140	*0.053	*0.038	
LNO214-LSCF (60:40)	SDC	1100	Pt paste	-	-	*1.635	*0.398	*0.145	*0.077	*0.045	
LNO214-LSCF (50:50)	SDC	1100	Pt paste		-	*1.719	*0.462	*0.162	*0.090	*0.049	
LN214-LDC45 (Co-synthesised)	SDC	1100	Not spec.	-	-	-	-	**0.21**	**0.06**	-	[334]
LNO214-LDC45 (Separately mixed)	SDC	1100	Not spec.	-	-	-	-	**0.26**	**0.09**	-	
LNO214-Infil-YSZ	YSZ	850	Ag paste	-	-	-	-	-	**0.120**	-	[386]
LNO214-infil-LSCF	YSZ | GDC	1150 900	Pt paste + mesh	-	-	*0.247	*0.105	**0.042**	**0.023**	-	[253]
LNO214-Infil-YSZ	YSZ	900	Au grid	-	-	**0.350**	-	-	-	-	[387]
LNO214-Infil.GDC	YSZ | GDC	900	Au grid	-	-	*0.310	-	-	-	-	
LNO214-Infil.GDC	GDC	900	Au grid	-	-	**0.150**	-	-	-	-	
LNO214-Infil.-into-LSCF (6x infiltration)	YSZ | GDC	1050 (LSCF backbone) 900 (after infiltration)	Pt mesh	-	-	*0.600	*0.210	*0.070	*0.030		[388]
LNO214 nanorods	YSZ	400	Au mesh + Au paste	-	-	*1.416	*0.678	*0.337	*0.174		[256]

LNO214-Infil.-into LSCF	GDC	800	Pt mesh	-	-	*4.100	*1.900	*0.800	*0.310		[389]
LNO327	YSZ	1000	Not spec.	-	-		*2.600	*0.970	*0.390	*0.200	[311]
LNO327	GDC	1000	Au mesh	*17.783	*7.0795	*3.590	*1.778	*1.000	*0.501		[233]
LNO327	LSGM	900	Not spec.	-	-	*25.900	*11.273	*4.809	*2.695	*1.461	[205]
LNO4310	GDC	1000	Au mesh	*39.810	*15.849	*6.170	*2.818	*1.500	*0.708	-	[233]
LNO4310	LSGM	1200	Not spec.	-	-	*12.698	*5.451	*2.328	-	-	[240]
LNO4310	GDC	950	Au mesh	-	-	*372.759	*162.114	*72.410	*37.278	*18.860	[232]
LNO4310	GDC	950	Au mesh	-	-	*39.242	*19.708	*12.780	*6.629	*4.200	
LNO4310	GDC	950	Au mesh	-	-	*6.168	*3.329	*2.210	*1.462	*0.840	
LNO4310	GDC	950 1050 1100	Au mesh	-	-	*1.991	*0.765	*0.300	*0.110	*0.050	
LNO4310	LSGM	900	Not spec.	-	-	*27.498	*12.048	*5.106	*2.222	*1.127	[205]

Table D.1 – Single cell testing of lanthanum nickelate electrodes in various studies. Current density values measured at 0.7V ($i_{0.7V}$). Partially presented in [95].

Category	Anode	Electrolyte	Cathode	Contact Config (Ano/Cat)	Current density at 0.7 V ($i_{0.7V}$) [Acm^{-2}]								Ref
					550˚C	600˚C	650˚C	700˚C	750˚C	800˚C	850˚C	900˚C	
La-Ni-O Cmp	Ni-BZCY	BZCY	LNO214-LNF64 (70-30wt%)	Ag paste/ Ag paste	0.225	0.400	0.550	0.700	-	-	-	-	[335]
La-Ni-O Infil	Ni-BZCY	BZCY	31wt% LNF64-infil-LNO214	Not spec/Ag paste	0.300	0.450	0.750	1.400	-	-	-	-	[390]
La-Ni-O Cmp	Ni-BZCY	BZCY	LNO214-LNF64 (optimised)	Not spec./Ag paste	-	0.425	0.625	0.8	-	-	-	-	[340]
LNF-Cmp	Ni-BZCY	BZCY	LNF64-SDC	Not spec./Ag paste	-	0.260	0.380	0.510	-	-	-	-	[340]
214-Cmp	Ni-YSZ (1000 µm)	YSZ	LNO214 | LSC	Ni mesh/Ag mesh	-	-	-	-	-	0.357	-	-	[236]
214-Cmp	Ni-YSZ (1000 µm)	YSZ	LNO214-SDC | LNO214	Ni mesh/Ag mesh	-	-	-	-	-	0.430	-	-	[236]
214-Cmp	Ni-YSZ (1000 µm)	YSZ	LNO214-SDC | LSM	Ni mesh/Ag mesh	-	-	-	-	-	1.357	-	-	[236]
214-Cmp	Ni-YSZ (1000 µm)	YSZ	LNO214-SDC | LSC	Ni mesh/Ag mesh	-	-	-	-	-	2.314	-	-	[236]
214-Cmp	Ni-YSZ (500 µm)	YSZ	LNO214-SDC | LSC	Ni mesh/Ag mesh	-	0.500	-	1.275	-	2.714	-	-	[236]
214 SP	Ni-BZCY	BZCY	LNO214 (nanofiber)	Not specified	0.092	0.133	0.400	0.489	-	-	-	-	[238]
LNF SP	Ni-BZCY	BZCY	LNF64 (nanofiber)	Not specified	0.191	0.332	0.500	0.678	-	-	-	-	[238]
214-Cmp	Ni-SDC	SDC	LNO214-SDC	Au ink/Pt ink	-	-	-	-	0.105	0.140	-	-	[270]

214-Infil.	Ni-YSZ	YSZ	LNO214-infil-YSZ	Ag paste/Ag paste	-	-	0.322	0.500	0.746	0.959	-	-	[386]
327-Infil.	Ni-YSZ	YSZ	LNO327-infil-YSZ	Ag paste/Ag paste	-	-	0.406	0.632	0.983	1.226	-	-	[386]
4310-Infil	Ni-YSZ	YSZ	LNO4310-infil-YSZ	Ag paste/Ag paste	-	-	0.356	0.589	0.857	1.101	-	-	[386]
214-SP	Ni-SDC	SDC | LSGM	LNO214	Au ink/Pt ink	-	0.027	0.065	0.126	0.207	0.293	-	-	[268]
327-SP	Ni-YSZ	YSZ	LNO327	Not spec.	-	-	0.664	0.931	1.184	1.528	-	-	[311]
214-Infil	Ni-YSZ	YSZ | GDC	LNO214-infil-LSCF	Ni paste/Pt paste	-	-	-	-	0.847	-	-	-	[253]
214-Infil	LNO214-LSGM	LSGM	LNO214-infil-LSGM	Ag paste/Ag paste	-	0.150	0.250	0.367	0.522	0.666	-	-	[267]
214-Infil	LNO214-SDC	SDC	LNO214-infil-SDC	Ag paste/Ag paste	-	0.323	0.500	0.700	0.925	1.107	-	-	[267]
214-SP	LNO214	SDC	LNO214	Ag paste/Ag paste	-	0.122	0.179	0.200	0.212	0.212	-	-	[267]
4310-InfII	Ce-Pd-YSZ	YSZ	LNO4310-infil-YSZ	Ag paste/Ag paste	0.071	0.161	0.303	0.500	-	-	-	-	[327]
La-Ni-O Infil	Ni-YSZ	YSZ	LNO214-infil-GDC | LNF64	Ni foam / Au grid	-	0.250	-	1.000	-	2.000	-	-	[387]
214-Cmp	Ni-YSZ	YSZ | GDC	LNO214-GDC | LNO214-LSC| LSC	Not spec.	-	-	-	0.619	1.240	2.000	-	-	[222]
214-SP	Ni-SDC	LSGM	LNO214	Ag paste / Ag paste	-	-	0.200	0.301	0.451	0.557	-	-	[294]
214-Infil	Ni-YSZ	YSZ | GDC	LNO214-inflil-PBSCF	Ag paste / Pt paste	-	0.289	0.508	0.722	1.108	-	-	-	[391]
214-SP	Ni-YSZ	YSZ | GDC	LNO214	Not spec.	-	-	-	0.235	-	0.625	-	1.214	[392]
214-Infil	Ni-YSZ	YSZ | GDC	Pr-infil-LNO214	Not spec.	-	-	-	2.000	-	2.553	-	2.785	[392]
214-SP	Ni-SDC	YSZ | SDC	LNO214	Pt wire/Pt mesh	-	-	-	0.314	0.469	0.585	-	-	[393]

214-Infil	Ni-YSZ	YSZ | GDC	LNO214-infil-LSCF	Not specified	0.231	0.508	-	-	-	-	-	-	[394]
La-Ni-O Cmp	Ni-SDC	SSZ-Triple layer	LNO214-SDC-CuO | LNF64-CuO	-	-	-	-	-	0.125	0.168	0.200	-	[341]
214-Infil	Ni-YSZ	YSZ	LNO214-infil-YSZ (nano-spheres)	Au paste, grids (both)	-	0.168	-	0.375	-	-	-	-	[256]
214-Infil	Ni-YSZ	YSZ	LNO214-infil-YSZ (nanorods)	Au paste, grids (both)	-	0.230	-	0.764	-	-	-	-	[256]
La-Ni-O Cmp	Ni-SDC	SDC	LNO214-LNO327-LDC	Ag paste/Ag paste	-	.0.048	0.083	0.102	0.122	0.139	-	-	[336]
214-SP	Ni-SDC	YSZ | SDC	LNO214	Pt-mesh (Cathode)	-	-	-	0.178	0.272	0.137	-	-	[395]
214-SP	Ni-SDC	YSZ | SDC	LNO214 (with Au-layer)	Au-paste + Pt-mesh (Cathode)	-	-	-	0.184	0.44	0.44	-	-	[395]
214-SP	Ni-YSZ	YSZ | GDC	LNO214	Pt-paste + Pt-mesh (both)	-	-	0.303	0.567	0.947	1.397	-	-	[396]
214-Cmp	Ni-SDC	SDC	LNO214-LDC	Ag-paste (both)	-	-	-	0.091	-	0.117	-	-	[334]
214-Cmp	LST	YSZ	LNO214 | LSC	Stainless Steel/Pt mesh	-	-	-	0.143	0.229	0.336	-	-	[342]
4310-SP	Not specified	YSZ	LNO4310	Ag paste/Ag paste	-	-	0.581	0.921	1.221	1.529	-	-	[358]
Other	Ni-GDC	LSGM | LDC	LNC64	Pt gauze & paste / Pt gauze & paste	-	-	-	-	0.310	0.690	1.080	-	[324]
LNF-SP	Ni-GDC	LSGM | LDC	LNF64	Pt gauze & paste / Pt gauze & paste	-	-	-	-	0.380	0.490	0.850	-	[324]

Other	LNF-YSZ + LNF-ScYSZ	GDC	LNC64-GDC	Ni mesh/Au mesh	-	-	-	-	1.280	-	-	-	[257]
Other	LNF-YSZ + LNF-ScYSZ	GDC	LSC-infil-LNC64-GDC	Ni mesh/Au mesh	-	-	-	-	1.480	-	-	-	[257]
LNF-SP	Ni-SASZ	SASZ	LNF64	Pt mesh/ Pt mesh	-	-	0.500	0.900	1.250	2.000	-	-	[323]
LNF-SP	Ni-YSZ	SASZ	LNF64	Pt mesh / Pt mesh	-	-	-	-	0.380	0.600	-	0.660	[397]
LNF-Cmp	Ni-BZCY	BZCY	LNF64-BZCY	Ag paste / Ag paste	0.100	0.275	0.525	0.800	-	-	-	-	[344]
LNF-SP	Ni-YSZ	YSZ	LNF64	Ag paste / Ag paste	-	-	-	-	-	0.125	-	-	[243]
LNF-Cmp	Ni-YSZ	YSZ	LNF (FL) | LNF (porous)	Ag paste / Ag paste	-	-	-	-	-	0.240	-	-	[243]
LNF-Cmp	Ni-YSZ	YSZ	GDC | LNF64 (FL) | LNF (porous)	Ag paste / Ag paste	-	-	-	-	-	0.265	-	-	[243]
LNF-SP	Ni-SDC	SDC	LNF64	Not spec./Ag paste	-	-	-	0.035	-	-	-	-	[398]
LNF-Infil	Ni-SDC	SDC	LNF64-infil-BSC	Not spec./Ag paste	-	-	-	0.110	-	-	-	-	[398]
LNF-SP	Ni-YSZ	YSZ | SDC	LNF64	Ni grids & gauze / Pt grids and gauze	-	-	0.175	0.425	0.750	-	-	-	[372]
Other	Ni-YSZ	YSZ | SDC	LSNF7382	Ni ink and gauze / Pt ink and gauze	-	-	0.150	0.350	0.750	-	-	-	[372]
LNF-Cmp	Ni-BZY	BZY	LNF64-BZY	Not specified	-	0.060	0.150	0.300	-	-	-	-	[345]
LNF-Infil	Ni-YSZ | Ni-ScSZ	ScSZ	LNF64-infil-GDC	Ag mesh + Ni paste / Ag mesh + LSC	-	-	-	0.700	1.200	1.500	-	-	[262]

LNF-Infil	LNF-YSZ	YSZ	LNF64-infil-YSZ	Ag paste/Not clear	-	-	0.250	0.540	1.040	1.360	-	-	[399]
LNF-Infil	Pd-infil-YSZ	YSZ	LNF64-infil-YSZ	Ag paste/Ag paste	-	-	-	0.480	-	-	-	-	[400]
Other	Pd-infil-YSZ	YSZ	LSNF910964-infil-YSZ	Ag paste/Ag paste	-	-	-	0.465	-	-	-	-	[400]
Other	LSNF8273-GDC	LSGM | GDC	LSNF8273-GDC	Pt ink & mesh/ Pt ink & mesh	-	-	0.180	0.290	0.410	0.700	-	-	[371]
Other	Ni-YSZ	YSZ | GDC	LSNF5808020	Ni mesh/ Pt mesh	-	0.170	-	0.520	-	1.030	-	-	[401]
LNF-Cmp	Ni-YSZ	YSZ | YDC	LNF64-EDB | LNF64-EDB-3%CuO	Pt paste / Pt grid	-	-	-	-	0.763	-	-	-	[343]
LNF-Cmp	Ni-YSZ	YSZ | YDC	LNF64-SDC | LNF64-EDB-3%CuO	Pt paste / Pt grid	-	-	-	-	0.892	-	-	-	[343]

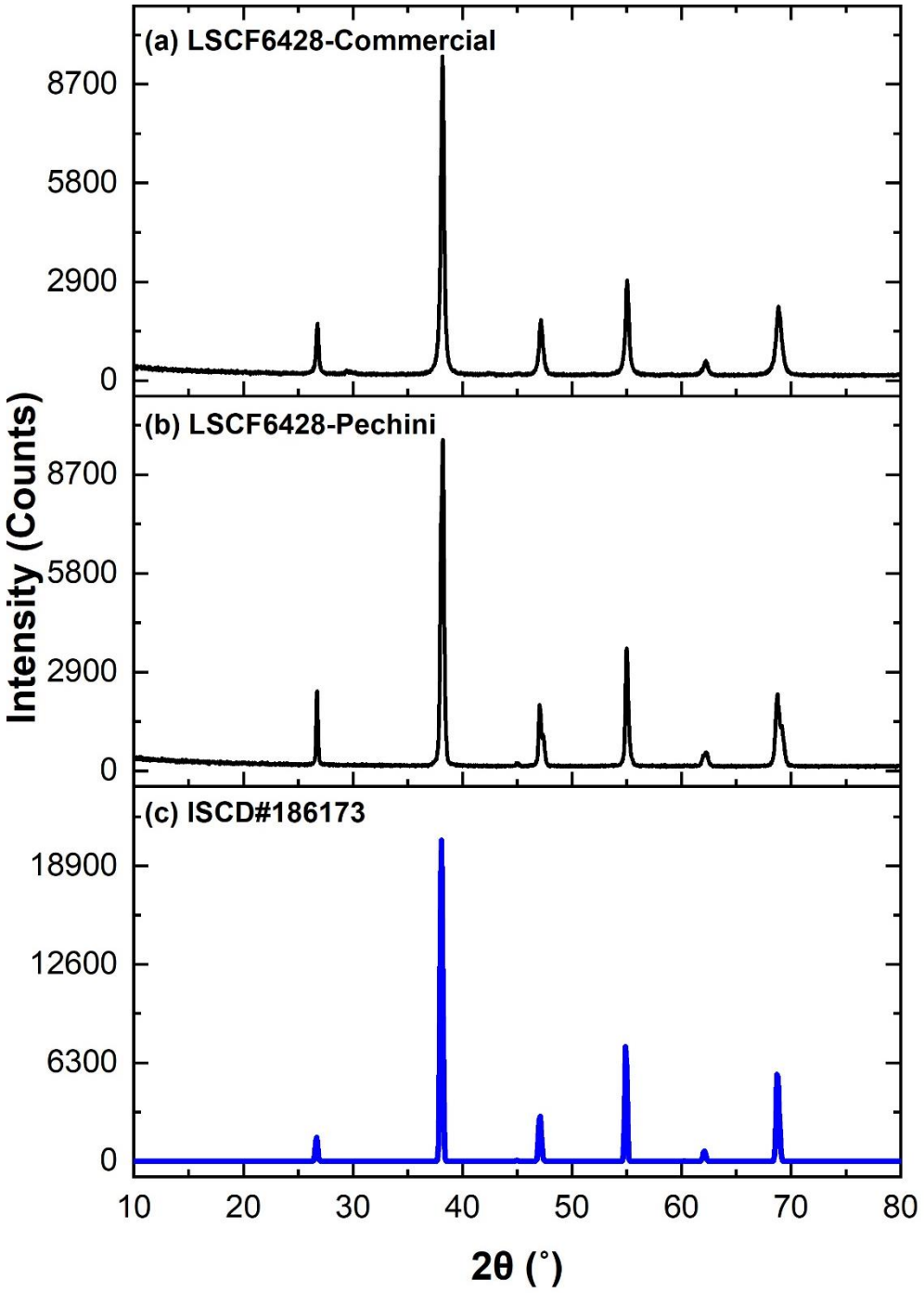


Figure E.1 – XRD data taken from scans of (a) commercial LSCF6428 and (b) Pechini-synthesised LSCF6428 compared with (c) data from the ISCSD database (ICSD#186173)

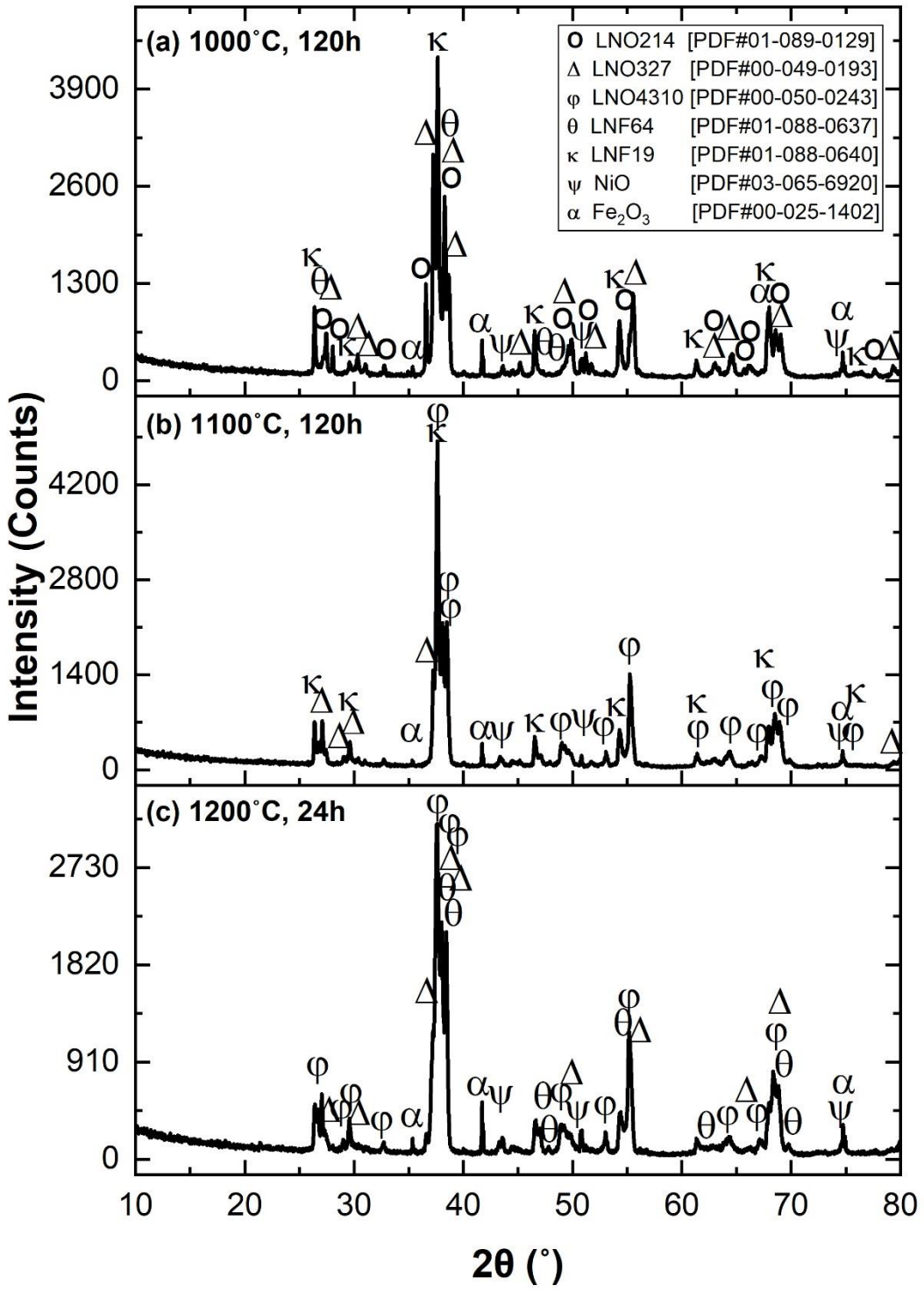


Figure E.2 - Attempts to synthesise LNF64 via solid-state route at (a) 1000˚C, (b) 1100˚C and (c) 1200˚C

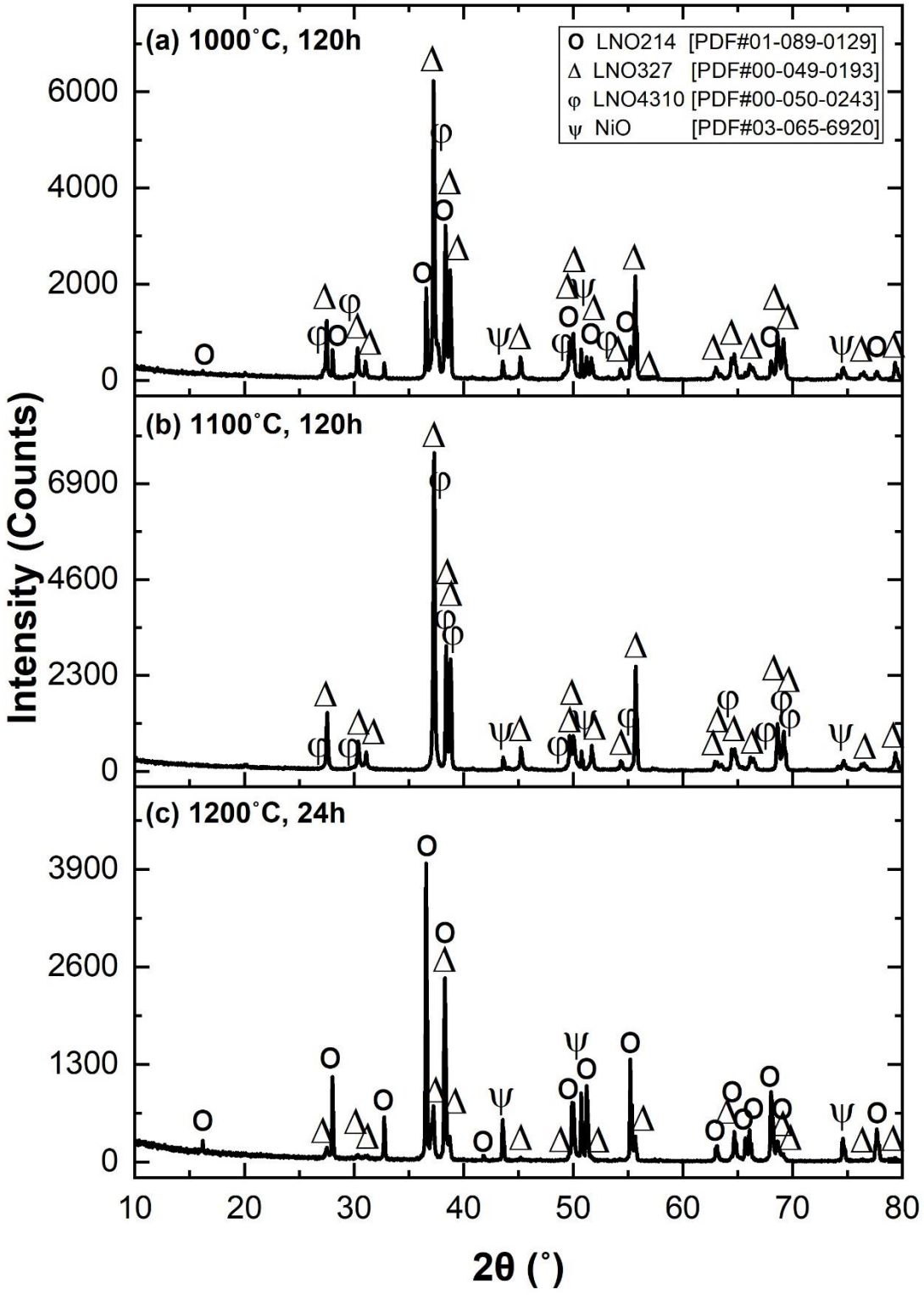


Figure E.3 – Attempts to synthesise LNO4310 via solid-state route at (a) 1000˚C, (b) 1100˚C and (c) 1200˚C

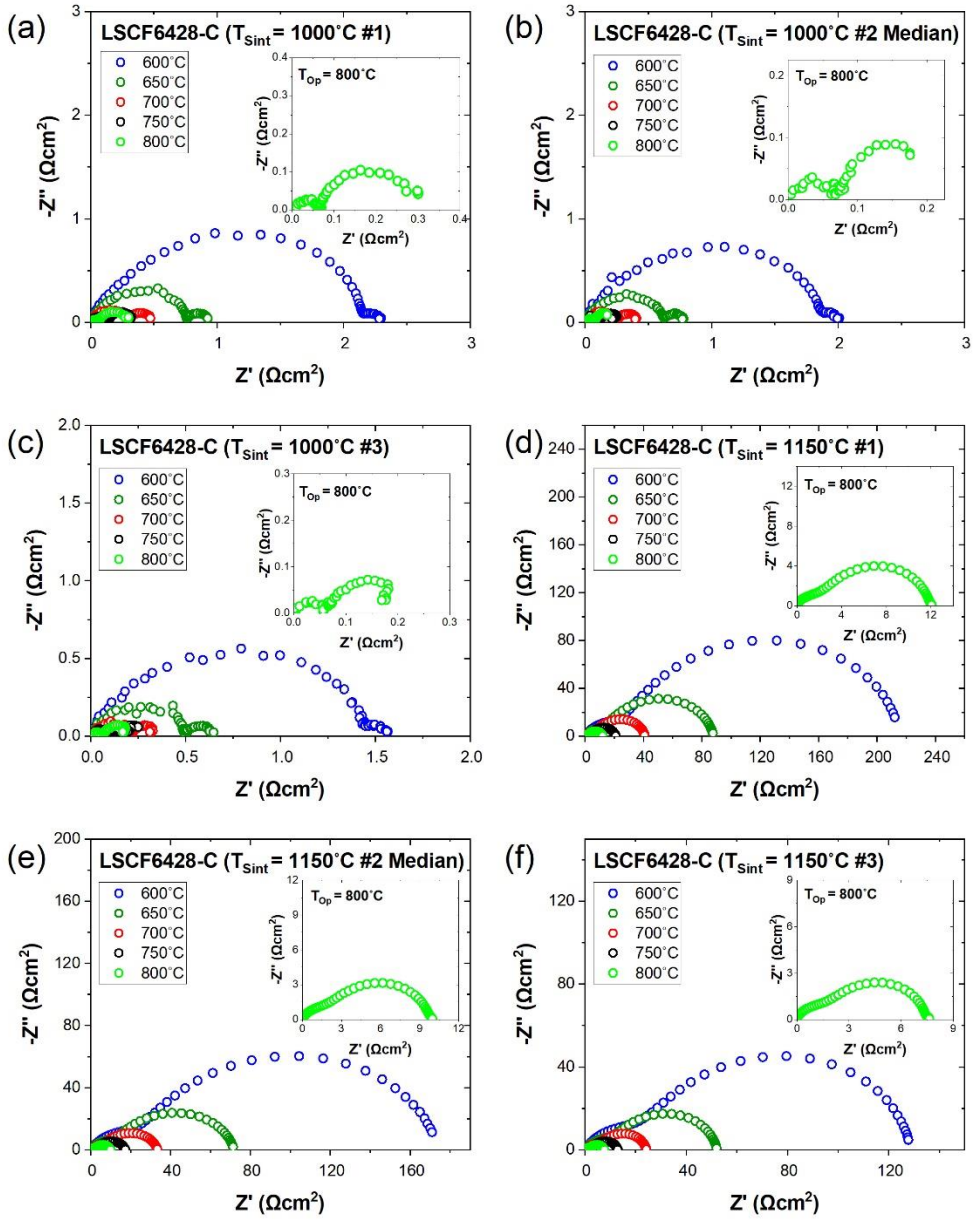


Figure F.1 –symmetrical cell testing data (Nyquist plots) for commercial LSCF6428 electrodes tested in this work (a-c) electrodes sintered at 1000˚C and (d-f) electrodes sintered at 1150˚C [tests without CCL]

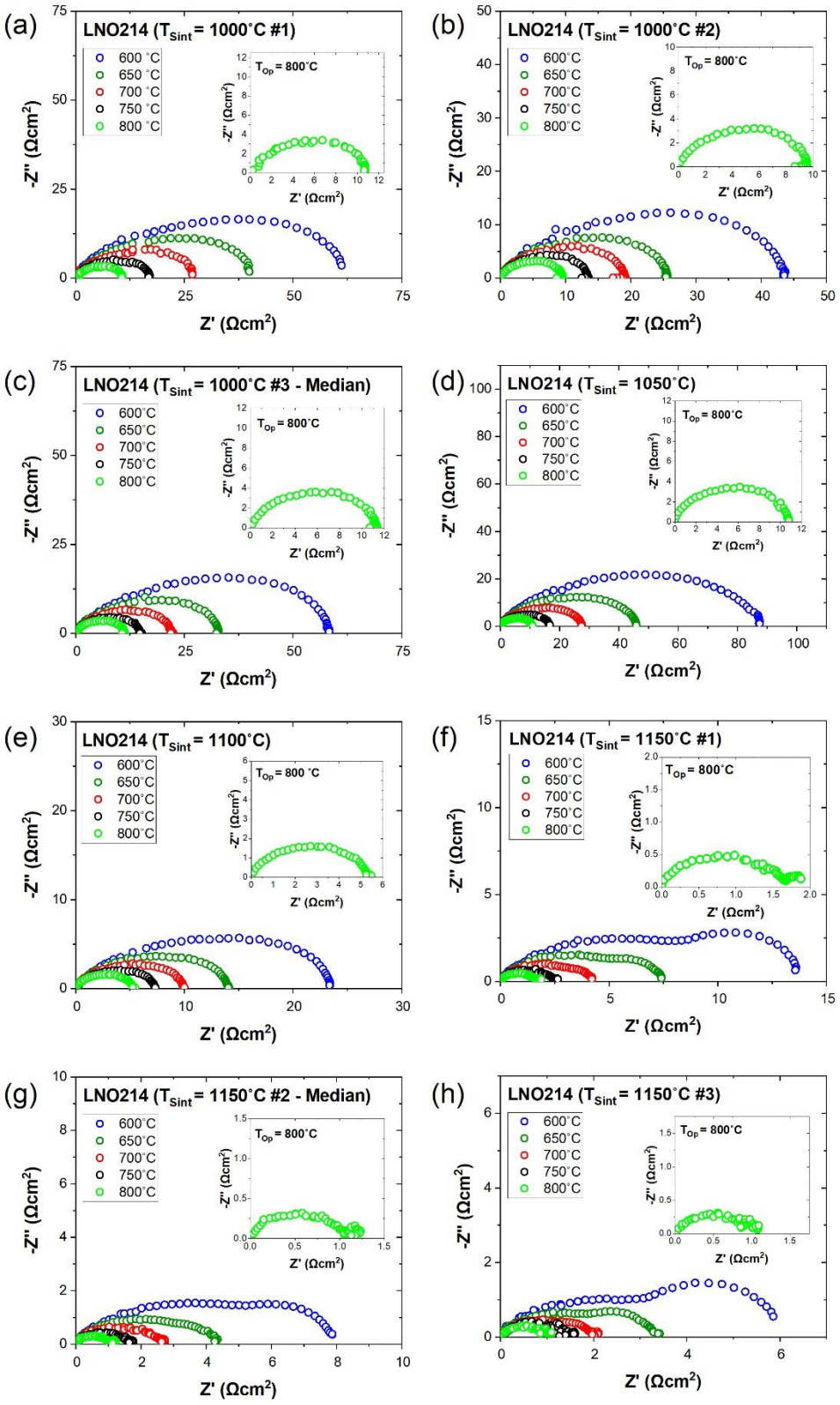


Figure F.2 - complete symmetrical cell testing data (Nyquist plots) for Pechini-synthesised LNO214 electrodes tested in this work (a-c) electrodes sintered at 1000˚C, (d) 1050˚C, (e) 1100˚C and (f-h) electrodes sintered at 1150˚C [tests without CCL]

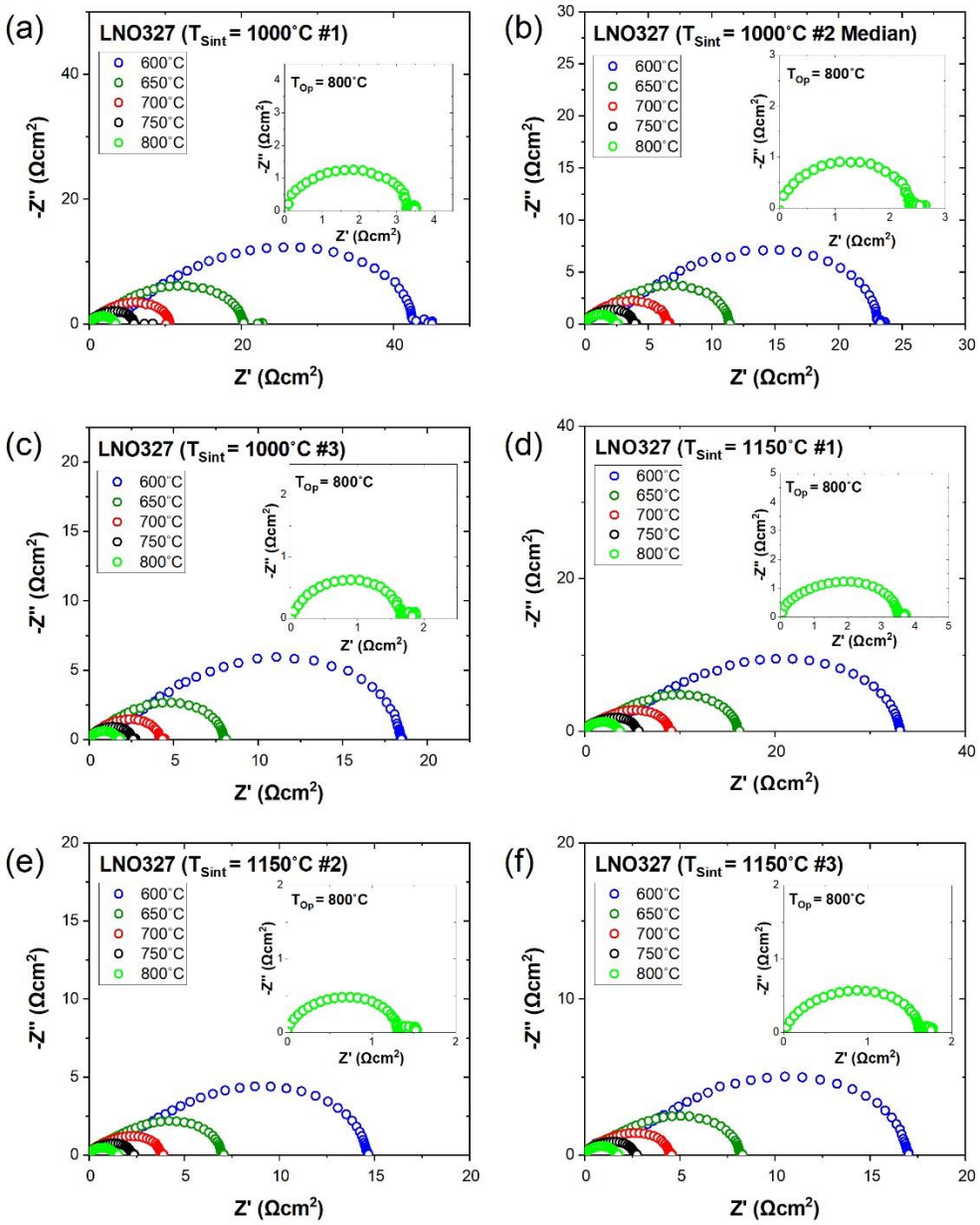


Figure F.3 - complete symmetrical cell testing data (Nyquist plots) for Pechini-synthesised LNO327 electrodes tested in this work (a-c) electrodes sintered at 1000˚C and (d-f) electrodes sintered at 1150˚C [tests without CCL]

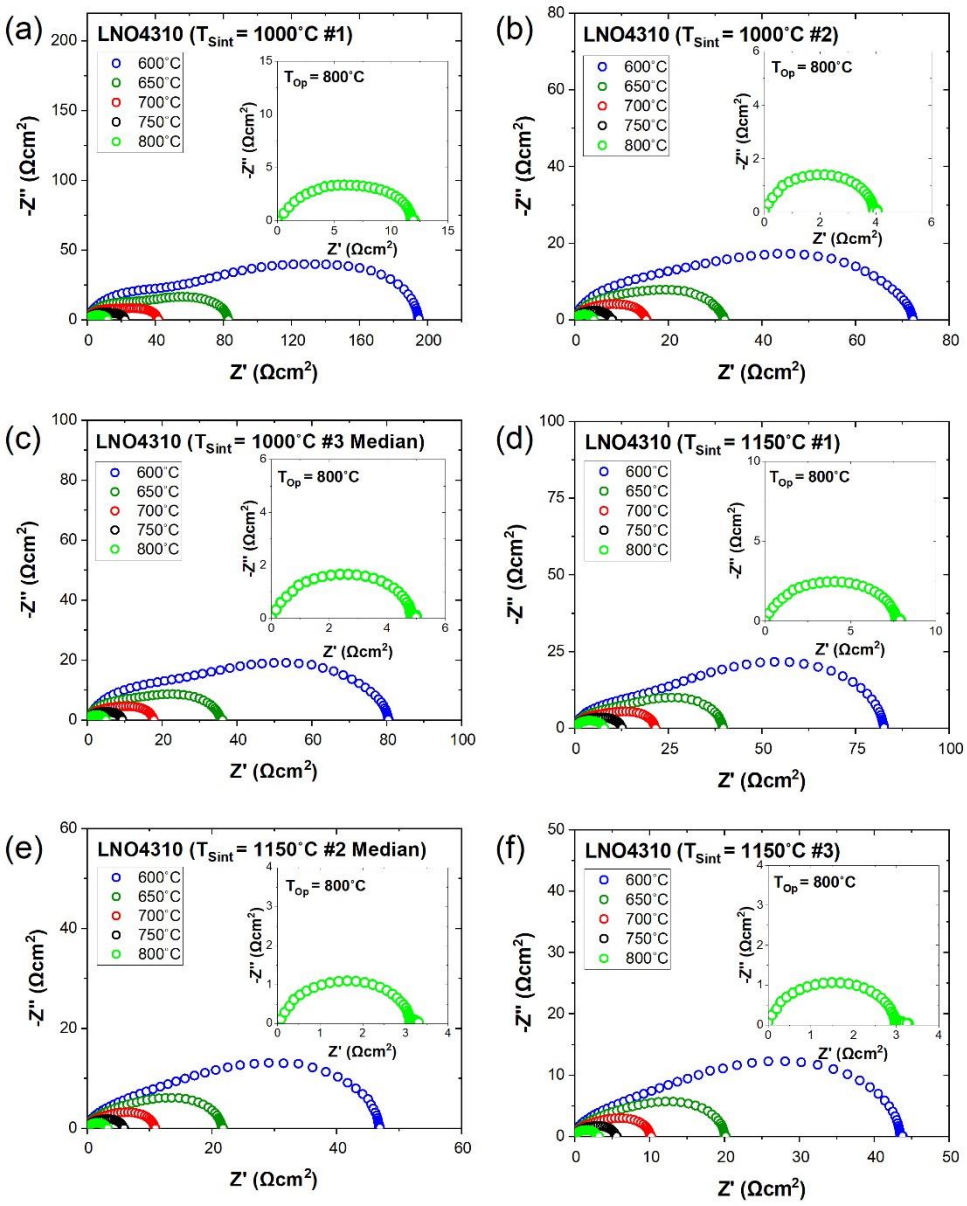


Figure F.4 – complete symmetrical cell testing data (Nyquist plots) for Pechini-synthesised LNO4310 electrodes tested in this work (a-c) electrodes sintered at 1000˚C and (d-f) electrodes sintered at 1150˚C [tests without CCL]

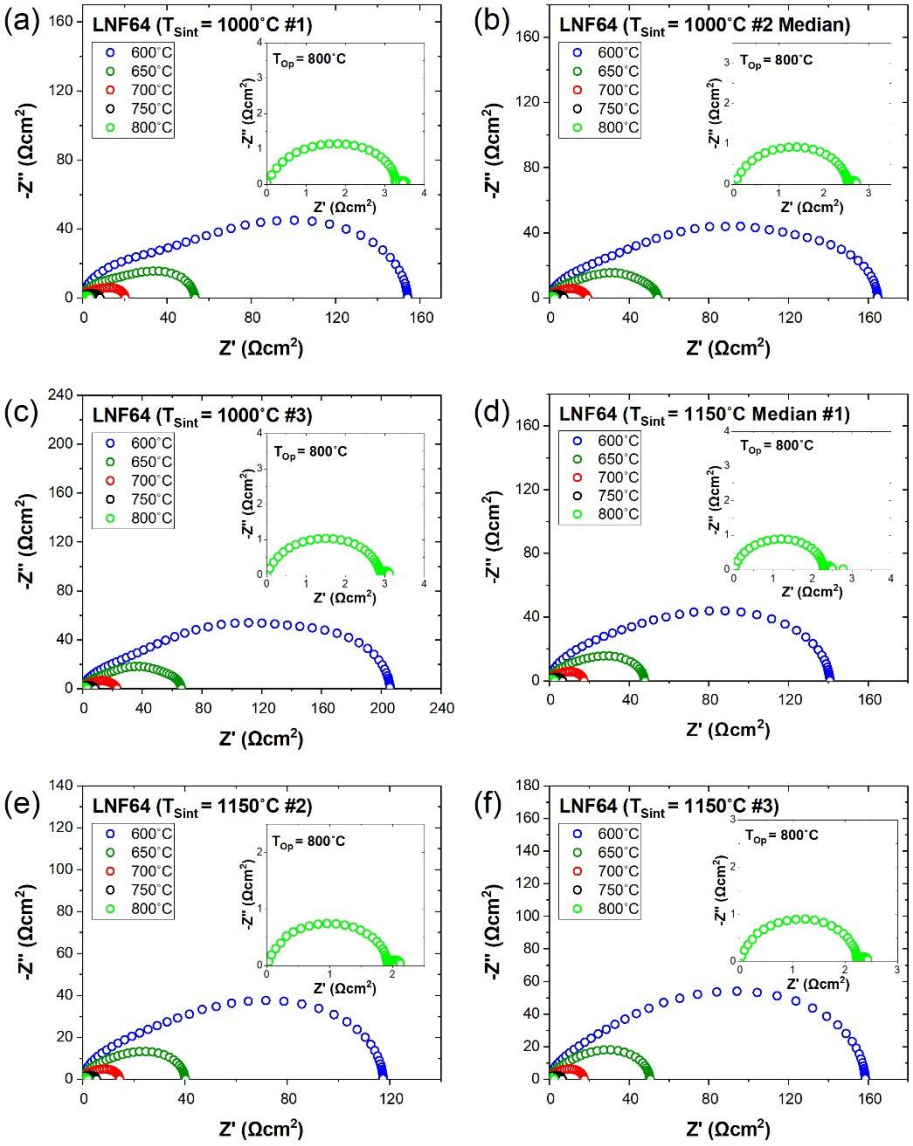


Figure F.5 - complete symmetrical cell testing data (Nyquist plots) for Pechini-synthesised LNF64 electrodes tested in this work (a-c) electrodes sintered at 1000˚C and (d-f) electrodes sintered at 1150˚C [tests without CCL]

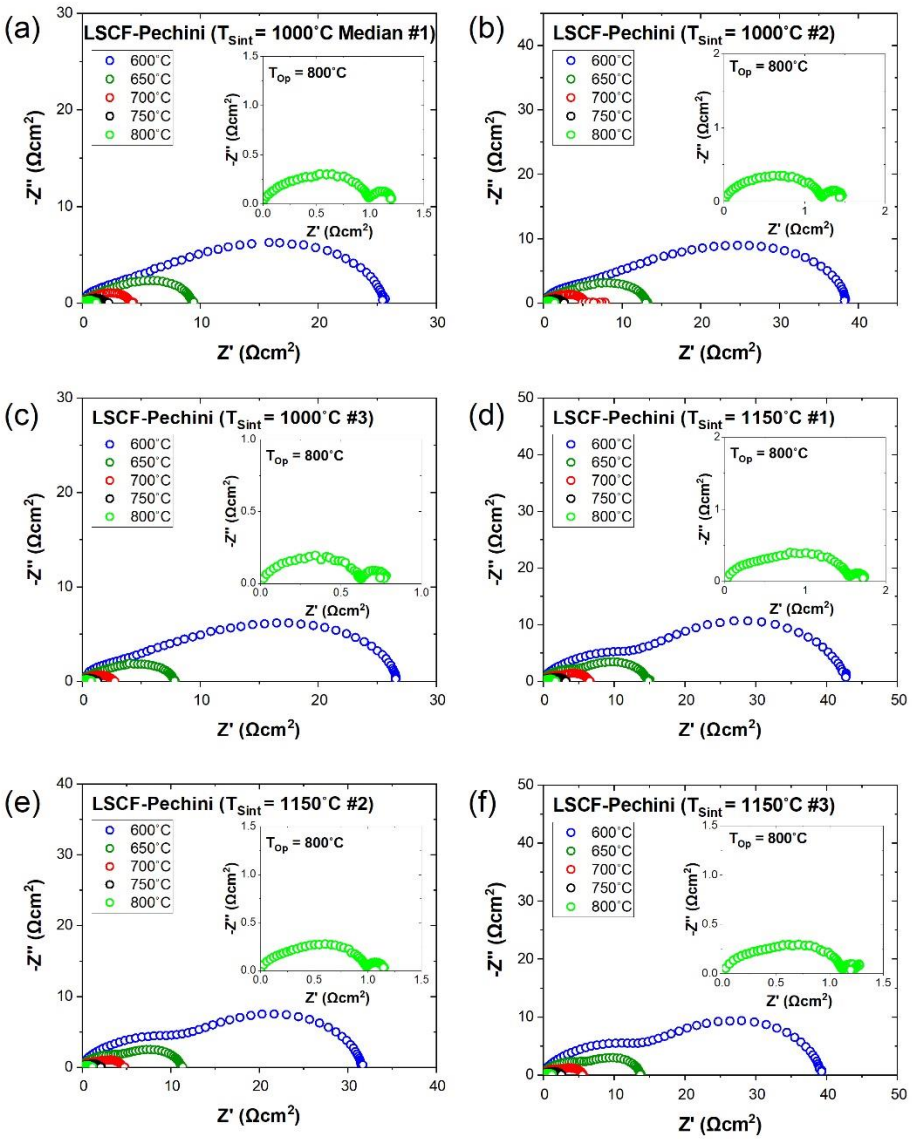


Figure F.6 - complete symmetrical cell testing data (Nyquist plots) for Pechini-synthesised LSCF6428 electrodes tested in this work (a-c) electrodes sintered at 1000˚C and (d-f) electrodes sintered at 1150˚C [tests without CCL]

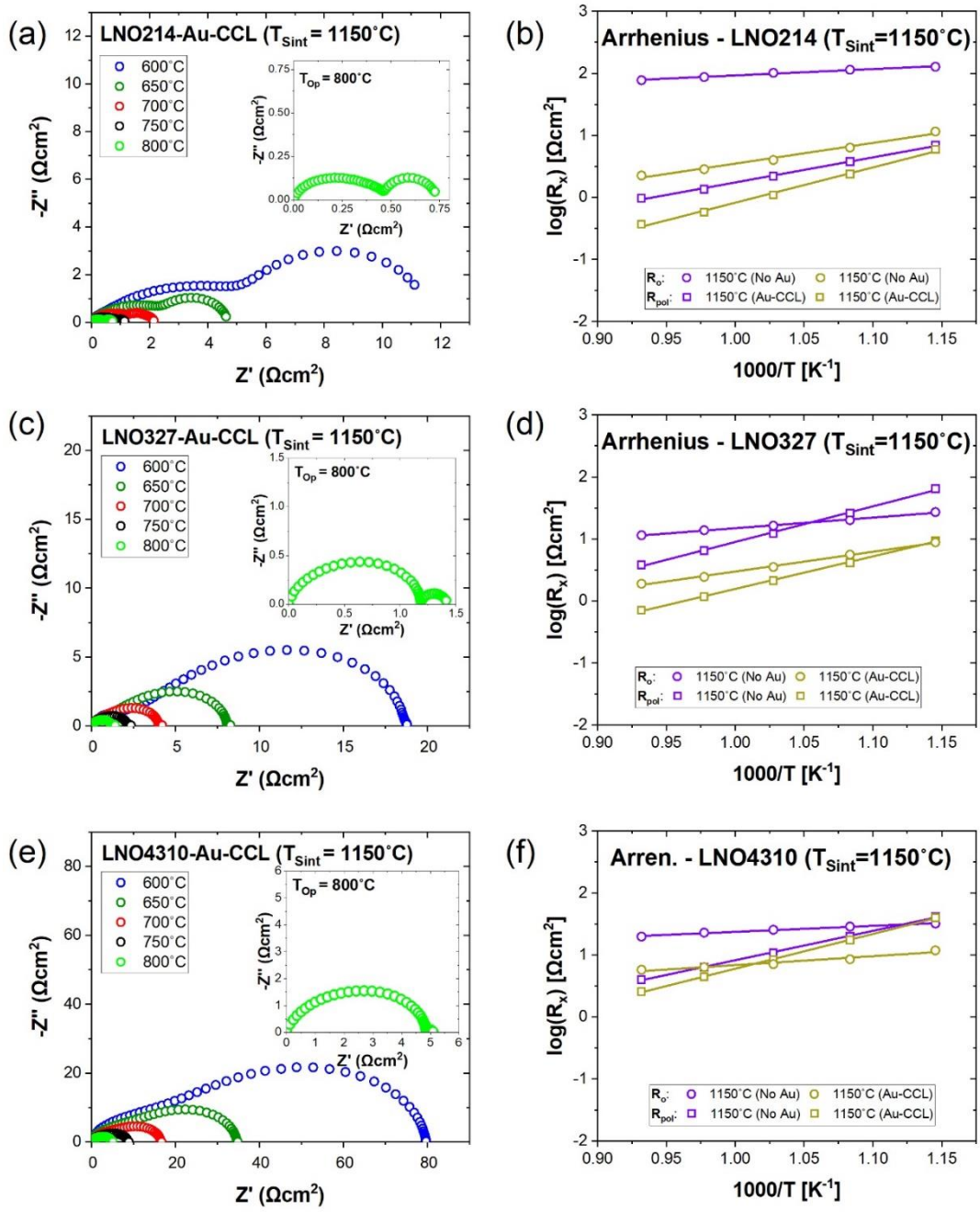


Figure F.7 - Effect of Au-CCL on electrodes sintered at 1150˚C; (a, b) LNO214, (c, d) LNO327, (e, f) LNO4310). Panels on the left show Nyquist results. Panels on the right show R_o and R_{pol} Arrenhius plots.

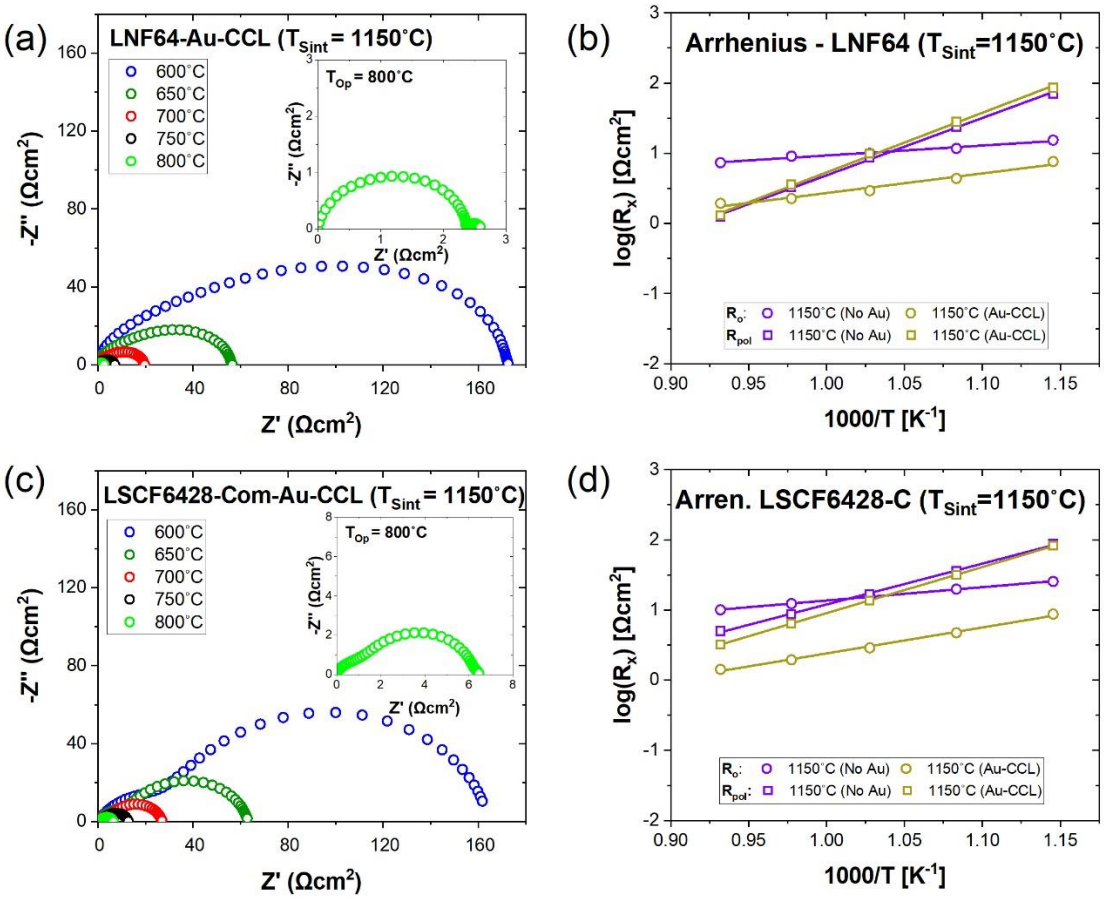


Figure F.8 - Effect of Au-CCL on electrodes sintered at 1150˚C; (a, b) LNF64, (c, d) commercial LSCF6428. Panels on the left show Nyquist results. Panels on the right show R_o and R_{pol} Arrenhius plots.

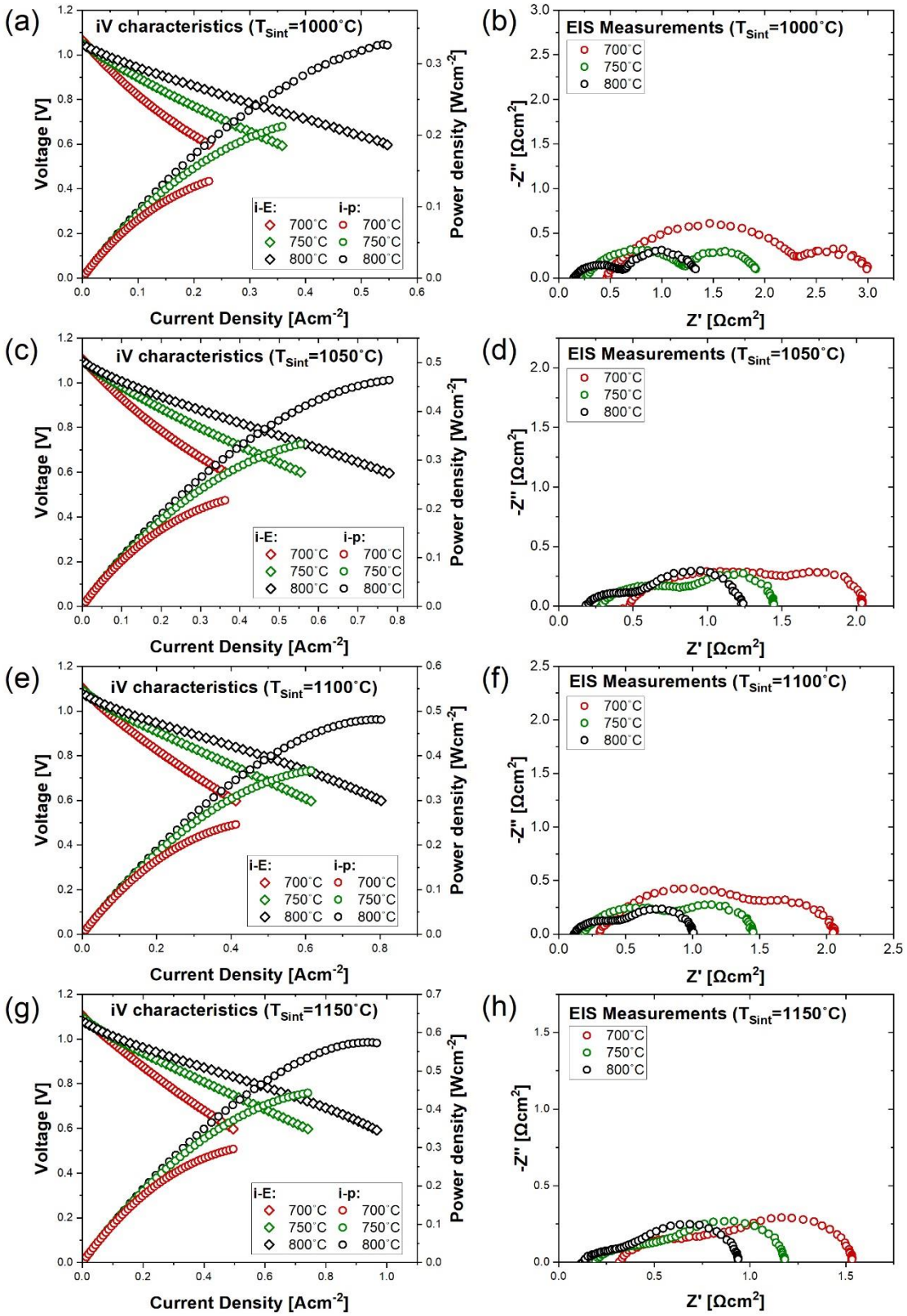


Figure G.1 - Voltage-current and impedance data for LNO214 electrodes sintered at (a, b) 1000˚C, (c, d) 1050˚C, (e, f) 1100˚C, (g, h) 1150˚C,

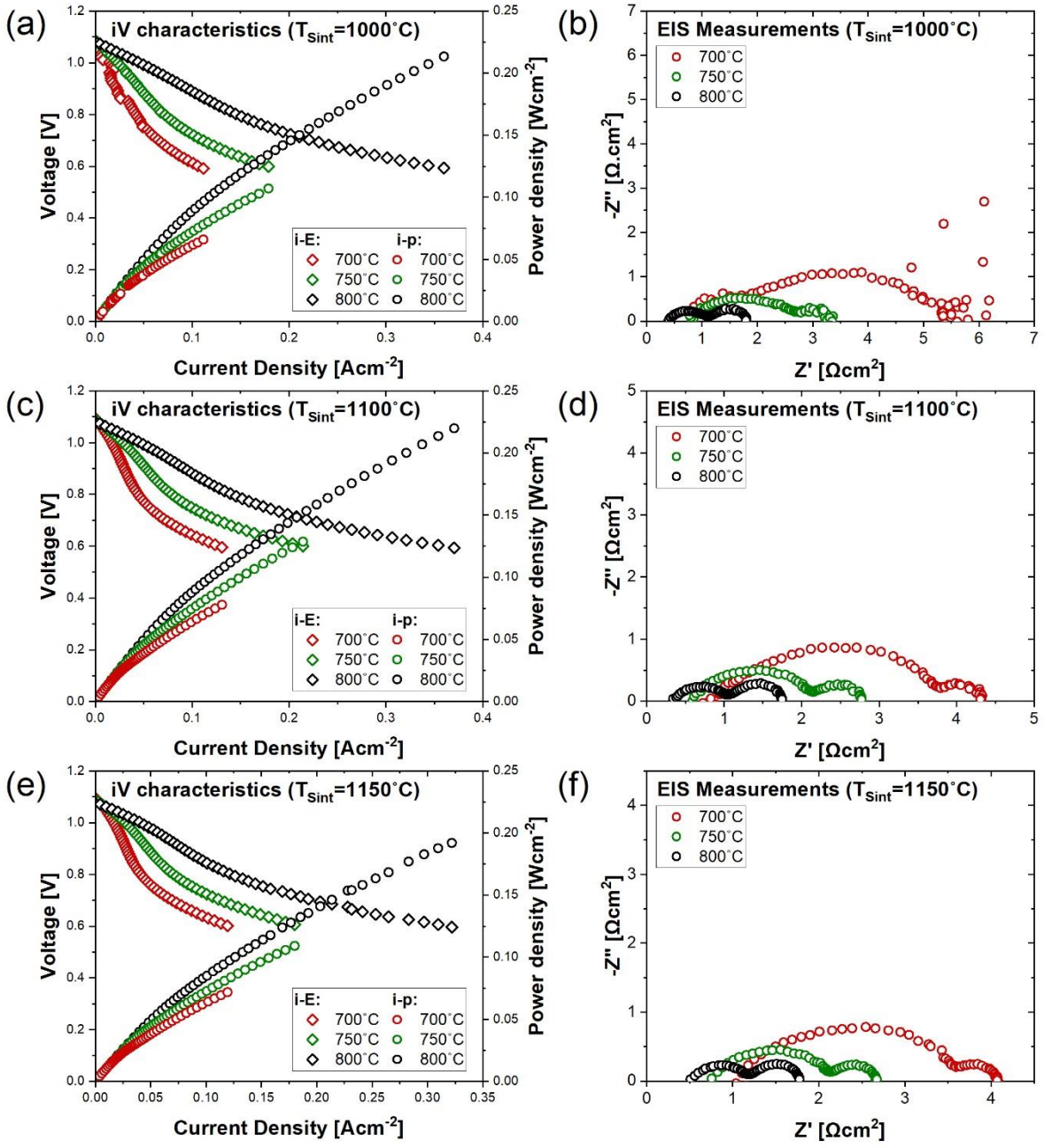


Figure G.2 - Voltage-current and impedance data for LNO327 electrodes sintered at (a, b) 1000˚C, (c, d) 1100˚C, (e, f) 1150˚C.

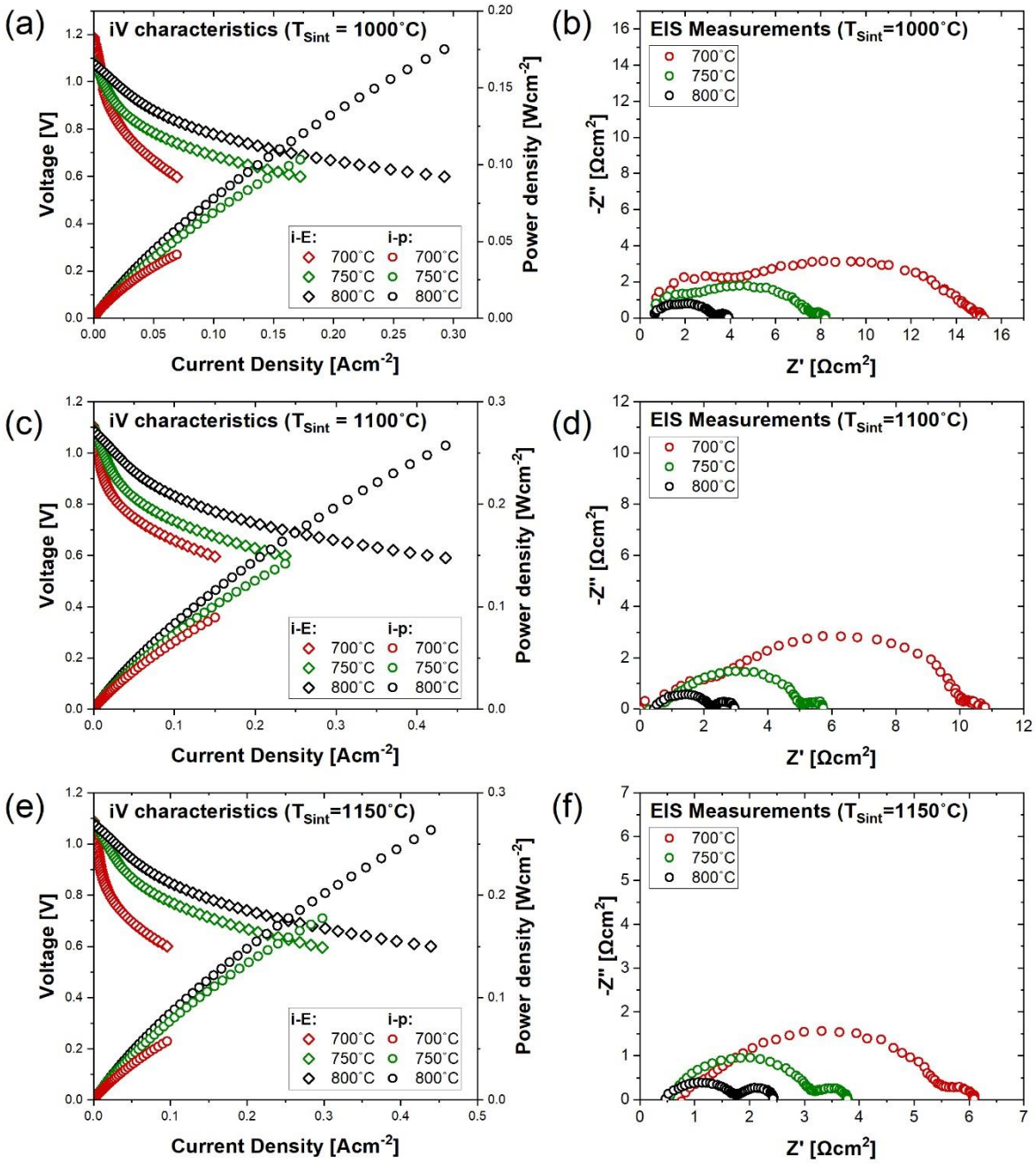


Figure G.3 - Voltage-current and impedance data for LNO4310 electrodes sintered at (a, b) 1000˚C, (c, d) 1050˚C, (e, f) 1100˚C, (g, h) 1150˚C

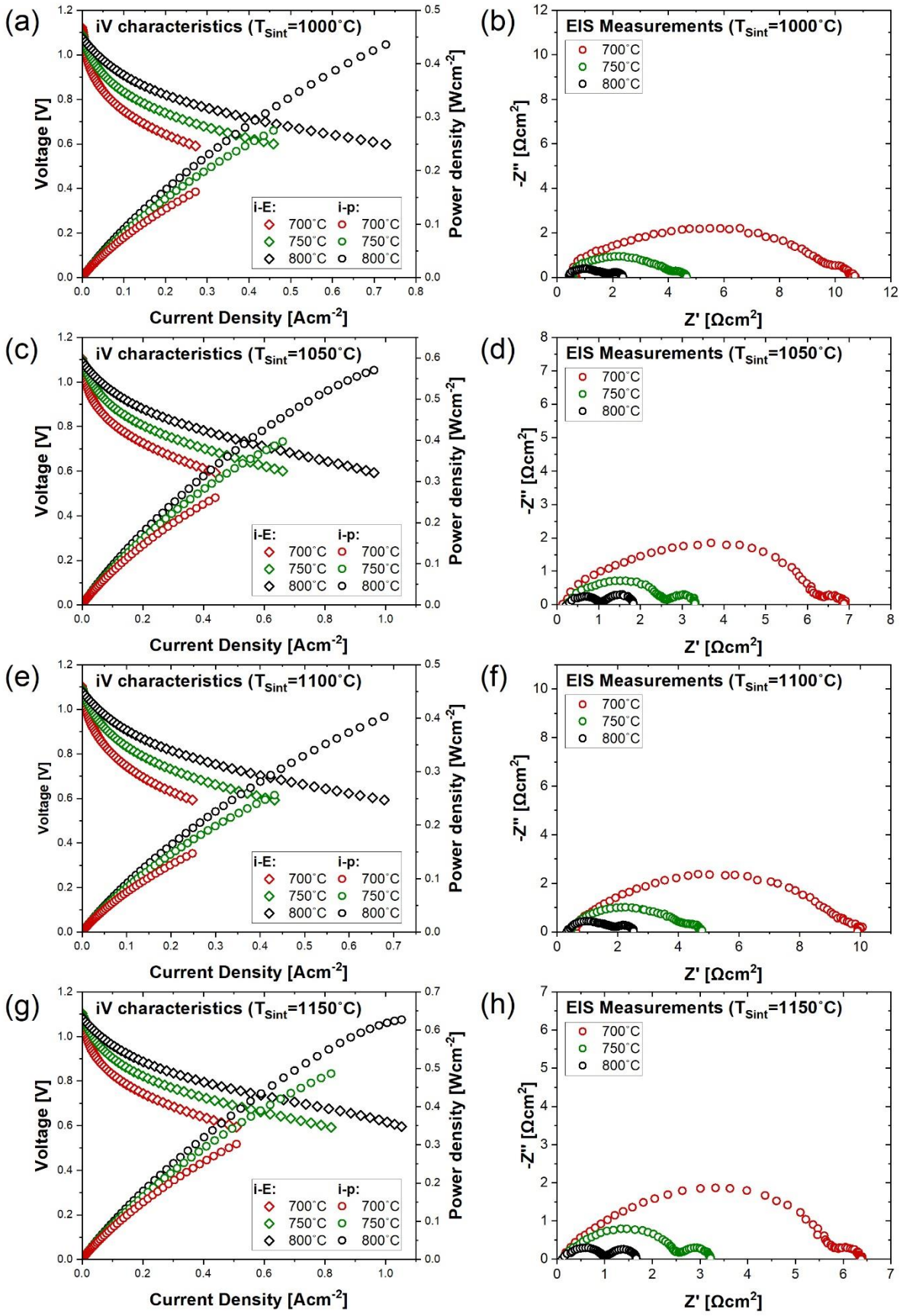


Figure G.4 - Voltage-current and impedance data for LNF64 electrodes sintered at (a, b) 1000˚C, (c, d) 1050˚C, (e, f) 1100˚C, (g, h) 1150˚C.

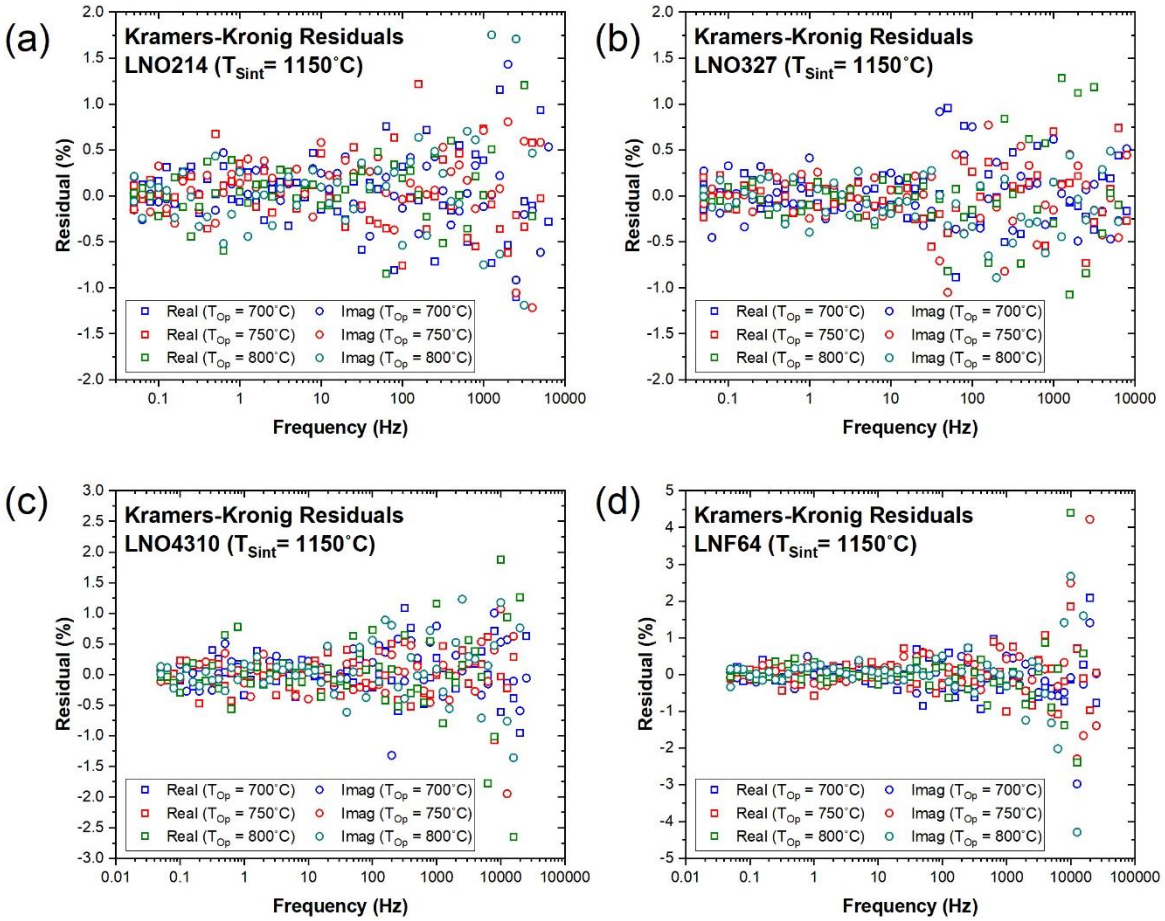


Figure G.5 – Kramers-Kronig residuals for lanthanum nickelate electrodes sintered at 1150˚C

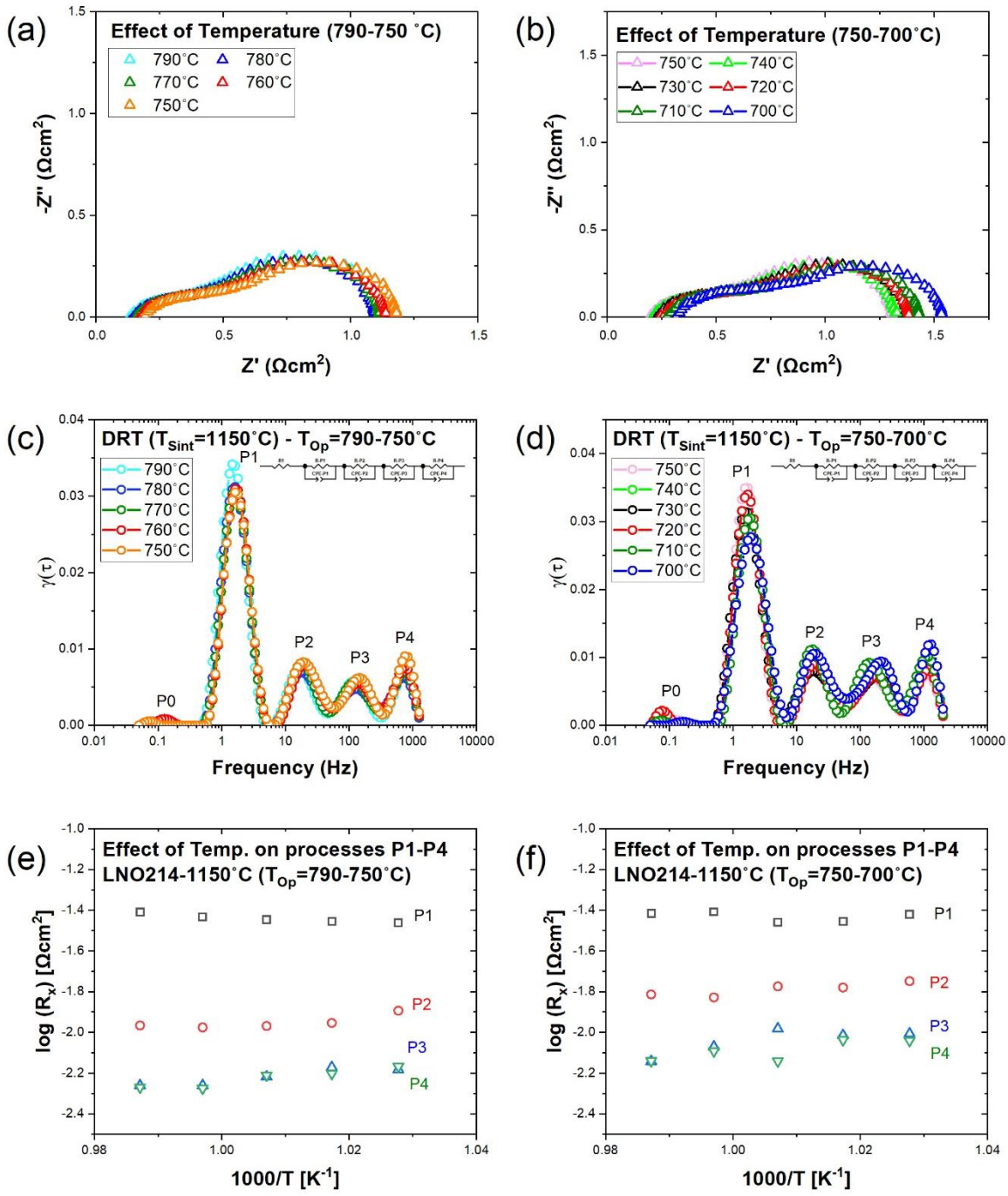


Figure G.6 – Attempt to identify processes via DRT analysis of single cells with $La_2NiO_{4+\delta}$ electrode sintered at 1150˚C (part 1 – effect of temperature); (a, b) EIS spectra in two different temperature ranges, (c, d) corresponding DRT spectra, (e, f) Arrhenius plots to identify which processes (P1-P4) are impacted by temperature

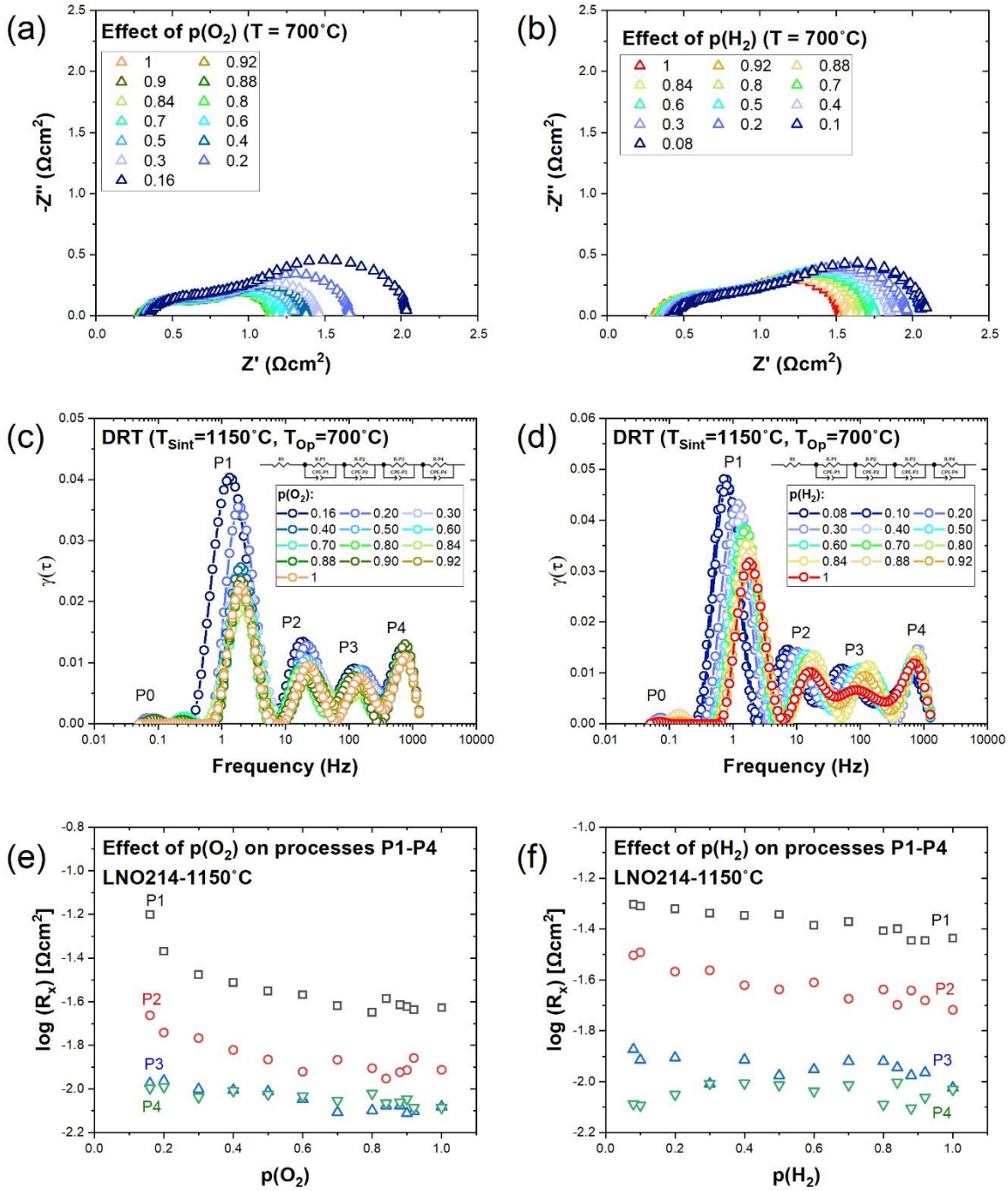


Figure G.7 - Attempt to identify processes via DRT analysis of single cells with $La_2NiO_{4+\delta}$ electrode sintered at 1150˚C (part 2 – effect of gas pressures); (a, b) EIS spectra in variable oxygen-nitrogen and hydrogen-nitrogen environments, respectively, (c, d) corresponding DRT spectra, (e, f) plots to identify which processes (P1-P4) are impacted by $p(O_2)$ and which are impacted by $p(H_2)$. [Note: this analysis does not successfully identify the processes that are impacted by changes to the partial pressure of oxygen only and it is, therefore, not possible to identify the oxygen electrode contribution].

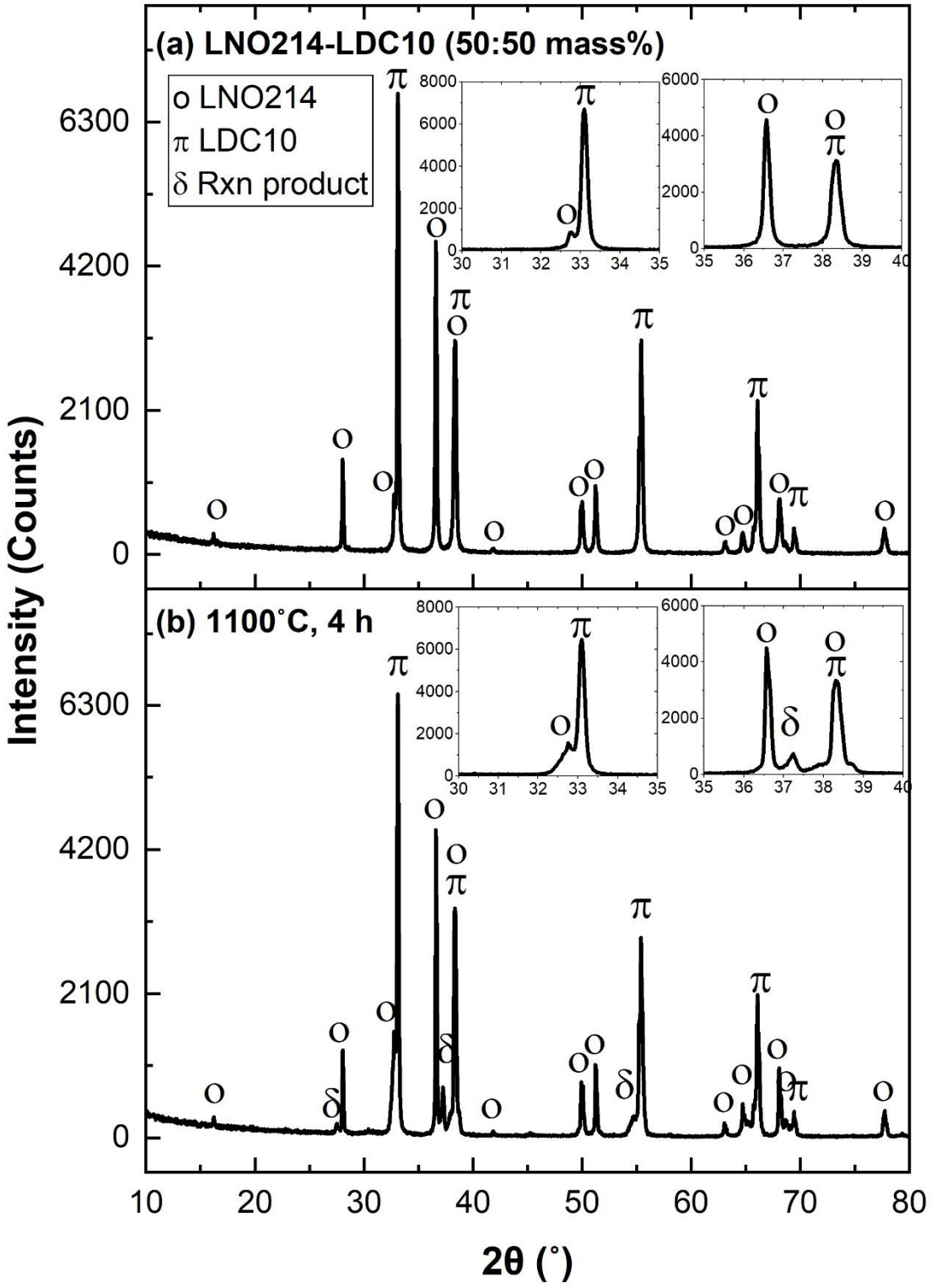


Figure H.1 - Reactivity test of $La_2NiO_{4+\delta}$ and $La_{0.10}Ce_{0.90}O_2$; XRD results of (a) 50:50 mass% mix of materials prior to heating and (b) after heating to 1100˚C for 4 hours.

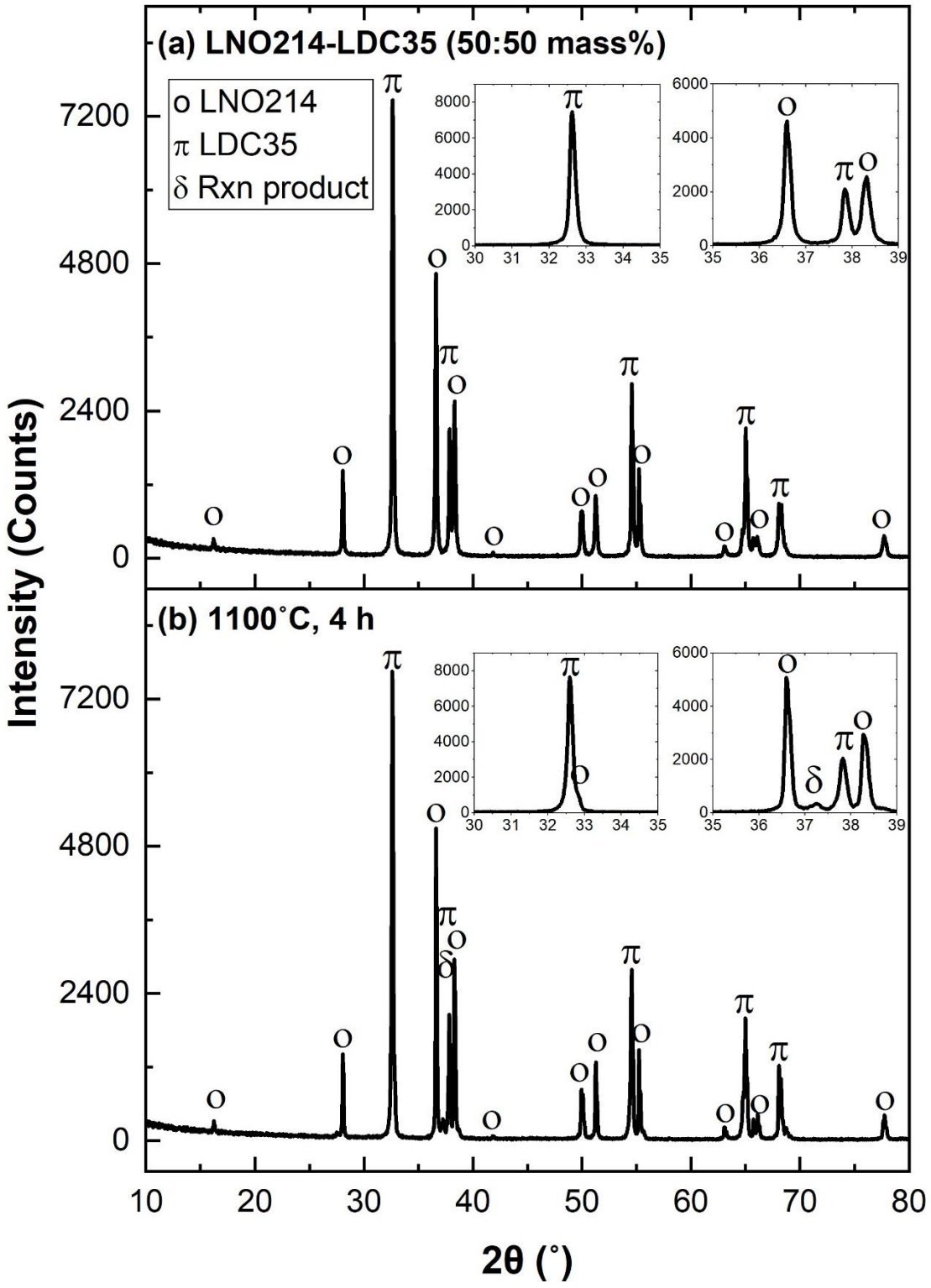


Figure H.2 - Reactivity test of $La_2NiO_{4+\delta}$ and $La_{0.35}Ce_{0.65}O_2$; XRD results of (a) 50:50 mass% mix of materials prior to heating and (b) after heating to 1100˚C for 4 hours.

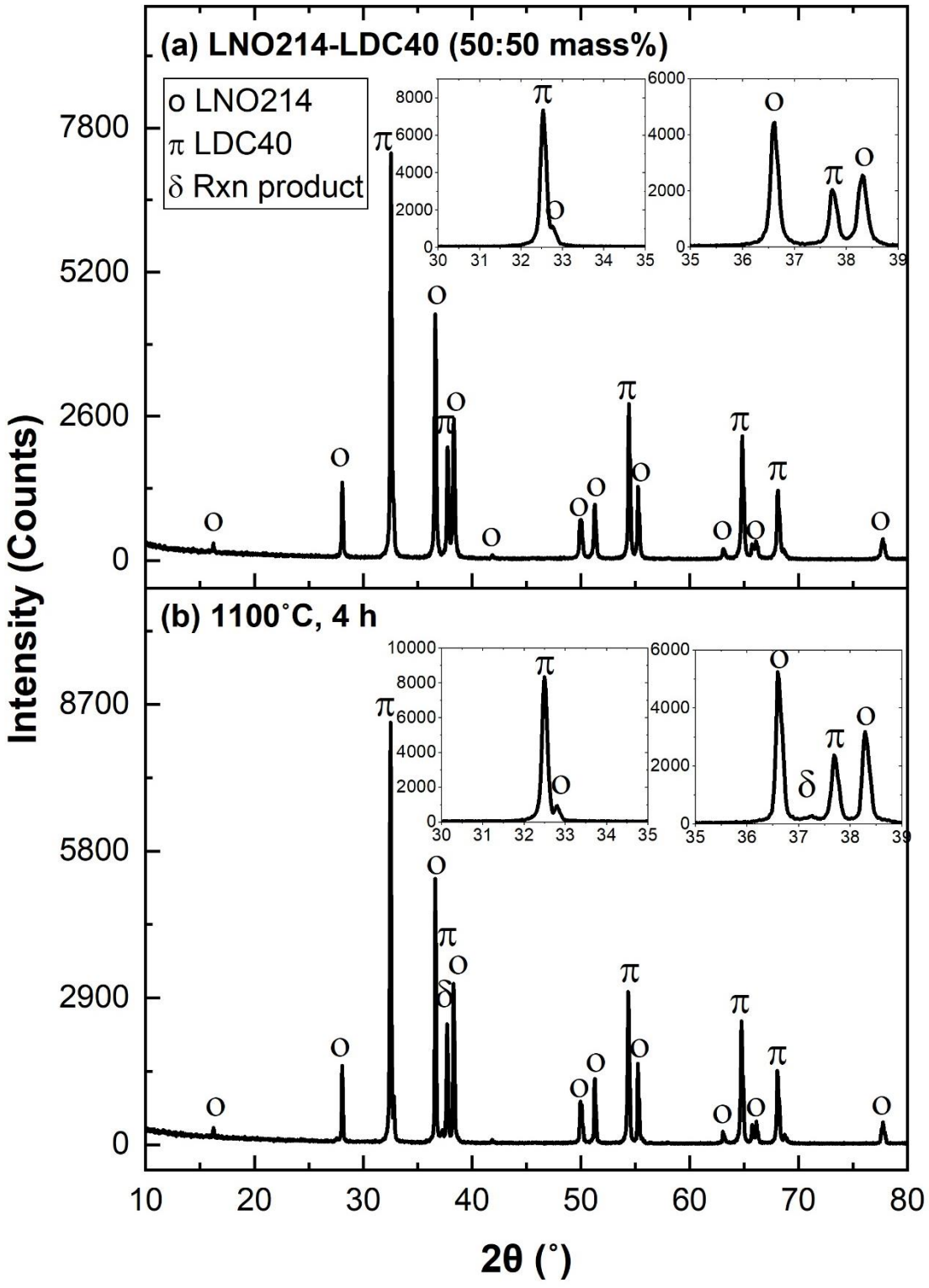


Figure H.3 - Reactivity test of $La_2NiO_{4+\delta}$ and $La_{0.40}Ce_{0.60}O_2$; XRD results of (a) 50:50 mass% mix of materials prior to heating and (b) after heating to 1100˚C for 4 hours.

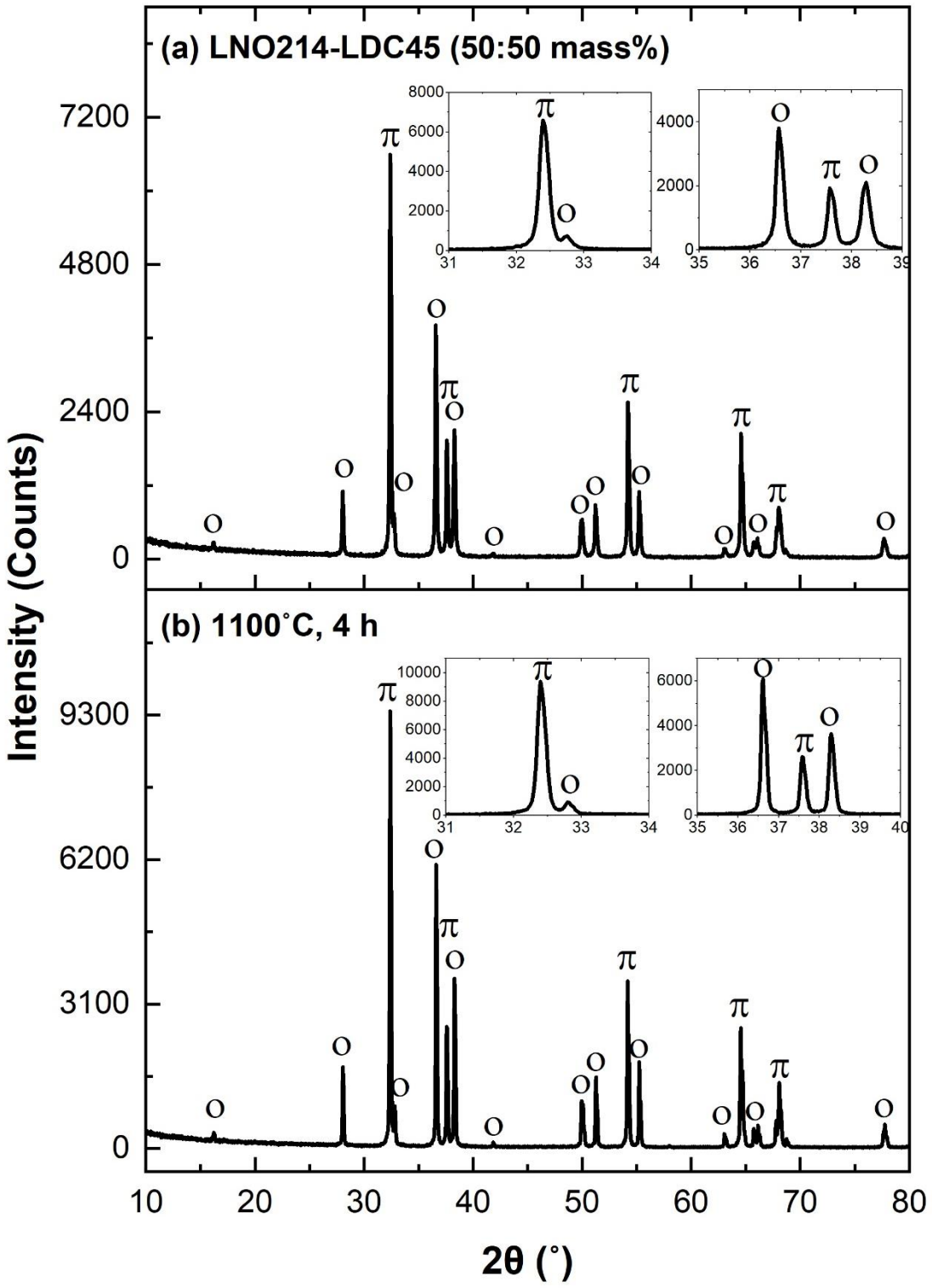


Figure H.4 - Reactivity test of $La_2NiO_{4+\delta}$ and $La_{0.45}Ce_{0.55}O_2$; XRD results of (a) 50:50 mass% mix of materials prior to heating and (b) after heating to 1100˚C for 4 hours.

Appendix I - Explainer of box and whisker plots

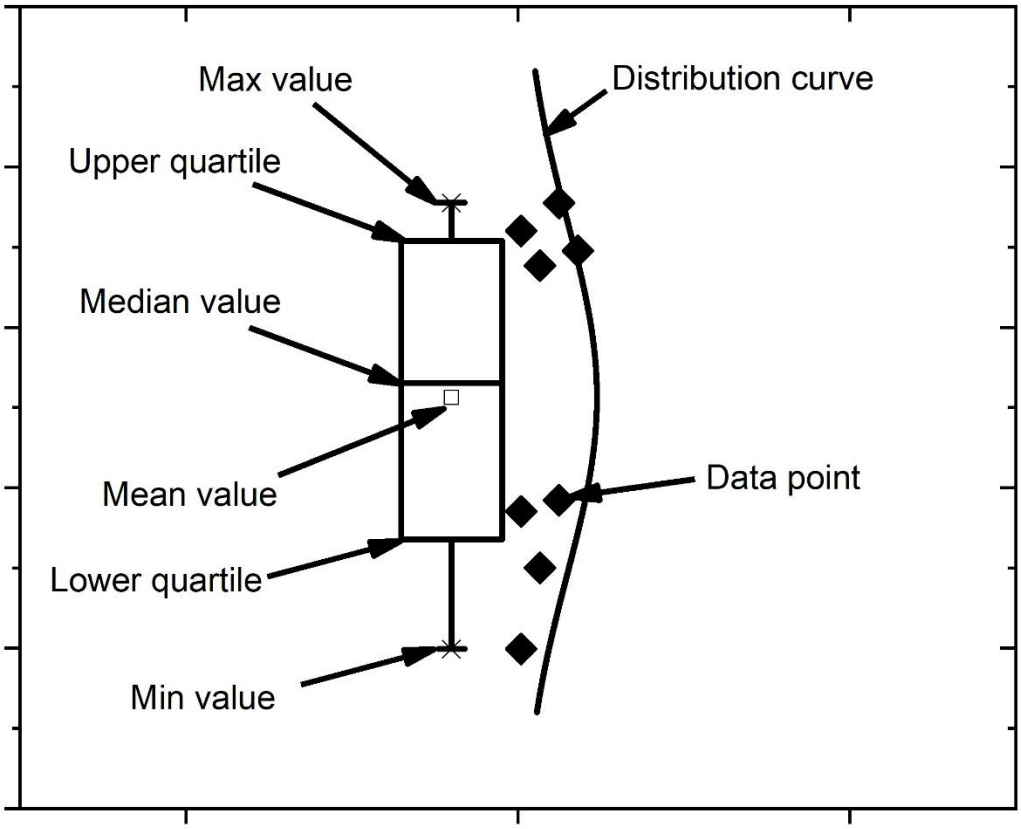


Figure I.1 – Overview/explainer of box and whisker plot. The upper quartile represents the median of the upper half of the dataset. The lower quartile represents the median of the lower half of the dataset.

References

1. IPCC. Summary for Policymakers. In: Masson-Delmotte, V., P. Zhai, H.-O. Pörtner, D. Roberts, J. Skea, P.R. Shukla, A. Pirani, W. Moufouma-Okia, C. Péan, R. Pidcock, S. Connors, J.B.R. Matthews, Y. Chen, X. Zhou, M.I. Gomis, E. Lonnoy, T. Maycock, M. Tignor, Waterfield T, editor. Global Warming of 15°C An IPCC Special Report on the impacts of global warming of 15°C above pre-industrial levels and related global greenhouse gas emission pathways, in the context of strengthening the global response to the threat of climate change. Cambridge, UK and New York, NY, USA: Cambridge University Press; 2018. pp. 3–24. DOI: 10.1017/9781009157940.001.

2. Stern N. Part II Impacts of Climate Change on Growth and Development. In: The economics of climate change: The Stern Review. Cambridge: Cambridge University Press; 2006. pp. 55–167. DOI: https://doi.org/10.1017/CBO9780511817434

3. Taylor M, Watts J, Bartlett J. Climate crisis: 6 million people join latest wave of global protests. The Guardian. 2019 [accessed 2 November 2022]; Available from: https://www.theguardian.com/environment/2019/sep/27/climate-crisis-6-million-people-join-latest-wave-of-worldwide-protests

4. BBC. School strike for climate: Protests staged around the world. BBC News. 2019 [accessed 25 January 2020]; Available from: https://www.bbc.co.uk/news/world-48392551

5. McGrath M. Climate change: Biggest global poll supports “global emergency.” BBC News. 2021 [accessed 30 January 2020]; Available from: https://www.bbc.co.uk/news/science-environment-55802902

6. Ritchie H, Roser M. Fossil Fuels. Our World in Data. 2017 [accessed 25 January 2020]; Available from: https://ourworldindata.org/fossil-fuels#:~:text=Based on BP’s Statistical Review,oil and natural gas remaining.

7. United Nations. The Paris Agreement. unfccc.int. 2021 [accessed 25 January 2020]; Available from: https://unfccc.int/process-and-meetings/the-paris-agreement/the-paris-agreement

8. European Commission. Climate Strategies and targets: 2050 long-term strategy. ec.europe.eu. 2020 [accessed 25 January 2020]; Available from: https://ec.europa.eu/clima/policies/strategies/2050_en

9. McSweeney R, Tandon A. Global Carbon Project: Coronavirus causes ‘record fall’ in fossil-fuel emissions in 2020. CarbonBrief. 2020 [accessed 25 January 2020]; Available from: https://www.carbonbrief.org/global-carbon-project-coronavirus-causes-record-fall-in-fossil-fuel-emissions-in-2020

10. Crippa M, Guizardi D, Banja M, Solazzo E, Muntean M, Schaaf E, Pagani F, Monforti-Ferrario F, Olivier JGJ, Quadrelli R, Risquez Martin A, Taghavi-Moharamli P, Grassi G, Rossi S, Oom D, Branco A, San-Miguel J, Vignati E. CO2 emissions of all world countries. Brussels: European Commission; 2022. DOI: 10.2760/07904

11. International Monetary Fund. Greening the Recovery. Washington: International Monetary Fund; 2020.

12. Organisation for Economic Co-operation and Development. Making the green recovery work for jobs, income and growth. OECD.org. 2020 [accessed 25 January 2020]; Available from: https://www.oecd.org/coronavirus/policy-responses/making-the-green-recovery-work-for-

jobs-income-and-growth-a505f3e7/

13. European Parliament. Green Deal: key to a climate-neutral and sustainable EU. europarl.europa.eu. 2020 [accessed 25 January 2020]; Available from: https://www.europarl.europa.eu/news/en/headlines/society/20200618STO81513/green-deal-key-to-a-climate-neutral-and-sustainable-eu

14. UK Government. PM commits £350 million to fuel green recovery. gov.uk. 2020 [accessed 25 January 2020]; Available from: https://www.gov.uk/government/news/pm-commits-350-million-to-fuel-green-recovery

15. Lee JH, Woo J. Green new deal policy of South Korea: Policy innovation for a sustainability transition. Sustainability (Switzerland). 2020;12(23);pp.:1–17. DOI: 10.3390/su122310191

16. IEA. Renewables 2020. IEA.org. 2020 [accessed 25 January 2021]; Available from: https://www.iea.org/reports/renewables-2020

17. Staffell I, Jansen M, Green R, Gross R, Green T, McNally P. Electric Insights Quarterly (Q2 2020). Selby: Drax; 2020.

18. Wilson IAG, Styring P. Why Synthetic Fuels Are Necessary in Future Energy Systems. Frontiers in Energy Research. 2017;5(19);pp.:1–10. DOI: 10.3389/fenrg.2017.00019

19. Golden R, Paulos B. Curtailment of Renewable Energy in California and Beyond. The Electricity Journal. 2015;28(6);pp.:36–50. DOI: 10.1016/j.tej.2015.06.008

20. Bird L, Lew D, Milligan M, Carlini EM, Estanqueiro A, Flynn D, Gomez-Lazaro E, Holttinen H, Menemenlis N, Orths A, Eriksen PB, Smith JC, Soder L, Sorensen P, Altiparmakis A, Yasuda Y, Miller J. Wind and solar energy curtailment: A review of international experience. Renewable and Sustainable Energy Reviews. 2016;65;pp.:577–86. DOI: 10.1016/j.rser.2016.06.082

21. Lever A, Evans H, Ravishankar M, Romanidis N, Richards O, Buchanan F, Pudjianto D, Strbac G. Flexibility in Great Britain. London: Imperial College London, Carbon Trust; 2021.

22. Balducci P, Mongird K, Weimar M. Understanding the Value of Energy Storage for Power System Reliability and Resilience Applications. Current Sustainable/Renewable Energy Reports. 2021;8(3);pp.:131–7. DOI: 10.1007/s40518-021-00183-7

23. Elshurafa AM. The value of storage in electricity generation: A qualitative and quantitative review. Journal of Energy Storage. 2020;32;p.:101872. DOI: 10.1016/j.est.2020.101872

24. National Grid ESO. Future Energy Scenarios. London: National Grid ESO; 2019.

25. BEIS. Clean Growth - Transforming Heating - Overview of Current Evidence. London: Department for Business Energy & Industrial Strategy; 2018.

26. Vivid economics, Imperial College London. Accelerated electrification and the GB electricity system. London: Vivid Economics; 2019.

27. Wilson IAG. Multi-vector energy diagram Great Britain - daily resolution. researchgate.net. 2018 [accessed 2 November 2022]; Available from: https://www.researchgate.net/project/multi-vector-energy-analytics

28. Speirs J, Balcombe P, Johnson E, Martin J, Brandon N, Hawkes A. A greener gas grid: what are the options. London: Imperial College London, Sustainable Gas Institute; 2017.

29. Howard R, Bengherbi Z. Too Hot to Handle? How to Decarbonise Domestic Heating. London: Policy Exchange; 2016.

30. Crabtree GW, Dresselhaus MS, Buchanan M V. The Hydrogen economy. Physics Today. 2004;57(12);pp.:39–45. DOI: 10.1063/1.1878333

31. Edwards PP, Kuznetsov VL, David WIF, Brandon NP. Hydrogen and fuel cells: Towards a sustainable energy future. Energy Policy. 2008;36(12);pp.:4356–62. DOI: 10.1016/j.enpol.2008.09.036

32. Marbán G, Valdés-Solís T. Towards the hydrogen economy? International Journal of Hydrogen Energy. 2007;32(12);pp.:1625–37. DOI: 10.1016/j.ijhydene.2006.12.017

33. Bockris JOM. The hydrogen economy: Its history. International Journal of Hydrogen Energy. 2013;38(6);pp.:2579–88. DOI: 10.1016/j.ijhydene.2012.12.026

34. Taibi E, Blanco H, Miranda R, Carmo M. Green Hydrogen Cost Reduction. Abu Dhabi: IRENA; 2020.

35. IEA. Global Hydrogen Review 2021. Paris: IEA; 2021.

36. IRENA. Hydrogen: a Renewable Energy Perspective. IRENA. Abu Dhabi; 2019.

37. The Hydrogen Council. Hydrogen decarbonization pathways: a life-cycle assessment. Brussels: The Hydrogen Council; 2021.

38. Department for Business Energy and Industrial Strategy. Hydrogen production costs by production source. London: HM Government; 2018.

39. Howarth RW, Jacobson MZ. How green is blue hydrogen? Energy Science and Engineering. 2021;9(10);pp.:1676–87. DOI: 10.1002/ese3.956

40. European Commission. A hydrogen strategy for a climate-neutral Europe. Brussels: European Commission; 2020.

41. Sadler D, Anderson HS, Sperrink M, Cargill A, Sjevoll M, Assen KI, Finnesand JE, Melien T, Thorsen R, Hagesaeteher L, Ringrose P, Nazarian B, Kvadsheim, Havard H. H21 North of England Report. Leeds: Northern Gas Networks; 2017.

42. HyDeploy. Positive progress to reduce UK CO2 emissions - HyDeploy. hydeploy.co.uk. [accessed 29 March 2019]; Available from: https://hydeploy.co.uk/

43. Hy4Heat. Hy4Heat. hy4heat.info. 2018 [accessed 14 October 2019]; Available from: https://www.hy4heat.info/

44. Hart D, Lehner F, Jones S, Lewis J. The Fuel Cell Industry Review. London: E4Tech; 2019.

45. Blum L, De Haart LGJ, Malzbender J, Menzler NH, Remmel J, Steinberger-Wilckens R. Recent results in Jülich solid oxide fuel cell technology development. Journal of Power Sources. 2013;241;pp.:477–85. DOI: 10.1016/j.jpowsour.2013.04.110

46. elcogen. How SOFC can change the world? elcogen.com. 2022 [accessed 21 October 2022]; Available from: https://elcogen.com/for-investors/how-sofc-can-change-the-world/

47. Cooper SJ, Brandon NP. Chapter 1 – An Introduction to Solid Oxide Fuel Cell Materials, Technology and Applications. In: Brandon NP, Ruiz-Trejo E, Boldrin P, editors. Solid Oxide Fuel Cell Lifetime and Reliability. London: Elsevier; 2017. pp. 1–18. DOI: 10.1016/B978-0-08-101102-7.00001-5

48. Milcarek RJ, Ahn J, Zhang J. Review and analysis of fuel cell-based, micro-cogeneration for residential applications: Current state and future opportunities. Science and Technology for the Built Environment. 2017;23(8);pp.:1224–43. DOI: 10.1080/23744731.2017.1296301

49. Delphi demos SOFC tech for truck APU. Fuel Cells Bulletin. 2010(12);p.:3. DOI: 10.1016/S1464-2859(10)70334-5

50. Washington State researchers develop SOFC for aircraft APU. Fuel Cells Bulletin. 2014(7);p.:10. DOI: 10.1016/S1464-2859(14)70206-8

51. Nissan. Nissan unveils world's first Solid-Oxide Fuel Cell vehicle. Nissan News: Official Europe Newsroom. 2016 [accessed 2 March 2019]; Available from: https://europe.nissannews.com/en-GB/releases/release-148671#

52. Bloom Energy. Customers – Energy Case Studies | Bloom Energy. [accessed 25 October 2018]; Available from: https://bloomenergy.com/customers

53. Nirasawa H. Current Status of National SOFC Projects in Japan. ECS Transactions. 2017;78(1);pp.:33–40. DOI: 10.1149/07801.0033ecst

54. COGEN Europe. Pathway to a Competitive European Fuel Cell micro-Cogeneration Market. pace-energy.eu. 2021 [accessed 2 November 2022]; Available from: https://pace-energy.eu/

55. Ceres. SteelCell®. ceres.tech. 2021 [accessed 3 February 2021]; Available from: https://www.ceres.tech/technology/steelcell/

56. Mahato N, Banerjee A, Gupta A, Omar S, Balani K. Progress in Material Selection for Solid Oxide Fuel Cell Technology: A Review. Journal of Progress in Materials Science. 2015;72;pp.:141–337. DOI: 10.1016/j.pmatsci.2015.01.001

57. da Silva FS, de Souza TM. Novel materials for solid oxide fuel cell technologies: A literature review. International Journal of Hydrogen Energy. 2017;42(41);pp.:26020–36. DOI: 10.1016/J.IJHYDENE.2017.08.105

58. Huang K. Solid Oxide Fuel Cells. In: Gasik M, editor. Materials for fuel cells. Cambridge: Woodhead Publishing Limited; 2008. pp. 280–343.

59. Mukerjee S, Leah R, Selby M, Stevenson G, Brandon NP. Chapter 9 – Life and Reliability of Solid Oxide Fuel Cell-Based Products: A Review. In: Brandon NP, Ruiz-Trejo E, Boldrin P, editors. Solid Oxide Fuel Cell Lifetime and Reliability. London: Elsevier; 2017. pp. 173–91. DOI: 10.1016/B978-0-08-101102-7.00009-X

60. Knibbe R, Hauch A, Hjelm J, Ebbesen SD, Mogensen M. Durability of solid oxide cells. Green. 2011;1(2);pp.:141–69. DOI: 10.1515/GREEN.2011.015

61. Arachi Y, Sakai H, Yamamoto O, Takeda Y, Imanishai N. Electrical conductivity of the ZrO2-Ln2O3 (Ln = lanthanides) system. Solid State Ionics. 1999;121(1);pp.:133–9. DOI: 10.1016/S0167-2738(98)00540-2

62. Hohnke D. Ionic conduction in doped oxides with the fluorite structure. Solid State Ionics. 1981;5;pp.:531–4. DOI: 10.1016/0167-2738(81)90309-X

63. Filal M, Petot C, Mokchah M, Chateau C, Carpentier JL. Ionic conductivity of yttrium-doped zirconia and the "composite effect." Solid State Ionics. 1995;80(1–2);pp.:27–35. DOI: 10.1016/0167-2738(95)00137-U

64. Dalslet B, Blennow P, Hendriksen PV, Bonanos N, Lybye D, Mogensen M. Assessment of doped ceria as electrolyte. Journal of Solid State Electrochemistry. 2006;10(8);pp.:547–61. DOI: 10.1007/s10008-006-0135-x

65. Ishihara T. Perovskite Oxide for Solid Oxide Fuel Cells. Ishihara T, editor. New York: Springer; 2009. DOI: 10.1007/978-0-387-77708-5

66. Hossain S, Abdalla AM, Jamain SNB, Zaini JH, Azad AK. A review on proton conducting electrolytes for clean energy and intermediate temperature-solid oxide fuel cells. Renewable and Sustainable Energy Reviews. 2017;79;pp.:750–64. DOI: 10.1016/j.rser.2017.05.147

67. Fabbri E, Pergolesi D, Traversa E. Materials challenges toward proton-conducting oxide fuel cells: A critical review. Chemical Society Reviews. 2010;39(11);pp.:4355–69. DOI: 10.1039/b902343g

68. McEvoy A. Anodes. In: Singhal SC, Kendall K, editors. High Temperature and Solid Oxide Fuel Cells. Oxford: Elsevier; 2003. pp. 149–71. DOI: 10.1016/B978-185617387-2/50023-4

69. Jacobson AJ. Materials for solid oxide fuel cells. Chemistry of Materials. 2010;22(3);pp.:660–74. DOI: 10.1021/cm902640j

70. Costa P, Pinto F, André RN, Marques P. Integration of gasification and solid oxide fuel cells (SOFCs) for combined heat and power (CHP). Processes. 2021;9(2);pp.:1–26. DOI: 10.3390/pr9020254

71. Li R, Zhang C, Liu J, Zhou J, Xu L. A review on the electrical properties of doped SrTiO3 as anode materials for solid oxide fuel cells. Materials Research Express. 2019;6(10);p.:102006. DOI: 10.1088/2053-1591/ab4303

72. Korjus. File:Perovskite ABO3.jpg. wikimedia commons. 2011 [accessed 31 October 2022]; Available from: https://commons.wikimedia.org/wiki/File:Perovskite_ABO3.jpg

73. Cava R. Perovskite Structure and Derivatives. Princeton.edu. [accessed 31 October 2022]; Available from: https://www.princeton.edu/~cavalab/tutorials/public/structures/perovskites.html

74. Perovskite-info.com. An introduction to Perovskites. [accessed 31 October 2022]; Available from: https://www.perovskite-info.com/introduction

75. Mizusaki J, Yonemura Y, Kamata H, Ohyama K, Mori N, Takai H, Tagawa H, Dokiya M, Naraya K, Sasamoto T, Inaba H, Hashimoto T. Electronic conductivity, Seebeck coefficient, defect and electronic structure of nonstoichiometric La1-xSrxMnO3. Solid State Ionics. 2000;132(3–4);pp.:167–80. DOI: 10.1016/S0167-2738(00)00662-7

76. Grenier JC, Bassat JM, Mauvy F. Novel cathodes for solid oxide fuel cells. In: Kilner JA, Skinner SJ, Irvine SJC, Edwards PP, editors. Functional Materials for Sustainable Energy Applications. Cambridge: Woodhead Publishing; 2012. pp. 402–44. DOI: 10.1533/9780857096371.3.402

77. Sasaki K. The Impact of Fuels on Solid Oxide Fuel Cell Anode Lifetime: The Relationship Between Fuel Composition, Fuel Impurities, and Anode Lifetime and Reliability. In: Brandon NP, Ruiz-Trejo E, Boldrin P, editors. Solid Oxide Fuel Cell Lifetime and Reliability. Academic Press; 2017. pp. 37–50. DOI: 10.1016/B978-0-08-101102-7.00003-9

78. Ratcliff M, Bain R. Fuel Cell Integration – A Study of the Impacts of Gas Quality and Impurities. Golden (Colorado, US): National Renewable Energy Laboratory; 2001.

79. Błesznowski M, Jewulski J, Zieleniak A. Determination of H2S and HCl concentration limits in the fuel for anode supported SOFC operation. Central European Journal of Chemistry. 2013;11(6);pp.:960–7. DOI: 10.2478/s11532-013-0228-1

80. Matsuzaki Y, Yasuda I. The poisoning effect of sulfur-containing impurity gas on a SOFC anode: Part I. Dependence on temperature, time, and impurity concentration. Solid State Ionics. 2000;132(3–4);pp.:261–9. DOI: 10.1016/S0167-2738(00)00653-6

81. Aphale A, Liang C, Hu B, Singh P. Chapter 6 – Cathode Degradation From Airborne

Contaminants in Solid Oxide Fuel Cells: A Review. In: Brandon NP, Ruiz-Trejo E, Boldrin P, editors. Solid Oxide Fuel Cell Lifetime and Reliability. London: Elsevier; 2017. pp. 101–19. DOI: 10.1016/B978-0-08-101102-7.00006-4

82. Offer GJ, Mermelstein J, Brightman E, Brandon NP. Thermodynamics and Kinetics of the Interaction of Carbon and Sulfur with Solid Oxide fuel Cell Anodes. Journal of the American Ceramic Society. 2009;92(4);pp.:763–80. DOI: 10.1111/j.1551-2916.2009.02980.x

83. Sasaki K, Teraoka Y. Equilibria in Fuel Cell Gases. Journal of The Electrochemical Society. 2003;150(7);pp.:A878–84. DOI: 10.1149/1.1577337

84. Tariq F, Bertei A, Ruiz-Trejo E, Boldrin P, Brandon NP. Chapter 5 – Microstructural Degradation: Mechanisms, Quantification, Modeling and Design Strategies to Enhance the Durability of Solid Oxide Fuel Cell Electrodes. In: Brandon NP, Ruiz-Trejo E, Boldrin P, editors. Solid Oxide Fuel Cell Lifetime and Reliability. London: Elsevier; 2017. pp. 79–99. DOI: 10.1016/B978-0-08-101102-7.00005-2

85. Atkinson A. Chapter 2 – Solid Oxide Fuel Cell Electrolytes—Factors Influencing Lifetime. In: Brandon NP, Ruiz-Trejo E, Boldrin P, editors. Solid Oxide Fuel Cell Lifetime and Reliability. London: Elsevier; 2017. pp. 19–35. DOI: 10.1016/B978-0-08-101102-7.00002-7

86. Wood T, Ivey DG. Chapter 4 – The Impact of Redox Cycling on Solid Oxide Fuel Cell Lifetime. In: Brandon NP, Ruiz-Trejo E, Boldrin P, editors. Solid Oxide Fuel Cell Lifetime and Reliability. London: Elsevier; 2017. pp. 51–77. DOI: 10.1016/B978-0-08-101102-7.00004-0

87. Park K, Yu S, Bae J, Kim H, Ko Y. Fast performance degradation of SOFC caused by cathode delamination in long-term testing. International Journal of Hydrogen Energy. 2010;35(16);pp.:8670–7. DOI: 10.1016/j.ijhydene.2010.05.005

88. Figueiredo F, Frade JR, Marques FMB. Electrical and electrochemical behaviour of LaCoO3-d+La2(Zr,Y)2O7-based electrode materials. Solid State Ionics. 1999;118(1–2);pp.:81–7. DOI: 10.1016/S0167-2738(98)00470-6

89. Tietz F. Thermal expansion of SOFC materials. Ionics. 1999;5(1–2);pp.:129–39. DOI: 10.1007/BF02375916

90. Lee YH, Muroyama H, Matsui T, Eguchi K. Degradation of nickel-yttria-stabilized zirconia anode in solid oxide fuel cells under changing temperature and humidity conditions. Journal of Power Sources. 2014;262;pp.:451–6. DOI: 10.1016/j.jpowsour.2014.03.031

91. Koo B, Kim K, Kim JK, Kwon H, Han JW. Sr Segregation in Perovskite Oxides : Why It Happens and How It Exists. Joule. 2018;2(8);pp.:1476–99. DOI: 10.1016/j.joule.2018.07.016

92. Kim WH, Song HS, Moon J, Lee HW. Intermediate temperature solid oxide fuel cell using (La,Sr)(Co,Fe)O3-based cathodes. Solid State Ionics. 2006;177(35–36);pp.:3211–6. DOI: 10.1016/j.ssi.2006.07.049

93. Harrison CM, Slater PR, Steinberger-Wilckens R. A review of Solid Oxide Fuel Cell cathode materials with respect to their resistance to the effects of chromium poisoning. Solid State Ionics. 2020;354;p.:115410. DOI: 10.1016/j.ssi.2020.115410

94. Wu J, Liu X. Recent Development of SOFC Metallic Interconnect. Journal of Materials Science and Technology. 2010;26(4);pp.:293–305. DOI: 10.1016/S1005-0302(10)60049-7

95. Harrison CM, Slater PR, Steinberger-Wilckens R. Lanthanum nickelates and their application in Solid Oxide Cells – The LaNi1-xFexO3 system and other ABO3-type nickelates. Solid State Ionics. 2021;373(October);p.:115799. DOI: 10.1016/j.ssi.2021.115799

96. Brett DJL, Atkinson A, Brandon NP, Skinner SJ. Intermediate temperature solid oxide fuel cells. Chemical Society Reviews. 2008;37(8);p.:1568. DOI: 10.1039/b612060c

97. Steele BCH. Material science and engineering: The enabling technology for the commercialisation of fuel cell systems. Journal of Materials Science. 2001;36(5);pp.:1053–68. DOI: 10.1023/A:1004853019349

98. Steinberger-Wilckens R, Bucheli O, De Haart LGJ, Hagen A, Kiviaho J, Larsen J, Pyke S, Rietveld B, Sfeir J, Tietz F, Zahid M. Real-SOFC - A joint European effort to improve SOFC durability. ECS Transactions. 2009;25(2 PART 1);pp.:43–56. DOI: 10.1149/1.3205507

99. Yokokawa H, Hori Y, Shigehisa T, Suzuki M, Inoue S, Suto T, et al. Recent Achievements of NEDO Durability Project with an Emphasis on Correlation Between Cathode Overpotential and Ohmic Loss. Fuel Cells. 2017;17(4);pp.:473–97. DOI: 10.1002/fuce.201600186

100. Vora SD, Lundberg WL, Pierre JF. Overview of U.S. Department of energy office of Fossil energy's solid oxide fuel cell program. ECS Transactions. 2017;78(1);pp.:3–19. DOI: 10.1149/07801.0003ecst

101. Skafte TL, Hjelm J, Blennow P, Graves C. Quantitative review of degradation and lifetime of solid oxide cells and stacks. EFCF 2016 proceedings. 2016;12(B0501);pp.:8–26.

102. Fang Q, Blum L, Stolten D. Electrochemical Performance and Degradation Analysis of an SOFC Short Stack Following Operation of More than 100,000 Hours. Journal of the Electrochemical Society. 2019;166(16);pp.:F1320–5. DOI: 10.1149/2.0751916jes

103. Fang Q, Batfalsky P, Niewolak L, Blum L, Quadakkers WJ. Post-test Characterization of Metallic Materials and Adjacent Components in an SOFC Stack After 34,000 h Operation at 700°C. Fuel Cells. 2019;19(1);pp.:84–95. DOI: 10.1002/fuce.201800050

104. Menzler NH, Sebold D, Sohn YJ, Zischke S. Post-test characterization of a solid oxide fuel cell after more than 10 years of stack testing. Journal of Power Sources. 2020;478;p.:228770. DOI: 10.1016/j.jpowsour.2020.228770

105. Yokokawa H. Report of Five-Year NEDO Project on Durability/Reliability of SOFC Stacks. ECS Transactions. 2013;57(1);pp.:299–308. DOI: 10.1149/05701.0299ecst

106. Yokokawa H. Towards Comprehensive Description of Stack Durability/Reliability Behavior. Fuel Cells. 2015;15(5);pp.:652–68. DOI: 10.1002/fuce.201400182

107. Ido A, Asano K, Morita H, Yamamoto T, Mugikura Y. Degradation Analysis of SOFC Performance (1) — Severe Operation with High Fuel Utilization. ECS Transactions. 2019;91(1);pp.:801–8. DOI: 10.1149/09101.0801ecst

108. Singhal SC. Advances in Tubular Solid Oxide Fuel Cell Technology. ECS Proceedings Volumes. 1995;1995–1(1);pp.:195–207. DOI: 10.1149/199501.0195PV

109. Groß-Barsnick SM, Fang Q, Batfalsky P, Niewolak L, Blum L, Quadakkers WJ. Post-test Characterization of Metallic Materials and Adjacent Components in an SOFC Stack After 34,000 h Operation at 700 °C. Fuel Cells. 2019;19(1);pp.:84–95. DOI: 10.1002/fuce.201800050

110. Blum L, Fang Q, Groß-Barsnick SM, de Haart LGJ (Bert), Malzbender J, Menzler NH, Quadakkers WJ. Long-term operation of solid oxide fuel cells and preliminary findings on accelerated testing. International Journal of Hydrogen Energy. 2020;45(15);pp.:8955–64. DOI: 10.1016/j.ijhydene.2020.01.074

111. Bianco M, Ouweltjes JP, Van herle J. Degradation analysis of commercial interconnect materials for solid oxide fuel cells in stacks operated up to 18000 hours. International Journal

of Hydrogen Energy. 2019;44(59);pp.:31406–22. DOI: 10.1016/j.ijhydene.2019.09.218

112. Borglum B, Tang E, Patsula M. The Status of SOFC Development at Versa Power Systems. ECS Proceedings Volumes. 2005;2005-07(1);pp.:89–97. DOI: 10.1149/200507.0089PV

113. Yang J, Huang W, Wang X, Li J, Yan D, Pu J, Chi B, Li J. Study on component interface evolution of a solid oxide fuel cell stack after long term operation. Journal of Power Sources. 2018;387;pp.:57–63. DOI: 10.1016/j.jpowsour.2018.03.040

114. De Haart LGJ, Mougin J, Posdziech O, Kiviaho J, Menzler NH. Stack degradation in dependence of operation parameters; the real-SOFC sensitivity analysis. Fuel Cells. 2009;9(6);pp.:794–804. DOI: 10.1002/fuce.200800146

115. Chen K, Jiang SP. Surface Segregation in Solid Oxide Cell Oxygen Electrodes : Phenomena , Mitigation Strategies and Electrochemical Properties. Electrochemical Energy Reviews. 2020;3(4);pp.:730–65. DOI: 10.1007/s41918-020-00078-z

116. Li Y, Zhang W, Zheng Y, Chen J, Yu B, Chen Y, Liu M. Controlling cation segregation in perovskite-based electrodes for high electro-catalytic activity and durability. Chemical Society Reviews. 2017;46(20);pp.:6345–78. DOI: 10.1039/C7CS00120G

117. Jiang SP, Love JG. Origin of the initial polarization behavior of Sr-doped LaMnO3 for O2 reduction in solid oxide fuel cells. Solid State Ionics. 2001;138(3–4);pp.:183–90. DOI: 10.1016/S0167-2738(00)00806-7

118. Pan Z, Liu Q, Zhang L, Zhang X, Chan SH. Effect of Sr Surface Segregation of La 0.6 Sr 0.4 Co 0.2 Fe 0.8 O 3 − δ Electrode on Its Electrochemical Performance in SOC. Journal of The Electrochemical Society. 2015;162(12);pp.:F1316–23. DOI: 10.1149/2.0371512jes

119. Yin X, Bencze L, Motalov V, Spatschek R, Singheiser L. Thermodynamic perspective of Sr-related degradation issues in SOFCs. International Journal of Applied Ceramic Technology. 2018;15(2);pp.:380–90. DOI: 10.1111/ijac.12809

120. Tu H., Takeda Y, Imanishi N, Yamamoto O. Ln0.4Sr0.6Co0.8Fe0.2O3−δ (Ln=La, Pr, Nd, Sm, Gd) for the electrode in solid oxide fuel cells. Solid State Ionics. 1999;117(3);pp.:277–81. DOI: 10.1016/S0167-2738(98)00428-7

121. Yang Z, Guo M, Wang N, Ma C, Wang J, Han M. A short review of cathode poisoning and corrosion in solid oxide fuel cell. International Journal of Hydrogen Energy. 2017;42(39);pp.:24948–59. DOI: 10.1016/j.ijhydene.2017.08.057

122. Lee W, Han JW, Chen Y, Cai Z, Yildiz B. Cation size mismatch and charge interactions drive dopant segregation at the surfaces of manganite perovskites. Journal of the American Chemical Society. 2013;135(21);pp.:7909–25. DOI: 10.1021/ja3125349

123. Lee W, Yildiz B. Factors that Influence Cation Segregation at the Surfaces of Perovskite Oxides. ECS Transactions. 2013;57(1);pp.:2115–23. DOI: 10.1149/05701.2115ecst

124. Kwon H, Lee W, Han JW. Suppressing cation segregation on lanthanum-based perovskite oxides to enhance the stability of solid oxide fuel cell cathodes. RSC Advances. 2016;6(74);pp.:69782–9. DOI: 10.1039/c6ra15253h

125. Kostogloudis GC, Tsiniarakis G, Ftikos C. Chemical reactivity of perovskite oxide SOFC cathodes and yttria stabilized zirconia. Solid State Ionics. 2000;135(1–4);pp.:529–35. DOI: 10.1016/S0167-2738(00)00433-1

126. Petric A, Huang P, Tietz F. Evaluation of La–Sr–Co–Fe–O perovskites for solid oxide fuel cells and gas separation membranes. Solid State Ionics. 2000;135(1–4);pp.:719–25. DOI:

10.1016/S0167-2738(00)00394-5

127. Arregui A, Rodriguez-Martinez LM, Modena S, Bertoldi M, Van Herle J, Sglavo VM. Stability of ferritic perovskite cathodes in anode-supported solid oxide fuel cells under different processing and operation parameters. Electrochimica Acta. 2011;58(1);pp.:312–21. DOI: 10.1016/j.electacta.2011.09.048

128. Gindorf C, Singheiser L, Hilpert K. Chromium vaporisation from Fe,Cr base alloys used as interconnect in fuel cells. Steel Research. 2001;72(11–12);pp.:528–33. DOI: 10.1002/srin.200100163

129. Yang Z, Weil KS, Paxton DM, Stevenson JW. Selection and Evaluation of Heat-Resistant Alloys for SOFC Interconnect Applications. Journal of The Electrochemical Society. 2003;150(9);pp.:A1188–201. DOI: 10.1149/1.1595659

130. Hilpert K, Das D, Miller M, Peck D., Weiss R. Chromium Vapor Species over Solid Oxide Fuel Cell Interconnect Materials and Their Potential for Degradation Processes. Journal of The Electrochemical Society. 1996;143(11);pp.:3642–7. DOI: 10.1149/1.1837264

131. Gindorf C, Singheiser L, Hilpert K. Vaporisation of chromia in humid air. Journal of Physics and Chemistry of Solids. 2005;66(2–4);pp.:384–7. DOI: 10.1016/J.JPCS.2004.06.092

132. Taniguchi S, Kadowaki M, Kawamura H, Yasuo T, Akiyama Y, Miyake Y, Saitoh T. Degradation phenomena in the cathode of a solid oxide fuel cell with an alloy separator. Journal of Power Sources. 1995;55(1);pp.:73–9. DOI: 10.1016/0378-7753(94)02172-Y

133. Beez A, Yin X, Menzler NH, Spatschek R, Bram M. Insight into the Reaction Mechanism of (La 0.58 Sr 0.40)(Co 0.20 Fe 0.80)O 3-δ Cathode with Volatile Chromium Species at High Current Density in a Solid Oxide Fuel Cell Stack. Journal of The Electrochemical Society. 2017;164(10);pp.:F3028–34. DOI: 10.1149/2.0051710jes

134. Das D, Miller M, Nickel H, Hilpert K. Chromium evaporation from SOFC interconnector alloys and degradation process by chromium transport. In: Bossel U, editor. 1st European Solid Oxide Fuel Cell Forum. Lucerne: European Fuel Cell Forum; 1994. pp. 703–14.

135. Quadakkers WJ, Piron-Abellan J, Shemet V, Singheiser L. Metallic interconnectors for solid oxide fuel cells – a review. Materials at High Temperatures. 2003;20(2);pp.:115–27. DOI: 10.1179/mht.2003.015

136. Mah JCW, Muchtar A, Somalu MR, Ghazali MJ. Metallic interconnects for solid oxide fuel cell: A review on protective coating and deposition techniques. International Journal of Hydrogen Energy. 2017;42(14);pp.:9219–29. DOI: 10.1016/J.IJHYDENE.2016.03.195

137. Bianco M, Linder M, Larring Y, Greco F, Van herle J. Chapter 7 – Lifetime Issues for Solid Oxide Fuel Cell Interconnects. In: Brandon NP, Ruiz-Trejo E, Boldrin P, editors. Solid Oxide Fuel Cell Lifetime and Reliability. Elsevier; 2017. pp. 121–44. DOI: 10.1016/B978-0-08-101102-7.00007-6

138. Konysheva E, Penkalla H, Wessel E, Mertens J, Seeling U, Singheiser L, Hilpert K. Chromium Poisoning of Perovskite Cathodes by the ODS Alloy Cr5Fe1Y2O3 and the High Chromium Ferritic Steel Crofer22APU. Journal of The Electrochemical Society. 2006;153(4);pp.:A765–73. DOI: 10.1149/1.2172563

139. Simner SP, Anderson MD, Xia GG, Yang Z, Pederson LR, Stevenson JW. SOFC Performance with Fe-Cr-Mn Alloy Interconnect. Journal of The Electrochemical Society. 2005;152(4);pp.:A740–5. DOI: 10.1149/1.1864332

140. Krumpelt M, Cruse TA, Hash MC. Chromium Interactions with Cathode Materials. ECS Proceedings Volumes. 2005;2005-07(1);pp.:1578–83. DOI: 10.1149/200507.1578PV

141. Wang R, Sun Z, Pal UB, Gopalan S, Basu SN. Mitigation of chromium poisoning of cathodes in solid oxide fuel cells employing CuMn1.8O4spinel coating on metallic interconnect. Journal of Power Sources. 2018;376;pp.:100–10. DOI: 10.1016/j.jpowsour.2017.11.069

142. Kurokawa H, Jacobson CP, DeJonghe LC, Visco SJ. Chromium vaporization of bare and of coated iron–chromium alloys at 1073 K. Solid State Ionics. 2007;178(3–4);pp.:287–96. DOI: 10.1016/J.SSI.2006.12.010

143. Li X, Lee J won, Popov BN. Performance studies of solid oxide fuel cell cathodes in the presence of bare and cobalt coated E-brite alloy interconnects. Journal of Power Sources. 2009;187(2);pp.:356–62. DOI: 10.1016/j.jpowsour.2008.11.018

144. Fujita K, Ogasawara K, Matsuzaki Y, Sakurai T. Prevention of SOFC cathode degradation in contact with Cr-containing alloy. Journal of Power Sources. 2004;131(1–2);pp.:261–9. DOI: 10.1016/j.jpowsour.2003.12.051

145. Hu B, Krishnan S, Liang C, Heo SJ, Aphale AN, Ramprasad R, Singh P. Experimental and thermodynamic evaluation of La1−xSrxMnO3±δ and La1−xSrxCo1−yFeyO3−δ cathodes in Cr-containing humidified air. International Journal of Hydrogen Energy. 2017;42(15);pp.:10208–16. DOI: 10.1016/J.IJHYDENE.2017.01.040

146. Li J, Yan D, Zhang W, Pu J, Chi B, Jian L. The investigation of Cr deposition and poisoning effect on Sr-doped lanthanum manganite cathode induced by cathodic polarization for intermediate temperature solid oxide fuel cell. Electrochimica Acta. 2017;255;pp.:31–40. DOI: 10.1016/j.electacta.2017.09.112

147. Jiang SP, Zhang JP, Apateanu L, Foger K. Deposition of Chromium Species at Sr-Doped LaMnO[sub 3] Electrodes in Solid Oxide Fuel Cells. I. Mechanism and Kinetics. Journal of The Electrochemical Society. 2000;147(11);pp.:4013–22. DOI: 10.1149/1.1394012

148. Jiang SP, Zhang S, Zhen YD. Deposition of Cr Species at (La,Sr)(Co,Fe)O3 Cathodes of Solid Oxide Fuel Cells. Journal of The Electrochemical Society. 2006;153(1);pp.:A127–34. DOI: 10.1149/1.2136077

149. Jiang SP, Zhang JP, Zheng XG. A comparative investigation of chromium deposition at air electrodes of solid oxide fuel cells. Journal of the European Ceramic Society. 2002;22(3);pp.:361–73. DOI: 10.1016/S0955-2219(01)00280-1

150. Wang CC, Becker T, Chen K, Zhao L, Wei B, Jiang SP. Effect of temperature on the chromium deposition and poisoning of La0.6Sr0.4Co0.2Fe0.8O3-δcathodes of solid oxide fuel cells. Electrochimica Acta. 2014;139;pp.:173–9. DOI: 10.1016/j.electacta.2014.07.028

151. Jiang SP, Zhang S, Zhen YD. Early interaction between Fe–Cr alloy metallic interconnect and Sr-doped LaMnO3 cathodes of solid oxide fuel cells. Journal of Materials Research. 2005;20(3);pp.:747–58. DOI: 10.1557/JMR.2005.0101

152. Wang R, Würth M, Pal UB, Gopalan S, Basu SN. Roles of humidity and cathodic current in chromium poisoning of Sr-doped LaMnO3-based cathodes in solid oxide fuel cells. Journal of Power Sources. 2017;360;pp.:87–97. DOI: 10.1016/j.jpowsour.2017.06.005

153. Chen X, Zhen Y, Li J, Jiang SP. Chromium deposition and poisoning in dry and humidified air at (La0.8Sr0.2)0.9MnO3+δ cathodes of solid oxide fuel cells. International Journal of Hydrogen Energy. 2010;35(6);pp.:2477–85. DOI: 10.1016/J.IJHYDENE.2009.12.185

154. Wang R, Pal UB, Gopalan S, Basu SN. Chromium Poisoning Effects on Performance of (La,Sr)MnO 3 -Based Cathode in Anode-Supported Solid Oxide Fuel Cells. Journal of The Electrochemical Society. 2017;164(7);pp.:F740–7. DOI: 10.1149/2.0441707jes

155. Konysheva E, Mertens J, Penkalla H, Singheiser L, Hilpert K. Chromium Poisoning of the Porous Composite Cathode Effect of Cathode Thickness and Current Density. Journal of The Electrochemical Society. 2007;154(12);pp.:B1252–64. DOI: 10.1149/1.2784197

156. Jiang SP, Zhang JP, Foger K. Deposition of Chromium Species at Sr-Doped LaMnO3 Electrodes in Solid Oxide Fuel Cells II. Effect on O2 Reduction Reaction. Journal of The Electrochemical Society. 2000;147(9);pp.:3195–205. DOI: 10.1149/1.1393883

157. Jiang SP, Zhang JP, Foger K. Deposition of Chromium Species at Sr-Doped LaMnO[sub 3] Electrodes in Solid Oxide Fuel Cells: III. Effect of Air Flow. Journal of The Electrochemical Society. 2001;148(7);pp.:C447–55. DOI: 10.1149/1.1374446

158. Jiang SP, Zhen Y. Mechanism of Cr deposition and its application in the development of Cr-tolerant cathodes of solid oxide fuel cells. Solid State Ionics. 2008;179(27–32);pp.:1459–64. DOI: 10.1016/j.ssi.2008.01.006

159. Zhen YD, Tok AIY, Jiang SP, Boey FYC. La(Ni,Fe)O3 as a cathode material with high tolerance to chromium poisoning for solid oxide fuel cells. Journal of Power Sources. 2007;170(1);pp.:61–6. DOI: 10.1016/j.jpowsour.2007.03.079

160. Komatsu T., Arai H., Chiba R., Nozawa K., Arakawa M., Sato K. Cr poisoning suppression in solid oxide fuel cells using LaNi(Fe)O 3 electrodes. Electrochemical and Solid-State Letters. 2006;9(1);pp.:A9–12. DOI: 10.1149/1.2130309

161. Komatsu T, Chiba R, Arai H, Sato K. Chemical compatibility and electrochemical property of intermediate-temperature SOFC cathodes under Cr poisoning condition. Journal of Power Sources. 2008;176(1);pp.:132–7. DOI: 10.1016/j.jpowsour.2007.10.068

162. Zhen Y, Tok AIY, Boey FYC, Jiang SP. Development of Cr-Tolerant Cathodes of Solid Oxide Fuel Cells. Electrochemical and Solid-State Letters. 2008;11(3);pp.:B42–6. DOI: 10.1149/1.2828212

163. Stodolny MK, Boukamp BA, Blank DHA, van Berkel FPF. Impact of Cr-poisoning on the conductivity of LaNi0.6Fe0.4O3. Journal of Power Sources. 2011;196(22);pp.:9290–8. DOI: 10.1016/J.JPOWSOUR.2011.07.070

164. Stodolny MK, Boukamp BA, Blank DHA, van Berkel FPF. Cr-poisoning of a LaNi0.6Fe0.4O3 cathode under current load. Journal of Power Sources. 2012;209;pp.:120–9. DOI: 10.1016/j.jpowsour.2012.02.083

165. Stodolny M, van Berkel FP., Boukamp BA. La(Ni,Fe)O 3 Stability in the Presence of Cr Species - Solid State Reactivity Study. ECS Transactions. 2009;25(2);pp.:2915–22. DOI: 10.1149/1.3205857

166. Zhen YD, Jiang SP. Transition Behavior for O2 Reduction Reaction on (La,Sr)MnO3/YSZ Composite Cathodes of Solid Oxide Fuel Cells. Journal of The Electrochemical Society. 2006;153(12);pp.:A2245–54. DOI: 10.1149/1.2357712

167. Lu K, Shen F. Long term behaviors of La0.8Sr0.2MnO3and La0.6Sr0.4Co0.2Fe0.8O3as cathodes for solid oxide fuel cells. International Journal of Hydrogen Energy. 2014;39(15);pp.:7963–71. DOI: 10.1016/j.ijhydene.2014.03.046

168. Schrödl N, Bucher E, Gspan C, Egger A, Ganser C, Teichert C, Hofer F, Sitte W. Phase decomposition in the chromium- and silicon-poisoned IT-SOFC cathode materials La 0.6 Sr 0.4

CoO 3-δ and La 2 NiO 4+δ. Solid State Ionics. 2016;288;pp.:14–21. DOI: 10.1016/j.ssi.2016.01.006

169. Chen X, Zhang L, Liu E, Jiang SP. A fundamental study of chromium deposition and poisoning at (La0.8Sr0.2)0.95(Mn1−xCox)O3 ± δ (0.0≤ x ≤1.0) cathodes of solid oxide fuel cells. International Journal of Hydrogen Energy. 2011;36(1);pp.:805–21. DOI: 10.1016/J.IJHYDENE.2010.09.087

170. Li W, Lu K, Xia Z. Interaction of (La1-xSrx)nCo 1-yFeyO3-δ cathodes and AISI 441 interconnect for solid oxide fuel cells. Journal of Power Sources. 2013;237;pp.:119–27. DOI: 10.1016/j.jpowsour.2013.03.012

171. Horita T, Xiong Y, Kishimoto H, Yamaji K, Brito ME, Yokokawa H. Chromium Poisoning and Degradation at (La,Sr)MnO3 and (La,Sr)FeO3 Cathodes for Solid Oxide Fuel Cells. Journal of The Electrochemical Society. 2010;157(5);pp.:B614–20. DOI: 10.1149/1.3322103

172. Zhen Y, Jiang SP. Characterization and performance of (La,Ba)(Co,Fe)O3cathode for solid oxide fuel cells with iron-chromium metallic interconnect. Journal of Power Sources. 2008;180(2);pp.:695–703. DOI: 10.1016/j.jpowsour.2008.02.093

173. Chen X, Zhang L, Jiang SP. Chromium Deposition and Poisoning on (La0.6Sr (0.4−x)Ba(x))(Co0.2Fe 0.8)O3 (0≤x≤0.4) Cathodes of Solid Oxide Fuel Cells. Journal of The Electrochemical Society. 2008;155(11);pp.:B1093–101. DOI: 10.1149/1.2969914

174. Chen X, Jiang SP. Highly active and stable (La0.24Sr0.16Ba0.6)(Co0.5Fe0.44Nb0.06)O3−δ (LSBCFN) cathodes for solid oxide fuel cells prepared by a novel mixing synthesis method. Journal of Materials Chemistry A. 2013;1(15);pp.:4871–8. DOI: 10.1039/c3ta10230k

175. Shen F, Lu K. Perovskite-type La0.6Sr0.4Co0.2Fe0.8O3, Ba0.5Sr0.5Co0.2Fe0.8O3, and Sm0.5Sr0.5Co0.2Fe0.8O3 cathode materials and their chromium poisoning for solid oxide fuel cells. Electrochimica Acta. 2016;211;pp.:445–52. DOI: 10.1016/j.electacta.2016.06.070

176. Kim YM, Chen X, Jiang SP, Bae J. Effect of Strontium Content on Chromium Deposition and Poisoning in Ba1−xSrxCo0.8Fe0.2O3−δ (0.3 ≤ x ≤ 0.7) Cathodes of Solid Oxide Fuel Cells. Journal of The Electrochemical Society. 2012;159(2);pp.:B185–94. DOI: 10.1149/2.092202jes

177. Magnone E, Seo MJ, Kim HJ, Park JH. Thermal characterization and compatibility studies of perovskite-type Ba0.5Sr0.5Co0.8Fe0.2O 3-δ (BSCF) oxide with Cr2O3 at high temperature. Journal of Thermal Analysis and Calorimetry. 2014;116(1);pp.:215–8. DOI: 10.1007/s10973-013-3496-2

178. Park E, Taniguchi S, Daio T, Chou JT, Sasaki K. Comparison of chromium poisoning among solid oxide fuel cell cathode materials. Solid State Ionics. 2014;262;pp.:421–7. DOI: 10.1016/j.ssi.2014.01.047

179. Zhao L, Cheng Y, Jiang SP. A new, high electrochemical activity and chromium tolerant cathode for solid oxide fuel cells. International Journal of Hydrogen Energy. 2015;40(45);pp.:15622–31. DOI: 10.1016/J.IJHYDENE.2015.09.091

180. Wang J, Yang Z, Yang K, Chen Y, Xiong X, Peng S. Chromium deposition and poisoning on Ba0.9Co0.7Fe0.2Nb0.1O3−δ cathode of solid oxide fuel cells. Electrochimica Acta. 2018;289;pp.:503–15. DOI: 10.1016/J.ELECTACTA.2018.08.092

181. Xiong C, Li W, Ding D, Pu J, Chi B, Li J. Chromium poisoning effect on strontium-doped samarium manganite for solid oxide fuel cell. International Journal of Hydrogen Energy. 2016;41(45);pp.:20660–9. DOI: 10.1016/j.ijhydene.2016.07.061

182. Matsuzaki Y, Yasuda I. Dependence of SOFC Cathode Degradation by Chromium-Containing Alloy on Compositions of Electrodes and Electrolytes. Journal of The Electrochemical Society. 2001;148(2);pp.:A126–31. DOI: 10.1149/1.1339869

183. Lee SN, Atkinson A, Kilner JA. Chromium Poisoning of La2NiO4+δ Cathodes. ECS Transactions. 2013;57(1);pp.:605–13. DOI: 10.1149/05701.0605ecst

184. Gong Y, Wang R, Banner J, Basu SN, Pal UB, Gopalan S. Improved Tolerance of Lanthanum Nickelate (La2NiO4+δ) Cathodes to Chromium Poisoning Under Current Load in Solid Oxide Fuel Cells. Jom. 2019;71(11);pp.:3848–58. DOI: 10.1007/s11837-019-03724-0

185. Andreas Schuler J, Lübbe H, Hessler-Wyser A, Van herle J. Nd-nickelate solid oxide fuel cell cathode sensitivity to Cr and Si contamination. Journal of Power Sources. 2012;213;pp.:223–8. DOI: 10.1016/J.JPOWSOUR.2012.03.112

186. Choe YJ, Lee KJ, Hwang HJ. Cr Poisoning On Nd2Ni0.95Cu0.05O4+δ Cathode for Solid Oxide Fuel Cells. Archives of Metallurgy and Materials. 2016;61(2);pp.:629–34. DOI: 10.1515/amm-2016-0107

187. Wei B, Schroeder M, Martin M. Surface Cation Segregation and Chromium Deposition on the Double-Perovskite Oxide PrBaCo2O5+δ. ACS Applied Materials and Interfaces. 2018;10(10);pp.:8621–9. DOI: 10.1021/acsami.7b17881

188. Wei B, Chen K, Wang CC, Lü Z, Jiang SP. Performance degradation of SmBaCo2O5+δ cathode induced by chromium deposition for solid oxide fuel cells. Electrochimica Acta. 2015;174;pp.:327–31. DOI: 10.1016/j.electacta.2015.06.019

189. Gu H, Chen H, Zheng Y, Guo L. Effect of chromium poisoning on the electrochemical properties of NdBaCo2O5+δ cathode for IT-SOFCs. International Journal of Hydrogen Energy. 2010;35(6);pp.:2457–62. DOI: 10.1016/J.IJHYDENE.2010.01.023

190. The Faraday Institution. Building a Responsible Cobalt Supply Chain. Didcot: The Faraday Institution; 2020.

191. Reuters. Booming electric vehicle sales drive surge in cobalt prices. Reuters. 2021 [accessed 21 July 2021]; Available from: https://www.reuters.com/article/us-cobalt-prices-graphic-idUSKBN2B41YB

192. Trading Economics. Cobalt. Tradingeconomics.com. 2022 [accessed 19 November 2022]; Available from: https://tradingeconomics.com/commodity/cobalt

193. Obayashi H, Kudo T. Some Crystallographic, Electric and Thermochemical Properties of the Perovskite-Type La 1- x M x NiO 3 (M: Ca, Sr and Ba). Japanese Journal of Applied Physics. 1975;14(3);pp.:330–5. DOI: 10.1143/JJAP.14.330

194. Odier P, Nigara Y, Coutures J, Sayer M. Phase relations in the La-Ni-O system: Influence of temperature and stoichiometry on the structure of La2NiO4. Journal of Solid State Chemistry. 1985;56(1);pp.:32–40. DOI: 10.1016/0022-4596(85)90249-X

195. Falcón H, Goeta AE, Punte G, Carbonio RE. Crystal Structure Refinement and Stability of LaFexNi1−xO3Solid Solutions. Journal of Solid State Chemistry. 1997;133(2);pp.:379–85. DOI: 10.1006/jssc.1997.7477

196. Konysheva E, Suard E, Irvine JTS. Effect of Oxygen Non Stoichiometry and Oxidation State of Transition Elements on High-Temperature Phase Transition in A-Site Deficient. Chemistry of Materials. 2009;21(12);pp.:5307–18. DOI: 10.1021/cm902443n

197. Bannikov DO, Cherepanov VA. Thermodynamic properties of complex oxides in the La–Ni–O

system. Journal of Solid State Chemistry. 2006;179(8);pp.:2721–7. DOI: 10.1016/j.jssc.2006.05.026

198. Chiba R, Yoshimura F, Sakurai Y. An investigation of LaNi1−xFexO3 as a cathode material for solid oxide fuel cells. Solid State Ionics. 1999;124(3–4);pp.:281–8. DOI: 10.1016/S0167-2738(99)00222-2

199. Hrovat M, Katsarakis N, Reichmann K, Bernik S, Kuscer D, Holc J. Characterisation of LaNi1 − xCoxO3 as a possible SOFC cathode material. Solid State Ionics. 1996;83(1–2);pp.:99–105. DOI: 10.1016/0167-2738(95)00224-3

200. Xu X, Pan Y, Zhong Y, Ran R, Shao Z. Ruddlesden–Popper Perovskites in Electrocatalysis. Materials Horizons. 2020;7(10);pp.:2519–65. DOI: 10.1039/D0MH00477D

201. Boehm E, Bassat J, Dordor P, Mauvy F, Grenier J, Stevens P. Oxygen diffusion and transport properties in non-stoichiometric Ln2-xNiO4 oxides. Solid State Ionics. 2005;176(37–38);pp.:2717–25. DOI: 10.1016/j.ssi.2005.06.033

202. Skinner S., Kilner JA. Oxygen diffusion and surface exchange in La2−xSrxNiO4+δ. Solid State Ionics. 2000;135(1–4);pp.:709–12. DOI: 10.1016/S0167-2738(00)00388-X

203. Zinkevich M, Aldinger F. Thermodynamic analysis of the ternary La-Ni-O system. Journal of Alloys and Compounds. 2004;375(1–2);pp.:147–61. DOI: 10.1016/j.jallcom.2003.11.138

204. Zinkevich M, Solak N, Nitsche H, Ahrens M, Aldinger F. Stability and thermodynamic functions of lanthanum nickelates. Journal of Alloys and Compounds. 2007;438(1–2);pp.:92–9. DOI: 10.1016/j.jallcom.2006.08.047

205. Amow G, Davidson I., Skinner S. A comparative study of the Ruddlesden-Popper series, Lan+1NinO3n+1 (n=1, 2 and 3), for solid-oxide fuel-cell cathode applications. Solid State Ionics. 2006;177(13–14);pp.:1205–10. DOI: 10.1016/j.ssi.2006.05.005

206. Amow G, Davidson IJ. Preliminary investigation of the higher-order ruddlesden-popper phases for IT-SOFC cathodes, Lan+1NinO3n+1 (n = 2 and 3). Proceedings - Electrochemical Society. 2005;PV 2005-07;pp.:1745–50. DOI: 10.1149/200507.1745pv

207. Takahashi S, Nishimoto S, Matsuda M, Miyake M. Electrode properties of the ruddlesden-popper series, Lan+1NinO3n+1 (n=1, 2, and 3), as intermediate-temperature solid oxide fuel cells. Journal of the American Ceramic Society. 2010;93(8);pp.:2329–33. DOI: 10.1111/j.1551-2916.2010.03743.x

208. Song J, Ning D, Boukamp B, Bassat JM, Bouwmeester HJM. Structure, electrical conductivity and oxygen transport properties of Ruddlesden–Popper phases Ln n+1 Ni n O 3n+1 (Ln = La, Pr and Nd; n = 1, 2 and 3). Journal of Materials Chemistry A. 2020;00;pp.:1–16. DOI: 10.1039/D0TA06731H

209. Amow G, Skinner SJ. Recent developments in Ruddlesden-Popper nickelate systems for solid oxide fuel cell cathodes. Journal of Solid State Electrochemistry. 2006;10(8);pp.:538–46. DOI: 10.1007/s10008-006-0127-x

210. Sun C, Hui R, Roller J. Cathode materials for solid oxide fuel cells: A review. Journal of Solid State Electrochemistry. 2010;14(7);pp.:1125–44. DOI: 10.1007/s10008-009-0932-0

211. Mahato N, Banerjee A, Gupta A, Omar S, Balani K. Progress in material selection for solid oxide fuel cell technology: A review. Progress in Materials Science. 2015;72;pp.:141–337. DOI: 10.1016/j.pmatsci.2015.01.001

212. Zhao H, Mauvy F, Lalane C, Bassat J, Fourcade S, Grenier J. New cathode materials for ITSOFC:

Phase stability, oxygen exchange and cathode properties of La2−xNiO4+δ. Solid State Ionics. 2008;179(35–36);pp.:2000–5. DOI: 10.1016/j.ssi.2008.06.019

213. Minervini L, Grimes RW, Kilner JA, Sickafus KE. Oxygen migration in La2NiO4 + δ. Journal of Materials Chemistry. 2000;10(10);pp.:2349–54. DOI: 10.1039/b004212i

214. Gao P, Bolon A, Taneja M, Xie Z, Orlovskaya N, Radovic M. Thermal expansion and elastic moduli of electrolyte materials for high and intermediate temperature solid oxide fuel cell. Solid State Ionics. 2017;300;pp.:1–9. DOI: 10.1016/j.ssi.2016.11.015

215. Kharton V V., Figueiredo FM, Navarro L, Naumovich EN, Kovalevsky A V., Yaremchenko AA, Viskup AP, Carneiro A, Marques FMB, Frade JR. Ceria-based materials for solid oxide fuel cells. Journal of Materials Science. 2001;36(5);pp.:1105–17. DOI: 10.1023/A:1004817506146

216. Nishi M, Horita T, Yamaji K, Yokokawa H, Shimonosono T, Kishimoto H, Brito ME, Cho DH, Wang F. Oxide Ion Conductivity of LaNi 0.6 Fe 0.4 O 3. ECS Transactions. 2012;45(1);pp.:171–80. DOI: 10.1149/1.3701306

217. Budiman RA, Uzumaki Y, Hong HJ, Miyazaki T, Hashimoto S, Nakamura T, Yashiro K, Amezawa K, Kawada T. Oxygen nonstoichiometry and transport properties of LaNi0.6Co0.4O3−. Solid State Ionics. 2016;292;pp.:52–8. DOI: 10.1016/j.ssi.2016.05.005

218. Armstrong EN, Duncan KL, Wachsman ED. Effect of A and B-site cations on surface exchange coefficient for ABO3 perovskite materials. Physical Chemistry Chemical Physics. 2013;15(7);pp.:2298–308. DOI: 10.1039/c2cp42919e

219. Berenov A V., Atkinson A, Kilner JA, Bucher E, Sitte W. Oxygen tracer diffusion and surface exchange kinetics in La 0.6Sr0.4CoO3 - δ. Solid State Ionics. 2010;181(17–18);pp.:819–26. DOI: 10.1016/j.ssi.2010.04.031

220. Carter S, Selcuk A, Chater RJ, Kajda J, Kilner JA, Steele BCH. Oxygen transport in selected nonstoichiometric perovskite-structure oxides. Solid State Ionics. 1992;53–56;pp.:597–605. DOI: 10.1016/0167-2738(92)90435-R

221. Orui H, Watanabe K, Chiba R, Arakawa M. Application of LaNi(Fe)O3 as SOFC Cathode. Journal of The Electrochemical Society. 2004;151(9);pp.:A1412–7. DOI: 10.1149/1.1779628

222. Jeong C, Lee JH, Park M, Hong J, Kim H, Son JW, Lee JH, Kim BK, Yoon KJ. Design and processing parameters of La2NiO4+δ-based cathode for anode-supported planar solid oxide fuel cells (SOFCs). Journal of Power Sources. 2015;297;pp.:370–8. DOI: 10.1016/j.jpowsour.2015.08.023

223. Hrovat M, Holc J, Samardžija Z, Bernik S. Subsolidus phase equilibria in the La2O3-CeO2-NiO system. Journal of Materials Science Letters. 2000;19(3);pp.:233–5. DOI: 10.1023/A:1006714909627

224. Pérez-Coll D, Aguadero A, Escudero MJ, Núñez P, Daza L. Optimization of the interface polarization of the La2NiO4-based cathode working with the Ce1-xSmxO2-δ electrolyte system. Journal of Power Sources. 2008;178(1);pp.:151–62. DOI: 10.1016/j.jpowsour.2007.12.030

225. Pérez-Coll D, Aguadero A, Escudero MJ, Daza L. Effect of DC current polarization on the electrochemical behaviour of La2NiO4+δ and La3Ni2O7+δ-based systems. Journal of Power Sources. 2009;192(1);pp.:2–13. DOI: 10.1016/j.jpowsour.2008.10.073

226. Philippeau B, Mauvy F, Mazataud C, Fourcade S, Grenier JC. Comparative study of electrochemical properties of mixed conducting Ln2NiO4+δ (Ln=La, Pr and Nd) and

La0.6Sr0.4Fe0.8Co0.2O3−δ as SOFC cathodes associated to Ce0.9Gd0.1O2−δ, La0.8Sr0.2Ga0.8Mg0.2O3−δ and La9Sr1Si6O26.5 electrolytes. Solid State Ionics. 2013;249–250;pp.:17–25. DOI: 10.1016/j.ssi.2013.06.009

227. Sayers R, Liu J, Rustumji B, Skinner SJ. Novel K 2 NiF 4 -Type Materials for Solid Oxide Fuel Cells: Compatibility with Electrolytes in the Intermediate Temperature Range. Fuel Cells. 2008;8(5);pp.:338–43. DOI: 10.1002/fuce.200800023

228. Lou Z, Peng J, Dai N, Qiao J, Yan Y, Wang Z, Wang J, Sun K. High performance La 3Ni 2O 7 cathode prepared by a facile sol-gel method for intermediate temperature solid oxide fuel cells. Electrochemistry Communications. 2012;22(1);pp.:97–100. DOI: 10.1016/j.elecom.2012.06.004

229. Kim S, Choi S, Jun A, Shin J, Kim G. Scale-Down and Sr-Doping Effects on La 4 Ni 3 O 10- δ –YSZ Nanocomposite Cathodes for IT-SOFCs. Journal of The Electrochemical Society. 2014;161(14);pp.:F1468–73. DOI: 10.1149/2.0791414jes

230. Choi S, Kim G. Electrochemical Properties of La 4 Ni 3 O 10 -GDC Composite Cathode by Facile Sol-gel Method for IT-SOFCs. Journal of the Korean Ceramic Society. 2014;51(4);pp.:265–70. DOI: 10.4191/kcers.2014.51.4.265

231. Tucker MC, Cheng L, Dejonghe LC. Selection of cathode contact materials for solid oxide fuel cells. Journal of Power Sources. 2011;196(20);pp.:8313–22. DOI: 10.1016/j.jpowsour.2011.06.044

232. Sharma RK, Burriel M, Djurado E. La4Ni3O10-δ as an efficient solid oxide fuel cell cathode: Electrochemical properties versus microstructure. Journal of Materials Chemistry A. 2015;3(47);pp.:23833–43. DOI: 10.1039/c5ta07862h

233. Sharma RK, Burriel M, Dessemond L, Bassat JM, Djurado E. Lan+1NinO3n+1 (n = 2 and 3) phases and composites for solid oxide fuel cell cathodes: Facile synthesis and electrochemical properties. Journal of Power Sources. 2016;325;pp.:337–45. DOI: 10.1016/j.jpowsour.2016.06.047

234. Ding D, Li X, Lai SY, Gerdes K, Liu M. Enhancing SOFC cathode performance by surface modification through infiltration. Energy and Environmental Science. 2014;7(2);pp.:552–75. DOI: 10.1039/c3ee42926a

235. Budiman RA, Hashimoto S ichi, Yashiro K, Amezawa K, Kawada T. Electrochemical Performance and Reaction Mechanism of LaNi 0.6 Fe 0.4 O 3-δ – Ce 0.9 Gd 0.1 O 1.95 Composite Electrode for Solid Oxide Fuel Cell. ECS Transactions. 2013;57(1);pp.:1873–8. DOI: 10.1149/05701.1873ecst

236. Laberty C, Zhao F, Swider-Lyons KE, Virkar A V. High-performance solid oxide fuel cell cathodes with lanthanum-nickelate- based composites. Electrochemical and Solid-State Letters. 2007;10(10);pp.:170–4. DOI: 10.1149/1.2760188

237. Huang S, Feng S, Wang H, Li Y, Wang C. LaNi0.6Fe0.4O3-Ce0.8Sm0.2O1.9-Ag composite cathode for intermediate temperature solid oxide fuel cells. International Journal of Hydrogen Energy. 2011;36(17);pp.:10968–74. DOI: 10.1016/j.ijhydene.2011.05.135

238. Tang H, Jin Z, Wu Y, Liu W, Bi L. Cobalt-free nanofiber cathodes for proton conducting solid oxide fuel cells. Electrochemistry Communications. 2019;100;pp.:108–12. DOI: 10.1016/j.elecom.2019.01.022

239. Chiu TW, Lin YT, Yen IF, Hsieh HH, Wang SF. Properties and performance of La2NiO4+δ-LaNiO3 composite cathodes for intermediate-temperature solid oxide fuel cells.

Ferroelectrics. 2013;457(1);pp.:105–10. DOI: 10.1080/00150193.2013.848763

240. Woolley RJ, Skinner SJ. Novel La 2 NiO 4+δ and La 4 Ni 3 O 10−δ composites for solid oxide fuel cell cathodes. Journal of Power Sources. 2013;243;pp.:790–5. DOI: 10.1016/j.jpowsour.2013.06.106

241. Pikalova EY, Bogdanovich NM, Kolchugin AA, Osinkin DA, Bronin DI. Electrical and electrochemical properties of La2NiO4+δ-based cathodes in contact with Ce0.8Sm0.2O2-δ electrolyte. Procedia Engineering. 2014;98;pp.:105–10. DOI: 10.1016/j.proeng.2014.12.495

242. Sharma RK, Burriel M, Dessemond L, Martin V, Bassat JM, Djurado E. An innovative architectural design to enhance the electrochemical performance of La2NiO4+δ cathodes for solid oxide fuel cell applications. Journal of Power Sources. 2016;316;pp.:17–28. DOI: 10.1016/j.jpowsour.2016.03.067

243. Molin S, Jasinski PZ. Improved performance of LaNi 0 . 6 Fe 0 . 4 O 3 solid oxide fuel cell cathode by application of a thin interface cathode functional layer. Materials Letters. 2017;189;pp.:252–5. DOI: 10.1016/j.matlet.2016.11.101

244. Pikalova EY, Bogdanovich NM, Kolchugin AA, Ananyev MV, Pankratov AA. Influence of the synthesis method on the electrochemical properties of bilayer electrodes based on La2NiO4 + δ and LaNi0.6Fe0.4O3 − δ. Solid State Ionics. 2016;288;pp.:36–42. DOI: 10.1016/J.SSI.2016.01.014

245. Chrzan A, Karczewski J, Gazda M. Investigation of thin perovskite layers between cathode and doped ceria used as buffer layer in solid oxide fuel cells. Journal of Solid State Electrochemistry. 2015;19;pp.:1807–15. DOI: 10.1007/s10008-015-2815-x

246. Rieu M, Sayers R, Laguna-Bercero MA, Skinner SJ, Lenormand P, Ansart F. Investigation of Graded La[sub 2]NiO[sub 4+δ] Cathodes to Improve SOFC Electrochemical Performance. Journal of The Electrochemical Society. 2010;157(4);pp.:B477–80. DOI: 10.1149/1.3298439

247. Sayers R, Rieu M, Lenormand P, Ansart F, Kilner JA, Skinner SJ. Development of lanthanum nickelate as a cathode for use in intermediate temperature solid oxide fuel cells. Solid State Ionics. 2011;192(1);pp.:531–4. DOI: 10.1016/j.ssi.2010.02.014

248. Chiba R, Komatsu T, Orui H, Taguchi H, Nozawa K, Arai H. SOFC Cathodes Composed of LaNi0.6Fe0.4O3 and Pr-Doped CeO2. Electrochemical and Solid-State Letters. 2009;12(5);pp.:B69–72. DOI: 10.1149/1.3086726

249. Huang B, Zhu X jian, Nie H wen, Niu Y ran, Li Y, Cheng N. Comparison of the electrochemical properties of impregnated and functionally gradient LaNi0.6Fe0.4O3–Gd0.2Ce0.8O2 composite cathodes for Solid Oxide Fuel Cell. Journal of Power Sources. 2013;235;pp.:20–8. DOI: 10.1016/J.JPOWSOUR.2013.02.010

250. Woolley RJ, Skinner SJ. Functionally graded composite La2NiO4+δ and La4Ni3O10-δ solid oxide fuel cell cathodes. Solid State Ionics. 2014;255;pp.:1–5. DOI: 10.1016/j.ssi.2013.11.041

251. Vibhu V, Rougier A, Grenier JC, Bassat JM. Mixed Nickelates Pr2-XLaxNiO4+ Used as Cathodes in Metal Supported SOFCs. ECS Transactions. 2013;57(1);pp.:2093–100. DOI: 10.1149/05701.2093ecst

252. Chauveau F, Mougin J, Mauvy F, Bassat JM, Grenier JC. Electrochemical Performances of Cells Containing Alternative Oxygen Electrodes, Ln 2 NiO 4+δ (Ln=Nd, La). ECS Transactions. 2009;25(2);pp.:2557–64. DOI: 10.1149/1.3205812

253. Zhang X, Zhang H, Liu X. High performance La2NiO4+δ-infiltrated (La 0.6Sr0.4)0.995Co0.2Fe

0.8O3-δ cathode for solid oxide fuel cells. Journal of Power Sources. 2014;269;pp.:412–7. DOI: 10.1016/j.jpowsour.2014.06.132

254. Montenegro-Hernández A, Soldati A, Mogni L, Troiani H, Schreiber A, Soldera F, Caneiro A. Reactivity at the Ln2NiO4+δ/electrolyte interface (Ln = La, Nd) studied by Electrochemical Impedance Spectroscopy and Transmission Electron Microscopy. Journal of Power Sources. 2014;265;pp.:6–13. DOI: 10.1016/j.jpowsour.2014.04.082

255. Lu L, Guo Y, Zhang H, Jin J. Electrochemical performance of La2NiO4+δ-La0.6Sr0.4Co0.2Fe0.8O 3-δ composite cathodes for intermediate temperature solid oxide fuel cells. Materials Research Bulletin. 2010;45(9);pp.:1135–40. DOI: 10.1016/j.materresbull.2010.05.031

256. Carneiro JSA, Brocca RA, Lucena MLRS, Nikolla E. Optimizing cathode materials for intermediate-temperature solid oxide fuel cells (SOFCs): Oxygen reduction on nanostructured lanthanum nickelate oxides. Applied Catalysis B: Environmental. 2017;200;pp.:106–13. DOI: 10.1016/j.apcatb.2016.06.073

257. Hjalmarsson P, Mogensen M. La0.99Co0.4Ni0.6O3-δ- Ce0.8Gd0.2O1.95 as composite cathode for solid oxide fuel cells. Journal of Power Sources. 2011;196(17);pp.:7237–44. DOI: 10.1016/j.jpowsour.2010.11.065

258. Lou X, Wang S, Liu Z, Yang L, Liu M. Improving La0.6Sr0.4Co0.2Fe0.8O3−δ cathode performance by infiltration of a Sm0.5Sr0.5CoO3−δ coating. Solid State Ionics. 2009;180(23–25);pp.:1285–9. DOI: 10.1016/j.ssi.2009.06.014

259. Klotz D, Weber A, Ivers-Tiffée E. Practical Guidelines for Reliable Electrochemical Characterization of Solid Oxide Fuel Cells. Electrochimica Acta. 2017;227;pp.:110–26. DOI: 10.1016/j.electacta.2016.12.148

260. Komatsu T, Yoshida Y, Watanabe K, Chiba R, Taguchi H, Orui H, Arai H. Degradation behavior of anode-supported solid oxide fuel cell using LNF cathode as function of current load. Journal of Power Sources. 2010;195(17);pp.:5601–5. DOI: 10.1016/J.JPOWSOUR.2010.03.078

261. Huang B, Zhu X jian, Ren R xuan, Hu Y xing, Ding X yi, Liu Y bin, Liu Z yao. Chromium poisoning and degradation at Gd0.2Ce0.8O2-impregnated LaNi0.6Fe0.4O3−δ cathode for solid oxide fuel cell. Journal of Power Sources. 2012;216;pp.:89–98. DOI: 10.1016/J.JPOWSOUR.2012.05.058

262. Shaur A, Rehman SU, Kim H sung, Song R hyun, Lim T hyoung, Hong J eun, Park S joo, Lee S bok. Hybrid Electrochemical Deposition Route for the Facile Nanofabrication of a Cr-Poisoning-Tolerant La (Ni , Fe) O 3 − δ Cathode for Solid Oxide Fuel Cells. Applied Materials & Interfaces. 2020;12;pp.:5730–8. DOI: 10.1021/acsami.9b17807

263. Vibhu V, Flura A, Rougier A, Nicollet C, Fourcade S, Hungria T, Grenier JC, Bassat JM. Electrochemical ageing study of mixed lanthanum/praseodymium nickelates La2-xPrxNiO4+δ as oxygen electrodes for solid oxide fuel or electrolysis cells. Journal of Energy Chemistry. 2020;46;pp.:62–70. DOI: 10.1016/j.jechem.2019.10.012

264. Orui H, Nozawa K, Watanabe K, Sugita S, Chiba R, Komatsu T, Arai H, Arakawa M. Development of Practical Size Anode-Supported Solid Oxide Fuel Cells with Multilayer Anode Structures. Journal of the Electrochemical Society. 2008;155(11);pp.:B1110–6. DOI: 10.1149/1.2969942

265. Komatsu T, Watanabe K, Arakawa M, Arai H. A long-term degradation study of power generation characteristics of anode-supported solid oxide fuel cells using

LaNi(Fe)O3electrode. Journal of Power Sources. 2009;193(2);pp.:585–8. DOI: 10.1016/j.jpowsour.2009.04.014

266. Yokoo M, Tabata Y, Yoshida Y, Orui H, Hayashi K, Nozaki Y, Nozawa K, Arai H. Development of 1 kW class solid oxide fuel cell stack using anode-supported planar cells. Journal of Power Sources. 2008;184;pp.:84–9. DOI: 10.1016/j.jpowsour.2008.05.083

267. Yang G, Su C, Ran R, Tade MO, Shao Z. Advanced symmetric solid oxide fuel cell with an infiltrated K 2NiF4-Type La2NiO4 electrode. Energy and Fuels. 2014;28(1);pp.:356–62. DOI: 10.1021/ef401473w

268. Escudero MJ, Fuerte A, Daza L. La2NiO4+δ potential cathode material on La 0.9Sr0.1Ga0.8Mg0.2O2.85 electrolyte for intermediate temperature solid oxide fuel cell. Journal of Power Sources. 2011;196(17);pp.:7245–50. DOI: 10.1016/j.jpowsour.2010.11.068

269. Taguchi H, Chiba R, Komatsu T, Orui H, Watanabe K, Hayashi K. LNF SOFC cathodes with active layer using Pr 6 O 11 or Pr-doped CeO2. Journal of Power Sources. 2013;241;pp.:768–75. DOI: 10.1016/j.jpowsour.2013.04.141

270. Pérez-Coll D, Aguadero A. Electrochemical performance of La2NiO4-based cathode for solid oxide fuel cells. Single cell test. Fuel Cells. 2011;11(1);pp.:91–101. DOI: 10.1002/fuce.201000066

271. Pechini MP. Method of preparing lead and alkaline earth titanates and niobates and coating method using the same to form a capacitor. United States Patent Office. USA: United States Patent Office; 3,330,697, 1967.

272. Danks AE, Hall SR, Schnepp Z. The evolution of “sol-gel” chemistry as a technique for materials synthesis. Materials Horizons. 2016;3(2);pp.:91–112. DOI: 10.1039/c5mh00260e

273. West AR. Basic Solid State Chemistry. 2nd ed. Chichester: John Wiley & Sons; 2000.

274. Dimesso L. Handbook of Sol-Gel Science and Technology. Klein L, Aparicio M, Jitianu A, editors. Handbook of Sol-Gel Science and Technology. Cham: Springer International Publishing; 2018. DOI: 10.1007/978-3-319-32101-1

275. Somalu MR, Muchtar A, Daud WRW, Brandon NP. Screen-printing inks for the fabrication of solid oxide fuel cell films: A review. Renewable and Sustainable Energy Reviews. 2017;75;pp.:426–39. DOI: 10.1016/j.rser.2016.11.008

276. Li T, Wang W. Testing of electrodes, cells and short stacks. In: Singhal SC, Kendall K, editors. High-Temperature Solid Oxide Fuel Cells for the 21st Century. Oxford: Elsevier; 2016. pp. 383–406. DOI: 10.1016/B978-0-12-410453-2.00012-9

277. Winkler J, Hendriksen P V., Bonanos N, Mogensen M. Geometric Requirements of Solid Electrolyte Cells with a Reference Electrode. Journal of The Electrochemical Society. 1998;145(4);pp.:1184–92. DOI: 10.1149/1.1838436

278. Huang QA, Hui R, Wang B, Zhang J. A review of AC impedance modeling and validation in SOFC diagnosis. Electrochimica Acta. 2007;52(28);pp.:8144–64. DOI: 10.1016/j.electacta.2007.05.071

279. Finklea H, Chen X, Gerdes K, Pakalapati S, Celik I. Analysis of SOFCs using reference electrodes. Journal of the Electrochemical Society. 2013;160(9). DOI: 10.1149/2.093309jes

280. Chen X. Aging Effects of the Cathode and Determination of Single Electrode Performance in a Solid Oxide Fuel Cell. West Virginia University; 2013.

281. Mogensen M, Hendriksen PV. Testing of Electrodes, Cells and Short Stacks. In: Singhal SC, Kendall K, editors. High-temperature Solid Oxide Fuel Cells: Fundamentals, Design and Applications. Oxford: Elsevier Ltd; 2003. pp. 261–89. DOI: 10.1016/B978-185617387-2/50027-1

282. Klotz D. Characterization and Modeling of Electrochemical Energy Conversion Systems by Impedance Techniques. KIT Scientific Publishing. Karlsruher Institute for Technology; 2012.

283. Jørgensen MJ, Primdahl S, Mogensen M. Characterization of composite SOFC cathodes using electrochemical impedance spectroscopy. Electrochimica Acta. 1999;44(24);pp.:4195–201. DOI: 10.1016/S0013-4686(99)00134-6

284. Jørgensen MJ, Mogensen M. Impedance of Solid Oxide Fuel Cell LSM/YSZ Composite Cathodes. Journal of The Electrochemical Society. 2001;148(5);pp.:A433–42. DOI: 10.1149/1.1360203

285. Tanasini P, Cannarozzo M, Costamagna P, Faes A, Van Herle J, Hessler-Wyser A, Comninellis C. Experimental and Theoretical Investigation of Degradation Mechanisms by Particle Coarsening in SOFC Electrodes. Fuel Cells. 2009;9(5);pp.:740–52. DOI: 10.1002/fuce.200800192

286. Sonn V, Leonide A, Ivers-Tiffée E. Combined Deconvolution and CNLS Fitting Approach Applied on the Impedance Response of Technical Ni⁄8YSZ Cermet Electrodes. Journal of The Electrochemical Society. 2008;155(7);pp.:B675–9. DOI: 10.1149/1.2908860

287. Karlsruhe Institute of Technology. Kramers-Kronig Validity Test Lin-KK for Impedance Spectra. iam.kit.edu. Karlsruhe: Karlsruher Institut fur Technologie; 2021.

288. Henry D, Eby N, Goodge J, Mogk D. X-ray reflection in accordance with Bragg's Law. Carleton.edu. 2018 [accessed 27 November 2022]; Available from: https://serc.carleton.edu/msu_nanotech/methods/BraggsLaw.html

289. International Centre for Diffraction Data. Powder Diffraction File Database. 2022.

290. Bruker. DIFFRAC.EVA. 2022.

291. Research group electrochemical and surface engineering. Scanning Electron Microscopy & Energy Dispersive X-Ray Spectroscopy. [accessed 27 November 2022]; Available from: http://web.iyte.edu.tr/~serifeyalcin/lectures/chem502/L8.pdf

292. Thermofisher. How to Mix Backscattered and Secondary Electron Images. Azo Materials. 2022 [accessed 27 November 2022]; Available from: https://www.azom.com/article.aspx?ArticleID=16390

293. Aguadero A, Alonso JA, Escudero MJ, Daza L. Evaluation of the La 2 Ni 1 − x Cu x O 4 + δ system as SOFC cathode material with 8YSZ and LSGM as electrolytes. Solid State Ionics. 2008;179;pp.:393–400. DOI: 10.1016/j.ssi.2008.01.099

294. Zhang X, Zhang L, Meng J, Zhang W, Meng F, Liu X, Meng J. Highly enhanced electrochemical property by Mg-doping La2Ni1-xMgxO4+Δ (x = 0.0, 0.02, 0.05 and 0.10) cathodes for intermediate-temperature solid oxide fuel cells. International Journal of Hydrogen Energy. 2017;42(49);pp.:29498–510. DOI: 10.1016/j.ijhydene.2017.10.091

295. Escudero MJ, Aguadero A, Alonso JA, Daza L. A kinetic study of oxygen reduction reaction on La2NiO4 cathodes by means of impedance spectroscopy. Journal of Electroanalytical Chemistry. 2007;611(1–2);pp.:107–16. DOI: 10.1016/j.jelechem.2007.08.006

296. Sayers R, Rieu M, Lenormand P, Ansart F, Kilner JA, Skinner SJ. Development of lanthanum

nickelate as a cathode for use in intermediate temperature solid oxide fuel cells. Solid State Ionics. 2011;192(1);pp.:531–4. DOI: 10.1016/j.ssi.2010.02.014

297. Zhao K, Xu Q, Huang DP, Chen W, Chen M, Kim BH. Microstructure and electrochemical properties of porous La 2NiO 4+δ electrode screen-printed on Ce 0.8Sm 0.2O 1.9 electrolyte. Journal of Solid State Electrochemistry. 2012;16(1);pp.:9–16. DOI: 10.1007/s10008-010-1270-y

298. Ferkhi M, Ringuedé A, Khaled A, Zerroual L, Cassir M. La 1.98Ni0 4±δ, a new cathode material for solid oxide fuel cell: Impedance spectroscopy study and compatibility with gadolinia-doped ceria and yttria-stabilized zirconia electrolytes. Electrochimica Acta. 2012;75;pp.:80–7. DOI: 10.1016/j.electacta.2012.04.064

299. Solís C, Navarrete L, Serra JM. Study of Pr and Pr and Co doped La2NiO4+δ as cathodes for La5.5WO11.25-δ based protonic conducting fuel cells. Journal of Power Sources. 2013;240;pp.:691–7. DOI: 10.1016/j.jpowsour.2013.05.055

300. Sharma RK, Khamidy NI, Bassat J marc, Djurado E. La 2-X Pr x NiO 4+δ -Based Efficient SOFC Cathodes: Effect of Microstructure, Composition and Architecture . ECS Transactions. 2017;78(1);pp.:581–91. DOI: 10.1149/07801.0581ecst

301. Bevilacqua M, Montini T, Tavagnacco C, Fonda E, Fornasiero P, Graziani M. Preparation, Characterization, and Electrochemical Properties of Pure and Composite LaNi 0.6 Fe 0.4 O 3 -Based Cathodes for IT-SOFC. Chemistry of Materials. 2007;19(24);pp.:5926–36. DOI: 10.1021/cm071622n

302. Zhu JH, Ghezel-Ayagh H. Cathode-side electrical contact and contact materials for solid oxide fuel cell stacking: A review. International Journal of Hydrogen Energy. 2017;42(38);pp.:24278–300. DOI: 10.1016/j.ijhydene.2017.08.005

303. Pikalova EY, Bogdanovich NM, Kolchugin AA, Ananyev M V., Pankratov AA. Influence of the synthesis method on the electrochemical properties of bilayer electrodes based on La2NiO4 + δ and LaNi0.6Fe0.4O3 - δ. Solid State Ionics. 2016;288;pp.:36–42. DOI: 10.1016/j.ssi.2016.01.014

304. Montenegro-Hernández A, Vega-Castillo J, Mogni L, Caneiro A. Thermal stability of Ln2NiO4+δ (Ln: La, Pr, Nd) and their chemical compatibility with YSZ and CGO solid electrolytes. International Journal of Hydrogen Energy. 2011;36(24);pp.:15704–14. DOI: 10.1016/j.ijhydene.2011.08.105

305. Kiselev EA, Proskurnina N V, Voronin VI, Cherepanov VA. Phase Equilibria and Crystal Structures of Phases in the La – Fe – Ni – O System at 1370 K in Air. Inorganic Materials. 2007;43(2);pp.:209–17. DOI: 10.1134/S0020168507020148

306. Ohzeki T, Hashimoto T, Shozugawa K, Matsuo M. Preparation of LaNi 1 − x Fe x O 3 single phase and characterization of their phase transition behaviors. Solid State Ionics. 2010;181;pp.:1771–82. DOI: 10.1016/j.ssi.2010.09.041

307. Woolley RJ, Illy BN, Ryan MP, Skinner SJ. In situ determination of the nickel oxidation state in La 2NiO4+δ and La4Ni3O 10-δ using X-ray absorption near-edge structure. Journal of Materials Chemistry. 2011;21(46);pp.:18592–6. DOI: 10.1039/c1jm14320d

308. Skinner SJ, Munnings C., Amow G, Whitfield P, Davidson I. Evaluation of La 2 Ni 1 − x Co x O 4 ± δ as a SOFC Cathode Material. Proceedings of The Electrochemical Society. 2003;2003–7;pp.:552–60. DOI: 10.1149/200307.0552PV

309. Niwa E, Uematsu C, Miyashita E, Ohzeki T, Hashimoto T. Conductivity and sintering property

of LaNi 1 − x Fe x O 3 ceramics prepared by Pechini method ☆. Solid State Ionics. 2011;201;pp.:87–93. DOI: 10.1016/j.ssi.2011.08.004

310. Morishima Y, Niwa E, Hashimoto T. Analysis of thermal stability of LaNi1-xFexO3-δ(x = 0.0, 0.2, 0.4) by thermogravimetry and high-temperature X-ray diffraction under controlled oxygen partial pressures. Journal of Thermal Analysis and Calorimetry. 2016;123(3);pp.:1769–75. DOI: 10.1007/s10973-015-4702-1

311. Lou Z, Peng J, Dai N, Qiao J, Yan Y, Wang Z, Wang J, Sun K. High performance La 3Ni 2O 7 cathode prepared by a facile sol-gel method for intermediate temperature solid oxide fuel cells. Electrochemistry Communications. 2012;22(1);pp.:97–100. DOI: 10.1016/j.elecom.2012.06.004

312. Voronin VI, Berger IF, Cherepanov VA, Gavrilova LY, Petrov AN, Ancharov AI, Tolochko BP, Nikitenko SG. Neutron diffraction, synchrotron radiation and EXAFS spectroscopy study of crystal structure peculiarities of the lanthanum nickelates Lan+1NinOy (n=1,2,3). Nuclear Instruments and Methods in Physics Research, Section A: Accelerators, Spectrometers, Detectors and Associated Equipment. 2001;470(1–2);pp.:202–9. DOI: 10.1016/S0168-9002(01)01036-1

313. Kalinina EG, Pikalova EY, Kolchugin AA, Pikalov SM, Kaigorodov AS. Cyclic electrophoretic deposition of electrolyte thin- films on the porous cathode substrate utilizing stable suspensions of nanopowders. Solid State Ionics. 2017;302;pp.:126–32. DOI: 10.1016/j.ssi.2017.01.016

314. National Institute of Standards and Technology. NIST Inorganic Crystal Structure Database. Gaithersburg MD; DOI: https://doi.org/10.18434/M32147

315. Harrison CM, Sarruf BJ., Klotz D, Slater PR, Steinberger-Wilkens R. The effects of sintering temperature on the performance of lanthanum nickelate electrodes in Solid Oxide Fuel Cells. Journal TBD. Volume TBD(Issue TBD).

316. Hauch A, Mogensen MB. Testing of electrodes, cells, and short stacks. Vol. 574, CISM International Centre for Mechanical Sciences, Courses and Lectures. Elsevier Ltd; 2017. 31-76 pp. DOI: 10.1007/978-3-319-46146-5_2

317. Primdahl S, Mogensen M. Gas Conversion Impedance: A Test Geometry Effect in Characterization of Solid Oxide Fuel Cell Anodes. Journal of The Electrochemical Society. 1998;145(7);pp.:2431–8. DOI: 10.1149/1.1838654

318. Hernández AM, Mogni L, Caneiro A. La2NiO4+δ as cathode for SOFC: Reactivity study with YSZ and CGO electrolytes. International Journal of Hydrogen Energy. 2010;35(11);pp.:6031–6. DOI: 10.1016/j.ijhydene.2009.12.077

319. Nicollet C, Flura A, Vibhu V, Rougier A, Bassat JM, Grenier JC. La2NiO4+δ infiltrated into gadolinium doped ceria as novel solid oxide fuel cell cathodes: Electrochemical performance and impedance modelling. Journal of Power Sources. 2015;294;pp.:473–82. DOI: 10.1016/j.jpowsour.2015.06.077

320. Yeyongchaiwat J, Nonthawissarut K, Charojrochkul S, Sukpirom N. Compatibility and conductivity of La2Ni1-xFexO4+δ and LaNi0•6Fe0•4O3–δ with GDC electrolyte. Energy Materials: Materials Science and Engineering for Energy Systems. 2015;10(2);pp.:1–8. DOI: 10.1179/1743676114Y.0000000203

321. Nørskov JK, Rossmeisl J, Logadottir A, Lindqvist L, Kitchin JR, Bligaard T, Jónsson H. Origin of the overpotential for oxygen reduction at a fuel-cell cathode. Journal of Physical Chemistry B.

2004;108(46);pp.:17886–92. DOI: 10.1021/jp047349j

322. Simner SP, Anderson MD, Pederson LR, Stevenson JW. Performance variability of La(Sr)FeO3 SOFC cathode with Pt, Ag, and Au current collectors. Journal of the Electrochemical Society. 2005;152(9);pp.:1851–9. DOI: 10.1149/1.1995687

323. Orui H, Watanabe K, Chiba R, Arakawa M. Application of LaNi(Fe)O3 as SOFC Cathode. Journal of The Electrochemical Society. 2004;151(9);pp.:A1412–7. DOI: 10.1149/1.1779628

324. Li Y, Cai JW, Alonso A, Lian HQ, Cui XG, Goodenough JB. Evaluation of LaNi0.6M0.4O3 (M=Fe,Co) cathodes in LSGM-electrolyte-supported solid-oxide fuel cells. International Journal of Hydrogen Energy. 2017;2;pp.:1–9. DOI: 10.1016/j.ijhydene.2017.09.031

325. Morán-ruiz A, Vidal K, Laguna-bercero MÁ, Larrañaga A, Arriortua MI. Effects of using (La0.8Sr0.2)0.95Fe0.6Mn0.3Co0.1O3 (LSFMC), LaNi0.6Fe0.4O3-d (LNF) and LaNi0.6Co0.4O3-d (LNC) as contact materials on solid oxide fuel cells. Journal of Power Sources. 2014;248;pp.:1067–76. DOI: 10.1016/j.jpowsour.2013.10.031

326. Amow G, Whitfield PS, Davidson IJ, Hammond RP, Munnings CN, Skinner SJ. Structural and sintering characteristics of the La 2 Ni 1 − x Co x O 4 + δ series. Ceramics International. 2004;30;pp.:1635–9. DOI: 10.1016/j.ceramint.2003.12.164

327. Kim S, Choi S, Jun A, Shin J, Kim G. Scale-Down and Sr-Doping Effects on La 4 Ni 3 O 10- δ –YSZ Nanocomposite Cathodes for IT-SOFCs. Journal of The Electrochemical Society. 2014;161(14);pp.:F1468–73. DOI: 10.1149/2.0791414jes

328. Yoo S, Choi S, Shin J, Liu M, Kim G. Electrical properties, thermodynamic behavior, and defect analysis of Lan+1NinO3n+1+δ infiltrated into YSZ scaffolds as cathodes for intermediate-temperature SOFCs. RSC Advances. 2012;2(11);pp.:4648–55. DOI: 10.1039/c2ra20402a

329. Ivers-Tiffee E, Weber A. Evaluation of electrochemical impedance spectra by the distribution of relaxation times. Journal of the Ceramic Society of Japan. 2017;125(4);pp.:193–201. DOI: 10.2109/jcersj2.16267

330. Leonide A, Sonn V, Weber A, Ivers-Tiffée E. Evaluation and Modeling of the Cell Resistance in Anode-Supported Solid Oxide Fuel Cells. Journal of The Electrochemical Society. 2008;155(1);pp.:B36–41. DOI: 10.1149/1.2801372

331. Udomsilp D, Lenser C, Guillon O, Menzler NH. Performance Benchmark of Planar Solid Oxide Cells Based on Material Development and Designs. Energy Technology. 2021;9(4);pp.:1–18. DOI: 10.1002/ente.202001062

332. Baharuddin NA, Muchtar A, Somalu MR. Short review on cobalt-free cathodes for solid oxide fuel cells. International Journal of Hydrogen Energy. 2017;42(14);pp.:9149–55. DOI: 10.1016/j.ijhydene.2016.04.097

333. Sereda V V, Tsvetkov DS, Ivanov IL, Zuev AY. Oxygen nonstoichiometry , defect structure and related properties of LaNi0.6Fe0.4O3-d. Journal of Materials Chemistry A. 2015;3;pp.:6028–37. DOI: 10.1039/c4ta05882h

334. Li P, Wang Z, Huang X, Zhu L, Cao Z, Zhang Y, Wei B, Zhu X, Lü Z. Enhanced electrochemical performance of co-synthesized La2NiO4+δ-Ce0.55La0.45O2-δcomposite cathode for IT-SOFCs. Journal of Alloys and Compounds. 2017;705;pp.:105–11. DOI: 10.1016/j.jallcom.2017.02.131

335. Hou J, Zhu Z, Qian J, Liu W. A new cobalt-free proton-blocking composite cathode La2NiO4+d-LaNi0.6Fe0.4O3-d for BaZr0.1Ce0.7Y0.2O3-d-based solid oxide fuel cells. Journal of Power

Sources. 2014;264;pp.:67–75. DOI: 10.1016/j.jpowsour.2014.04.089

336. Li P, Huang X, Wei B, Wang Z, Zhang Y, Zhu X, Zhang L, Zhu L, Lü Z. A novel La2NiO4+d-La3Ni2O7-d-Ce0.55La0.45O2-d ternary composite cathode prepared by the co-synthesis method for IT-SOFCs. International Journal of Hydrogen Energy. 2017;42(27);pp.:17202–10. DOI: 10.1016/j.ijhydene.2017.05.202

337. Lang HJ. Effect of Grain Boundaries on Electrical Conductivity and Oxygen Exchange Behaviour of Polycrystalline Lanthanum-Doped Ceria. ECS Proceedings Volumes. 1999;1999–19;pp.:233–43. DOI: 10.1149/199919.0233pv

338. Dikmen S, Shuk P, Greenblatt M. Hydrothermal synthesis and properties of Ce1−xLaxO2−δ solid solutions. Solid State Ionics. 1999;126(1–2);pp.:89–95. DOI: 10.1016/S0167-2738(99)00146-0

339. Adler SB, Lane JA, Steele BCH. Electrode Kinetics of Porous Mixed-Conducting Oxygen Electrodes. Journal of The Electrochemical Society. 1996;143(11);pp.:3554–64. DOI: 10.1149/1.1837252

340. Hou J, Qian J, Bi L, Gong Z, Liu W. The effect of oxygen transfer mechanism on the cathode performance based on proton-conducting solid oxide fuel cells. Journal of Materials Chemistry A. 2015;3;pp.:2207–15. DOI: 10.1039/c4ta04397a

341. Osinkin DA, Antonova EP, Lesnichyova AS, Tropin ES, Chernov ME, Chernov EI, Farlenkov AS, Khodimchuk A V., Eremin VA, Kovrova AI, Kuzmin A V., Ananyev M V. Application of promising electrode materials in contact with a thin-layer ZrO2-based supporting electrolyte for solid oxide fuel cells. Energies. 2020;13(5). DOI: 10.3390/en13051190

342. Li S, Tu H, Yu L, Anwar MT. Fabrication and Performance of Solid Oxide Fuel Cells with La0.2Sr0.7TiO3–δas Anode Support and La2NiO4+δas Cathode. Fuel Cells. 2016;16(6);pp.:822–8. DOI: 10.1002/fuce.201600158

343. Pikalova E, Bogdanovich N, Kolchugin A, Shubin K. Development of composite LaNi0.6Fe0.4O3-based air electrodes for solid oxide fuel cells with a thin- film bilayer electrolyte. International Journal of Hydrogen Energy. 2021;46(32);pp.:16947–64. DOI: 10.1016/j.ijhydene.2021.02.217

344. Zhu Z, Qian J, Wang Z, Dang J, Liu W. High-performance anode-supported solid oxide fuel cells based on nickel-based cathode and Ba(Zr0.1Ce0.7Y0.2)O3-d electrolyte. Journal of Alloys and Compounds. 2013;581;pp.:832–5. DOI: 10.1016/j.jallcom.2013.07.210

345. Chen K, Dai H, He S, Bi L. LaNi0.6Fe0.4O3-d as a promising cathode for Stable Proton-conducting Solid Oxide Fuel Cells. Fuel Cells. 2018;18(4);pp.:561–5. DOI: 10.1002/fuce.201700224

346. Vibhu V, Rougier A, Nicollet C, Flura A, Grenier JC, Bassat JM. La2 - XPrxNiO4 + δ as suitable cathodes for metal supported SOFCs. Solid State Ionics. 2015;278;pp.:32–7. DOI: 10.1016/j.ssi.2015.05.005

347. Aguadero A, Alonso JA, Martínez-Lope MJ, Fernández-Díaz MT, Escudero MJ, Daza L. In situ high temperature neutron powder diffraction study of oxygen-rich La2NiO4+δ in air: Correlation with the electrical behaviour. Journal of Materials Chemistry. 2006;16(33);pp.:3402–8. DOI: 10.1039/b605886h

348. A. Sadykov V, Pikalova E, A. Kolchugin A, F. Eremeev N, M. Bogdanovich N, F. Khasanov A, I. Skriabin P, V. Krasnov A, M. Sadovskaya E, N. Shmakov A, S. Vinokurov Z, V. Ishchenko A, M. Pikalov S, A. Filonova E. Transport Properties of Ca-Doped Ln2NiO4. In: 10th International

Conference on Sustainable Energy and Environmental Protection. Bled; 2017. pp. 87–96. DOI: 10.18690/978-961-286-054-7.8

349. Tsvinkinberg VA, Tolkacheva AS, Filonova EA, Gyrdasova OI, Pikalov SM, Vorotnikov VA, Vylkov AI, Moskalenko NI, Pikalova EY. Structure, thermal expansion and electrical conductivity of La2–xGdxNiO4+δ (0.0 ≤x≤ 0.6) cathode materials for SOFC applications. Journal of Alloys and Compounds. 2021;853;p.:156728. DOI: 10.1016/j.jallcom.2020.156728

350. Takahashi S, Nishimoto S, Matsuda M, Miyake M. Electrode Properties of the Ruddlesden-Popper Series, Lan+1NinO3n+1 (n=1, 2, and 3), as Intermediate-Temperature Solid Oxide Fuel Cells. Journal of the American Ceramic Society. 2010;93(8);pp.:2329–33. DOI: 10.1111/j.1551-2916.2010.03743.x

351. Kuterbekov KA, Bekmyrza KZ, Aidarbekov NK, Nikonov A V., Pavzderin NB, Khrustov VR, Semenova I V., Medvedev AI, Gyrdasova OI. Effect of the cobalt content on properties of La2Ni1-xCoxO4+δ. Solid State Ionics. 2021;363;p.:115594. DOI: 10.1016/j.ssi.2021.115594

352. Kharton V V., Tsipis E V., Naumovich EN, Thursfield A, Patrakeev M V., Kolotygin VA, Waerenborgh JC, Metcalfe IS. Mixed conductivity, oxygen permeability and redox behavior of K2NiF4-type La2Ni0.9Fe0.1O4+δ. Journal of Solid State Chemistry. 2008;181(6);pp.:1425–33. DOI: 10.1016/j.jssc.2008.03.019

353. Wang YP, Xu Q, Huang DP, Zhao K, Chen M, Kim BH. Diagnosis on improved electrocatalytic activity of La 2 Ni 0.8 Cu 0.2 O 4+δ electrodes towards oxygen reduction reaction. Applied Surface Science. 2017;423;pp.:995–1002. DOI: 10.1016/j.apsusc.2017.06.238

354. Huang D ping, Xu Q, Zhang F, Chen W, Liu H xing, Zhou J. Synthesis and electrical conductivity of La2NiO4+δ derived from a polyaminocarboxylate complex precursor. Materials Letters. 2006;60(15);pp.:1892–5. DOI: 10.1016/j.matlet.2005.12.044

355. Al Daroukh M. Oxides of the AMO3 and A2MO4-type: structural stability, electrical conductivity and thermal expansion. Solid State Ionics. 2003;158(1–2);pp.:141–50. DOI: 10.1016/S0167-2738(02)00773-7

356. Lyagaeva J, Medvedev D, Pikalova E, Plaksin S, Brouzgou A. A detailed analysis of thermal and chemical compatibility of cathode materials suitable for electrolytes for solid oxide fuel cell application. Internation Journal of Hydrogen Energy. 2016;42;pp.:1715–23. DOI: 10.1016/j.ijhydene.2016.07.248

357. Flura A, Dru S, Nicollet C, Vibhu V, Fourcade S, Lebraud E, Rougier A, Bassat JM, Grenier JC. Chemical and structural changes in Ln2NiO4+δ (Ln=La, Pr or Nd) lanthanide nickelates as a function of oxygen partial pressure at high temperature. Journal of Solid State Chemistry. 2015;228;pp.:189–98. DOI: 10.1016/j.jssc.2015.04.029

358. Lou Z, Dai N, Wang Z, Dai Y, Yan Y, Qiao J, Peng J, Wang J, Sun K. Preparation and electrochemical characterization of Ruddlesden-Popper oxide La4Ni3O10 cathode for IT-SOFCs by sol-gel method. Journal of Solid State Electrochemistry. 2013;17(10);pp.:2703–9. DOI: 10.1007/s10008-013-2150-z

359. Swierczek K, Marzec J, Palubiak D, Zajac W, Molenda J. LFN and LSCFN perovskites — structure and transport properties. Solid State Ionics. 2006;177;pp.:1811–7. DOI: 10.1016/j.ssi.2006.03.038

360. Nagamoto H, Mochida I, Kagotani K, Inoue H, Negishi A. Change of thermal expansion coefficient and electrical conductivity of LaCo1-xMxO3 (M = Fe,Ni). Journal of Materials Research. 1993;8(12);pp.:3158–62. DOI: 10.1557/JMR.1993.3158

361. Huang K, Lee HY, Goodenough JB. Sr - and Ni - Doped LaCoO 3 and LaFeO 3 Perovskites : New Cathode Materials for Solid - Oxide Fuel Cells. Journal of The Electrochemical Society. 1998;145(9);pp.:3220–7. DOI: 10.1149/1.1838789

362. Wain-Martin A, Moran-Ruiz A, Vidal K, Larrañaga A, Laguna-Bercero MA, Arriortua MI. Scalable synthetic method for SOFC compounds. Solid State Ionics. 2017;313;pp.:52–7. DOI: 10.1016/j.ssi.2017.08.021

363. Chen JY, Rebello J, Vashook V, Trots DM, Wang SR, Wen TL, Zosel J, Guth U. Thermal stability, oxygen non-stoichiometry and transport properties of LaNi0.6Fe0.4O3. Solid State Ionics. 2011;192(1);pp.:424–30. DOI: 10.1016/j.ssi.2010.04.019

364. Bevilacqua M, Montini T, Tavagnacco C, Vicario G, Fornasiero P, Graziani M. Influence of synthesis route on morphology and electrical properties of LaNi0.6Fe0.4O3. Solid State Ionics. 2006;177(33–34);pp.:2957–65. DOI: 10.1016/j.ssi.2006.08.018

365. Vidal K, Morán-ruiz A, Larrañaga A, Porras-vázquez JM, Slater PR, Arriortua MI. Characterization of LaNi0.6Fe0.4O3 perovskite synthesized by glycine-nitrate combustion method. Solid State Ionics. 2015;269;pp.:24–9. DOI: 10.1016/j.ssi.2014.11.002

366. Basu RN, Tietz F, Wessel E, Buchkremer HP, Stöver D. Microstructure and electrical conductivity of LaNi0.6Fe 0.4O3 prepared by combustion synthesis routes. Materials Research Bulletin. 2004;39(9);pp.:1335–45. DOI: 10.1016/j.materresbull.2004.03.015

367. Niwa E, Uematsu C, Hashimoto T. Sintering temperature dependence of conductivity, porosity and specific surface area of LaNi0.6Fe0.4O3 ceramics as cathode material for solid oxide fuel cells - Superiority of Pechini method among various solution mixing processes. Materials Research Bulletin. 2013;48(1);pp.:1–6. DOI: 10.1016/j.materresbull.2012.09.055

368. Yeyongchaiwat J, Nonthawissarut K, Charojrochkul S, Sukpirom N. Compatibility and conductivity of La 2 Ni 1 − x Fe x O 4 + δ La 2 Ni 1 2 x Fe x O 4 + d and LaNi 0.6 Fe 0.4 O 3 - d with GDC electrolyte. Advances in Applied Ceramics. 2015;114;pp.:1–8. DOI: 10.1179/1743676114Y.0000000203

369. Hjalmarsson P, Søgaard M, Hagen A, Mogensen M. Structural properties and electrochemical performance of strontium- and nickel-substituted lanthanum cobaltite. Solid State Ionics. 2008;179(17–18);pp.:636–46. DOI: 10.1016/j.ssi.2008.04.026

370. Kharton V V, Kovalevsky A V, Tikhonovich VN, Naumovich EN, Viskup AP. Mixed electronic and ionic conductivity of LaCo (M) O 3 (M = Ga , Cr , Fe or Ni) II. Oxygen permeation through Cr- and Ni-substituted LaCoO3. Solid State Ionics. 1998;110;pp.:53–60. DOI: https://doi.org/10.1016/S0167-2738(98)00116-7

371. Ben Mya O, dos Santos-Gomez L, Porras-vázquez JM, Omari M, Ramos-Barrado J., Marrero-Lopez D. La1-xSrxFe0.7Ni0.3O3-d as both cathode and anode materials for Solid Oxide Fuel Cells. International Journal of Hydrogen Energy. 2017;2;pp.:1–10. DOI: 10.1016/j.ijhydene.2017.07.150

372. Simner SP, Bonnett JF, Canfield NL, Meinhardt KD, Sprenkle VL, Stevenson JW. Optimized Lanthanum Ferrite-Based Cathodes for Anode-Supported SOFCs. Electrochemical and Solid-State Letters. 2002;5(7);pp.:A173–5. DOI: 10.1149/1.1483156

373. Kharton V V, Viskup AP, Bochkov DM, Naumovich EN, Reut OP. Mixed electronic and ionic conductivity of LaCo (M) O 3 (M 5 Ga , Cr , Fe or Ni) III. Diffusion of oxygen through LaCo1-x-yFexNiyO3+/-d ceramics. Solid State Ionics. 1998;110;pp.:61–8. DOI: https://doi.org/10.1016/S0167-2738(98)00117-9

374. Tian D, Yang Y, Chen Y, Lu X, Lin B. Alkaline-earth-free quasi-ternary La(Co, Ni, Fe)O 3− δ perovskite as potential cathode for solid oxide fuel cells . Materials Research Express. 2019;6(9);p.:096310. DOI: 10.1088/2053-1591/ab2ee8

375. Tai LW, Nasrallah MM, Anderson HU, Sparlin DM, Sehlin SR. Structure and electrical properties of La1 − xSrxCo1 − yFeyO3. Part 2. The system La1 − xSrxCo0.2Fe0.8O3. Solid State Ionics. 1995;76(3–4);pp.:273–83. DOI: 10.1016/0167-2738(94)00245-N

376. Chen M, Moon BH, Kim SH, Kim BH, Xu Q, Ahn BG. Characterization of La0.6Sr0.4Co0.2Fe0.8O3-δ + La2NiO4+δ Composite Cathode Materials for Solid Oxide Fuel Cells. Fuel Cells. 2012;12(1);pp.:86–96. DOI: 10.1002/fuce.201100106

377. Tai LW, Nasrallah MM, Anderson HU, Sparlin DM, Sehlin SR. Structure and electrical properties of La1−xSrxCo1−yFeyO3. Part 1. The system La0.8Sr0.2Co1−yFeyO3. Solid State Ionics. 1995;76(3–4);pp.:259–71. DOI: 10.1016/0167-2738(94)00244-M

378. Tietz F, Arul Raj I, Zahid M, Stover D. Electrical conductivity and thermal expansion of La0.8Sr0.2(Mn,Fe,Co)O3-δ perovskites. Solid State Ionics. 2006;177(19–25);pp.:1753–6. DOI: 10.1016/j.ssi.2005.12.017

379. Tao Y, Shao J, Wang J, Wang WG. Synthesis and properties of La0.6Sr0.4CoO3-δ nanopowder. Journal of Power Sources. 2008;185(2);pp.:609–14. DOI: 10.1016/j.jpowsour.2008.09.021

380. Matsuda M, Ihara K, Miyake M. Influences of Ga doping on lattice parameter, microstructure, thermal expansion coefficient and electrical conductivity of La0.6Sr 0.4CoO3-y. Solid State Ionics. 2004;172(1–4 SPEC. ISS.);pp.:57–61. DOI: 10.1016/j.ssi.2004.02.030

381. Pikalova E, Bogdanovich N, Kolchugin A, Ermakova L, Khrustov A, Farlenkov A, Bronin D. Methods to increase electrochemical activity of lanthanum nickelate-ferrite electrodes for intermediate and low temperature SOFCs. International Journal of Hydrogen Energy. 2021;46(72);pp.:35923–37. DOI: 10.1016/j.ijhydene.2021.01.226

382. Kang H sen, Grewal S, Li H, Lee MH. Effect of Surface-Specific Treatment by Infiltration into LaNi 6 Fe 4 O 3- δ Cathodic Backbone for Solid Oxide Fuel Cells. Journal of The Electrochemical Society. 2019;166(4);pp.:F255–63. DOI: 10.1149/2.0421904jes

383. Khoshkalam MAFS, Tong X, Chen M, Hendriksen PV. Enhanced Activity of Pr6O11 and CuO Infiltrated Ce0.9Gd0.1O2 Based Composite Oxygen Electrodes. Journal of the Electrochemical Society. 2020;167(2);p.:024505. DOI: 10.1149/1945-7111/ab6821

384. Ovtar S, Chen M, Samson AJ, Kiebach R. In-situ formed Ce0.8Gd0.2O1.9 barrier layers on yttria stabilized zirconia backbones by infiltration - A promising path to high performing oxygen electrodes of solid oxide cells. Solid State Ionics. 2017;304;pp.:51–9. DOI: 10.1016/j.ssi.2017.03.019

385. Sharma RK, Djurado E. Functionally graded and homogeneous composites of La2NiO4+: δ and Lan +1NinO3 n +1 (n = 2 and 3) solid oxide fuel cell cathodes. Journal of Materials Chemistry A. 2017;5(42);pp.:22277–87. DOI: 10.1039/c7ta06245a

386. Choi S, Yoo S, Shin JY, Kim G. High Performance SOFC Cathode Prepared by Infiltration of Lan + 1NinO3n + 1 (n = 1, 2, and 3) in Porous YSZ. Journal of The Electrochemical Society. 2011;158(8);pp.:B995–9. DOI: 10.1149/1.3598170

387. Nicollet C, Flura A, Vibhu V, Rougier A, Bassat JM, Grenier JC. Lanthanum Nickelate Infiltration into Porous Gd-Doped Ceria As Cathode for Solid Oxide Fuel Cells. ECS Transactions. 2015;68(1);pp.:837–45. DOI: 10.1149/06801.0837ecst

388. Ghamarinia M, Babaei A, Zamani C. Electrochemical characterization of La2NiO4-infiltrated La0.6Sr0.4Co0.2Fe0.8O3-δ by analysis of distribution of relaxation times. Electrochimica Acta. 2020;353;pp.:1–9. DOI: 10.1016/j.electacta.2020.136520

389. Li Y, Zhang SL, Li CX, Wei T, Yang GJ, Li CJ, Liu M. La2NiO4+δ Infiltration of Plasma-Sprayed LSCF Coating for Cathode Performance Improvement. Journal of Thermal Spray Technology. 2016;25(1–2);pp.:392–400. DOI: 10.1007/s11666-015-0369-1

390. Tang H, Gong Z, Wu Y, Jin Z, Liu W. Electrochemical performance of nanostructured LNF infiltrated onto LNO cathode for BaZr0.1Ce0.7Y0.2O3-d-based solid oxide fuel cell. International Journal of Hydrogen Energy. 2018;43(42);pp.:19749–56. DOI: 10.1016/j.ijhydene.2018.09.008

391. Li J, Zhang Q, Qiu P, Jia L, Chi B, Pu J, Li J. A CO2-tolerant La2NiO4+δ-coated PrBa0.5Sr0.5Co1.5Fe0.5O5+δcathode for intermediate temperature solid oxide fuel cells. Journal of Power Sources. 2017;342;pp.:623–8. DOI: 10.1016/j.jpowsour.2016.12.106

392. Koval'chuk AN, Kuz'min A V., Osinkin DA, Farlenkov AS, Solov'ev AA, Shipilova A V., Ionov I V., Bogdanovich NM, Beresnev SM. Single SOFC with Supporting Ni-YSZ Anode, Bilayer YSZ/GDC Film Electrolyte, and La2NiO4 + δ Cathode. Russian Journal of Electrochemistry. 2018;54(6);pp.:541–6. DOI: 10.1134/S1023193518060101

393. Wang YP, Zhao K, Xu Q, Huang DP, Chen M, Kim BH. Optimization on the electrochemical properties of La2NiO4+Δ cathodes by tuning the cathode thickness. International Journal of Hydrogen Energy. 2018;43(9);pp.:4482–91. DOI: 10.1016/j.ijhydene.2018.01.024

394. Jang DY, Han GD, Choi HR, Kim MS, Choi HJ, Shim JH. La 0.6 Sr 0.4 Co 0.2 Fe 0.8 O 3-δ cathode surface-treated with La 2 NiO 4+δ by aerosol-assisted chemical vapor deposition for high performance solid oxide fuel cells. Ceramics International. 2019;45(9);pp.:12366–71. DOI: 10.1016/j.ceramint.2019.03.162

395. Zhao K, Wang YP, Chen M, Xu Q, Kim BH, Huang DP. Electrochemical evaluation of La2NiO4+δ as a cathode material for intermediate temperature solid oxide fuel cells. International Journal of Hydrogen Energy. 2014;39(13);pp.:7120–30. DOI: 10.1016/j.ijhydene.2014.02.106

396. Lee Y, Kim H. Electrochemical performance of La2NiO4+δ cathode for intermediate-temperature solid oxide fuel cells. Ceramics International. 2015;41(4);pp.:5984–91. DOI: 10.1016/j.ceramint.2015.01.037

397. Nozawa K, Orui H, Chiba R, Arakawa M. Fabrication and Characterization of SOFC Cells with ScSZ Electrolyte and LaNi 1-x Fe x O 3 Cathode for Reduced Temperature Operation. ECS Proceedings Volumes. 2001;2001–16;pp.:983–8. DOI: 10.1149/200116.0983pv

398. Ding X, Ding L, Wang L, Zhu W, Hua G, Liu H, Gao Z, Yuan G. Improved electrochemical activity and stability of LaNi0.6Fe0.4O3-d cathodes achieved by an in-situ reaction. Electrochimica Acta. 2017;236;pp.:378–83. DOI: 10.1016/j.electacta.2017.03.184

399. Luo T, Liu X, Meng X, Wu H, Wang S, Zhan Z. In situ formation of LaNi 0 . 6 Fe 0 . 4 O 3-d - carbon nanotube hybrids as anodes for direct-methane solid oxide fuel cells. Journal of Power Sources. 2015;299;pp.:472–9. DOI: 10.1016/j.jpowsour.2015.09.035

400. Lee S, Bevilacqua M, Fornasiero P, Vohs JM, Gorte RJ. Solid oxide fuel cell cathodes prepared by infiltration of LaNi 0 . 6 Fe 0 . 4 O 3 and La0.91Sr0.09Ni0.6Fe0.4O3 in porous yttria-stabilized zirconia. Journal of Power Sources. 2009;193;pp.:747–53. DOI: 10.1016/j.jpowsour.2009.04.046

401. Haanappel VAC, Bar B, Tropartz C, Mertens J, Tietz F. Various Lanthanum Ferrite-Based

Cathode Materials With Ni and Cu Substitution for Anode-Supported Solid Oxide Fuel Cells. Journal of Fuel Cell Science and Technology. 2010;7;pp.:7–10. DOI: 10.1115/1.4001355

402. Egger A, Sitte W. Enhanced oxygen surface exchange of La2NiO4+δ by means of a thin surface layer of silver. Solid State Ionics. 2014;258;pp.:30–7. DOI: 10.1016/j.ssi.2014.01.038